Imperial College London



Thermoset-Acrylic/Layered-Silicate Nanocomposites: Synthesis and Structure Property Relationships

Anne Elizabeth Tarrant

Imperial College London

A thesis submitted for the degree of
Doctor of Philosophy of the University of London
and the diploma of Imperial College

September 28, 2004



Abstract

Nanocomposites are defined as any two-phase material where one of the phases has one dimension in the nano-scale. The work presented here is concerned with the synthesis and structure-property relationships of thermoset acrylic layered silicate nanocomposites.

The nanocomposites were prepared via in-situ polymerisation from a thermoset type of poly(methyl methacrylate), PMMA, and various commercially available organoclays. The effect of altering certain processing variables (organoclay surfactant, polymerisation initiator, etc) on the microstructure of the composites was investigated using X-ray diffraction (XRD). From analysis of the XRD data it was concluded that all the composites produced possessed intercalated nanocomposite microstructures, this was confirmed by transmission electron microscopy of the composites. Analysis of the XRD data revealed that each organoclay had a maximum achievable intergallery spacing in this system and that as the organoclay content increased the proportion of clay platelets achieving that spacing decreased.

The effect of nanocomposite formation on the glass transition temperature, T_g, and the storage modulus of the composites were examined using dynamic mechanical thermal analysis (DMTA). These tests revealed that effect on T_g and storage modulus was governed by a delicate balance between the matrix plasticisation by the organoclays' surfactant and the confining/reinforcing effect of polymer chains being near to or between clay platelets. Thermogravitmetric analysis revealed that several of the composites had excellent potential as char forming materials, in particular those formed using Cloisite 25A as the organoclay.

Tensile and fracture testing revealed that the composites formed had increased Young's modulus but that the fracture toughness and energy of the composites were severely decreased. This was also found to be the case for the core-shell toughened PMMA-organoclay composites. Examination of the composite fracture surfaces revealed no correlation between the reduced toughness and increased roughness of the composite fracture surfaces, leading to the conclusion that the clay particles act as flaws.

Acknowledgments

There are many individuals to whom I owe a debt of thanks to for supporting and helping me throughout the duration of this project. First and foremost I wish to express my deepest gratitude to my supervisors Professor Anthony Kinloch and Dr Ambrose Taylor for their careful guidance, enthusiasm and encouragement throughout the entirety of this project

I wish to express my gratitude to Mr Richard Sweeney for his guidance in the use of the X-ray diffractometer and for his constant encouragement. Thanks are also due to Dr Mahmoud Ardakani for his patience and the help that he gave me in using the transmission electron microscope.

I wish also to express my thanks to the EPSRC and ICI's Strategic Technology Group for their financial support which was much appreciated. My thanks also go to Dr Gordon Seeley for insightful input to the project.

I am grateful to all my friends for their constant companionship, I owe particular thanks to Mr Reza Mohammed, Mrs Ruth Brooker and Mr Alexander Mills for their proof reading skills and their support.

Finally but by no means least I would like to thank my family for their constant care and belief in me.

.

I Mam a Dad

(For Mam and Dad)

Contents

Abstract 2

Acknowledgments 3

Contents 5

List of Figures 10

List of Tables 20

Abbreviations 23

Nomenclature 25

Chapter 1 – Introduction 27

Chapter 2 – Literature Review 32

2.0 Introduction 32

2.1 Polymers 33

2.1.1 Basics 33

2.1.2 Polymerisation 38

2.1.3 Acrylates 42

2.2 Clays and Layered-Silicates 44

2.2.1 Clay Minerals 44

2.2.2 Classification 47

2.3 Surfactants 50

2.3.1 The Role of a Surfactant 51

2.4 Methods of Nanocomposites Synthesis 53

2.4.1 Synthesis of Nanocomposites 53

2.5 Nanocomposites 60

2.6 Properties of Nanocomposites 64

2.6.1 Effect of Tensile Properties 64

2.6.2 Effect on Viscoelastic Properties 66

2.6.3 Effect on Fracture Properties 71

2.6.4 Other Properties 74

2.7 Theoretical Models for Predicting Certain Properties 79

2.7.1 The Rule of Mixtures 80

2.7.2 The Halpin-Tsai Model 80

2.7.3 The Mori-Tanaka Model 81

2.7.4 The Faber and Evans Model 82

2.8 Toughening of Acrylic Polymers 83

2.8.1 What are Core-Shell Particles? 84

2.8.2 How are Core-shell Particles Formed? 85

2.8.3 What Mechanisms do Core-Shell Particles Employ to Toughen Polymers? 86

2.9 Concluding Remarks 89

Chapter 3 – Materials and Experimental Procedures 90

3.0 Materials 90

3.1 Preparation of Composites 92

3.1.1 Preparation of PMMA-Clay Nanocomposites 92

3.1.2 Preparation of Toughened PMMA-Clay Nanocomposites 94
3.2 Experimental Procedures 95
3.2.1 X-Ray Diffraction 95
3.2.2 Thermogravimetric Analysis 95
3.2.3 Dynamic Mechanical Thermal Analysis 95
3.2.4 Fracture Toughness Testing 96
3.2.5 Tensile Testing 97
3.2.6 Transmission Electron Microscopy 98
3.3 Concluding Remarks 99

Chapter 4 – Results – Microstructure 100

4.0 Introduction 100
4.1 Interpreting X-Ray Diffraction Patterns 101
4.2 Effect of Processing Variables 105
4.2.1 Effect of Surfactant Type 106
4.2.2 Effect of Mixing Time 111
4.2.3 Effect of Percentage Clay Loading 114
4.2.4 Confirmation of X-Ray Diffraction Results using Transmission Electron Microscopy 120
4.2.5 Effect of Choice of Polymerisation Initiator 129
4.3 Microstructure of Rubber Toughened Composites 135
4.4 Repeatability of Microstructure Results 140
4.5 Concluding Remarks 142

Chapter 5 – Results – Physical Properties **144**

5.0 Introduction 144

5.1 Dynamic Mechanical Thermal Analysis Results 145

5.1.1 Effect of Nanocomposite Formation 145

5.1.2 Effect of Choice of Polymerisation Initiator 155

5.1.3 Effect of Core-Shell Addition 159

5.2 Thermal Stability 170

5.2.1 Introduction 170

5.2.2 Thermal Stability of Organoclays 171

5.2.3 Effect of Nanocomposite Formation 174

5.3 Concluding Remarks 181

Chapter 6 – Results – Mechanical Properties **183**

6.0 Introduction 183

6.1 Tensile Properties 184

6.1.1 Effect of Nanocomposite Formation 184

6.1.2 Effect of Choice of Polymerisation Initiator 190

6.1.3 Effect of Core-Shell Addition 193

6.2 Fracture Properties 196

6.2.1 Effect of Nanocomposite Formation 196

6.2.2 Effect of Choice of Polymerisation Initiator 208

6.2.3 Effect of Core-Shell Addition 210

6.3 Comparison of Experimental Data to Theoretical Predictions 221

6.3.1 Introduction 221

6.3.2 Young's Modulus 221

6.3.3 Tensile Strength 224

6.3.4 Fracture Energy 225

6.4 Concluding Remarks 227

Chapter 7 – Conclusions **229**

Chapter 8 – Future Work **233**

References **237**

List of Figures

2.1	An Ethylene Monomer and Part of a Polyethylene Chain	33
2.2	Acrylamide Monomer and Poly(acrylamide).	34
2.3	The Polymer Family Tree.	36
2.4	A Crosslinked Polymer Network.	37
2.5	A Schematic Representation of Chain Growth.	38
2.6	Thermolysis of Benzoyl Peroxide.	40
2.7	Initiation.	40
2.8	Head-to-Head Termination.	41
2.9	A Disproportionation Type Termination.	42
2.10	The Basic Form of an Acrylate Monomer.	42
2.11	A Silicon-Oxygens Tetrahedron.	45
2.12	Tetrahedral Sheet.	45
2.13	Octahedron.	46
2.14(a)	Tri-octahedral Sheet.	46
2.14(b)	Di-octahedral Sheet.	46
2.15	A Scanning Electron Micrograph of Montmorillonite.	47
2.16	Structure of 2:1 Layered Silicates.	49
2.17	The Cation-Exchange Process between Alkylammonium Ions and Cations.	52

2.18	Possible Configurations for Alkylammonium Ions in the Interlayer Gallery.	52
2.19	XRD Pattern of PEO/Na^+-Montmorillonite Hybrid Heated to 80°C for 0, 2 and 6 Hours.	54
2.20	Schematic Representation of the Intercalation Process of PEI into the Organo-Montmorillonite (organo-MMT) and the Exfoliation of Montmorillonite.	55
2.21	A Proposed Pathway for the Formation of an Epoxy-Exfoliated Magadiite Nanocomposite.	56
2.22	XRD Pattern of Organically Modified Mica-Type Silicates/ Diglycidyl Ether of Bisphenol A/Benzyldimethylamine mixture (4° ovol MTS) Heated In-Situ to various Temperature.	58
2.23	The Three Major Possible Different Nanocomposite Microstructures.	61
2.24	XRD Pattern of PEO/Na^+-Montmorillonite Hybrid Heated to 80°C for 0, 2 and 6 Hours.	62
2.25	Different Microstructures for Nanocomposites.	63
2.26	XRD Patterns of Nanocomposites with Delaminated, Intercalated and Conventional (Immiscible) Microstructure.	63
2.27	Variation of Tensile Strength and Young's (Tensile) Modulus with Percentage Loading of Organoclay for Polysulfone-clay Nanocomposites.	66
2.28	Variation of the Storage Modulus for Pure PMMA and its Montmorillonite and Flurohectorite Nanocomposites.	68
2.29	Variation of the Storage Modulus with Temperature for Polyimide and for its 2wt° o Organoclay Nanocomposites.	69

2.30	Effect of Increasing Organically Modified Montmorillonite Content on the T_g of Polyimide Nanocomposites.	70
2.31	Scanning Electron Micrograph of the Fracture Surface of an Unsaturated Polyester Nanocomposites.	72
2.32	Effect of Surfactant Chain Length on the Fracture Toughness of Anhydride Cured Epoxy Nanocomposites.	73
2.33	Thermogravimetric Analysis of Polyetherimide and of Polyetherimide-clay Nanocomposites with Varying Microstructures.	75
2.34	Comparison of Heat Release Rate plot for Nylon-6 and Nylon-6 Silicate Nanocomposite (5wt%).	77
2.35	The Stair-like Structure Suggested by the Pinnavaia Group to Account for the Small Experimental Aspect Ratio Found.	79
2.36	Modes of Fracture.	82
2.37	Relative Fracture Energy Predictions for Initial Tilt and for Maximum Twist based on Crack Deflection Model for Disc-shaped Particles of two Aspect Ratios.	83
2.38	The Morphologies of Typical Core-Shell Particles.	84
2.39	Schematic of the Possible Routes to Forming Various Core-Shell Particles.	85
2.40	Transmission Electron Micrograph of 3-Layer Core-Shell Particles in a SAN/PBA blend.	86
2.41	Schematic of Shear-bands Caused by Shear Yielding.	87
2.42	Cavitated Rubber Particles. Particles formed through the Phase Separation Technique.	88
3.1	Small Compact Tension Specimens Used.	97

3.2	Schematic of Tensile Specimens including Dimensions.	98
4.1	XRD Pattern of Unmodified Clay, Nancor PGW.	101
4.2	XRD Pattern of Montmorillonite (Na^+).	102
4.3	XRD Patterns of an Untreated Clay (PGW), an Organoclay (Cloisite 30B) and of Pressure Sensitive Tape.	103
4.4	XRD Pattern of Cloisite 30B and of its 6wt% Composite.	104
4.5	XRD Pattern of PMMA.	104
4.6	Photograph of PMMA-Cloisite 6A Composite.	106
4.7	The Surfactant used in Cloisite 6A, 15A & 20A.	107
4.8	The Surfactant used in Cloisite 93A.	107
4.9	XRD Patterns of 3wt% Organoclay Composites.	108
4.10	XRD Patterns of 6wt% Organoclay Composites.	109
4.11	The XRD Patterns of Three Cloisite 25A 6wt% Composites Mixed for Variable Lengths of Time and of Cloisite 25A.	111
4.12	XRD Patterns of 6wt% Cloisite 25A Composites Mixed for 1½, 2 and 3 Hours.	113
4.13	XRD Patterns of Cloisite 10A and its 3wt%, 6wt% and 9wt% Composites.	114
4.14	XRD Patterns of Cloisite 25A and its 3wt%, 6wt% and 9wt% Composites.	116
4.15	XRD Patterns of Cloisite 93A and its 3wt%, 6wt%, 9wt% and 12wt% Composites.	117
4.16	XRD Patterns of Cloisite 30B and its 3wt%, 6wt% and 9wt% Composites.	118
4.17	Photograph of 1wt% Composite.	118

4.18	Transmission Electron Micrograph of a PMMA-3wt% Cloisite 25A Composite.	122
4.19	Transmission Electron Micrograph of a PMMA-3wt% Cloisite 93A Composite.	123
4.20	XRD Patterns of a PMMA-3wt% Cloisite 25A Composite and a PMMA-3wt% Cloisite 93A Composite.	124
4.21	Transmission Electron Micrographs of a PMMA-6wt% Cloisite 93A Composite.	125
4.22	Transmission Electron Micrographs of a PMMA-9wt% Cloisite 93A Composite.	126
4.23	XRD Pattern of a PMMA-9wt% Cloisite 93A Composite.	126
4.24	Transmission Electron Micrograph of a 3wt% Cloisite 93A Composite showing Particle Distribution.	127
4.25	Transmission Electron Micrographs of (a) 3wt% Cloisite 25A Composite and (b) 9wt% Cloisite 93A Composite, showing Clay Particle Size and Aspect Ratio.	128
4.26	XRD Patterns of PMMA Initiated with AIBN, Lauroyl Peroxide and Trigonox 23.	129
4.27	XRD Patterns of AIBN, Lauroyl Peroxide and Trigonox 23 Initiated PMMA-Cloisite 25A 6wt% Composites.	130
4.28	XRD Patterns of AIBN, Lauroyl Peroxide and Trigonox 23 Initiated PMMA-Cloisite 93A 6wt% Composites.	131
4.29	XRD Patterns of both Lauroyl Peroxide and Trigonox 23 Initiated 6wt% and 9wt% Cloisite 25A Composites.	134
4.30	XRD Patterns of both Lauroyl Peroxide and Trigonox 23 Initiated 6wt% and 9wt% Cloisite 93A Composites.	134

4.31	Scanning Electron Micrographs of the Core-Shell Particles used in this Work (a) XC42 (b) XC44 and (c) KM355.	136
4.32	Scanning Electron Micrographs of the Fracture Surfaces of a 5wt% KM355-PMMA Composite.	136
4.33	XRD Patterns of PMMA, PMMA-5wt% KM355, PMMA-5wt% XC42 and PMMA-5wt% XC44.	137
4.34	XRD Patterns of Cloisite 25A, its 6wt% Toughened Composites and of a PMMA-6wt% Cloisite 25A Composite.	138
4.35	XRD Patterns of a PMMA-6wt% Cloisite 25A Composite and Toughened PMMA-6wt% Cloisite Composites.	139
4.36	Replicate XRD Patterns of PMMA-3wt% Cloisite 93A Composites.	141
4.37	Replicate XRD Patterns of Toughened PMMA-Cloisite 25A 6wt% Composites.	142
5.1	The First Test Runs of Three Testing Bars of the same Specimen.	146
5.2	The Second Test Runs of Three Testing Bars of the same Specimen.	147
5.3	Variation of Glass Transition Temperature with Percentage Clay Loading for the Organoclays used.	148
5.4	Transmission Electron Micrographs of (a) a Cloisite 25A 3wt% Composite and (b) a Cloisite 93A 6wt% Composite.	149
5.5	The Surfactant of Cloisite 10A.	150
5.6	Typical Plot of the Logarithm of the Storage Modulus against Temperature for PMMA and a PMMA-clay Composite.	151
5.7	Storage Modulus at 20°C versus Clay Loading, for PMMA and Composites.	154

5.8	Storage Modulus at 160°C versus Clay Loading, for PMMA and Composites.	155
5.9	Variation of Tan δ with Temperature for PMMA-KM355 5wt% (10Hz).	159
5.10	The Tan δ Curves for Toughened PMMA and PMMA (2nd run, 10Hz).	161
5.11	Scanning Electron Micrograph of the Fracture Surface of PMMA-XC42.	162
5.12	Scanning Electron Micrograph of the Fracture Surface of PMMA-XC44.	162
5.13	Scanning Electron Micrograph of the Fracture Surface of PMMA-KM355.	163
5.14	Scanning Electron Micrograph of the Fracture Surface of PMMA-KM355.	163
5.15	Scanning Electron Micrograph of the Fracture Surface of KM355 toughened PMMA-Cloisite 25A 6wt% Composite.	165
5.16	XRD Patterns of XC44 toughened PMMA-Cloisite 25A 6wt% and PMMA-Cloisite 25A 6wt% Composites.	167
5.17	Typical Plot of the Logarithm of the Storage Modulus against Temperature for a Toughened PMMA (PMMA-XC42) and a Toughened PMMA-clay Composite.	168
5.18	Scanning Electron Micrograph of the Fracture Surface of PMMA-KM355.	169
5.19	Measured Temperature versus Time for TGA of PMMA-clay Composites Tested in Air and in Argon.	171
5.20	TGA Traces of Montmorillonite and the Organoclays Successfully Used in this Project.	172

5.21	TGA Traces of PMMA and its 3wt% Clay Composites.	175
5.22	TGA Traces of PMMA and its 6wt% Clay Composites.	176
5.23	TGA Traces of PMMA and its 9wt% Clay Composites.	176
5.24	Variation of Onset Temperature of Composites with Percentage Clay Loading for the different Organoclays.	177
6.1	Young's Modulus of PMMA and PMMA-clay Composites.	185
6.2	Tensile Strength of PMMA and PMMA-clay Composites.	188
6.3	Storage Modulus at 20°C of PMMA and PMMA-clay Composites.	189
6.4	Scanning Electron Micrographs of (a) the Fracture Surface of a PMMA-5wt% KM355 Specimen and (b) the Fracture Surface of a PMMA-5wt% KM355-6wt% Cloisite 25A Specimen.	195
6.5	Relative Fracture Energy Predictions for Initial Tilt and for Maximum Twist based on Crack Deflection Model for Disc-shaped Particles of two Aspect Ratios.	197
6.6	Schematic of a Compact Tension Specimen.	197
6.7	Fracture Toughness of PMMA and PMMA-clay Composites.	199
6.8	Fracture Energy of PMMA and PMMA-clay Composites.	201
6.9	Micrograph of Fracture Surface of PMMA.	202
6.10	Micrograph of Fracture Surface of PMMA showing River Markings.	203
6.11	Micrograph of Fracture Surface of PMMA.	203
6.12	Micrograph of Fracture Surface of PMMA-6wt% Cloisite 25A Specimen.	204
6.13	Micrograph of Fracture Surface of PMMA-6wt% Cloisite 25A Specimen.	205

6.14	Micrograph of Fracture Surface of PMMA-6wt% Cloisite 25A Specimen.	205
6.15	Micrograph of Cloisite 25A Particles Before Incorporation With PMMA.	206
6.16	Property Map of Fracture Toughness versus Young's Modulus for PMMA and its Composites.	207
6.17	Scanning Electron Micrograph of the Fracture Surface of KM355 Toughened PMMA.	211
6.18	Scanning Electron Micrograph Demonstrating Electron Beam Damage.	213
6.19	Scanning Electron Micrograph of the Fracture Surface of 5wt% XC42 Toughened PMMA.	213
6.20	Scanning Electron Micrograph of the Fracture Surface of 5wt% XC44 Toughened PMMA.	214
6.21	Scanning Electron Micrograph of the Fracture Surface of 5wt% KM355 Toughened PMMA.	214
6.22	Scanning Electron Micrograph of the Fracture Surface of PMMA.	215
6.23	Scanning Electron Micrographs of the Fracture Surface of 5wt% KM355 Toughened PMMA.	216
6.24	Scanning Electron Micrograph of the Fracture Surface of 5wt% XC42 Toughened PMMA-6wt% Cloisite 25A Composite.	217
6.25	Scanning Electron Micrograph of the Fracture Surface of 5wt% XC44 Toughened PMMA-6wt% Cloisite 25A Composite.	218
6.26	Scanning Electron Micrograph of the Fracture Surface of 5wt% KM355 Toughened PMMA-6wt% Cloisite 25A Composite.	218

6.27	Scanning Electron Micrograph of the Fracture Surface of PMMA-6wt% Cloisite 25A Composite.	219
6.28	Scanning Electron Micrograph of the Fracture Surface of 5wt% XC42 Toughened PMMA.	220
6.29	Experimental and Predicted Variation in Relative Modulus with Volume of Montmorillonite.	222
6.30	Experimental and Predicted Variation in Relative Modulus with Volume of Montmorillonite.	223
6.31	Comparison of Relative Strength Predicted form Linear and Power Laws.	224
6.32	Variation of Relative Tensile Strength with Volume Fraction of Montmorillonite for PMMA-Organoclay Composites.	225
6.33	Relative Fracture Energy Predictions for Initial Tilt and for Maximum Twist based on Crack Deflection Model for Disc-shaped Particles of two Aspect Ratios.	226
6.34	Experimental and Predicted Variation in Relative Fracture Energy with Volume of Montmorillonite.	226

List of Tables

2.1	Some Physical and Mechanical Properties of Low and High Density Polyethylene.	35
2.2	Comparison of Step and Chain Growth Polymerisation Mechanisms.	39
2.3	A Typical Structural Adhesive Formulation of PMMA.	43
2.4	The Clay Minerals.	48
2.5	Basal Spacings for Organomagadiites.	57
2.6	Possible Layered Host Lattices for Nanocomposites.	60
2.7	Storage Modulus and Glass Transition Temperature of Epoxy and Epoxy-clay Nanocomposites.	68
2.8	The Effect of Typical Platelet Length and CEC on the Microstructure Achieved of Polyimide-clay Nanocomposites for various Organoclays.	69
2.9	Typical Cone Calorimetry Data for Nylon-6 and its Nanocomposites and for Polystyrene and its Nanocomposites.	76
2.10	Rate of Water Absorption for Nylon-6, Nylon-6-clay Macro-composite (NCC-5) and for Nylon 6-clay Hybrid/Nanocomposite (NCH-5).	78
3.1	Clays used in this Study and their Suppliers.	91
3.2	Formulation of PMMA used in this Study.	93
4.1	Table of Organoclays and Clays used in this Work and their Effectiveness.	110
4.2	D-spacings for Cloisite 25A and its 6wt% Composites Formed with Varying Mixing Times.	112

4.3	D-spacings of All the Organoclays Used and their Composites.	115
4.4	D-spacings of 6wt% Cloisite 25A and Cloisite 93A Composites Initiated with either AIBN, Lauroyl Peroxide or Trigonox 23.	132
4.5	D-spacings of Toughened PMMA-6wt% Cloisite 25A Composites and of a PMMA-6wt% Cloisite 25A Composite.	139
5.1	Glass Transition Temperature, T_g, of PMMA-Cloisite 25A 3wt%.	147
5.2	DMTA Data for PMMA and its Composites.	152
5.3	The Glass Transition Temperatures of PMMA Initiated with either AIBN, Lauroyl Peroxide (LP), Trigonox 23 (Trig) and their respective Cloisite 25A and Cloisite 93A Composites.	156
5.4(a)	Cloisite 93A, DMTA Data for PMMA and Composites.	158
5.4(b)	Cloisite 25A, DMTA Data for PMMA and Composites.	158
5.5	The Glass Transition Temperature of Toughened ad Untoughened PMMA and their Cloisite 25A 6wt% Composites.	160
5.6	T_g Results for PMMA, Toughened PMMA and their Clay Composites.	164
5.7	DMTA Data for PMMA, Toughened PMMA and Composites.	169
5.8	TGA Data for Organoclays, Plus Percentage Weight loss on Ignition from reference 91.	173
5.9	TGA Data for PMMA and its Clay Composites.	178
5.10	Predicted and Experimental Montmorillonite Residue.	179
5.11	D-spacing Measured using XRD for the Composites.	180
6.1	The Tensile Test Data and the Storage Modulus at 20°C for PMMA and its Composites.	186
6.2(a)	Cloisite 93A, Tensile Data for PMMA and Composites.	190
6.2(b)	Cloisite 25A, Tensile Data for PMMA and Composites.	190

6.3	The Glass Transition Temperature, T_g, Young's Modulus and Standard Deviation of Young's Modulus of the Various PMMAs.	192
6.4	Young's modulus and Standard Deviation of Young's Modulus for Trigonox 23-PMMA and its Composites.	193
6.5	Tensile Data (Including Storage Modulus at 20°C) for PMMA and Core-Shell Toughened PMMA.	194
6.6	Tensile Data (Including Storage Modulus at 20°C) for PMMA, Core-Shell Toughened PMMA and their 6wt% Cloisite 25A Composites.	194
6.7	Fracture Data for PMMA and its Composites.	200
6.8(a)	Cloisite 93A, Fracture Data for PMMA and Composites.	209
6.8(b)	Cloisite 25A, Fracture Data for PMMA and Composites.	209
6.9	Fracture Properties and Young's Moduli of PMMA and Core-Shell Toughened PMMA.	210
6.10	Fracture Properties and Young's Moduli of PMMA, Core-Shell Toughened PMMA and their 6wt% Cloisite 25A Composites.	212

Abbreviations

AIBN-	2,2-azo-bis-isobutyronitrile
BDMA-	Benzyldimethylamine
CEC-	Cation exchange capacity
DBDPO-	Decabromo diphenyloxide
DEGMA-	Ethylene glycol dimethacrylate
DGEBA-	Diglycidylether of bisphenol A
DMA-	Dynamic mechanical analysis
DMA-	N,N-dimethylacetamide
DMSO-	N,N-dimethylsulfoxide
DMTA-	Dynamic mechanical thermal analysis
DSC-	Differential scanning calorimetry
FH-	Flurohectorite
H_c-	Heat of combustion
HDPE-	High density polyethylene
HRR-	Heat Release Rate
ICI-	Imperial Chemical Industries.
LDPE-	Low density polyethylene
LP-	Lauroyl Peroxide
MAA-	Methacrylic acid
MMA-	Methyl methacrylate
MMT-	Montmorillonite
MTS-	Mica type silicates

NMP-	N-methyl-2-pyrrolidone
OMMT-	Organically modified montmorillonite
OMTS-	Organically-modified mica type silicates
PEI-	Poly(etherimide)
PEO-	Poly(ethylene oxide)
PMMA-	Poly(methyl methacrylate)
PS-	Polystyrene
SAN/PBA-	Styrene-co-acrylonitrile/poly Butyl acrylate-co-styrene
SEA-	Specific extinction area
TEM-	Transmission electron microscope
TGA-	Thermogravimetric analysis
Trig-	Trigonox 23 (tert-Butyl peroxyneodecanoate)
XRD-	X-ray diffraction

Nomenclature

ζ - shape factor

θ - angle of incidence/diffraction

λ - wavelength

ν - Poisson's ratio

ν_m - Poisson's ratio of matrix

σ - tensile strength

tan δ - damping coefficient

T_g - Glass transition temperature

l - order of reflection

t - thickness of particle

w - length of particle

n - degree of diffraction

E' - Storage modulus

E"- Loss modulus

E - Young's modulus

E_c - composite Young's modulus

E_m - matrix Young's modulus

V_f - particle volume fraction

V_m - polymer volume fraction

P_u - unfilled peambility

P_p - filled peambility

d - intergallery distance

G_c - fracture energy (plane strain fracture energy)

K_c - fracture toughness (plane strain critical stress intensity factor)

Chapter 1

Introduction

In 1959 when the physicist and Nobel Laureate Richard Feynman gave his presentation "There's plenty of room at the bottom"[1] he was predicting an explosion in Nano-technology that would result in nano-devices and machines becoming commonplace in the world. Now nearly 50 years later his prediction is in part beginning to come true with a surge, over the last 20 years, in research into Nano-technology that will lay the foundations needed for nano-devices and machines.

The term "Nano-technology" covers a wealth of subject areas varying from electronics to biology. However, the area of interest for this work, nanocomposites, falls into the subject areas of material science and mechanical engineering.

What is a nanocomposite? A nanocomposite can be any two-phase material in which one of the phases has at least one dimension in the nano-range (10^{-9}m). From this definition it is apparent that there are a vast number of nanocomposites both synthetic (carbon nanotube-epoxy composite[2]) and naturally occurring (bones, shell etc[3]).

The work contained in this report has been solely based on polymer nanocomposites. With polymer nanocomposites, as with all other types, there are three different types of nanocomposites and their classification is based on the number of dimensions that the

filler particles or minor phase possess on the nanometer scale. An example of filler particles with all three dimensions in the nano range would be silica nanospheres; carbon nanotubes and cellulose whiskers are examples of fillers with two dimensions in the nano range.

The final possible type of nanocomposite comes from fillers with one dimension in the nano range. It is these sheet-like filler particles that are of interest here. Examples of this type of filler are carbon oxides (e.g. graphite oxide), metal phosphates and layered silicates and clays (e.g. montmorillonite, hectorite, magadiite, etc). It is this classification of nanocomposites that is generally known as polymer layered-crystal or polymer layered-silicate nanocomposites depending on whether the filler particles are silicates or not.

A reason for the study of this type of nanocomposite is that when a particulate composite is formed with filler particles that are on the micro-scale instead of the nano-scale; the composite produced has an improved tensile modulus and toughness but reduced strength when compared to the pristine polymer. This decrease in toughness of the composite has been researched, with several models being proposed to explain it. One of these models, the Kerner Equation, relates toughness, modulus, particle size, volume fraction and aspect ratio[4]. The Kerner equation suggests that as the size of the particle decreases, for a given volume fraction, the effect of its inclusion on the toughness of the composite decreases, whilst not adversely affecting the increase in the tensile strength and modulus.

The surge of both commercial and academic interest in research into polymer layered-silicate nanocomposites can in part be attributed to the findings published by the Toyota group of Japan (Okada et al.) for two reasons. The findings published were about a novel type of nylon 6-clay composite[5], a nanocomposite. This nanocomposite not only had greatly improved tensile modulus and strength when compared to both the pristine polymer and a regular particulate composite. In addition, the nanocomposites toughness was comparable to the toughness of the pristine polymer, seemingly showing Kerner's theory to be accurate.

Although this finding in itself was important the other (and in some ways more significant) finding to be reported was that this nylon 6-clay nanocomposite also had vastly improved thermal and barrier properties, with for example the heat distortion temperature increased by 133% compared to pristine nylon 6. This meant if other polymers followed the same trend it would enable them to be used in harsher environments than before. Subsequent research conducted on polymers such as polyurethane[6], polyester[7], polyimide[8], polypropylene[9] and epoxy[10] has shown similar findings to those of the Toyota group. Since this field is relatively new most of the research that has been conducted has concentrated on being able to produce nanocomposites with different polymers and then confirming that the composite produced does have the actual microstructure of a nanocomposite. However, very few of these reports cover the effect that the formation of a nanocomposite has on the fracture properties, in particular the fracture toughness, of the composite. Also very few reports attempt to relate the microstructure attained to the resultant mechanical properties.

These facts lead neatly into the objectives of this thesis. The objectives of this work are:-

- To investigate the effect that the inclusion of nano-particles has on the fracture toughness of a polymer.
- To produce PMMA-clay nanocomposites using commercially available clays.
- To characterize the composites produced, verifying that they are nanocomposites and determining what their overall microstructure is.
- To determine the physical, mechanical and thermal properties of the nanocomposite.
- To relate the properties of the nanocomposites to their microstructure.

- To produce toughened PMMA-clay nanocomposites and determine if any synergistic effects occur between the toughening agent and the clay.

From the objectives of this project it can be seen that the progress of the project was governed by being able to synthesise suitable specimens of the composites. This was at first a stumbling block to progress, although it was overcome at the start of the second year of the project, so as to then enable the start of the work on determining if any synergistic effects occurred with the toughened PMMA-clay nanocomposites.

This thesis is structured as follows. After this introduction to the project there will be a literature review, Chapter 2, covering the background information on the three components of nanocomposites (namely polymers, layered silicates and surfactants), the formation of nanocomposites, their characterisation and the properties affected.

Details on what materials were used in the course of this project will be included in Chapter 3, Materials and Experimental Procedures. Also included in this chapter will be details of any equipment and techniques used.

Next to follow over the course of three chapters will be the presentation and discussion of the results of experimental tests performed during the course of the project.

The first of these three results chapters, Chapter 4, is dedicated to the presentation and explanation of the results relating to the microstructure of the composites produced. Note that it is widely believed that nanocomposites possess such improved mechanical properties by virtue of their unique microstructure.

The results of experiments to investigate some of the physical properties, in particular the glass transition temperature and the thermal stability, of the composites produced are presented and discussed in the second results chapter, Chapter 5.

In Chapter 6, the final results chapter, the results of experiments to investigate the mechanical properties, in particular the fracture properties, of the composites produced

are presented and discussed. Chapter 6 also attempts to relate the microstructures achieved to the mechanical properties found.

The conclusions drawn from this work are what constitutes Chapter 7, Conclusions. The final chapter will be a future work chapter that will put forward a few avenues in which the project could progress.

Chapter 2

Literature Review

2.0 Introduction

The term "nanocomposite" and the possible benefits that can be reaped from nanocomposites were briefly discussed in the preceding introductory chapter. In this chapter, with the aid of some of the many published research papers, there is a more detailed discussion of nanocomposites and their potential benefits. The main objectives of this chapter are to give the reader a basic understanding of the formation, structure and properties of nanocomposites. This chapter will discuss the components that nanocomposites are composed of (namely polymers, layered silicates and surfactants), how nanocomposites are formed, the different nanocomposite microstructures that can be achieved and what effect the formation of nanocomposites has on the mechanical properties of the original polymer. The penultimate section of this chapter will deal with the background of some of the models used to describe and predict the mechanical properties of polymer composites. A brief discussion of rubber toughening of polymers, specifically acrylics, constitutes the final section of this chapter.

2.1 Polymers

As previously stated polymer-layered silicate nanocomposites are in general composed of three components: polymers, layered silicates and surfactants. In this study the major component is the polymer, with both the layered silicate and the surfactant being minor components, so polymers will be discussed here first. The discussion will at first be general then will concentrate on vinyl polymers.

2.1.1 Basics

A polymer is a large molecule, whose molecular weight is in the thousands or more, and is made up of many simple repeat units. The repeat units are usually called monomers. Monomers form polymers by joining together in a chain; this process of joining together is called polymerisation. Figure 2.1[11] below shows part of a polymer chain of polyethylene and an ethylene monomer.

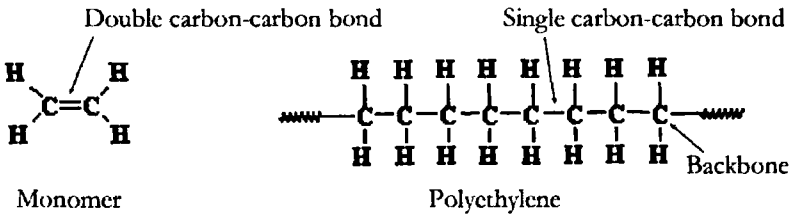


Figure 2.1: An Ethylene Monomer and Part of a Polyethylene Chain[11].

Figure 2.1 can serve to demonstrate what is meant by the terms backbone, pendant groups, vinyl monomer and polymer. Starting with the first term, backbone, this is the chain, in this case the carbon atoms that are lined up. The pendant groups are the atoms or groups of atoms which hang off the carbon atoms in the backbone, in this case the hydrogen atoms. A vinyl monomer is one in which there is a carbon-carbon double bond, another example of a vinyl monomer with different pendant groups is acrylamide which, when polymerised, becomes poly(acrylamide) (see Figure 2.2, taken from reference 11).

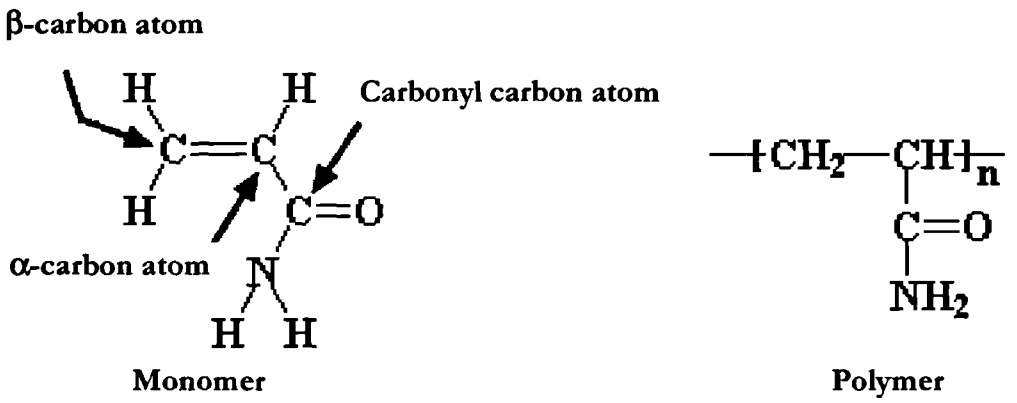


Figure 2.2: Acrylamide Monomer and Poly(acrylamide)[11].

The carbon atoms in the carbon-carbon double bond are designated α and β so as to indicate which carbon is being discussed. In general it can be said that there are very few monomers that will polymerise if the hydrogen atoms have been replaced on both carbon atoms. The "n" in Figure 2.2 denotes repetition of the structural unit contained within the square brackets. This is also the degree of polymerisation when the end groups are included. End groups are what terminate the polymer chain, they can be different to, or the same as, the monomers in the chain. End groups, if shown, are shown outside the square brackets. The degree of polymerisation is related to the chain length and the molecular weight of the polymer.

Molecular Weight and Glass Transition

The molecular weight of a sample of polymer will vary quite widely from chain to chain within that sample, and it is only with natural proteins that the molecular weight of a polymer can be said not to vary, i.e. for it to be monodisperse. Polymers exhibit polydispersity because of the variance in the molecular weight of their chains. The molecular weight of a polymer is important because it governs the physical and mechanical properties; for example compare the properties of low-density polyethylene with those of high-density polyethylene (shown in Table 2.1).

Table 2.1: Some Physical and Mechanical Properties of Low and High Density Polyethylene.

Property	*LDPE*	*HDPE*
Density, g/cm^3	0.912 – 0.925	0.962 – 0.968
Melt Temperature, °C	102 – 112	128 – 135
Glass Transition Temperature, °C	-3	27
Tensile Modulus, MPa	102 – 240	900 – 1200
Yield Elongation, %	20 – 40	5 – 8

As the molecular weight of a polymer increases the polymer chains increase in length, and thus for a set amount of polymer there are less chain ends and thus less free volume. (A polymer's free volume is the volume within a sample that is unoccupied by polymer chains, polymer chain ends have more free volume surrounding them than internal segments of the chain.) This leads to an increase in another important polymer property: the glass transition temperature, T_g. The glass transition temperature is a property of amorphous (disordered, random) polymers. The glass transition temperature is the temperature at which, when heating a polymer, it stops exhibiting glassy properties (i.e. hardness and brittleness). Around the T_g the polymer starts to behave more like a rubbery material, i.e. instead of the molecules vibrating about their equilibrium positions as they do in the glassy state. In the rubbery state much longer segments of chain can exhibit longer-range motion. The glass transition is a second order thermodynamic transition due to there being a change in the specific heat capacity that is not accompanied by any latent heat.

Classes of Polymer

The word polymer encompasses a wide family of different polymeric materials with a wide range of properties that can be sub-divided on the bases of superstructure into the following "family tree"[12].

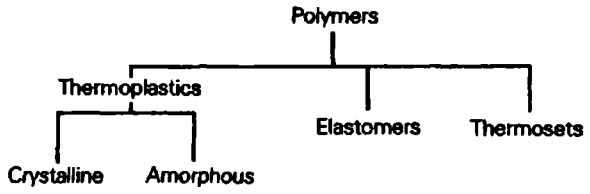


Figure 2.3: The Polymer Family Tree[12].

As can be seen from Figure 2.3, polymers are sub-divided into three different types: Thermoplastics, Elastomers and Thermosets.

Thermoplastics

Beginning with thermoplastics, briefly, these are what are more commonly termed plastics. They are linear or branched polymers that can melt when heated, so once formed they can be remoulded as many times as required. Figure 2.3 shows that the thermoplastic polymer group is sub-divided into crystalline and amorphous thermoplastic polymers. Crystalline thermoplastics are differentiated from amorphous thermoplastics by their structure. Polymer chains in a crystalline thermoplastic are ordered whereas in an amorphous thermoplastic they are not. This structural difference is the cause of one of the many differences between amorphous thermoplastics and crystalline thermoplastics. This difference is that most purely amorphous thermoplastics are soluble where as crystalline thermoplastics are not. However, producing a purely amorphous or purely crystalline thermoplastic polymer is very difficult so most thermoplastic polymers of commercial importance are semi-crystalline (i.e. partly crystalline and partly amorphous). Another differentiating characteristic of crystalline thermoplastics is that a purely crystalline polymer will exhibit only one thermodynamic phase transition when heated i.e. it will only have a melting temperature. Whereas, an amorphous thermoplastic will exhibit two thermodynamic phase transitions, the first being the glass transition followed by the melting of the polymer.

Elastomers

Elastomers are polymers that demonstrate the ability to be stretched easily, and when the applied stress is released, return to their original dimensions without any permanent deformation. The molecular structure of elastomers is what enables them to have this resilience. An elastomer's chains are either physically or chemically crosslinked. For polymer chains to be chemically crosslinked it means that two or more separate polymer chains are joined together via covalent bonds (see Figure 2.4 below) to form one single chain. Elastomers have a low crosslink density. Most elastomers, like thermoset polymers, cannot be remoulded, and they will not melt due to the crosslinks. Upon the application of heat elastomers degrade. (The exception being block copolymer elastomers.)

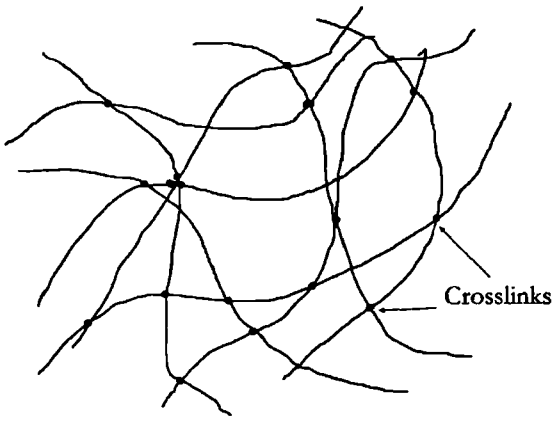


Figure 2.4: A Crosslinked Polymer Network.

Thermosets

Thermoset polymers have a very high crosslink density and form very rigid materials. Due to the high degree of crosslinking, the polymer chain motion is extremely limited. The glass transition temperatures of thermosetting polymers are very high, typically well above room temperature. Thermosetting polymers cannot be remoulded and are not soluble in their own monomers. Thermosetting polymers are generally very strong and

possess a relatively high modulus but are not very tough. They find applications in coatings and adhesives.

2.1.2 Polymerisation

As previously mentioned, polymers are synthesised from monomers by polymerisation processes. A prerequisite for all polymerisation processes is that each single monomer molecule has at least two functional groups so it may be chemically joined to two other monomers. There are many different methods of polymerisation. For example for vinyl polymers there are at least five different methods of polymerisation: free radical vinyl polymerisation, anionic vinyl polymerisation, cationic vinyl polymerisation, Ziegler-Natta catalysis, and metallocene catalysis polymerisation. The methods of polymerisation have been classified into two categories based on their mechanisms of polymerisation. The first category contains polymerisation methods in which the polymer chains grow step-wise by reactions occurring between any two molecular species e.g. a dimer and trimer, or a monomer and a quadmer can react together to form a pentamer. This category of methods is known as step growth polymerisations.

Another mechanism of polymerisation is the growth of a polymer chain by the reaction of a reactive end group of a growing polymer with single monomer molecule (see Figure 2.5 for a schematic representation).

$$\text{EN-m-m-m-m-m-} + \text{m} \longrightarrow \text{EN-m-m-m-m-m-m-}$$

m = monomer, EN = initiator

Figure 2.5: A Schematic Representation of Chain Growth.

Polymerisation processes using this mechanism are classified as chain growth polymerisations. Table 2.2 compares step growth polymerisation with chain growth polymerisation[13].

Table 2.2: Comparison of Step and Chain Growth Polymerisation Mechanisms[13].

Step Reaction	Chain Reaction
Growth occurs throughout matrix by reaction between monomers, oligomers, and polymer.	Growth occurs by successive addition of monomer units to limited number of growing chains.
Average degree of polymerisation low to moderate.	Average degree of polymerisation can be very high.
Monomer consumed rapidly while molecular weight increases slowly.	Monomer consumed relatively slowly, but molecular weight increases rapidly.
No initiator needed; same reaction mechanism throughout.	Initiation and propagation mechanisms different.
No termination step; end groups still reactive.	Usually chain-terminating step involved.
Polymerisation rate decreases steadily as functional groups consumed.	Polymerisation rate increases initially as initiator generated; remains relatively constant until monomer depleted.

The five methods of polymerisation of vinyl monomers previously mentioned all belong in the chain growth polymerisation category. The polymerisation method used extensively by industry, as it can be used to form the majority of vinyl polymers, is free radical polymerisation. Consequently it is the method of polymerisation used in this study, and will be explained in the next section.

Free Radical Polymerisation

Firstly some terminology, electrons are practically always found in pairs, when an electron is found on its own it is called a free radical, because the electron will react with anything to become part of a pair again. Free radicals are formed in two main ways that are: (i) homolytic scission (i.e. homolysis) of a single bond or (ii) by single electron transfer to or from an ion or molecule (e.g. Redox reactions).

Homolysis is the breaking up of a chemical bond within a compound or molecule with each of the fragments having an unpaired electron, i.e. a free radical. This process can be affected by heating and it is then called thermolysis. Thermolysis is a method of free radical production that is frequently used. Compounds which can be used to this end in polymerisation are called initiators; examples of common initiators are benzoyl peroxide and 2,2-azo-bis-isobutyronitrile (AIBN). These initiators produce active

centres, initiator fragments with free radicals on them. (See Figure 2.6 for a typical thermolysis reaction taken from ref. 12).

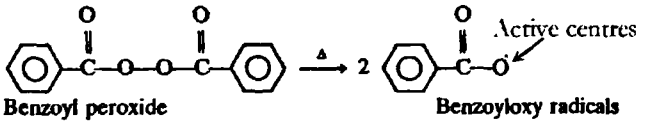


Figure 2.6: Thermolysis of Benzoyl Peroxide[12].

The free radical polymerisation process can be separated quite neatly into three different processes: initiation, propagation and termination.

Initiation consists of the formation of an active centre and its first reaction with a vinyl monomer. The method of this first reaction is as follows: the active centre and the vinyl monomer meet. The vinyl monomer has a carbon-carbon double bond. The active centres' free radical opens one of these carbon bonds and pairs up with one of the two electrons that form that bond. The other electron, now a free radical, migrates along to the end of the newly formed chain and waits there for another monomer molecule to come forward thus moving the active centre along the chain.

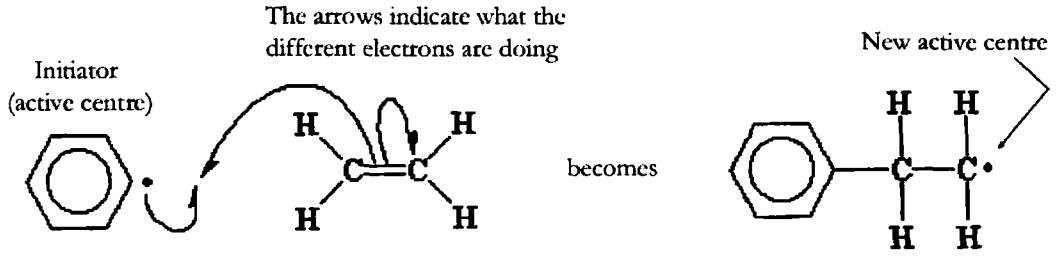


Figure 2.7: Initiation[11].

The next stage of the process is propagation, this is the addition of more monomer to the chain and the advancing of the active centre along the chain. This part of the process is rapid compared with the initiation stage. There are two possible modes of propagation based on which of the two carbon atoms, α or β, is made into the active

centre. A head-to-tail addition is one where the α-carbon becomes the active centre. And conversely a head-to-head addition is one where β-carbon becomes the active centre.

The final part of the process is termination. There are two types of termination reaction which frequently happen, these are combination and disproportionation.

Combination is also sometimes referred to as coupling. When two polymer chains both with active centre chain ends meet then the two free radicals will join together to form a chemical bond and so consume all the radicals. The linkage that results from this reaction is a head-to-head type[12].

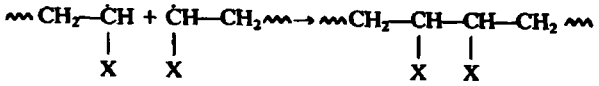


Figure 2.8: Head-to-Head Termination[12].

The other termination reaction is more complex. When the two growing chains meet, instead of the two radicals joining together to form a bond. One of the radicals attacks the bond between the carbon behind the active centre and one of that carbons' hydrogens on the other chain (see Figure 2.9). That radical then forms a bond with the electron from that bond which is attached to the hydrogen. This leaves one chain saturated with hydrogen and the other with two free radicals that are next to each other and so form a bond. Thus at the end of that chain there is a double carbon-carbon bond.

This can happen at any point in the chain, and when it happens far from the growing chain end the free radicals on the hydrogen unsaturated chain cannot join to form a bond. So the chain is now left with two active centres, one at the end of the chain and one at some point far from the end. This is how branched polymers occur.

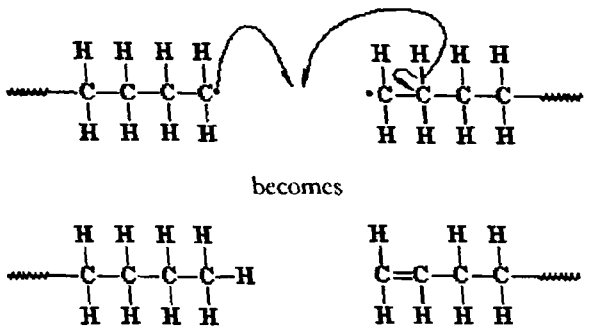


Figure 2.9: A Disproportionation Type Termination[11].

It was earlier said that one of the fundamental requirements for polymerisation to occur was that the monomers have a functionality of two or more. If the monomer does have a functionality greater than two then the resultant polymer will be crosslinked and so be a thermoset.

2.1.3 Acrylates

As the title of this thesis indicates the polymer used in this investigation belongs to the acrylate (acrylic) family of polymers. What follows here is a brief introduction to acrylates which swiftly focuses in on the acrylate used in this investigation.

There are many different acrylate monomers, for example methyl acrylate and acrylic acid to name just two. All these monomers however have the same basic form, shown in Figure 2.10[11], which is an ester that contains a vinyl group.

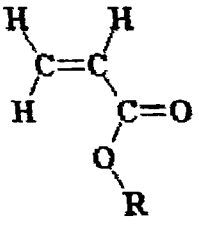


Figure 2.10: The Basic Form of an Acrylate Monomer[11].

It is apparent that this molecule can be modified readily by the substitution of one of the hydrogen atoms. A subgroup of the acrylate family is formed in this way. The hydrogen on the α-carbon is replaced by a methyl group to form the basis of the methacrylate monomers. The addition of this methyl group alters the properties of the final polymer from a soft easily malleable (acrylate) polymer to a hard rigid (methacrylate) polymer. The polymer used in this study comes from the methacrylate section of the acrylate group and is one of the most common polymethacrylates, Poly(methyl methacrylate), PMMA, with its monomer being methyl methacrylate. There are many different forms of PMMA. Only the two most common will be mentioned here. The first is the amorphous thermoplastic PMMA. This is in general a hard optically transparent homopolymer with a T_g of approximately 105°C and a refractive index of 1.48 to 1.50. This form of PMMA has many trade names which include Plexiglas®, Lucite® and Acrylite®. A few typical applications for thermoplastic PMMA are optical lenses, windows and outdoor signs. It is usually not used in structural applications due to its poor impact resistance.

The second is PMMA in its adhesive (thermosetting) form. A typical structural adhesive formulation of PMMA is given in Table 2.3[14], which is a rubber-toughened formulation so as to improve the impact resistance.

Table 2.3: A Typical Structural Adhesive Formulation of PMMA[14].

Component	*Parts By Weight*
Methyl Methacrylate	85
Methacrylic acid	15
Ethylene glycol dimethacrylate	2
Chlorosulfonated polyethylene	100
Cumene hydroperoxide	6
N, N-dimethylaniline	2

The rubber toughening agent is the chlorosulfonated polyethylene. Other than the rubber toughening agent the methyl methacrylate is the major component to this adhesive, hence it is either called PMMA or an acrylic adhesive. The functions of the other components in this formulation are as follows. The polymerisation reaction is

initiated by Redox initatiors, cumene hydroperoxide and N,N-dimethyaniline. The crosslinking monomer is the ethylene glycol dimethacrylate with methacrylic acid acting as an adhesion promoter for metals and also to improve the adhesives' heat resistance. Typical applications for similar acrylic adhesives are in dental filling, bone cements and as coatings.

2.2 Clays and Layered-Silicates

As was mentioned in the introduction to this chapter, nanocomposites consist of three components; polymers, layered-silicates (clays and clay minerals) and surfactants. The following section is concerned with layered-silicates. An overview of their structure, chemical composition and properties will be given. Included in this section is a discussion on montmorillonite and hectorite, two of the most common layered silicates used in nanocomposite research to date. The term layered-silicate in the context of this thesis refers to clay and clay minerals and both terms shall be used here.

2.2.1 Clay Minerals

Clays can be thought of being made up of two types of materials, those that give clay its plastic properties and those that do not. Clay minerals by their size, shape, structure and chemical composition are the group of materials that give clay most of its properties including its plastic properties. The other constituents can be thought of as "non-clay minerals" materials, for example quartz. However in this study the "non-clay minerals" are not of interest and so will not be discussed.

Oxygen anions (ions that have a negative charge) plus silicon and aluminium cations (ions that have a positive charge) form the polyhedral structures are the main chemical elements which make up clay minerals. There are two polyhedral structures that when combined form all clay minerals. The first to be discussed here is the silicon-oxygen tetrahedron (chemical formula SiO_4), since the majority of cations in clay are silicon cations. (The term silicate is given to clays and other earth forming minerals because of this.) A silicon cation can be surrounded by four oxygen anions only due to reasons of

bonding orbital geometry and ionic size. Figure 2.11, taken from reference 15, shows a diagrammatic illustration of a silicon-oxygen tetrahedron.

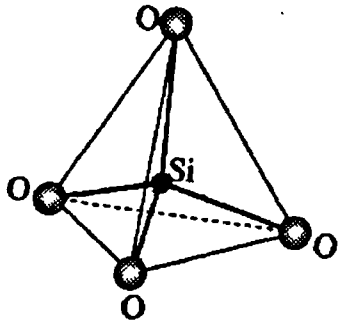


Figure 2.11: A Silicon-Oxygen Tetrahedron[15].

The tetrahedra join together by sharing three of their oxygens with their neighbouring silicon cations to form a tetrahedral sheet (see Figure 2.12[15]). From Figure 2.12 it can be seen that all the apices in the tetrahedral sheet all point in the same direction. These apical oxygens are shared with cations in the octahedral sheet (the other polyhedral structure) so as to connect the two sheets together and also so that the tetrahedral sheet can be electrically neutral.



Figure 2.12: Tetrahedral Sheet[15].

The other polyhedral structure is, as mentioned, the octahedral sheet. This is a sheet made up of octahedra, which are formed from a cation of aluminium, magnesium or iron with six oxygens or hydroxyls surrounding the cation (see Figure 2.13 [16]).

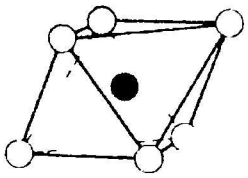


Figure 2.13: Octahedron [16].

There are, however, two different types of octahedral sheet depending on the valency of the cation: divalent cations such as magnesium (Mg^{2+}) yield tri octahedral sheets (Figure 2.14a [15]) and trivalent cations such as aluminium (Al^{3+}) yield di octahedral sheet (Figure 2.14b). The type of octahedral sheet is also used for classification purposes as will be shown later.

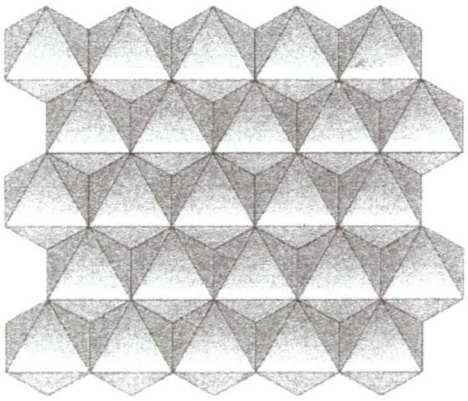


Figure 2.14 a : Tri octahedral Sheet [15].

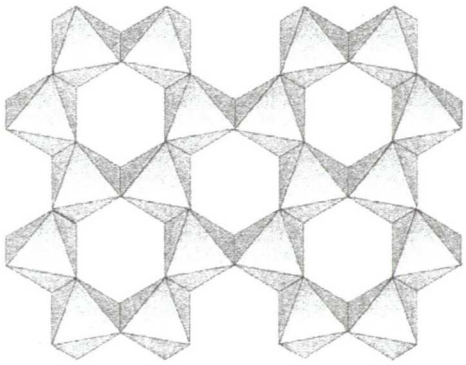


Figure 2.14(b : Di octahedral Sheet [15].

The particles of most, if not all, clay minerals are very fine and platy. This can be seen from Figure 2.15 a scanning electron micrograph of montmorillonite taken from reference 17.

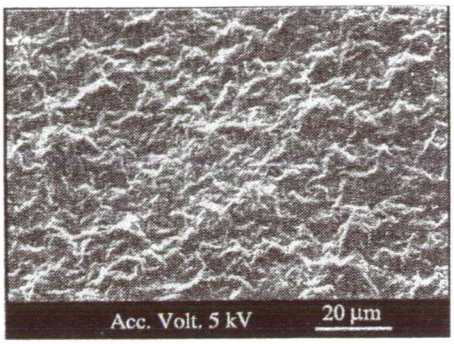


Figure 2.15: A Scanning Electron Micrograph of Montmorillonite [17].

Reasons for this are firstly the nature of the tetrahedral and octahedral sheet, secondly the sheets are stacked on top of each other imposing relative size restrictions on both the sheets. Thirdly any strain caused by misalignment of the sheets, due to variations in mesh size originating from cationic substitution in either of the sheets, would increase as the area of the sheet increased. Thus with some sheet combinations only very small crystals can grow [15].

2.2.2 Classification

Clay minerals can be sub divided into specific groups in many ways, however the most widely used method of classification is based on the different basal spacing (or interlayer distance) that the different groups of clay minerals possess. This will be the method followed here. A basal spacing is the distance in between two successive layers of clay mineral (see Figure 2.16). The most important of the clay layered mineral groups are: Kaolinites, with a basal spacing of 7.1Å, Illites, with a basal spacing of 10Å, Vermiculites, with a basal spacing of 14.4Å and Smectite, with a basal spacing of 15Å. A full summary of the properties of all these clay groups can be found in reference 18 on page 355. An abridged version appears here as Table 2.4.

Out of these four groups, the group of interest is the smectite group. The smectite set is of interest because it shows the property of expandability, i.e. these clay minerals will

take up water or organic molecules in between their structural layers. Smectite clays also have a comparatively high cation exchange capacity.

Table 2.4: The Clay Minerals.

	Kaolinite	Illites	Smectites	Vermiculites
Structure type:	1:1 tetrahedral & octahedral	2:1	2:1	2:1
Octahedral component:	Di-octahedral	Mostly di-octahedral	Di- or tri-octahedral	Mostly tri-octahedral
Principal interlayer cations:	Nil	K	Ca, Na	Mg
Interlayer water:	Only in halloysite	Some in hydromuscovite	Ca, 2 layers; Na, 1 layer	2 layers
Basal spacing:	7.1Å	10Å	Variable, most ~15 Å	Can be 14.4Å
Glycol uptake:	Taken up only halloysite	No effect	Takes 2 layers	Takes 1 layer
Mineral Formation:	Alteration of acid rocks, feldspar, etc. Acid conditions.	Alteration of micas, feldspar, etc. Alkaline conditions. High Al and K concentrations.	Alteration of basic rocks or volcanic material. Alkaline conditions. Availability of Mg and Ca; deficiency of K.	Alteration of biotite flakes or of volcanic material, chlorites, hornblende etc.

Cation exchange capacity is the measure of a clay's ability to exchange its usual cations, typically sodium (Na) or calcium (Ca) for smectite clays, for other species of cations, for example alkylammonium cations.

Smectite Clay Minerals

The structural group that all the smectite clay minerals fall into is the 2:1 layered silicates. This means that there are two tetrahedral sheets sandwiching an octahedral sheet. As can be seen from the Figure 2.16 [15], both tetrahedral sheets point inward towards the octahedral sheet.

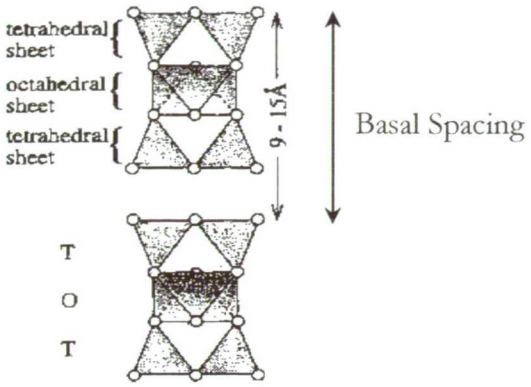


Figure 2.16: Structure of 2:1 Layered Silicates[15].

The smectite group consists of these principal clay minerals: sauconite, beidellite, hectorite, saponite, montmorillonite and nontronite. This group can be sub-divided again based on the structure of the octahedral sheets i.e. whether they are di-octahedral or tri-octahedral. The di-octahedral smectites are montmorillonite, beidellite and nontronite, and the rest are tri-octahedral smectites.

Montmorillonite and Hectorite

From this group the main clay minerals used so far to form nanocomposites have been montmorillonite and hectorite, so the structure of these two will now be discussed, taking the di-octahedral montmorillonite first. Montmorillonite is an aluminous mineral with the chemical formula $M^{I,II}(Al, Mg, Fe^{2+})_2\ Si_4O_{10}(OH)_2\ xH_2O$. The structure of montmorillonite is as shown in Figure 2.16 except that in the gallery (or interlayer) between two clay platelets there are, in montmorillonite, positive sodium or calcium ions, cations, and normally no more than two layers of water molecules[19]. The interlayer cations in montmorillonite are present due to there being a need to redress the charge imbalance caused by ion substitution of iron (Fe^{2+}) and magnesium (Mg^{2+}) for aluminium ions in the octahedral sheet. The charge imbalance is unlike that in mica-type clays such as glauconite whose charge imbalance is high, and thus the cation in the interlayer is bonded strongly to the mineral surfaces. The charge imbalance in montmorillonite, and all of the smectite clays, is of the low charge type, hence the

BIBL. LOUGHB. UNIV.

cations are not strongly bound to the surface of the clay making their exchange for other cations or organic molecules possible. The cation exchange capacity (CEC) of clay mineral is a measure of this. The units for the CEC are milliequivalents per 100 grams (meq/100g). For the smectite group of clay minerals the CEC ranges from 80 to 150meq/100g[16].

Hectorite is used quite frequently in the formation of nanocomposites. It is a magnesium-rich tri-octahedral smectite. The structure of hectorite is similar to montmorillonite as in there are two tetrahedral sheets sandwiching an octahedral sheet and in between these clay platelets there are cations and water molecules. The difference is that the octahedral sheet of hectorite is tri-octahedral as it mainly has magnesium in the octahedral sheet. If the octahedral sheet of hectorite was entirely composed of magnesium it would have no charge imbalance, causing there to be no interlayer cations. However, in hectorite's octahedral sheet, ion substitution of magnesium by lithium takes place resulting in there being a charge imbalance that is redressed by the interlayer cations and water molecules.

Montmorillonite and hectorite will lose most of their interlayer water on heating to between 100 and 250°C, thus their basal spacing will be reduced to around 10Å. On further heating up to approximately 750°C they will have lost their constitutional (OH) water and their basal spacings will drop to somewhere in the range of 9.6 to 10Å depending on the nature of the interlayer cation[15].

2.3 Surfactants

As has been mentioned in the introduction to this chapter nanocomposites are made up of three components: polymers, layered silicates (clay minerals) and surfactants. In the previous two sections background detail on both polymers and layered silicates (clay minerals) has been given. In the present section surfactants shall be discussed.

2.3.1 The Role of a Surfactant

When most polymer-clay mineral systems are combined the resulting composite is a macrocomposite not a nanocomposite. This is due to the fact that most polymers are hydrophobic whilst all unmodified clays are hydrophilic, so mixing most polymers with clay minerals is the equivalent of trying to mix oil with water.

The role of a surfactant is in a way a lot like that of common soap, in that its job is to bring together two compounds which under most circumstances do not like each other, i.e. with soap the compounds are water and organic fats. So as to be able to do this, like soaps, surfactants have an organophilic end and a hydrophilic end.

Clays are in the "raw" form very hydrophilic and very organophobic (this is what causes clays to swell in the presence of water); and not many polymers are hydrophilic. This means that dispersing clay in a polymer is very difficult. This is due partly to a mismatch in the polarities of the clay and the polymer, even very polar polymers like polyamides need a surfactant if they are to produce an exfoliated or delaminated nanocomposite[20]. In the present work the role of the surfactant is to reduce the surface polarity of the clay thus reducing the surface charge and improving the clay's organic wettability properties[21]. A secondary role is to increase the gallery spacing of the clay layers thus making it easier for the monomer molecules or the polymer chains to enter.

Many different types of surfactant are used to alter the surface properties of clays and turn them organophilic. Some of the first surfactants to be used in the formation of nanocomposites were amino acids, ω-amino acids ($H_3N^+(CH_2)_{n-1}COOH$), in producing a nylon 6 clay hybrid[5]. However the most popular type of surfactants, due to the ease with which they can be exchanged for interlayer cations within the clay, are alkylammonium ions ($CH_3(CH_2)_nNH_3^+$).

Other surfactants successfully used have included silanes, used in the formation of unsaturated polyester clay nanocomposites[22]. Silanes have also been used to alter the edges of the clay surfaces so as to encourage any polymer molecule encountered to enter the gallery spacing[23].

The primary method of attaching surfactants to clay is by cation exchange of the clays own interlayer cations for either alkylammonium ions or amino acids. The process is shown schematically in Figure 2.17, taken from reference 17.

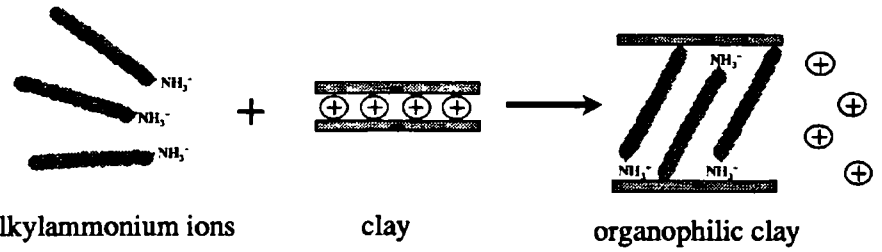


Figure 2.17: The Cation-Exchange Process between Alkylammonium Ions and Cations[17].

Once on the surface the surfactants can lie in any one of several positions shown in Figure 2.18[24], depending on their carbon chain lengths, the charge density of the clay and the surfactant, and their packing density.

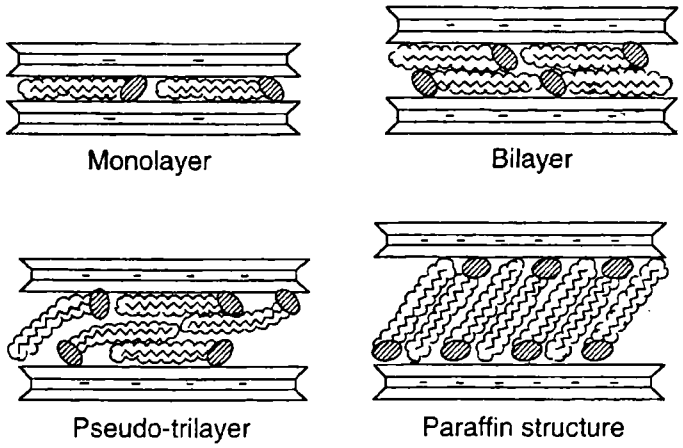


Figure 2.18: Possible Configurations for Alkylammonium Ions in the Interlayer Gallery [24].

Several researchers, Usuki et al.[25] and Shi et al.[26], have been examining the question of whether the length of the surfactant affects the final structure of the obtained composite. From their results it can be concluded that the length of the surfactant does

have a bearing on what type of composite is formed, i.e. whether nano or not, and whether exfoliated or intercalated (note that these terms are explained in section 2.5) for example. Although on the question of the exact number of carbon atoms needed in the alkylammonium ion or the amino acid to give an exfoliated nanocomposite, there are differing opinions. This could be due to the variance of definitions of what constitutes an exfoliated nanocomposite. The results of the studies do show that a minimum of eight to eleven carbon atoms achieves an exfoliated microstructure when not all of the interlayer cations have been exchanged[26]. (This is the normal state). Clays that have had their interlayer cations exchanged are termed organoclays.

2.4 Methods of Nanocomposites Synthesis

There are several methods of synthesising nanocomposites and the choice of method depends on both the polymer and the nanoparticle being used. Nanocomposites can be formed from the following methods: melt intercalation, in situ intercalative polymerisation, exfoliation-adsorption, chemical/thermal conversion and template synthesis. When the polymer is not already pre-formed, i.e. it is a monomer, any of these methods can be used except for melt intercalation which can only be used when the polymer in question is a pre-formed thermoplastic. Each method will now be explained in turn. Special emphasis has been placed on in-situ intercalative polymerisation, as it is the method used for this work.

2.4.1 Synthesis of Nanocomposites

By Melt Intercalation

Melt intercalation[21] and melt compounding[27] are two commonly used names both describing the same process.

In melt intercalation (the term used in this thesis) a pre-formed polymer sample is typically combined with organoclay by either mixing the polymer and clay together (if the polymer is liquid at room temperature) and then heating the mixture far above the

polymer's glass transition temperature. Or the polymer is combined with the organoclay by raising the polymer above its glass transition temperature or above its melting temperature for semi-crystalline polymers and mixing in the clay. With either of these two methods the polymer enters the expanded gallery by diffusion. The microstructure type of the composite achieved from melt intercalation is governed firstly by the thermodynamic interactions between the clay and the polymer, and by the diffusion of the polymer into the agglomerates. Thus the polymer clay mixture must be at a temperature above the diffusion activation temperature.

Another important factor in which type of nanocomposite microstructure is achieved is the time that the mixture spends at temperature. It can be seen from Figure 2.19 that after two hours of heating a mixture of poly(ethylene oxide) (PEO) and montmorillonite that there are still peaks in the X-ray diffraction pattern which correspond to non-intercalated montmorillonite and crystalline PEO.

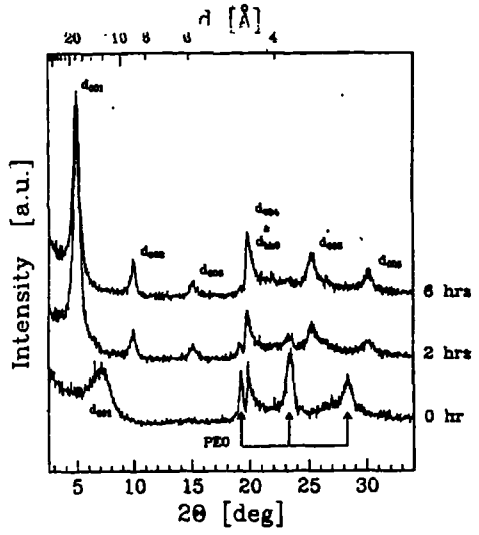


Figure 2.19: XRD Pattern of PEO/Na^+-Montmorillonite Hybrid Heated to 80°C for 0, 2 and 6 Hours[21].

So as to reduce the time needed to form a nanocomposite and to achieve either delaminated or exfoliated microstructures by this method another critical factor is the

amount of shear that the mixture is subjected to. Here researchers, Cho & Paul[27] and Huang et al.[28], agree that the stronger the shear field the better. The shear field that the mixture is subjected to forces the clay platelets to slip into a staircase like structure (see Figure 2.20, taken from reference 28).

With the melt intercalation process all types of nanocomposite microstructure can be achieved with most polymers. Even with non-polar polypropylene intercalated nanocomposites have been achieved[28]. Thus this method can be used to produce intercalated nanocomposites, if not exfoliated nanocomposites, with more polar polymers than polypropylene. Another advantage of this method is that it makes use of processing methods already used commercially in the production of macro-composites, like extrusion. Using melt intercalation is also more environmentally friendly and more cost effective than some of the other methods of producing nanocomposites, as there is no solvent required to disperse either the clay or the polymer.

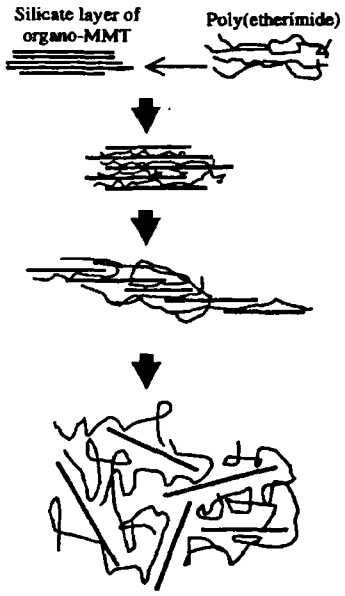


Figure 2.20: Schematic Representation of the Intercalation Process of PEI into the Organo-Montmorillonite (organo-MMT) and the Exfoliation of Montmorillonite[28].

However, melt intercalation can only be used with thermoplastic polymers or with thermosetting polymers that do not immediately form crosslinked networks, as thermosetting polymers will degrade rather than melt once they have been formed.

By In-Situ Intercalative Polymerisation

Melt intercalation, as mentioned above is not a process that can be easily used with thermosetting polymers. One of the approaches to nanocomposite formation is in-situ intercalative polymerisation. This method can actually be used on any type of polymer thermoset, thermoplastic[5, 29] or elastomer. In-situ intercalative polymerisation was the method used by Okada et al. in the formation of nylon 6 clay nanocomposites[5, 29] that originally sparked interest in this field. Since then it has been used to synthesise nanocomposites from clay and polymers such as polyaniline[30], epoxy[10, 31, 32, 33], polybenzoxazine[34] and poly(styrene)[35]. There is little information in the literature on the use of this technique with PMMA.

The process basically involves swelling of the layered silicate with the polymer's liquid precursor/s or liquid monomer/s. When the polymer forms it does so within the interlayer gallery of the silicate layers, thus forcing the layers apart. Polymerisation is initiated by either heat, radiation, diffusion of a suitable initiator or by the exchanged cations inside the interlayer of the layered silicates, introduced before the swelling of the silicate by the monomer[35, 36]. Figure 2.21[32] below shows the procedure schematically for a thermosetting polymer (an epoxy in this case).

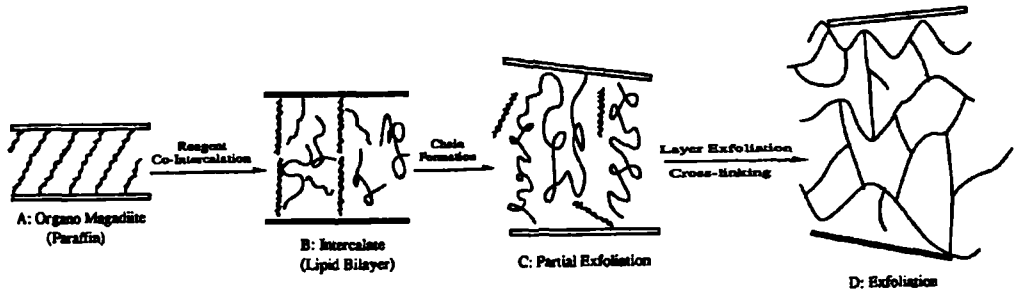


Figure 2.21: A Proposed Pathway for the Formation of an Epoxy-Exfoliated Magadiite Nanocomposite[32].

Studies conducted by researchers such as Messersmith & Giannelis[10] and Wang & Pinnavaia[32] found that for epoxies firstly the choice of surfactant and its configuration in the interlayer gallery was critical to whether an exfoliated microstructure or an intercalated microstructure nanocomposite was achieved. According to Wang & Pinnavaia for any hope of achieving an exfoliated microstructure the surfactants must be as shown in Figure 2.18 for a paraffin like structure[32]. As well as this they demonstrated that the surfactant should act as a catalyst for polymerisation, otherwise the interlayer gallery will not expand. This was shown by comparing the microstructures achieved using primary, secondary, tertiary and quaternary alkylammonium ions. The primary and secondary alkylammonium ions, being the more catalytic than the tertiary and quaternary alkylammonium ions, produced nanocomposites with an exfoliated microstructure and large interlayer gallery spacings, see Table 2.5[32]. (C18A-, C18A1M-, C18A2M- and C18A3M-magadiite represent nanocomposites that contain clays that have each been modified by primary, secondary, tertiary and quaternary alkylammonium ions respectfully.) The catalytic primary alkylammonium ions initiate the polymerisation reaction and then continue to draw in more epoxy precursors, thus expanding the interlayer gallery. Whereas the non catalytic quaternary alkylammonium ions do not, and the interlayer gallery expansion is determined mainly by the initial loading of resin and curing agent in the interlayer gallery.

Table 2.5: Basal Spacings for Organomagadiites[32].

Material designation	Air-dried	Epoxy Solvated	D-2000 Solvated	Epoxy & D-2000 solvated
C18A-magadiite	38.2	42.5	63.3	62.7
C18A1M-magadiite	37.4	41.9	52.4	51.4
C18A2M-magadiite	32.0	42.5	32.4	43.1
C18A3M-magadiite	34.1	41.7	34.2	39.1

N.B. 1. Units are Å.

2. Jeffamine D-2000 is the trade name of a curing agent (polyoxypropyleneamine) manufactured by Huntsman.

The other critical component that can affect the type of microstructure achieved when attempting to produce epoxy-clay nanocomposites is the curing agent[10]. Messersmith & Giannelis found that some curing agents caused reaggregation of exfoliated clay platelets in the epoxy gels during the curing stage of the formation[10]. This resulted in an intercalated nanocomposite. They found that with the curing agents that did not cause reaggragation of the clay platelets that delamination of the clay platelets appeared to have a threshold value that could be clearly seen from X-ray diffraction patterns (see Figure 2.22) as being approximately the temperature at which curing occurs, 100°C. This threshold value occurs when the peak at 40Å disappears.

In situ intercalative polymerisation is a method that can be used with polymers which are not soluble or those which have limited solubility like polyimides[8]. However, in this method the viscosity of the clay polymer mixture could pose processing difficulties, as there is a sharp increase in viscosity once the clay has been added. The increase is attributed to the "house of cards" effect[10]. (This is when the edge-to-edge and edge-to-face interactions occur between the dispersed clay platelets effectively straining the polymer like tea-leaves out of tea.)

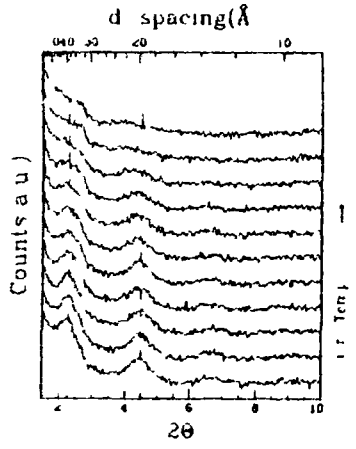


Figure 2.22: XRD Pattern of Organically Modified Mica-Type Silicates/Diglycidyl Ether of Bisphenol A/Benzyldimethylamine (OMTS/DGEBA/BDMA) mixture (4° ovol MTS) Heated In-situ to various temperatures (°C) (20, 40, 50, 60, 70, 80, 90, 100, 110, 130, 150)[10].

By the Exfoliation-Adsorption Process

When the polymer under investigation is one that is soluble either in water or in some other solvent the choice of nanocomposite formation process is widened further beyond in-situ intercalative polymerisation. The choice then includes the exfoliation-adsorption process[37] and the chemical/thermal conversion process. (This is the exfoliation-adsorption process but with one extra step at the end added to it.) In the exfoliation-adsorption technique the clay is dispersed in a solvent in which the chosen polymer is soluble. The polymer is then added and is able to adsorb onto the delaminated clay platelets. Then either the mixture is precipitated or the solvent is evaporated off, and the clay platelets then reassemble trapping the polymer within the layers of clay. This method at best affords an ordered multi-layer structure[36] i.e. a nanocomposite with either an intercalated or delaminated microstructure. However, having said that with some polymers the reaggregation of the clay platelets is impeded and a disordered exfoliated microstructure can form[35]. The chemical/thermal conversion technique is used for polymers that are insoluble in organic solvents but have a soluble high molecular weight precursor. Thus a mixture of polymer precursor and clay platelets is achieved in the same manner as for the exfoliation-adsorption technique. Then the precursor is converted to the final polymer by either chemically or thermally induced reactions [35].

By Template Synthesis

The final method of nanocomposite synthesis is template synthesis. This method is not widely used for the synthesis of polymer-clay nanocomposites but more for producing polymer-layered double hydroxide nanocomposites [3].

Unlike the previous methods described, the silicate layers are formed in-situ in an aqueous solution that contains both the polymer and the silicate precursors. This method relies on self-assembly forces to grow the silicate crystals. Their nucleation is aided by the presence of the polymer which then becomes trapped within the silicate layers as they grow. The silicate layers formed are usually a great deal smaller than

natural silicates which has a detrimental effect on their reinforcing characteristics (see reference 32 for a comparison of natural and synthetic clays).

2.5 Nanocomposites

In the introduction to this thesis a nanocomposite was described in its most general sense as any-two phase material in which one of the phases has at least one dimension in the nano-range (10^{-9}m). In the case being considered here however this description can be narrowed down somewhat. And so a nanocomposite can be defined as a particle filled polymer composite where at least one of the filler particle dimensions was in the nano-range. For this work the filler particle (nanoparticle) has one dimension, the thickness, in the nanometer range with the other two dimensions being very large in comparison i.e. the particle is sheet-like. Table 2.6, taken from reference 36, demonstrates the breadth of filler choice available. Thus far most work has been conducted on clay and layered silicates and in particular montmorillonite and hectorite.

Table 2.6: Possible Layered Host Lattices for Nanocomposites[36].

Layered Host Lattice	Examples
Elemental	Graphite, Black phosphorus
Metal halides	MY_2 (M= Cd, Ni, Pb; Y= Cl, CN, I)
Metal chalcogenides	MX_2 (M=Mo, Sn, Ta, Ti, Zr; X=S, Se, Te)
	MPX_3 (M= Cd, Fe, Mg, Mn, Zn; X=S, Se)
Carbon oxides	Graphite oxide
Metal oxides	M_0O_3,V_2O_5
Metal phosphates	$M(HPO_4)_2$ (M= Ce, Sn, Hf, Ti, Zr)
Niobates/Titanates	$KnbO_3$, $K_4Nb_6O_{17}$, $K_2Ti_4O_9$
Clays and layered silicates	Hectorite, montmorillonite, mica, laponite
Layered double hydroxides	$LiAl_2(OH)_6OH.2H_2O$

Polymer-layered silicate nanocomposites have many desirable properties such as high tensile strength, fire resistance and good optical properties. These properties rely on the morphology and structure of the nanocomposite. There are three different types of structure that the component parts of a nanocomposite can take up when a nanocomposite is being formed. These are that of a conventionally filled polymer

composite, an intercalated nanocomposite and a delaminated or exfoliated nanocomposite (see Figure 2.23)[36].

A conventionally filled polymer composite is one where the silicate layers have not dispersed in the polymer and have remained in tactoids of 10 - 20 silicate layers all aggregated together. This type of composite is sometimes called a macro/micro-composite (see Figure 2.23(a)).

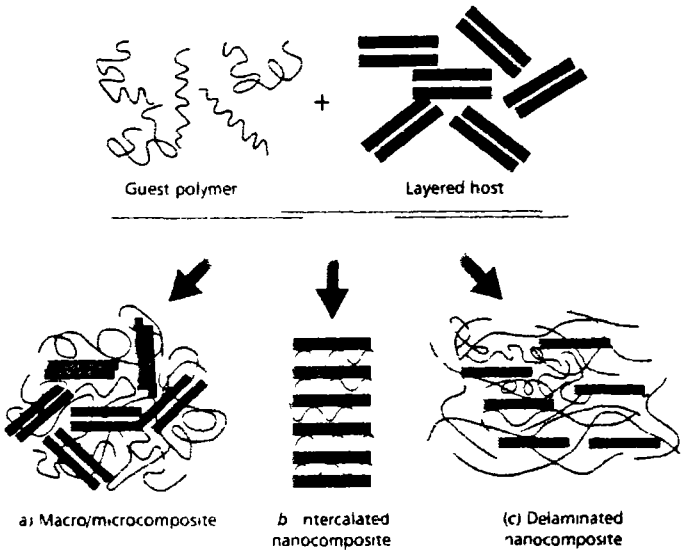


Figure 2.23: The Three Major Possible Different Nanocomposite Microstructures[36].

The next level up from a conventional macro-composite is one where there is either a single polymer chain or at most two polymer chains in between the individual silicate layers. This type of composite is deemed to be an intercalated nanocomposite (see Figure 2.23 (b)). It is characterised by the slight increase in the gallery spacing and the regularity of that spacing.

A typical X-ray diffraction pattern of an intercalated nanocomposite is shown in Figure 2.24, taken from reference 21. The figure shows the X-ray diffraction pattern of montmorillonite intercalated with poly(ethylene oxide) formed by melt intercalation. The fully formed intercalated nanocomposite is the X-ray diffraction pattern labelled 6 hours.

Some researchers split the third category into two groups, but others combine it together as one. So as to avoid confusion the group will be split in two and each group is described here.

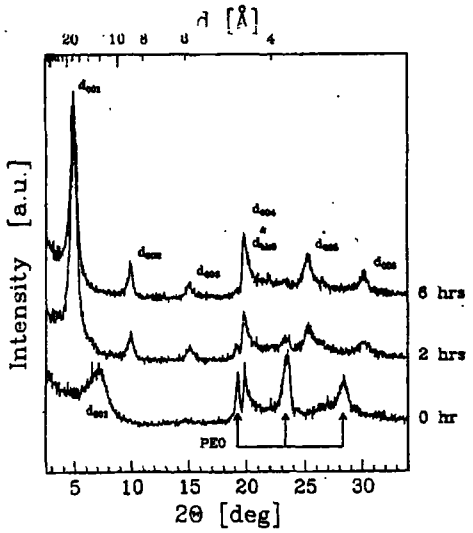


Figure 2.24: XRD Pattern of PEO/Na^+-Montmorillonite Hybrid Heated to 80°C for 0, 2 and 6 Hours[21].

After intercalated nanocomposites come delaminated or, as stated in reference 24, ordered exfoliated nanocomposites (see Figure 2.23 (c) or Figure 2.25(c)). And finally, the last type of nanocomposite is disordered exfoliated nanocomposite, normally just called an exfoliated nanocomposite (see Figure 2.25(d)).

For a nanocomposite to be either delaminated or exfoliated the individual silicate layers must be well dispersed in a continuous polymer matrix. The gallery spacing expansion in these two types of nanocomposites is comparable to the radius of gyration of the polymer and so is far greater than the expansion of the gallery spacing of intercalated nanocomposites.

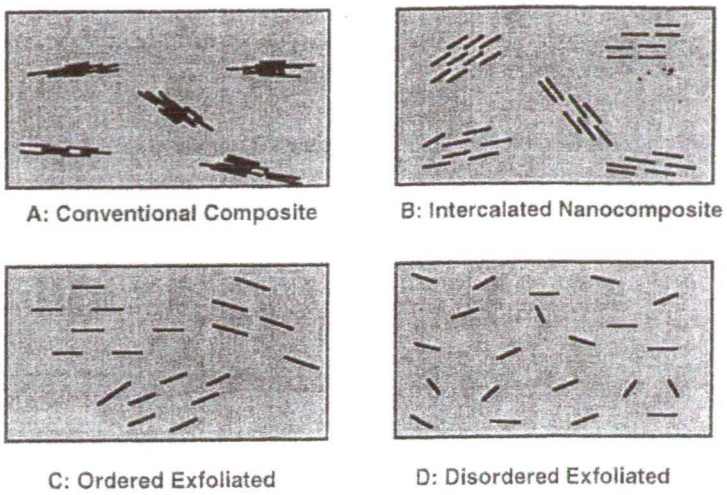


Figure 2.25: Different Microstructures for Nanocomposites[24].

Figure 2.26, taken from reference 35, compares the X-ray diffraction patterns of a macro/micro-composite, an intercalated nanocomposite and an exfoliated (delaminated) nanocomposite.

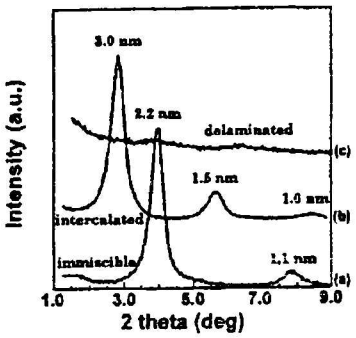


Figure 2.26: XRD Patterns of Nanocomposites with Delaminated, Intercalated and Conventional (Immiscible) Microstructure[35].(Note that 1nm=10Å.)

It can be seen that the exfoliated nanocomposite do not give any diffraction peaks. This can mean either one of two things, which are that the silicate layers are too far apart to produce a diffraction pattern (i.e. greater than 80Å, 8nm, apart) as in a delaminated nanocomposite. Alternatively that the silicate layers are far apart and, that there is no longer any ordering present anymore, as in an exfoliated nanocomposite. So

to be able to tell which of these situations is present in a particular sample, scanning electron microscopy or transmission electron microscopy needs to be performed.

2.6 Properties of Nanocomposites

Nanocomposites caused a stir of excitement in the research and commercial community when they were first reported as they held a promise of large improvements in certain properties without deteriorating others, at relatively little cost. In the following section of this chapter the effect that nanocomposite formation has on certain properties are discussed by reviewing the published findings of many researchers. The properties considered are the following:- tensile, viscoelastic, fracture, heat resistance and barrier properties.

2.6.1 Effect on Tensile Properties

The formation of polymer-clay nanocomposites can affect the tensile properties of the polymer quite dramatically. Various tensile properties have been investigated by researchers, for example tensile strength and Young's modulus to name only two. In this literature review Young's modulus or the tensile modulus will be used to assess the effect of nanocomposite formation on the polymer's tensile properties. The Young's modulus has been chosen, as it is the tensile property least affected by the surface finish of the specimens. The Young's modulus of a material is the stiffness in the elastic region. Since the Young's modulus of clay is approximately 170GPa[38] and that of acrylates is generally approximately 3GPa[39] it is expected that upon the addition of clay to an acrylic that the Young's modulus of the resultant composite should be greater than that of the original acrylic.

The Toyota group found that when the clay adopted an exfoliated nanocomposite microstructure with nylon-6 there was a dramatic increase in the Young's modulus of between 68% at room temperature and 221% at 120°C[40]. Studies conducted by other research groups found similar results, although sometimes a little less dramatic than the increase found by the Toyota group[41, 42, 43, 44]. It was found that the microstructure

adopted by the clay platelets, i.e. exfoliated or intercalated, affected the extent of the improvement in the Young's modulus; with exfoliated microstructures showing larger improvements than intercalated microstructures[44, 45]. This is expected since several theoretical models show that increasing the aspect ratio of the second phase is beneficial to the Young's modulus[46] of a polymer composite, and the aspect ratio is at its greatest when the clay platelets are exfoliated. In addition, a recent theoretical approach suggested by Shia et al[47] and supported by Strawhecker[42] is that the layer of polymer next to or bound to the filler surface has a larger Young's modulus than the bulk polymer, as it is constrained by the filler surface. As the degree of exfoliation increases so does the proportion of bound polymer, and hence the modulus.

The effect of increasing the clay content on the Young's modulus can be shown to be governed by the extent of exfoliation/intercalation of the clay platelets by the common findings presented in many studies[44, 45, 48]. The Young's modulus of a nanocomposite will increase with increasing clay content until a maximum is reached (i.e. an ideal loading of clay and which possess an exfoliated microstructure), then it will decline with further increases in the clay content. For example in a study conducted by Sur et al[44] on polysulfone-clay nanocomposites it was reported that the Young's modulus of the nanocomposites improved up to 3wt% loading then declined after this (see Figure 2.27 reproduced from reference 44). Their findings showed that at above 3wt% loading of clay the nanocomposite formed had a more of an intercalated microstructure than an exfoliated microstructure.

Strawhecker et al[42] also found evidence that the increase in Young's modulus with increasing clay concentration is non-linear for nanocomposites unlike conventional particulate composites where it is linear. Kornmann et al also made a similar observation from a study on epoxy-clay systems and proposed that the increase in Young's modulus was parabolic in form due to exfoliated tactoids (tactoids are aggregates of clay particles) increasing the apparent volume fraction of clay[49].

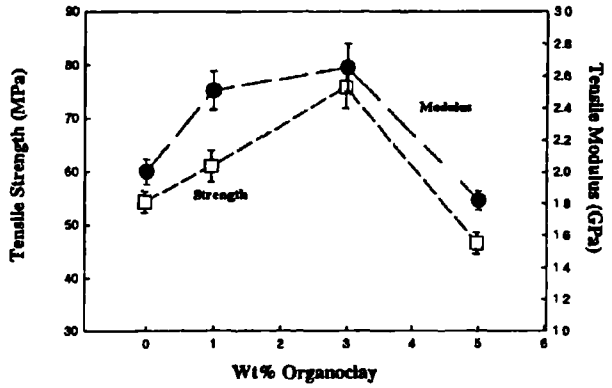


Figure 2.27: Variation of Tensile Strength and Young's (Tensile) Modulus with Percentage Loading of Organoclay for Polysulfone-clay Nanocomposites[44].

A study by Pinnavaia's group at Michigan State University on epoxy-clay nanocomposites[50] showed that the compressive modulus exhibited the same tendencies as the Young's (tensile) modulus i.e. an increasing modulus as the clay content increases, and that an exfoliated nanocomposite microstructure is more effective at reinforcing than an intercalated microstructure.

2.6.2 Effect on Viscoelastic Properties

The viscoelastic properties of a material can be probed using several techniques. However, for polymeric materials a common method used is by performing dynamic mechanical thermal analysis, DMTA, sometimes shortened to dynamic mechanical analysis, DMA. In this experiment the viscoelastic properties of the polymeric material are measured as a function of temperature. It involves applying an oscillatory strain to a sample and recording the in-phase and out-of-phase components of the resultant stress. The storage modulus, E', (the elastic response) is calculated from the in-phase component of the stress and the loss modulus, E", (the plastic response) from the out-of-phase component of the stress. The ratio E"/E' is equal to the tangent of the phase angle, δ, (i.e. tan δ = E"/E'). This ratio is a measure of the energy lost to the energy stored per cycle, i.e. it is the damping coefficient. In most DMTA experiments only the storage modulus, E', and the tan δ results are recorded, with the loss modulus, E", being calculated if needed. Tan δ is a particularly useful quantity as it goes through a

maximum at thermal transitions like the glass transition temperature. Thermal transitions are also accompanied by a decrease in the storage modulus but it is more common to define thermal transitions by their effect on tan δ. In the next few paragraphs the effects of nanocomposite formation and microstructure on both the viscoelastic properties of the polymer and on the polymer's glass transition will be discussed.

The findings of several studies[10, 50-55] performed on different polymer-clay systems show that when a nanocomposite microstructure is achieved, the storage modulus of the nanocomposite is increased both above and below T_g in comparison to the pure polymer. From these studies it can be concluded that the extent of the increase in storage modulus is greatly influenced by the extent of exfoliation, particularly in the rubbery region (above T_g). The storage modulus is increased more significantly with fully exfoliated systems than with partially exfoliated or intercalated systems. This was illustrated by a study performed on PMMA-montmorillonite and PMMA-fluorohectorite nanocomposites by Bandyopadhyay et al[51]. In this study PMMA-montmorillonite nanocomposites achieved a better exfoliated dispersion than the PMMA-fluorohectorite did, and consequently, had a larger increase in storage modulus than the fluorohectorite nanocomposites over the temperature range investigated as can be seen in Figure 2.28[51]. Other experiments conducted in the study showed the PMMA-montmorillonite nanocomposite to have a greater degree of bound polymer (40%) than the PMMA-fluorohectorite nanocomposite (7%). Bandyopadhyay et al proposed that the bound polymer would effectively act like crosslinks and increase the storage modulus especially in the rubbery region.

A study by Gam & Sue on epoxy-clay nanocomposites showed the effect of increasing clay content on the storage modulus (see Table 2.7)[31]. The storage modulus was increased as the clay content increased both above and below T_g.

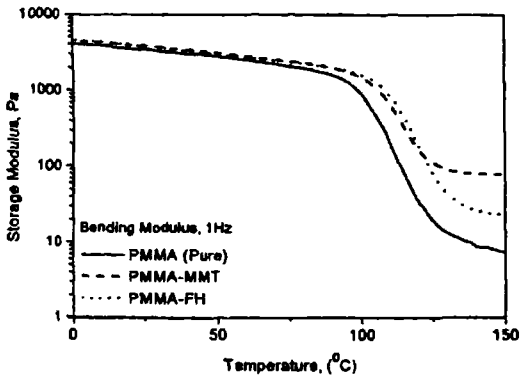


Figure 2.28: Variation of the Storage Modulus for Pure PMMA and its Montmorillonite and Flurohectorite Nanocomposites[51].

A study on polybenzoxazine nanocomposites by Takeichi et al[56] also demonstrated that increasing the clay content maintains the storage modulus to higher temperatures than pure polybenzoxazine. The reason for this increase, and for the higher storage moduli of the nanocomposites, is attributed to the decrease or restriction in segmental motion of the polymer chains near the interface with the clay platelets.

Table 2.7: Storage Modulus and Glass Transition Temperature of Epoxy and Epoxy-clay Nanocomposites[31].

	I.30E Content (wt%)	Inorganic portion (wt%)	T_g °C	Storage Modulus E' GPa at 25°C	MPa at 150°C
Control	0	0	45.7	1.13	3.9
5%	5.0	3.9	46.3	1.23	7.0
7.5%	7.5	5.4	46.3	1.36	10.6

Note: I30E is an organically modified montmorillonite (organoclay), see Table 3.1

A study by Okada et al[53, 54] on polyimide-clay nanocomposites revealed that it was not only the dispersion of the clay in the matrix that could greatly influence the storage modulus of nanocomposites. Their study investigated the effects of using various organoclays on both polyimide and also in the composites formed. The organoclays used in the study were hectorite, saponite, montmorillonite and synthetic mica. Table 2.8 lists the cation exchange capacity (CEC), length of a typical dispersed platelet and the microstructure of the composite formed with polyimide for each organoclay[53].

Table 2.8: The Effect of Typical Platelet Length and CEC on the Microstructure Achieved of Polyimide-clay Nanocomposites for various Organoclays[53].

Organoclay	CEC (meq/100g)	Length of dispersed platelet (Å)	Microstructure achieved
Hectorite Na^+	55	460	Intercalated
Saponite Na^+	100	1650	Partially Exfoliated
Montmorillonite Na^+	119	2180	Exfoliated
Synthetic Mica Na^+	119	12300	Exfoliated

Table 2.8 shows that both montmorillonite and synthetic mica achieved an exfoliated microstructure in polyimide. From Figure 2.29, showing the variation of storage modulus with temperature for all the nanocomposites formed with 2wt% organoclay and for polyimide, it can be seen that these two nanocomposites have the largest increase in storage modulus. Synthetic mica has a larger aspect ratio than montmorillonite the effect of which is to give the synthetic mica exfoliated nanocomposite a higher storage modulus than the montmorillonite exfoliated nanocomposite as can be seen in Figure 2.29.

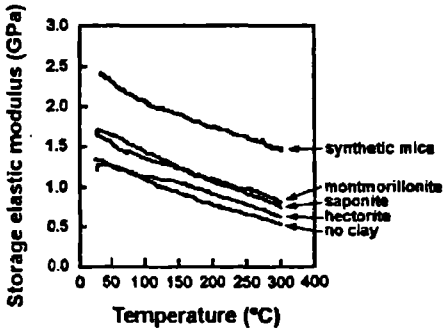


Figure 2.29: Variation of the Storage Modulus with Temperature for Polyimide and for its 2wt% Organoclay Nanocomposites[54].

The effect of nanocomposite formation on the glass transition temperature, T_g, can be investigated either by monitoring changes in the viscoelastic properties (both the maxima of tan δ and the loss modulus can be used to determine T_g) using DMTA or it can be probed using differential scanning calorimetry (DSC). In the literature both of these approaches have been utilised.

In general, it has been found that the formation of a nanocomposite microstructure causes an increase in T_g, and DMTA data has also shown a broadening of the glass transition[10]. This broadening of the glass transition region is attributed to chemical bonding at the interface of the silicate and polymer matrix leading to restricted relaxational mobility in polymer chains close to the interface. This would also cause the observed increase in T_g.

The effect of increasing clay content on the glass transition temperature can be seen in Figure 2.30[43]. The T_g of the polyimide nanocomposites is shown to increase with increasing clay content. This was also found to be the case with polybenzoxazine nanocomposites, although at relatively high clay loadings for nanocomposites (10wt%) the T_g was seen to decrease slightly. This was considered to be caused by the incomplete exfoliation of the clay at this high loading[56].

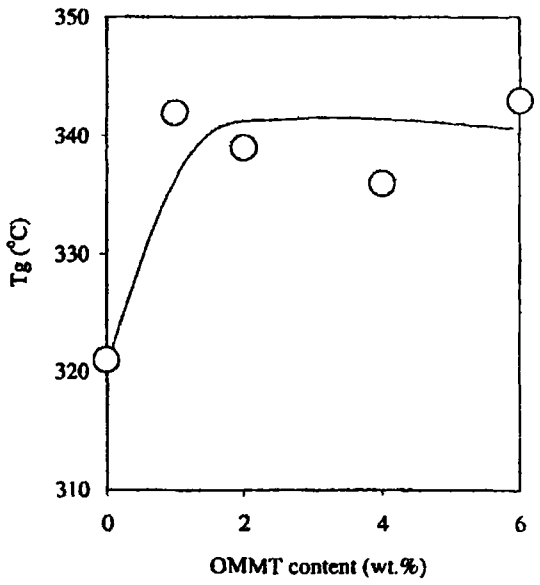


Figure 2.30: Effect of Increasing Organically Modified Montmorillonite (OMMT) Content on the T_g of Polyimide Nanocomposites[43].

This conclusion implies that the greatest increase in T_g can be achieved by an exfoliated nanocomposite microstructure and several studies have found this to be the case[28, 56]. However, some studies have found the opposite to be true as well. Bandyopadhyay et al[51] reported that for PMMA-clay nanocomposites a larger increase in T_g occurs for a

less exfoliated PMMA-fluorohectorite nanocomposite when compared with a totally exfoliated PMMA-montmorillonite nanocomposite. Also, Kinloch & Taylor [57] found for an epoxy-clay system that intercalated nanocomposites produced the largest increase in T_g when compared to both particulate and exfoliated composites. This increase was considered to be caused by the additional constraint on the polymer chains of not only being near to, but also between, the clay platelets.

The effects described in the literature and summarised here indicate that many factors that affect T_g are in play when a nanocomposite microstructure is formed. For example for a thermoset polymer the presence of exfoliated clay particles in the matrix could hinder the crosslinking of the matrix and be more of a detrimental effect on T_g than can be countered be the extent of polymer chains bound to the clay platelet surfaces. Thus the effect that the formation of a nanocomposite microstructure will have on the T_g of the resultant composite, is dependant on the specific system and it is difficult to generalise.

2.6.3 Effect on Fracture Properties

The two main fracture properties of a material are the fracture toughness, K_c, and the fracture energy, G_c. The fracture toughness is a measure of the resistance to fracture in the presence of flaws. Similarly, the fracture energy, G_c, is a measure of the energy per unit area of crack growth required for fracture. The fracture toughness is generally measured using the plane strain critical stress intensity factor, K_c and the fracture energy is measured using the plane strain fracture energy, G_c. The fracture energy, G_c, and the fracture toughness, K_c, are related to each other via equation 2.1. As shown in section 2.6.1, that Young's modulus, E, increases with clay content so too can K_c but it is then possible for G_c to decrease as can be deduced from equation 2.1.

$$G_c = \frac{K_c^{\,2}\left(1-\nu^2\right)}{E} \qquad \text{....}Equation\ 2.1$$

where ν is Poisson's ratio.

One study performed by Kornmann et al has shown for partially exfoliated unsaturated polyester-clay nanocomposites that both K_c and G_c increased with increasing clay content, at least up to 5vol% [22]. For example at 5vol% the K_c of the nanocomposite had doubled when compared to the pristine unsaturated polyester and the value of G_c had tripled. The fracture surfaces for these nanocomposites were also investigated and revealed not the featureless fracture surfaces of pure unsaturated polyester but, as can be seen in Figure 2.31, surfaces showing considerable roughness. The increased roughness of the fracture surfaces when compared to the pristine polymer points to the clay particles forcing the crack to travel along a more tortuous route, thus increasing the fracture toughness.

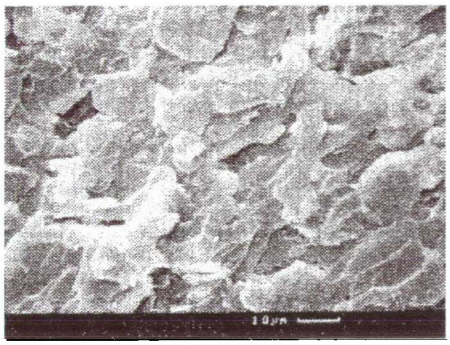


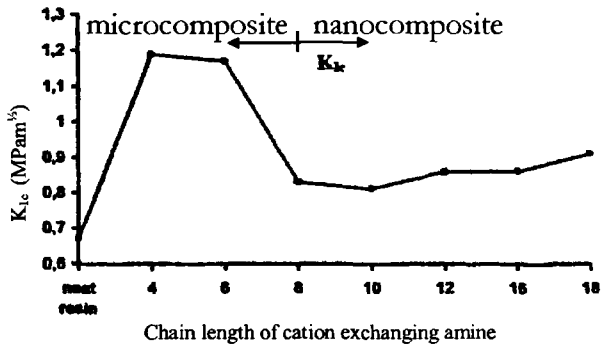
Figure 2.31: Scanning Electron Micrograph of The Fracture Surface of an Unsaturated Polyester Nanocomposites[22].

Another study by Kornmann et al[49] on an epoxy-clay system compared the fracture behaviour of conventionally-filled composites and nanocomposites (both intercalated and exfoliated). The study showed that although both nano and conventional composites increased the K_c and G_c values when compared to the pure polymer, the conventional composite out-performed the nanocomposites. Also the results indicated no improvement in performance when an exfoliated microstructure was formed compared with an intercalated microstructure.

The results from both these studies[17] indicate that the mechanisms governing fracture properties of thermoset-clay nanocomposites occur on the micro- not the nano-scale. This indication is supported by the findings of studies performed by both Zilg et al[58]

and Kinloch & Taylor[57], with Zilg et al reporting that microcomposites increased the fracture toughness of anhydride-cured epoxies more than nanocomposites (see Figure 2.32)[58].

Kinloch & Taylor's work revealed that for epoxy-clay composites formed with nanoclays the composite with the highest fracture toughness was that in which the clay had not been intercalated by the polymer i.e. it was a conventionally filled composite (microcomposite).



Note that a nanocomposite microstructure is only achieved once the number of carbon atoms in the surfactant exceeds 6.

Figure 2.32: Effect of Surfactant Chain Length on the Fracture Toughness of Anhydride Cured Epoxy Nanocomposites[58].

From reviewing the available literature for fracture properties it is revealed that at times the effect of nanocomposite formation can be detrimental[55, 59] on the fracture properties. For example Curliss & Chen[55] reported that for an epoxy clay nanocomposite containing 4.3% I.30E Nanomer (organically modified montmorillonite) the fracture toughness was reduced by nearly 30%.

The available literature also proposes that exfoliated clay platelets that are not randomly distributed but may retain their stacked arrangement. Hence they merely act as relatively large particles with a lower aspect ratio that leads to a less effective toughening effect.

In conclusion to this it is clear from the literature that the effect of nanocomposite microstructure on the fracture properties of the composites formed is very system

dependant. Having said this however it is apparent that for fracture properties a totally exfoliated nanocomposite microstructure is of no advantage. The effect of nanocomposite microstructures on fracture properties will be further discussed in Chapter 6.

2.6.4 Other Properties

Polymer-clay nanocomposites have received so much attention in recent years not only because of their ability to improve the tensile modulus and stiffness of polymers without a dramatically detrimental effect on the polymer's toughness, but also because they offer the unexpected opportunity to positively affect other polymer properties. These properties include the thermal stability, flammability resistance and barrier properties.

Thermal Stability

The thermal stability of a polymer can be assessed by investigating the temperature at which thermal degradation commences. This temperature is generally called the onset temperature, and this terminology will be used here, although in some of the literature it is also termed the decomposition temperature.

The usual effect that the formation of a nanocomposite has on the onset temperature is to increase this property. A study on polyetherimide by Giannelis et al[60] shows that there is an increase in the onset temperature for both intercalated and exfoliated polyetherimide nanocomposites. This study also demonstrated that the onset temperature of an immiscible polyetherimide–clay composite, i.e. a microcomposite, was unaffected when compared to pure polyetherimide (see Figure 2.33).

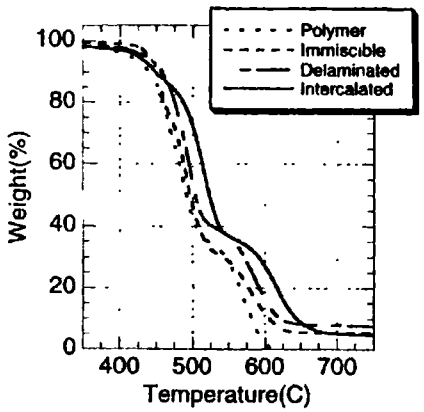


Figure 2.33: Thermogravimetric Analysis of Polyetherimide and of Polyetherimide-clay Nanocomposites with Varying Microstructures[60].

This finding indicates that it is not only the presence of clay that is needed for there to be an effect on the onset temperature but also the polymer needs to be present in the clay galleries. This finding agrees with that reported by Blumstein in 1965[61] and as summarised by Gilman[62]. Blumstein reported an increase in the onset temperature of a clay-rich intercalated PMMA-montmorillonite nanocomposite of 40-50°C showing it to have improved thermal stability over PMMA. Blumstein also demonstrated that the thermal stability of PMMA extracted from the clay galleries was also improved over PMMA made from solution. He proposed that this increase in thermal stability was caused by a decrease in the proportion of macromolecules terminated with a double bond due to being polymerised in the clay galleries. He found evidence that pointed to the argument that the improvement in thermal stability is not only due to a difference in structure but also to the restricted thermal motion of the polymer in the clay gallery. Recently other researchers working on other polymer systems[28, 43, 63-65] have found similar evidence that supports Blumstein's argument.

Flammability

The flammability of a material is often assessed by performing cone calorimetry experiments. In these tests the specimen is subjected to a given heat flux (usually 35kW/m^2) and then both its mass loss rate and heat release rate (HRR) are recorded as a function of time with its gas and soot production being recorded as well[35]. Table 2.9

taken from reference 62 shows typical cone calorimetry data, such as the mean heat of combustion (Mean H_c), the mean specific extinction area (Mean SEA) and the mean carbon monoxide yield, for two thermoplastic polymers and their nanocomposites. Figure 2.34 shows a comparison of the heat release rate data for nylon-6 and its 5% silicate nanocomposite, also reproduced from reference 62.

From Table 2.9 it can be seen that for both the nylon-6 and the polystyrene nanocomposites that the mean heat release rate and the peak heat release rate are both significantly reduced by the addition of the clay. Other studies[63, 66, 67] have also found similar reductions. For the nylon 6 nanocomposite this is also shown in Figure 2.34.

Table 2.9: Typical Cone Calorimetry Data for Nylon 6 and its Nanocomposites and for Polystyrene and its Nanocomposites[62].

Sample (structure)	Residue yield (%)±0.5	Peak HRR (Δ%) (kW/m^2)	Mean HRR(Δ%) (kW/m^2)	Mean H_c (MJ/m^2)	Mean SEA (m^2/kg)	Mean CO yield (kg/kg)
Nylon-6	1	1010	603	27	197	0.01
Nylon-6 silicate 2% *delaminated*	3	686	390	27	271	0.01
Nylon-6 silicate 5% *delaminated*	6	378	304	27	296	0.02
PS	0	1120	703	29	1460	0.09
PS silicate-mix 3% *immiscible*	3	1080	715	29	1840	0.09
PS silicate-3% *intercalated*	4	567	444	27	1730	0.08
PSw/DBDPO/ Sb_2O_3 30%	3	491	318	11	2580	0.14

Note: HRR:- Heat Release Rate; H_c:- Heat of Combustion; SEA:- Specific Extinction Area

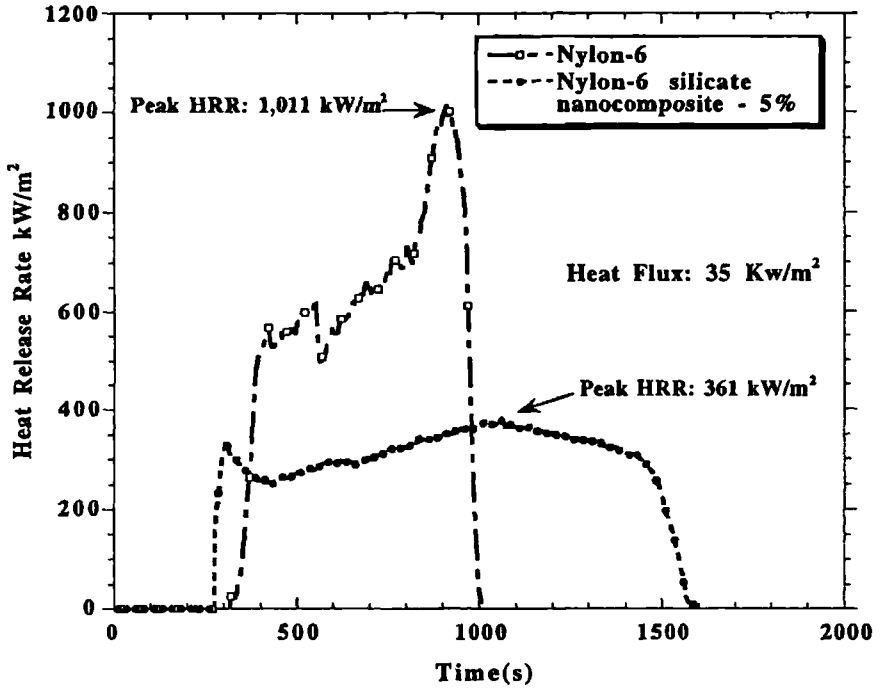


Figure 2.34: Comparison of Heat Release Rate plot for Nylon-6 and Nylon-6 Silicate Nanocomposite (5wt% o)[62].

Included in Table 2.9 are results from cone calorimetry experiments performed on a polystyrene that has been flame retarded with decabromo diphenyloxide (DBDPO) and Sb_2O_3. This flame retardant is one in which its flame-retardant properties operate in the gas phase. Comparison of the flame retarded polystyrene data with both the polystyrene and the polystyrene nanocomposite data shows distinct differences. For example, the specific extinction area (SEA), which is a measure of smoke yield, for the nanocomposite is comparable (an increase of 18.5% o) with the pure polystyrene whereas for the flame retarded polystyrene it is greatly increased (an increase of 76.7%). This is also true of the mean carbon monoxide, CO, yield. This serves to indicate that the improvement in flammability is not caused by a gas phase procedure but by a change in the combustion process of the condensed phase. Other experiments conducted by Gilman's team have shown that nanocomposites gain their flame retardant effect by the formation of char layers from the intercalated or exfoliated silicates. This forms a barrier that acts to insulate and retard transportation of mass (volatile decomposition

products). This can also be said to be true for thermoset polymer nanocomposites[68]. For further reading on this topic see the review written recently by Gilman[62].

Barrier Properties

Since the Toyota group published their findings on nylon 6-clay nanocomposites[29] presenting data, see Table 2.10, demonstrating that the formation of a 5wt% clay nylon-6 nanocomposite had a remarkably decreased water absorption rate at 23°C compared to pure nylon-6 (a 41% decrease), many other researchers have reported similar results for other polymers[7, 28, 50, 55, 69].

Table 2.10: Rate of Water Absorption for Nylon-6, Nylon 6-clay Macro-composite (NCC-5) and for Nylon 6-clay Hybrid/Nanocomposite (NCH-5)[29].

Specimen Montmorillonite (wt%)	Rate of Water Absorption 23°C 1 day (%)
NCH-5 (4.2)	0.51
NCC-5 (5.0)	0.90
Nylon 6 (0)	0.87

Other studies have shown that it is not only the water absorption rate that is decreased. For example Huang et al[28] showed that the uptake of common solvents such as ethanol and xylene by polyetherimide was reduced for a nanocomposite formed with as little as 5wt% montmorillonite. The study also showed that although pure polyetherimide was dissolved at 25°C in 24 hours by solvents such as N-methyl-2-pyrrolidone (NMP), N,N-dimethylacetamide (DMA) and N,N-dimethylsulfoxide (DMSO), that the nanocomposites were left intact by these solvents after 24 hours.

The decrease in permeability of nanocomposites can be explained by an increase in the tortuosity of the path that solvent molecules must take around the clay platelets. By using Nielsen's model for impenetrable filler particles[70] (equation 2.2) it can be seen that the greater the aspect ratio of the particle, w/t, the larger the decrease in permeability.

$$\frac{P_f}{P_u} = \frac{V_m}{1+\left(w/2t\right)V_f} \qquad \text{....Equation 2.2}$$

Where P_f, P_u are the filled and unfilled permeability, V_m and V_f are the volume fractions of the polymer and the filler particles respectively, w is the length of the filler particle and t is its thickness.

This analysis shows that an exfoliated nanocomposite microstructure will cause the largest decrease in permeability since the clay platelets can have an aspect ratio of approximately 2000[71]. However, experimental data gives a value for aspect ratio in the region of 200-100[7, 69]. An explanation proposed by the Pinnavaia group[71] for such a comparatively small aspect ratio is that the clay platelets aggregate but displace from their original positions slightly to form a stair-like structure, see Figure 2.35.

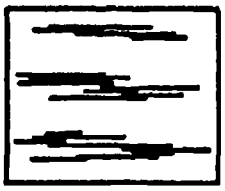


Figure 2.35: The Stair-like Structure Suggested by the Pinnavaia Group to Account for the Small Experimental Aspect Ratio Found[71].

2.7 Theoretical Models for Predicting Certain Properties

Over the years of research into polymer-composites many models have been developed to predict the properties of a polymer composite. Essentially all are based on the original properties of the component phases of the composite and the relative volume fraction of each component. Sometimes other features such as the particle shape or aspect ratio are taken into account. In the following section three models used to predict the composite Young's modulus, E, will be briefly discussed, along with one model used to predict fracture toughness, K_c. The Young's modulus models are the "rule of mixtures", the "Halpin-Tsai model" and the "Mori-Tanaka model". The model for predicting the toughness is the "Faber and Evans model".

Several of the assumptions used in the three models that shall be discussed here for predicting a composites Young's modulus are common to all three of the models. The assumptions are; that perfect bonding exists between the polymer matrix and the particles; that the particles are homogenously distributed in the polymer matrix; and that the Young's modulus of the surfactant is the same as that of the polymer matrix thus the volume fraction of the clay is the volume fraction of the organoclay minus the volume fraction of the surfactant.

2.7.1 The Rule of Mixtures

This model is the simplest one to be discussed here. The assumptions that the model uses are that each component is linearly elastic and that the particles (in our case this is the clay) are homogenously distributed through the polymer matrix. The model results in the following equation for the composite's Young's modulus, E_c[39]:-

$$E_c = V_f E_f + (1 - V_f) E_m \qquad \text{....Equation 2.3}$$

Where V_f and E_f are the filler particle's volume fraction and Young's modulus respectively, and E_m is the Young's modulus of the matrix. From the equation 2.3 it can be seen that this model neglects any effect that the aspect ratio of the filler particles has on Young's modulus.

2.7.2 The Halpin-Tsai Model

A shape factor, ζ, is included in this model so as to enable the model to predict the Young's modulus of a composite not only as a function of the polymer and filler particle moduli and volume fraction but also of the aspect ratio. For the case of surface treated clays the model assumes that there is no surfactant present on the clay surface (i.e. volume fraction of a surface modified clay used in this model is only the silicate (clay) portion). The surfactant is assumed to have the same or similar Young's modulus to the polymer and as such the surfactant's volume fraction is included in the polymer's volume fraction. The Halpin-Tsai equations are [72]

$$\frac{E_c}{E_m} = \frac{1+\zeta\eta V_f}{1-\eta V_f} \qquad \text{....Equation 2.4}$$

where

$$\eta = \left(\frac{E_f}{E_m} - 1\right) \Big/ \left(\frac{E_f}{E_m} - \zeta\right) \qquad \text{....Equation 2.5}$$

The shape factor recommended by Halpin-Tsai for discontinuous orientated square fibres (and a clay platelet can be assumed to take this form) is $\zeta = 2w/t$, where w/t is the aspect ratio. However, van Es[73] has shown that this is too large for most particulate composites and recommends the use of $\zeta = 2w/3t$. It is still however expected that even with this new modified shape factor that this model will generally over-predict for most particulate composites since the particles will be randomly orientated.

2.7.3 The Mori-Tanaka Model

This model was based on the principles of Eshelby's inclusion model for predicting an elastic stress field in and around an ellipsoidal particle in an infinite matrix[72]. To overcome the problem of finite filler concentrations Mori and Tanaka[74] considered a non-dilute composite consisting of many identical spheroidal particles causing the matrix to experience an average stress different from the applied stress, but so that equilibrium was maintained the volume average over the entire composite was made to equal the applied stress. Tandon and Weng[75] applied the Mori-Tanaka model to derive analytical solutions for the elastic moduli of an isotropic matrix filled with aligned spheroidal inclusions, equation 2.6 is their resulting equation for the longitudinal Young's modulus.

$$E_c = \frac{E_m}{1+V_f\left(-2\upsilon_m A_3 + (1-V_m)A_4 + (1+V_m)A_5 A\right)/2A} \qquad \text{....Equation 2.6}$$

Where E_c, E_m are the Young's modulus of the composite and the matrix respectively, V_f, V_m are the volume fraction of the particles (clay) and the matrix repsectively, ν_m is the Poisson's ratio of the matrix and A_3, A_4, A_5 and A are constants. These constants

are derived from another set of equations not included here but can be seen in reference 75.

2.7.4 The Faber and Evans Model

As previously stated in the introduction to this section of the literature review the Faber and Evans[77] model is used to predict the fracture energy or toughness of particulate-filled composites. The model predicts the normalised fracture energy of the composites with respect to the fracture energy of the unmodified polymer. The analysis performed by Faber and Evans used a fracture mechanics approach and is based on a crack deflection model. The crack deflection model assumes that as the crack approaches a particle in the composite it is deflected by the particle i.e. it tilts. The crack then experiences further tilt and twist as it comes across other particles in the composite. This crack deflection and twisting leads to an increase in the fracture surface area that can account for a small proportion of the increase in fracture energy of the composite material over the unmodified material. The majority of the remaining increase in fracture energy can be accounted for by the crack deflection and twisting inducing mixed mode fracture.

In fracture mechanics there are three modes of fracture, mode I is due to tensile opening, mode II is caused by in-plane shear loading and mode III is caused by anti-plane shear loading, see Figure 2.36. More energy is required to cause fracture in modes II and III than in mode I.

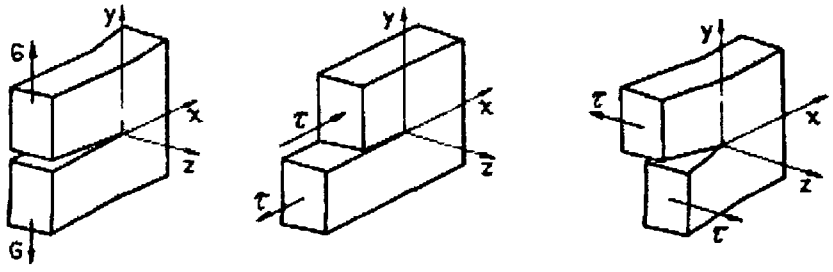


Figure 2.36: Modes of Fracture[76].

In the crack deflection process modes II and I occur, and in the crack twisting process modes III and I occur. Faber and Evans used this approach to produce predictions for composites where the filler particles were rods, discs or spheres. For the case of clay particles the most appropriate equations are those developed for disc-like particles. Figure 2.37 shows the relative toughness predictions for two different aspect ratio disc shaped particles using the Faber and Evans equations. The equations are not reproduced in this thesis but can be found in reference 77. From Figure 2.37 it can be observed that the aspect ratio of the particles plays a significant role in increasing the relative toughness of the composites for a given volume fraction.

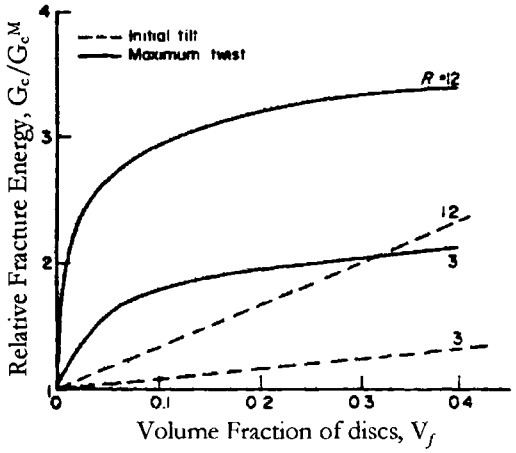


Figure 2.37: Relative Fracture Energy Predictions for Initial Tilt and for Maximum Twist based on Crack Deflection Model for Disc-shaped Particles of two Aspect Ratios (R)[77].

2.8 Toughening of Acrylic Polymers

Acrylic polymers are, as mentioned in section 2.1.3, brittle and susceptible to impact failure. This is a trait common to many polymers and many methods have been developed to toughen them. These methods vary from hard particle (glass spheres) inclusion, fibre (carbon fibre) inclusion, to rubber particle inclusion in various ways.

For this study attempts where made at producing rubber toughened PMMA using two methods, the first by dissolving solid rubber into the monomers, then upon

polymerisation allowing it to phase separate into small rubber spheres. The second method was by the inclusion of "core-shell" particles. The first of these two methods failed and so was abandoned in preference of the second "core-shell" method. This section of the literature review will therefore briefly explain what core-shell particles are, how they are made, and what toughening mechanisms they initiate.

2.8.1 What are Core-Shell Particles?

As previously mentioned there are in essence two routes to rubber toughened polymers; the "phase-separation route" and the "pre-formed particle route". Core-shell particles belong to this pre-formed particle route that became popular in the mid 1970s[78]. Core-shell particles are crosslinked rubbery layered particles that can be modified to optimise their toughening effect by varying both particle size and morphology, as well as their chemical composition. Figure 2.38 shows some typical core-shell morphologies.

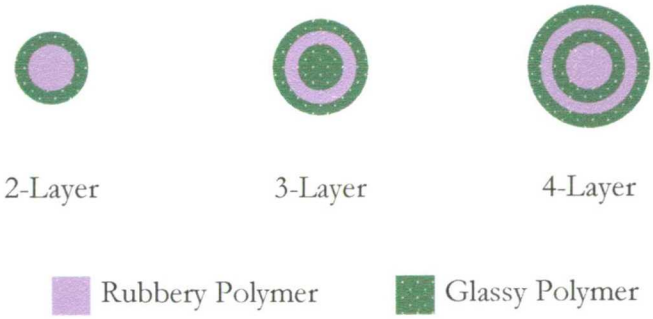


Figure 2.38: The Morphologies of Typical Core-Shell Particles[79].

As can be seen from Figure 2.38 core-shell particles are made up of two polymer types a crosslinked rubbery polymer, for PMMA this is typically poly[(n-butyl acrylate)-co-styrene][78], and a glassy polymer. Typically, but not always, the glassy polymer is either the matrix polymer or a polymer that is compatible with it. Figure 2.38 shows that, although the internal morphology of the particles may vary, the outer layer is always made from the glassy polymer[80]. Since core-shell particles are discrete pre-formed

particles they can be dispersed in both pre-formed thermoplastic polymers by extrusion blending or within a solution of monomers by high shear mixing before polymerisation.

2.8.2 How are Core-Shell Particles Formed?

Core-shell particles are formed by sequential emulsion polymerisation[9] carried out under monomer-starved conditions. The first step of the sequence is the formation of the seed particle (on which all other layers are grown) which can be formed of a crosslinked rubbery polymer (2- and 4-layer particles) or of a glassy polymer (3-layer particles). Figure 2.39, taken from reference 78, shows schematically the routes to 2-, 3- and 4-layer core-shell particles.

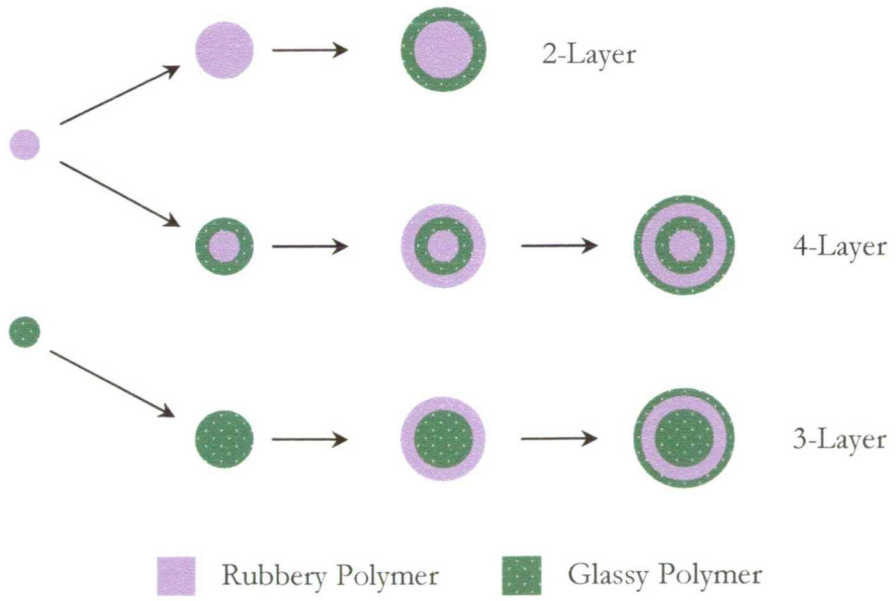


Figure 2.39: Schematic of the Possible Routes to Forming Various Core-Shell Particles[8].

Once all the layers have been polymerised onto the seed particle, the final layer being of glassy polymer, the particles are isolated from the emulsion in which they were formed. This can either be achieved by spray-drying or by coagulation of the emulsion[9]. The outer layer of all core-shell particles plays two important roles. The first is to provide a

degree of adhesion (the amount of which is system dependant) between the matrix polymer and the core-shell particle. The second role is that the outer layer of the particle must allow aggregated particles (caused by the final isolating step of their formation) to disperse easily within the matrix polymer, so as to give a good, agglomerate-free, dispersion of the particles. Figure 2.40, taken from reference 81, shows a TEM micrograph of core-shell particles(3-layer) in a SAN/PBA (styrene-co-acrylonitrile/poly butyl acrylate-co-stryene) blend.

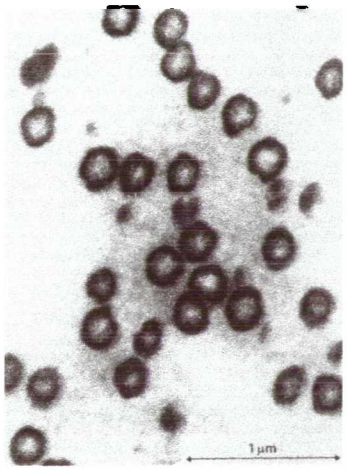


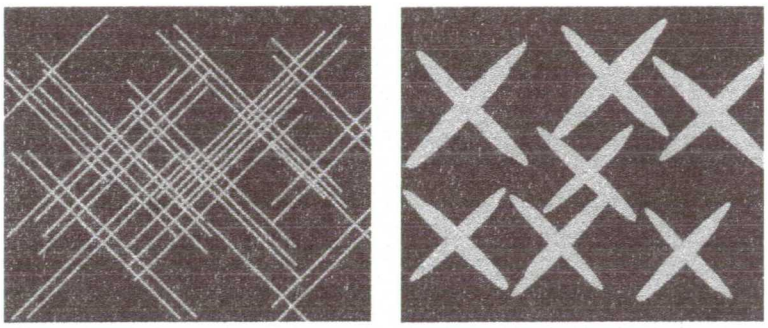
Figure 2.40: Transmission Electron Micrograph of 3-Layer Core-Shell Particles in a SAN/PBA blend[81].

2.8.3 What Mechanisms do Core-Shell Particles Employ to Toughen Polymers?

The main aim of adding any toughening agent into a polymer is to increase the amount of energy required to fracture the polymer, by increasing the extent to which the polymer can undergo plastic yielding. (Adding any toughening agent to a polymer that cannot yield would normally have no positive effect on the polymer's toughness[78].)

It can be said that, in general, materials undergo plastic deformation by two principal methods: shear yielding and crazing, which will be briefly described here as they form part of the mechanisms by which core-shell particles increase the toughness of the acrylic polymers.

Shear yielding in general is the permanent change in shape of a specimen at constant volume[82]. For polymers shear yielding involves the localised semi-permanent shearing of thin regions in the bulk of the polymer. The shear deformation in polymers is semi-permanent as it can be reversed when the polymer is heated to its glass transition temperature. The molecules that have undergone shearing will be orientated differently to those that are not within the sheared region and thus will have a different refractive index to the bulk polymer. The refractive index difference gives rise to shear bands (see Figure 2.41) that can be seen when examined using polarised light. Shear yielding can occur both under tensile and compressive stress fields[78].



Schematic for fine well-defined microshear bands

Schematic for diffuse shear bands as they would appear through crossed polarisers

Figure 2.41: Schematic of Shear-bands Caused by Shear Yielding[78].

Crazing is the other principal method of yielding and unlike shear yielding can only occur under a tensile stress field as it involves an increase in the sample volume. A simple clear description of what crazes are is to consider crazes as microcracks bridged by fibrils[82]. It is apparent from this description that the formation of a craze causes an increase in volume of the sample. Sometimes crazes can lead to brittle fracture as it is often found that crazes occur at crack tips, however multiple crazes can lead to general yielding[82]. Note that thermosetting polymers cannot form crazes.

A core-shell particle, for this explanation, can effectively be thought of as a rubber particle thus it has a high bulk modulus but there is a large difference in the shear and tensile moduli of the matrix polymer and the core-shell particles. The role of the core-

shell particle is to increase the likelihood of yielding which it does by acting as a stress concentrator[81]. The large difference in the moduli causes the stress in the matrix polymer next to the equator of the core-shell particle to be approximately twice the applied stress. The stress fields caused by the core-shell particles overlap increasing the stress in the matrix polymer. In the polymer, around the core-shell particle, a triaxial stress state is generated promoting such processes as crazing to occur. The stress developed within the core-shell particle can become large enough to cause the core-shell particle to cavitate or for hole growth to occur. A particle is said to have cavitated when it has ruptured internally[78](see Figure 2.42[83]).

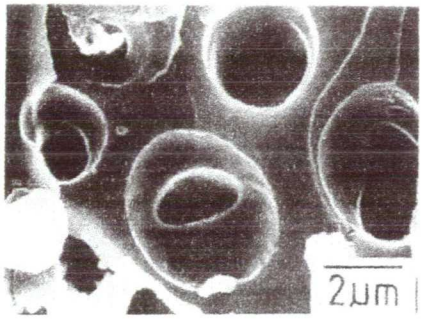


Figure 2.42: Cavitated Rubber Particles. Particles formed through the Phase Separation Technique[83].

When particle cavitation or hole growth occurs the triaxial stress state of the matrix polymer is relieved and causes shear yielding to occur local to the particle forming shear bands. Several studies [79, 81, 84, 85] have shown that core-shell toughened polymers experience extensive shear banding (shear whitening) with little increase in volume. This indicates that the main mechanism employed by core-shell particles in increasing toughness is by inducing shear yielding by either particle debonding or cavitation.

2.9 Concluding Remarks

In summary of this chapter, a nanocomposite can be described as a two phase material in which one of the phases has at least one dimension in the nano-scale (10^{-9}m). The three elements, namely polymers, layered-silicate and surfactants, that form polymer-

layered silicate nanocomposites have been discussed, along with the various methods of nanocomposite formation and the three possible nanocomposite microstructure (exfoliated, intercalated and conventional/immiscible) that can be achieved. The effects of these microstructures on the physical and mechanical properties of the composites formed has also been detailed. Also discussed in this chapter are the general physical and mechanical properties of thermoset acrylics and common methods of toughening this typically brittle polymer.

The following chapter, Chapter 3, details the materials used and the experimental procedure followed to produce both PMMA and toughened PMMA. It also sets out the test conditions used for each of the experiments performed so as to probe the microstructure, physical and mechanical properties of the composites formed. The results of these experiments are presented in Chapters 4, 5 and 6. In Chapter 4 the microstructure results are presented and discussed whilst in Chapters 5 and 6 it is the physical and mechanical properties of the composites formed that are presented.

Chapter 3

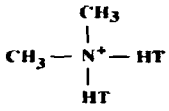
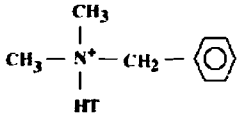
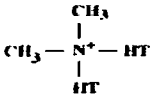
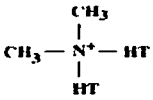
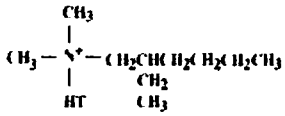
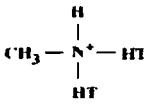
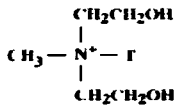
Materials and Experimental Procedures

3.0 Materials

The basic acrylate used in this study was a crosslinked form of poly(methyl methacrylate), PMMA. The PMMA was formed from the following monomers: ethylene glycol dimethacrylate (DEGMA), methacrylic acid (MAA) and methyl methacrylate (MMA). All these monomers were obtained from Sigma Aldrich and were polymerised using free radical polymerisation. Three different initiators were used during this study to form the PMMA and its composites. The initiator used for the bulk of this study was 2,2-azo-bis-isobutyronitrile (AIBN), obtained from Fisher Scientific. The other two initiators used were lauroyl peroxide obtained from Sigma Aldrich and trigonox 23 (chemical name, tert-Butyl peroxyneodecanoate) which was donated from the supplies held by Jon Hickey at Cambridge University.

The rubber toughened PMMA used was formed by the addition of either Hypalon (a chlorosulfonated polyethylene (a solid rubber)), recommended and donated by the ICI Strategic Technology Group, or one of three types of core-shell particle to the monomer solution.

Table 3.1 Clays Used in this Study and their Suppliers.

Commercial Clay Name	Surfactant	Surfactant Concentration	Supplier
Cloisite 6A		140 meq/100g clay	Southern Clay Products
Cloisite 10A		125 meq/100g clay	Southern Clay Products
Cloisite 15A		125 meq/100g clay	Southern Clay Products
Cloisite 20A		95 meq/100g clay	Southern Clay Products
Cloisite 25A		95 meq/100g clay	Southern Clay Products
Cloisite 93A		90 meq/100g clay	Southern Clay Products
Cloisite 30B		90 meq/100g clay	Southern Clay Products
Nanomer PGW	None	N/A	Nanocor
Nanomer I.30E	$CH_3(CH_2)_{16}CH_2NH_2$	20 – 30wt%	Nanocor
Somasif ME100	None	N/A	Co-op Chemical
Montmorillonite	None	N/A	Alfa Aesar

Note: T-Tallow; HT- Hydrogenated Tallow.

XC42 and XC44, donated by Lucite International, were two of the core-shell particles used to toughen PMMA. The other core-shell particles used were KM355 and were donated by Rohm & Haas. These core-shell particles were chosen on the advice of ICI and the manufacturers[86, 87]. This form of rubber toughening is discussed in detail in Chapter 2.

During the course of this work many different clays were used, both natural and synthetic (Somasif ME100, a synthetic montmorillonite), as well as surface modified and unmodified were used. These were used to produce composites with varying degrees of success. All of the clays used during the course of this work are based on the same clay mineral, montmorillonite. Table 3.1 contains a list of the clays used and their suppliers. Note that some of the surface modified clays used the same surfactant but at different concentrations, e.g. Cloisite 6A, 15A and 20A.

3.1 Preparation of Composites

3.1.1 Preparation of PMMA-Clay Nanocomposites

From the common applications of this form of PMMA, as a coating and an adhesive, it was decided to produce both bulk specimens and adhesively-bonded joints. It was decided to produce bulk plates of PMMA-clay composites first before attempting to produce adhesively-bonded joints as MMA, MAA and DEGMA are all volatile and evaporate quickly at room temperature. It was later found that the fabrication of adhesively-bonded joints was not possible in normal laboratory conditions since the monomer solution evaporated before the joint could be completed. (Note that the word composite is used here, as until the material produced has been characterised it is not known if it is a nanocomposite or a microcomposite.) The PMMA used in this study is based on a formulation found in John Comyn's "Adhesion Science" page 47 [14]. The modified formulation is shown in Table 3.2. In this study PMMA-clay composites have been produced with clay contents of 1wt% , 3wt% , 6wt%, 9wt% and 12wt% .

The method used to produce a PMMA-clay composite using AIBN as the initiator is as follows:-

The ingredients were measured out sequentially as they appear in Table 3.2 into the same glass bottle, except for the AIBN which was not added at this point. The clay was then added. The solution of clay and monomers was mixed using a Heidolph RZR 2102 Control overhead stirrer fitted with a radial flow impeller at 2000rpm for 2 hours. Once the mixing was complete the AIBN was added and allowed to dissolve and homogenise for 3 hours, during which time the bottle was agitated on rollers. This time also allowed any air trapped in the solution from the initial mixing to separate out of the solution. After this the solution was poured slowly and carefully into a prepared warm (40°C) mould. The size of the mould was 150 x 200 x 5 mm.

Table 3.2: Formulation of PMMA used in this Study.

Component	Parts by weight
Ethylene glycol dimethylarcylate (DEGMA)	2
Methacrylic acid (MAA)	15
Methyl methacrylate (MMA)	85
2,2'-azo-bis-isobutyrylnitrile (AIBN)	0.02

The mould consisted of two release-coated glass plates, separated by a hockey stick shaped rubber gasket, clamped together, leaving a small gap to allow the mould to be filled. A PTFE plunger/stop was used to seal the gap after the mould has been filled.

The filled mould was then sealed into plastic bags and placed into a water bath at 60°C for 20 hours to cure (polymerise). After this time the specimen was removed from the plastic bags and was then post cured in an oven. The post cure for this polymer consists of 3 steps: 2 hours at 80°C; 2 hours at 100°C; and finally 2 hours at 120°C.

The method used to produce a PMMA-clay composite using lauroyl peroxide as the initiator was the same as that detailed for AIBN, except that before the clay was added to the monomer solution approximately 30ml of the solution was set aside in a small glass bottle. Into this portion of the solution the lauroyl peroxide was added and allowed to dissolve and homogenise for 2 hours. The quantity of lauroyl peroxide added was 0.02 parts by weight of all the monomer solution. The rest of the procedure was as detailed for the AIBN with the lauroyl peroxide-monomer solution being added to the clay-monomers solution after 2 hours of mixing with the Heidolph impeller.

Similarly most of the procedure followed to produce PMMA-clay composites with trigonox 23 as initiator was the same as for when AIBN was used as the initiator except for two alterations. The first alteration to the AIBN procedure was that the initiator, 2ml of trigonox 23, was not added until the monomer-clay solution has been on the rollers for 2 hours 40 minutes. The trigonox 23 was then allowed to homogenise within the monomer-clay solution for 20 minutes on the rollers. The solution was then carefully poured into a warm pre-prepared mould. The second, and last, alteration was that the water bath, in which the bagged mould was placed, was maintained at 40°C for 20 hours and not 60°C for 20 hours.

3.1.2 Preparation of Toughened PMMA-clay Nanocomposites

Two approaches to producing toughened PMMA-clay composites were attempted. The first approach used a solid rubber, Hypalon, as the toughening agent whilst the second approach used core-shell particles as the toughening agent.

The method used with the solid rubber Hypalon was very similar to the method used to produce PMMA-clay composites with AIBN as the initiator. The only difference was that 5% by weight (attempts were made at 10wt% solution but the viscosity increase made the solution unprocessable) of finely chopped solid rubber chunks were added to the monomer solution and allowed to dissolve into the solution until the solution appeared "chunk-free" (approximately 24 hours after the rubber's addition) before the

clay was added to the monomer solution. During the dissolving time the solution was kept in constant motion to aid the dispersion of the rubber by being on the rollers.

When core-shell particles were used as the toughening agent the only alteration to the method used to produce PMMA-clay composites with AIBN as initiator was that when the clay was added to the monomer solution, so too were 5% by weight of core-shell particles.

3.2 Experimental Procedures

3.2.1 X-Ray Diffraction

The X-ray diffraction patterns of both clay and the composite samples were measured using a Philips PW171 diffractometer with Cu radiation (40kV, 40mA), a step size of 0.04° and scanning speed of 0.48°/min. The start and end angles were 3° and 25° respectively. The composite samples were cut from plates to a size of 25 x 25 x 5mm. The clay samples were mounted on to a single crystal silicon sample disc using pressure-sensitive tape.

3.2.2 Thermogravimetric Analysis

The thermogravimetric analysis was performed using a Stanton Redcroft 780 Series Simultaneous Thermal Analyser. Approximately 10mg of sample was placed in a platinum crucible and was heated along with a reference platinum crucible containing approximately 10mg of highly pure alumina at a rate of 10°C/min from 30°C to 1000°C. Either an argon atmosphere or an air atmosphere was used, with a gas flow rate of 60cm^3/min in both cases.

3.2.3 Dynamic Mechanical Thermal Analysis

The viscoelastic properties of PMMA, toughened PMMA and their polymer-clay composites were investigated using a Combined 300°C Rheometric Scientific Dynamic Mechanical Thermal Analyser in dual cantilever beam mode. Two temperature ranges

were used, the first being 10°C to 180°C which was used for PMMA and its composites. The second temperature range was -80°C to 180°C and was used for toughened PMMA and its composites as a lower starting temperature was required to pick up the T_g of the rubber phase. Note that for both temperature ranges a temperature ramp of 2°C/min was used. Frequencies of 1 Hz and 10Hz were used for all experiments. The strain level was 1 and the torque applied to the fixtures was 10Nm. The sample was machined from a plate to the dimensions 3 x 2 x40mm. The storage modulus, E', damping factor, δ, and glass transition temperature, T_g, (the peak of the tan δ curve, 10 Hz data) were determined for each experiment.

3.2.4 Fracture Toughness Testing

The fracture toughnesses of PMMA, toughened PMMA and their composites were determined using a linear elastic fracture mechanics approach with compact tension specimens. Two sizes of specimen were used, initially plates were machined into 60 x 62.5 mm specimens. However, it was subsequently decided to machine the plates to 24.5 x 25.5 mm specimens so that more test pieces could be produced from each specimen plate. Figure 3.1 shows a diagram of the second size of specimen including dimensions. The dimensions of the specimens and the test method followed the international standard ISO13586:2000(E)[88]. The tests were performed on a 5584 Instron machine using a 5kN load cell at a testing speed of 1 mm/min at standard room temperature (21°) and humidity.

The notch was sharpened by tapping a fresh razor blade into the tip of the notch of each test piece. The K_{1C} values were calculated, and the G_{1C} values were calculated when required using the relationship shown in Equation 3.1, as discussed in Chapter 2.

$$G_{1C} = \frac{K_{1C}^{\ 2}}{E}\left(1-\upsilon^2\right) \qquad \text{....}Equation\ 3.1$$

The fracture surfaces of a selection of the broken test pieces were examined using a scanning electron microscope. Specimens were sputter coated with gold prior to observation.

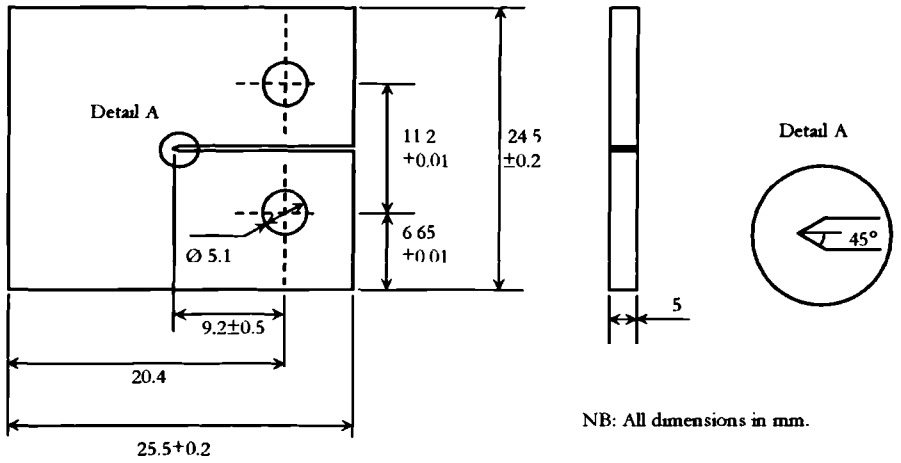


Figure 3.1: Small Compact Tension Specimens Used.

3.2.5 Tensile Testing

Tensile tests were performed on PMMA, toughened PMMA and on their polymer-clay composites according to the test procedure set out in ASTM D638-01[89]. Figure 3.2 contains a diagram of a typical specimen including the dimensions to which the specimens were machined. The tests were performed on a 5584 Instron machine fitted with a video-extensometer at a test speed of 1mm/min using a 150kN load cell at room temperature and pressure. The Young's (tensile) modulus was recorded for each specimen tested.

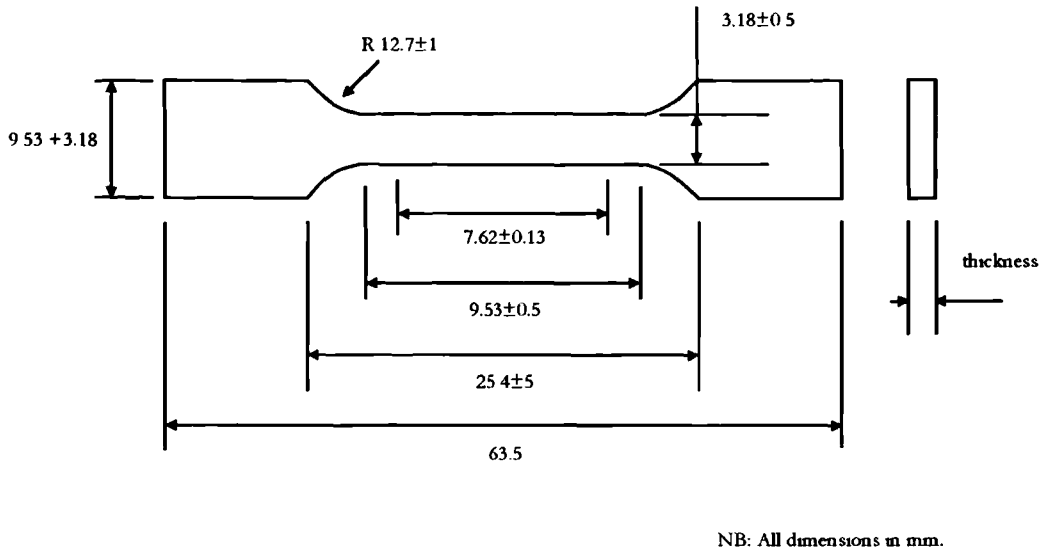


Figure 3.2: Schematic of Tensile Specimens including Dimensions.

3.2.6 Transmission Electron Microscopy

Transmission electron microscopy was conducted on the polymer-clay composites using a JEOL JEM-2000FX II microscope. In preparation the samples were ultramicrotomed to a thickness of between 700 to 1000Å and mounted on sticky copper grids.

3.3 Concluding Remarks

In summary of this chapter, the materials used to fabricate the thermoset PMMA-clay composites were detailed and the fabrication method, based on in-situ intercalative polymerisation, was described. The materials used to fabricate the toughened thermoset PMMA-clay composites were detailed and the fabrication method for these composites was also described. The procedure followed for the tests conducted to characterise the microstructures of the composites was detailed, along with the experimental procedures followed for the physical and mechanical testing that was performed on the composites to assess the effect of the microstructures achieved on the properties of the composites.

The following chapter, Chapter 4, presents the microstructural results found from both X-ray diffraction and transmission electron microscopy. The results of the physical and mechanical testing are presented in Chapter 5 and 6 respectively.

Chapter 4

Results - Microstructure

4.0 Introduction

This chapter is dedicated to the presentation and interpretation of the microstructure of the composites produced. From Chapter 2, the literature review, it can be concluded that there are two principal methods of microstructure determination. These are firstly the use of X-ray diffraction (XRD) patterns to determine the overall intergallery spacing, and secondly the use of transmission electron microscopy (TEM) to visualise the intergallery spacing. In addition TEM can differentiate between delaminated and exfoliated nanocomposite microstructures. Both these methods have been used in the course of this project and the results will be presented shortly.

First, however, a short section showing typical XRD patterns and discussing their main features will follow this introduction.

4.1 Interpreting X-Ray Diffraction Patterns

Figure 4.1 shows a typical X-ray diffraction pattern for unmodified clay (Nanocor PGW). The ordinate shows the number of diffracted X-rays that hit the detector in an allotted time. The abscissa gives the angle at which the X-rays are diffracted. This angle can be converted into the intergallery distance using Bragg's Law (see equation 4.1).

$$n\lambda = 2d\sin\theta \qquad \ldots Equation\ 4.1$$

Where n is the degree of diffraction and is always an integer, λ is the wavelength of X-rays, θ is the angle of incidence/diffraction and d is the intergallery distance.

Unfortunately the number of counts (intensity) cannot be used quantitatively to determine the number of clay platelets that are at a given intergallery spacing[90]. The intensity does, however, give some qualitative information.

The peaks that can be seen on Figure 4.1 represent one of two types of crystallographic feature, either a *00l* basal reflection or an *hk* diffraction band.

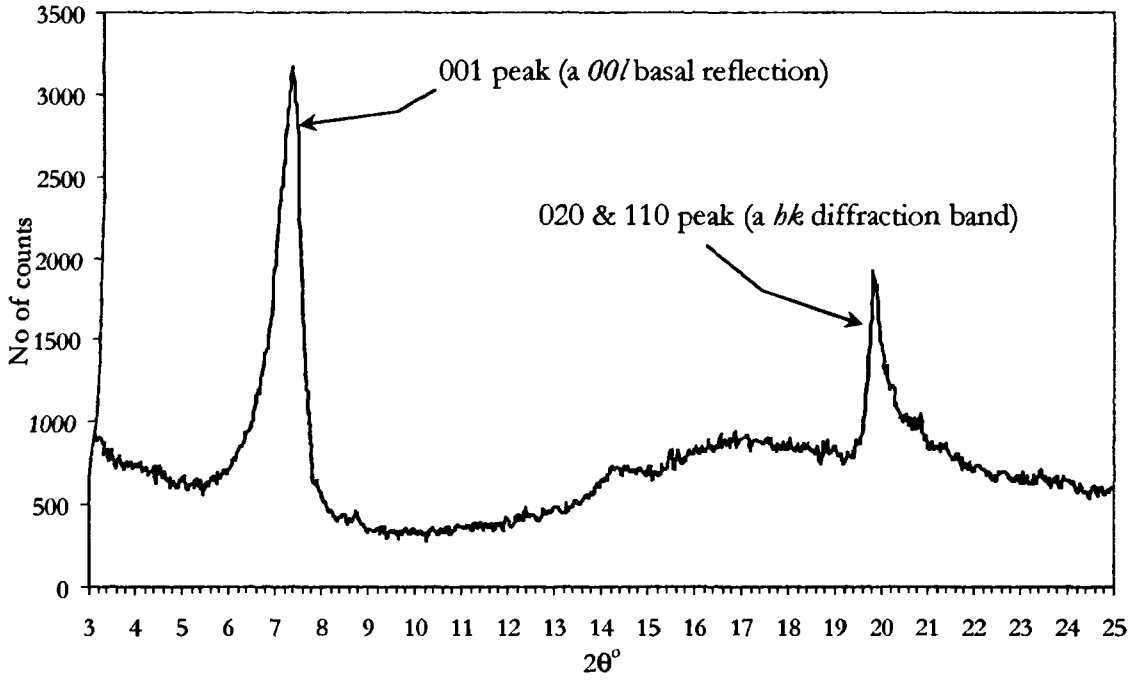


Figure 4.1: XRD Pattern of Unmodified Clay, Nanocor PGW

The positions of the *00l* basal reflections indicate the distance between successive clay platelets. The position depends firstly on the type of intergallery cation (i.e. whether the intergallery cations are sodium or alkyl ammonium cations etc.); and secondly on the number of layers of water in-between the clay platelets (i.e. the clay's state of hydration). The *hk* diffraction band positions remain fixed for the same clay type as they indicate the internal structure of the clay platelets themselves and will only alter with clay type, unlike the *00l* basal reflections. Figure 4.2, taken from Kommann[17] shows both the *00l* basal reflections and the *hk* diffraction bands. In this study the *hk* diffraction bands are of little use as all the organoclays used are based on montmorillonite, and it is the *00l* basal reflections that are of interest. In particular it is the position of the 001 basal reflection peak (relating to the 001 plane) that can be used to calculate the intergallery spacing.

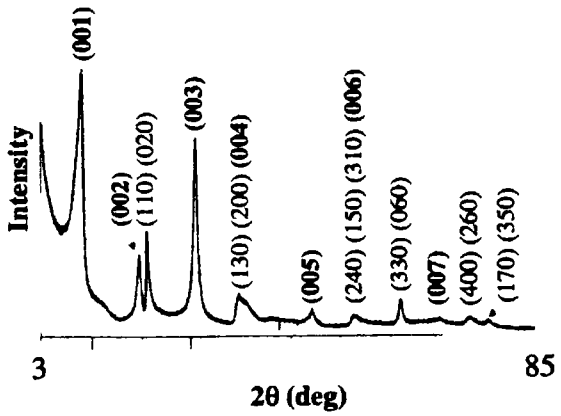


Figure 4.2: XRD Pattern of Montmorillonite (Na^+).

Note that the *00l* basal reflections are in bold and the *hk0* diffraction bands are not in bold.

Figure 4.3 shows typical X-ray diffraction patterns obtained in this study for the untreated clay PGW, the surface treated Cloisite 30B (organoclay) and the supporting pressure sensitive tape. In this figure a distinct region can be seen in both clay XRD patterns, a broad amorphous peak occurring between approximately $2\theta=14°$ and $2\theta=21°$. This region also occurs in the pressure sensitive tape XRD. This region of the XRD patterns can be attributed totally in the XRD pattern of PGW (untreated clay)

and partially in the XRD pattern of Cloisite 30B (organoclay) to the pressure sensitive tape used to secure the clay onto the sample holder. In the Cloisite 30B the amorphous peak can only be attributed partially to the pressure sensitive tape, as some of this broad peak will be caused by the organic surfactant on the clay platelets surface, in Cloisite 30B a methyl, tallow, bis-2-hydroxyethyl, quaternary ammonium cation[91] is present.

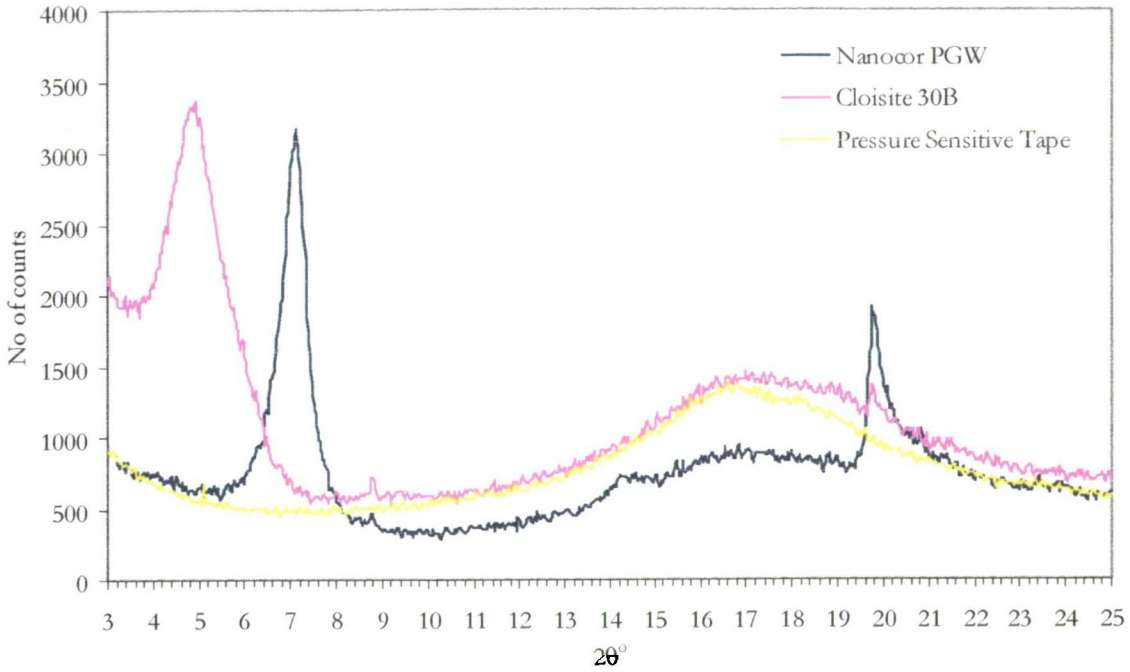


Figure 4.3: XRD Patterns of an Untreated Clay (PGW), an Organoclay (Cloisite 30B) and of Pressure Sensitive Tape.

Figure 4.4 shows typical X-ray diffraction patterns for an organoclay and for the composites produced during this project. Figure 4.5 is the X-ray diffraction pattern of the polymer used in this project, an amorphous thermoset PMMA. By comparison it can be seen that the large amorphous peak commencing at $2\theta \approx 10°$ and continuing until $2\theta \approx 22°$ can be attributed to the amorphous polymer PMMA. The peak appears in all the composite XRD patterns. It should be noted that none of the amorphous peak shown in both the PMMA XRD and the composite's XRD patterns can be attributed to the pressure sensitive tape since none was used when the XRD patterns of the PMMA and the composites were taken, (i.e. pressure sensitive tape was only used

for powder samples). Included in Figure 4.4 is the XRD pattern of Cloisite 30B, the organoclay used in this composite. The 001 peak in the organoclay which appears at $2\theta = 4.92°$ (this is confirmed by comparison with published results[91]) has, in the composite, shifted to beyond (i.e. less than) $2\theta = 3°$, the limit of the diffractometer.

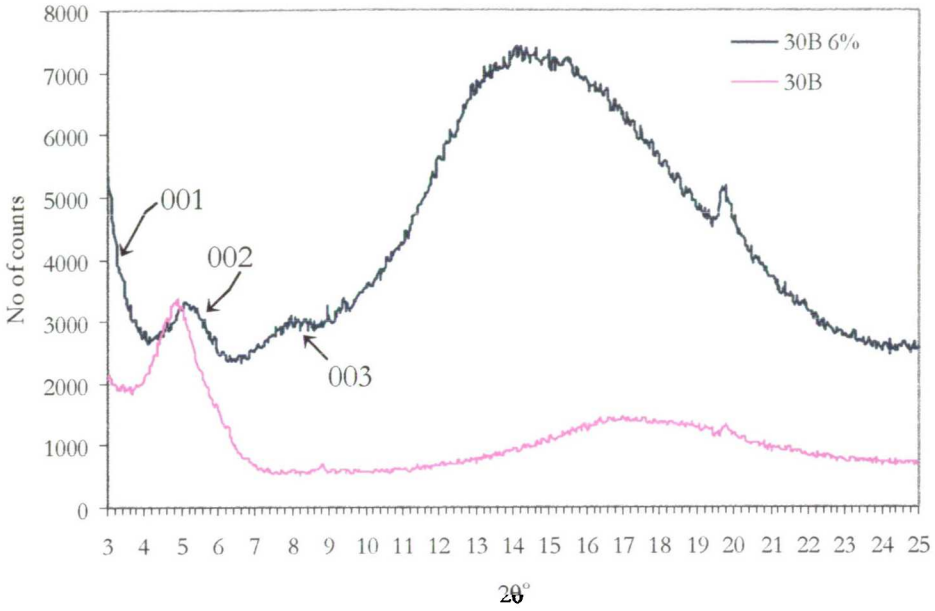


Figure 4.4: XRD Pattern of Cloisite 30B and of its 6wt% Composite.

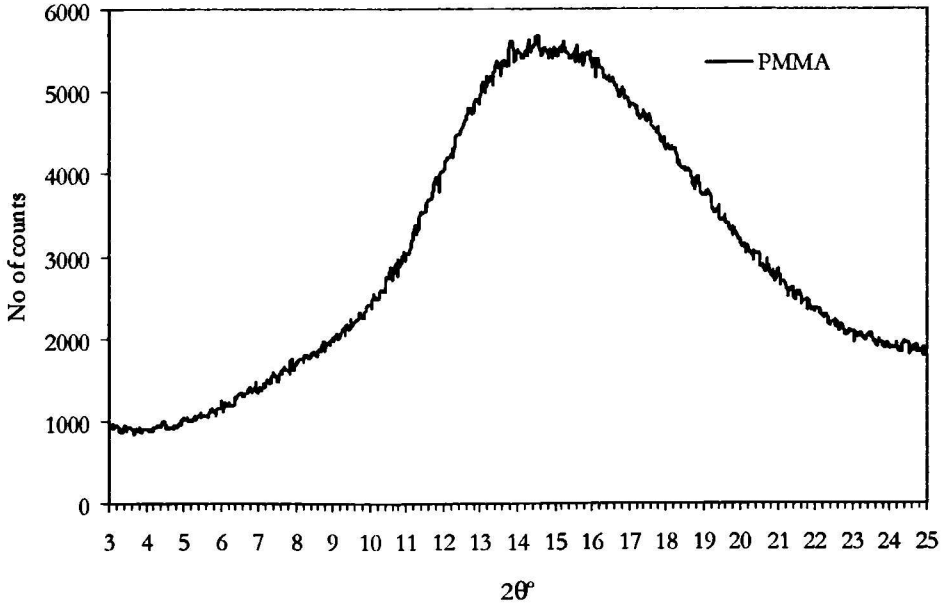


Figure 4.5: XRD Pattern of PMMA.

This behaviour is typical of the majority of the composites fabricated, as the d-spacing of the majority of the composites fabricated is greater than 29.4Å. Since, as is demonstrated in Figure 4.4, the 001 peak is not visible it was decided to utilise the position of the 002 peak, which is visible for the majority of the composite XRD patterns, to calculate the position of the 001 peak. The relationship that allows the position of the 001 peak to be calculated from the position of the 002 is based on the fact that the 002 peak is a second order reflection of the 001 plane. The relationship is detailed in full in Brown[92] (pages 26-27) and results in Equation 4.2 where *l* is the order of the reflection of interest and d is its spacing.

$$d_{00l} = \frac{d(001)}{l} \qquad \ldots Equation\ 4.2$$

Thus for d_{002}, which is a 2nd order reflection (i.e. $l = 2$), Equation 4.2 becomes

$$d_{002} = \frac{d(001)}{2} \qquad \ldots Equation\ 4.3$$

Thus the d_{002}-spacing is half the d_{001}-spacing. This relationship can be confirmed by examining the XRD pattern of organoclay where the 002 peak occurs at $2\theta = 8.8°$, see Figure 4.4, thus according to the above equation the 001 peak should occur at $2\theta = 4.4°$ which is well within an experimental error band of ±10% of the recorded 001 peak position of $2\theta = 4.92°$. Note that the error is relatively large because the peaks are broad.

4.2 Effects of Processing Variables

In attempts to produce an exfoliated nanocomposite microstructure the effects of altering certain processing variables, such as clay surfactant, type of initiator etc., on the microstructure of the composites formed have been studied. The effects found are discussed in the following sections.

4.2.1 Effect of Surfactant Type

The surface modified clays, organoclays, have in general combined better with the PMMA system than the untreated clays. The untreated clays tended to settle out almost immediately after the mixing with the monomer solution and formed a layer at the bottom of the mixing vessel. Out of the organoclays used there have been three which have exhibited similar separation behaviour to the untreated clay, although to a lesser extent, see Figure 4.6 showing a photograph illustrating the separation behaviour. The organoclays that exhibited this behaviour were Cloisite 6A, Cloisite 15A and Cloisite 20A, see Table 4.1 and Figure 4.7 (showing the chemical structure of the surfactant).

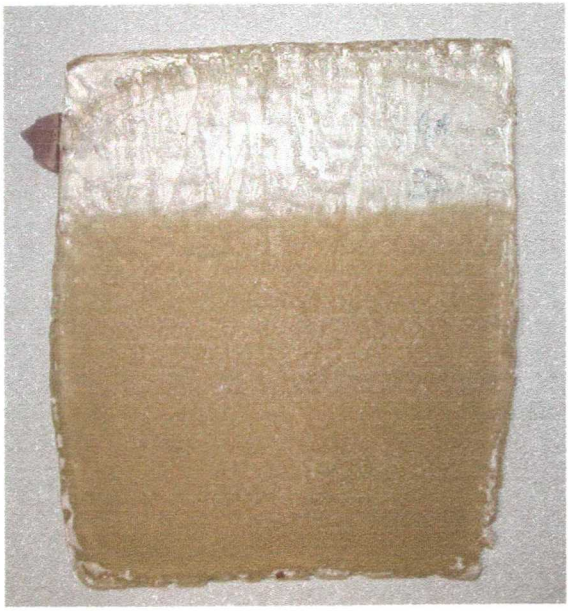


Figure 4.6: Photograph of PMMA-Cloisite 6A Composite.

These clays, when combined with the monomer solution, solidified to form two separate layers: one predominately polymer and the other clay plus polymer. The organoclay contained in the clay-polymer bottom layer was not as compacted as with the untreated clays. A common factor with all three of these clays is that they have all been surface treated with the same surfactant (shown in Figure 4.7) but to differing extents. This type of surfactant is quite bulky when compared to other surfactants in the Cloisite range, having two methyl groups and two hydrogenated tallow groups on it, this can be clearly seen when the d_{001}-spacing for the Cloisite range of organoclays are

compared. For example Cloisite 20A with a modifier concentration of 95meq/100g clay of the surfactant shown in Figure 4.7 has a d_{001}-spacing of 24.2Å, whereas Cloisite 25A with the same modifier concentration but a different modifier with only one hydrogenated tallow group has a d_{001}-spacing of 18.6Å. This indicates that the gallery spacing being wide, although an important factor in the entry of polymer chains into the gallery spacing, is not the most important factor as Cloisite 25A remains suspended in the polymer.

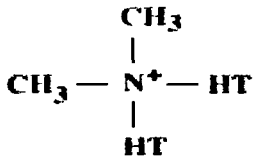


Figure 4.7: The Surfactant used in Cloisite 6A, 15A & 20A (dimethyl, dihydrogenated tallow, quaternary ammonium cation)[91].

Another organoclay, Cloisite 93A, also has two hydrogenated tallow groups similar to Cloisite 6A, 15A and 20A, however it can remain suspended in composites formed with PMMA. This indicates that it is not the presence of the extra hydrogenated tallow group alone which causes the sedimentation of Cloisite 6A, 15A and 20A. Looking at the molecule overall it can be seen that it is not particularly polar as there is little difference in the electronegativities of carbon, 2.5, and nitrogen, 3.0.

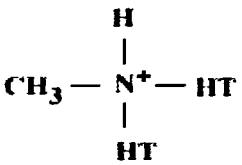


Figure 4.8: The Surfactant used in Cloisite 93A (methyl, dihydrogenated tallow ammonium cation)[91].

When looking at PMMA, it can be seen that when compared to dimethyl dihydrogenated tallow ammonium chloride, PMMA is the more polar molecule. Thus

the dimethyl dehydrogenated tallow ammonium chloride can exert no dipole attraction force on the PMMA polymer chains and so there is nothing to encourage the polymer into the clay galleries. However, with the Cloisite 93A the modifier, shown in Figure 4.8, is relatively polar compared to Cloisite 6A, 15A and 20A due to the nitrogen-hydrogen bond and so is capable of drawing the PMMA chains into the clay galleries. From this evidence it can be concluded that for any type of nanocomposite to be formed with PMMA and clay, the surfactant used has to be polar. Table 4.1 contains a summary of the types of surfactants tried and whether they remained in solution.

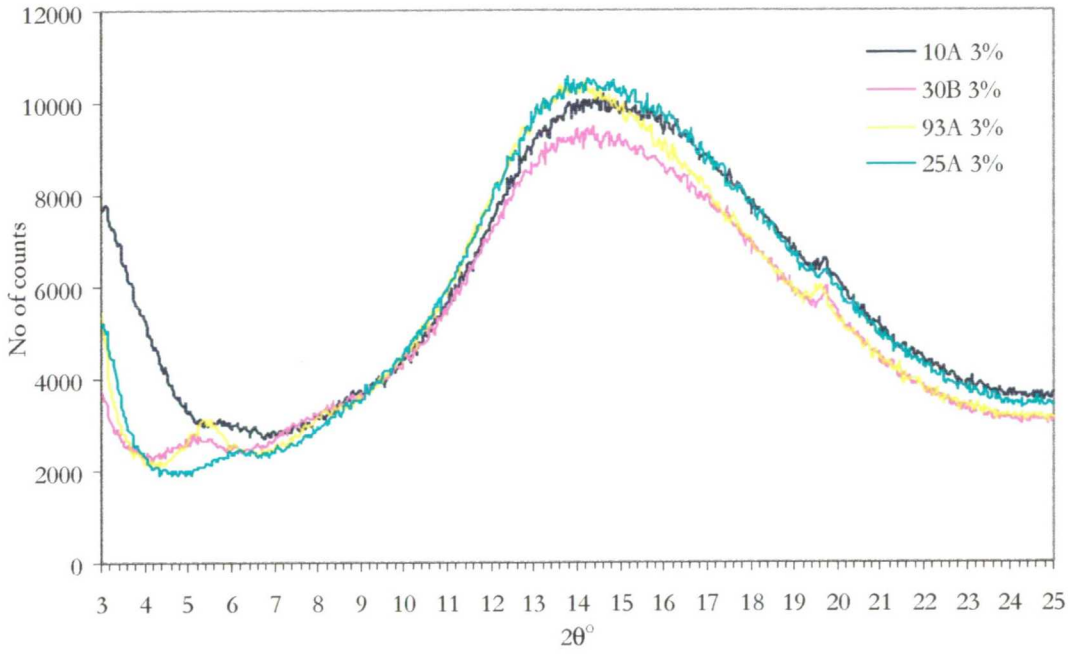


Figure 4.9: XRD Patterns of 3wt% Organoclay Composites.

From Table 4.1 the organoclays which remained in solution and formed homogenous composites were Cloisite 93A, Cloisite 25A, Cloisite 10A and Cloisite 30B. Figures 4.9 and 4.10 show the XRD patterns of 3wt% organoclay composites and of 6wt% organoclay composites respectively. From these figures it can be seen that none of the XRD patterns of the composites in the region between $2\theta = 3°$ and $2\theta \approx 10°$ are featureless as would be expected if either a delaminated or exfoliated nanocomposite microstructure had been formed. However it can also be clearly seen that the most

featureless XRD patterns result from the 3wt% and 6wt% composites fabricated using Cloisite 30B as the organoclay. This result confirms the above conclusion from the organoclays which remained in solution: namely that Cloisite 30B is a relatively polar organoclay, having two OH groups.

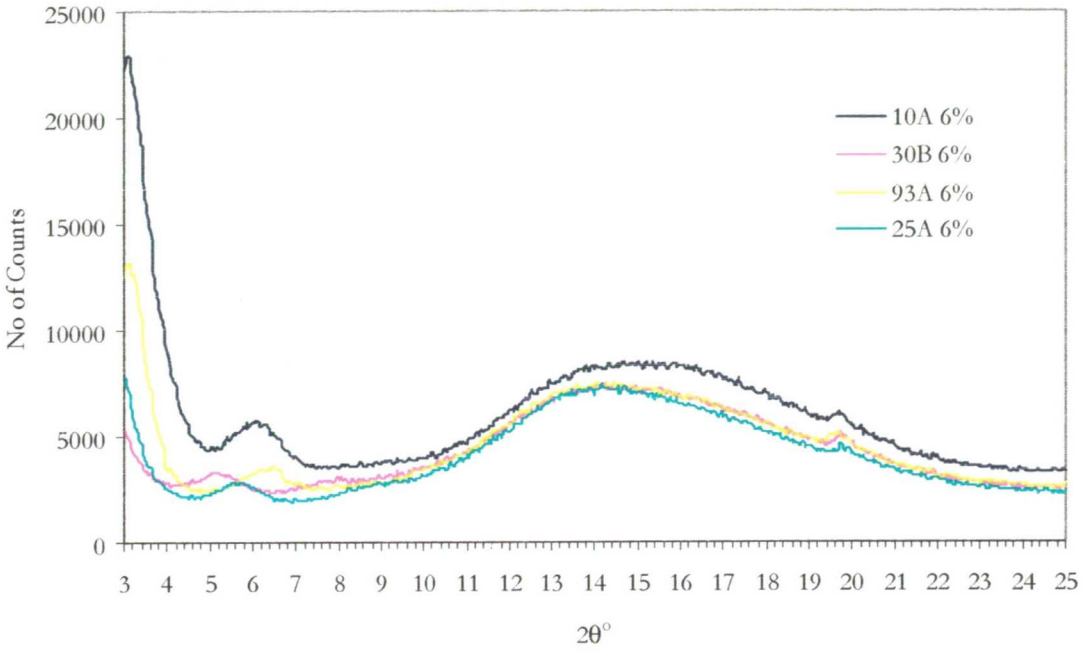
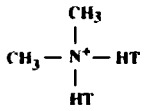
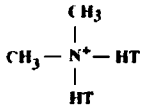
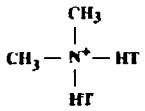
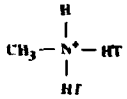
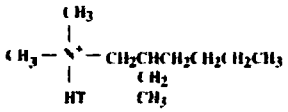
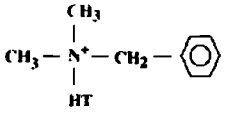
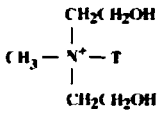


Figure 4.10: XRD Patterns of 6wt% Organoclay Composites.

Table 4.1: Table of the Organoclays and Clays used in this Work and their Effectiveness.

Commercial Clay Name	Surfactant	Surfactant Concentration	Stayed in Solution?
Cloisite 6A		140 meq /100g clay	Separated out
Cloisite 15A		125 meq /100g clay	Separated out
Cloisite 20A		95 meq /100g clay	Separated out
Cloisite 93A		90 meq /100g clay	Stayed in solution
Cloisite 25A		95 meq /100g clay	Stayed in solution
Cloisite 10A		125 meq /100g clay	Stayed in solution
Cloisite 30B		90 meq /100g clay	Stayed in solution
Nanomer PGW	Unmodified clay	N/A	Separated out
Nanomer I.30E	$CH_3(CH_2)_{16}CH_2NH_2$	20 – 30wt%	Separated out
Somasif ME100	Unmodified synthetic clay	N/A	Separated out
Montmorillonite	Unmodified clay	N/A	Separated out

4.2.2 Effect of Mixing Time

The X-ray diffraction patterns of three identical composition composites (6wt% Cloisite 25A) mixed for different lengths of time are shown in Figure 4.11. Included in this figure is the XRD pattern of the organoclay Cloisite 25A. Figure 4.11 serves to demonstrate the effect that the processing variable, mixing time, has on the microstructure of the resulting composite. The presence of a peak in the XRD patterns of all three composites at $2\theta = 19.7°$ confirms that all three composites contain clay. This can be said since this peak can always be found in the XRD pattern of the organoclay at the same position and represents the 020 and 110 planes of the clay platelets. The positions of the other XRD peaks for both the organoclay and the composites are listed in Table 4.2.

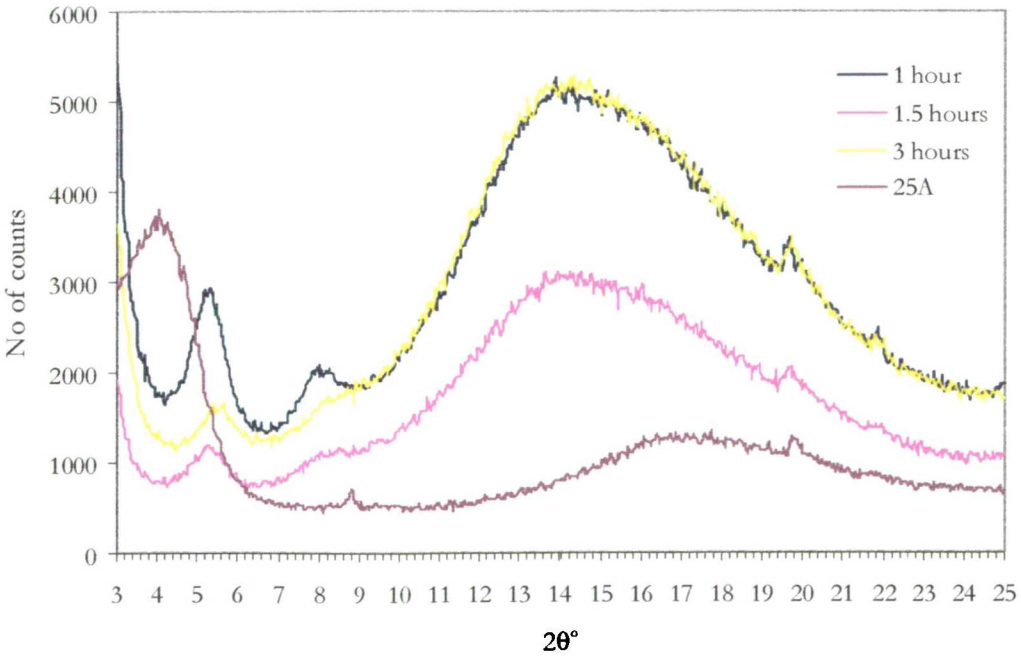


Figure 4.11: The XRD Patterns of Three Cloisite 25A 6wt% Composites Mixed for Variable Lengths of Time and of Cloisite 25A.

For the composites, from both Table 4.2 and Figure 4.11 it can be seen that the peak corresponding to the 001 plane in the organoclay (at $2\theta = 4.04°$ in Figure 4.11) has moved to a position beyond $2\theta = 3°$ (the limit of the diffractometer used). This demonstrates that the clay galleries in the composites have expanded to allow polymer chains to enter between the clay platelets. However, it can also be seen by the presence in the composite XRD patterns of the 002 basal reflection peaks (at on average $2\theta = 5.3°$) that the clay platelets remain in ordered stacks. Thus the microstructures of all the composites shown in Figure 4.11 can be said to be of the intercalated nanocomposite type.

Table 4.2: D-spacings for Cloisite 25A and its 6wt% Composites Formed with Varying Mixing Times.

Sample	d-spacings, Å (2θ,°)		
	001	002	003
Cloisite 25A	21.85 (4.04)	9.99 (8.84)	Not apparent
1 hour mix	unable to view	16.60 (5.32)	10.99 (8.04)
1½ hour mix	unable to view	16.85 (5.24)	10.37 (8.52)
3 hour mix	unable to view	16.35 (5.4)	Not apparent

From Table 4.2 it can be seen that the position of the peak that corresponds to the 002 basal reflection occurs in approximately the same position, $d_{002} = 16.5Å$ ($2\theta = 5.35°$), for all the composites and appears to be unaffected by the mixing time. Looking at the d_{002}-spacing alone would imply that any mixing time greater than 1 hour would increase the clay galleries' spacing as much as possible, unless the system is very favourable. However, Figure 4.11 demonstrates the effect of longer mixing times. In the figure the XRD pattern of the composite mixed for 1 hour shows two very distinct peaks (both are relatively tall and thin) at $2\theta = 5.32°$ corresponding to the 002 basal reflection and at $2\theta = 8.04°$ corresponding to the 003 basal reflection. The XRD patterns for the composites mixed for longer than an hour (i.e. 1½ hours and 3 hours) show these two

peaks becoming less distinct (they are relatively squat compared to those in the 1 hour pattern) and in the composite mixed for 3 hours the peak corresponding to the 003 basal reflection is undefinable. The flattening out and ultimate disappearance of these peaks indicates that more clay platelets are moving to larger d-spacings. Thus from both Figure 4.11 and Table 4.2 it can be concluded that a mixing time of between 1½ hours to 3 hours should be utilised. Supporting this argument for longer mixing times are the gradients of the beginnings of the 001 peaks of the composites, which appear to be steeper for the composite mixed for an hour than those mixed for longer time periods. This steeper gradient implies that the peak of the 001 basal reflection is at a higher angle of 2θ (i.e. smaller d_{001}-spacing) for the composite mixed for an hour than those mixed for longer.

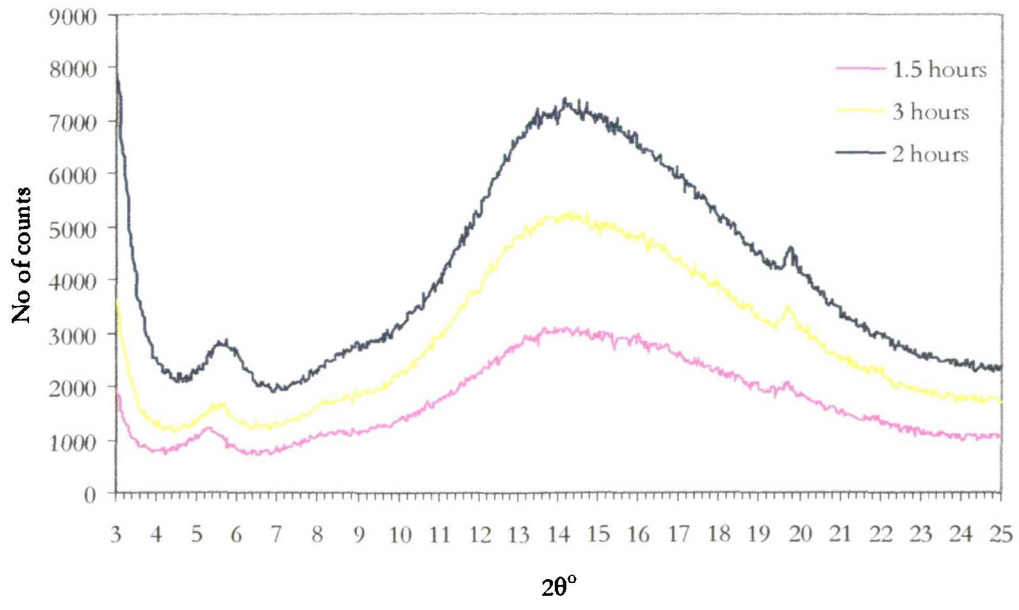


Figure 4.12: XRD Patterns of 6wt% Cloisite 25A Composites Mixed for 1½, 2 and 3 Hours.

A mixing time of 2 hours was chosen for convenience since it exceeded the 1½ hour minimum and allowed two composite plates to be produced in a day, Figure 4.12 compares the XRD pattern of a composite mixed for 2 hours with the XRD patterns of composites mixed for 1½ and 3 hours. These results imply that in a non-viscous

system, like the one used in this study, the application of high shear mixing can only go so far, and that the major driving force in achieving an exfoliated nanocomposite microstructure is the thermodynamics of the system (if the system is favourable).

4.2.3 Effect of Percentage Clay Loading

In this section the effect of the percentage clay loading on the microstructure achieved will be discussed. PMMA-clay composites were formed using the organoclays Cloisite 25A, Cloisite 10A, Cloisite 93A and Cloisite 30B, see Table 4.1. Other organoclays and untreated clays were tried with the PMMA system but as previously detailed failed to remain in solution (Table 4.1 lists the clay types tried and whether or not they remained in solution).

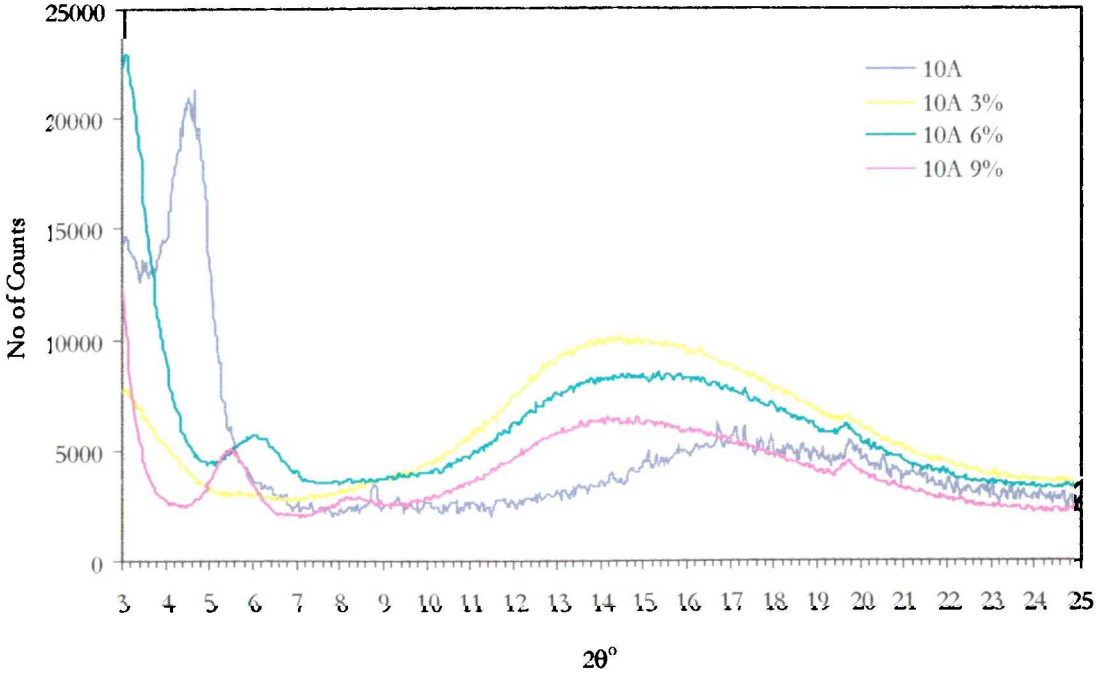


Figure 4.13: XRD Patterns of Cloisite 10A and its 3wt% , 6wt% and 9wt% Composites.

Composites were formed with all the above organoclays at clay percentage loadings of 1wt%, 3wt%, 6wt% and 9wt%, with Cloisite 93A also having a 12wt% loaded composite fabricated as well. Figures 4.13, 4.14, 4.15 and 4.16 show the XRD patterns for all the composites formed. Also included for comparison purposes in these figures are the XRD patterns of the organoclays used. Table 4.3 details the d-spacings of all

Table 4.3: D-spacings of All the Organoclays Used and their Composites.

	d-spacings, Å (2θ,°)														
	3wt%			6wt%			9wt%			12wt%			Neat Clay		
	001	002	003	001	002	003	001	002	003	001	002	003	001	002	003
Cloisite 10A	UV *30.88*	15.44 (5.72)•	NA	28.66 (3.08) *29.04*	14.52 (6.08)	NA	UV *32.22*	16.11 (5.48)	10.47 (8.44)	-	-	-	19.02 (4.64)	9.69 (9.12)	NA
Cloisite 25A	UV *28.48*	14.24 (6.2)#	NA	UV *31.54*	15.77 (5.6)	NA	UV *31.32*	15.66 (5.64)	10.47 (8.44)	-	-	-	21.85 (4.04)	9.73 (9.08)	NA
Cloisite 93A	UV *32.7*	16.35 (5.4)	NA	28.30 (3.12) *27.24*	13.62 (6.48)	NA	UV *31.98*	15.99 (5.52)	10.42 (8.48)	UV *30.66*	15.33 (5.76)	10.32 (8.56)	25.37 (3.48)	13.30 (6.64)•	NA
Cloisite 30B	UV *34.48*	17.24 (5.12)	NA	UV *34.48*	17.24 (5.12)	11.10 (7.96)#	UV *34.48*	17.24 (5.12)	11.38 (7.76)	-	-	-	17.94 (4.92)	9.69 (9.12)	NA

Notes

UV - unable to view peak.

NA - peak not apparent.

• - peak more like a shoulder than peak.

- peak more like a raised plateau.

the composites formed and of the organoclays used. Note that in Table 4.3 the 001-spacing values that appear in italics are values calculated from the 002-spacings.

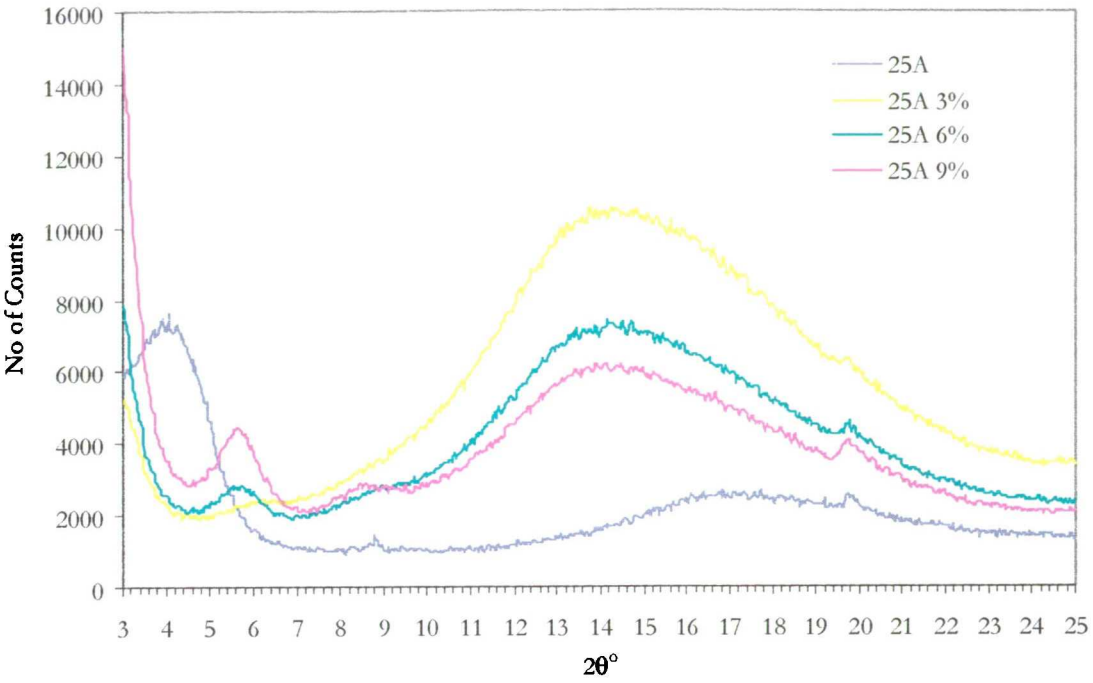


Figure 4.14: XRD Patterns of Cloisite 25A and its 3wt%, 6wt% and 9wt% Composites.

It can be seen in Table 4.3 and Figure 4.13 to 4.16 that no data for the 1wt% composites has been included in the Table or the Figures. This is because all of the 1wt% composites separated out into two layers; one predominantly polymer and the other predominantly clay, see Figure 4.17. However, since at all other percentage loadings all these clays remained in solution, it is not considered that the reason for the failure of the 1wt% composites to remain in solution is to do with the surfactant in the organoclay. It is considered to be caused by the non-viscous nature of the monomer solution and that the 1wt% loading was unable to cause sufficient increase in viscosity of the monomer solution for the clay to remain in solution.

The presence of a peak at $2\theta = 19.7°$ in all the composite XRD patterns shown in Figures 4.13 to 4.16 indicates that all the composites contain clay as the peak relates to the 020 and 110 planes of the clay platelets themselves. This peak also appears in the

organoclay XRD patterns at the same position 2θ = 19.7° (it is a *hk* diffraction band therefore its position is constant).

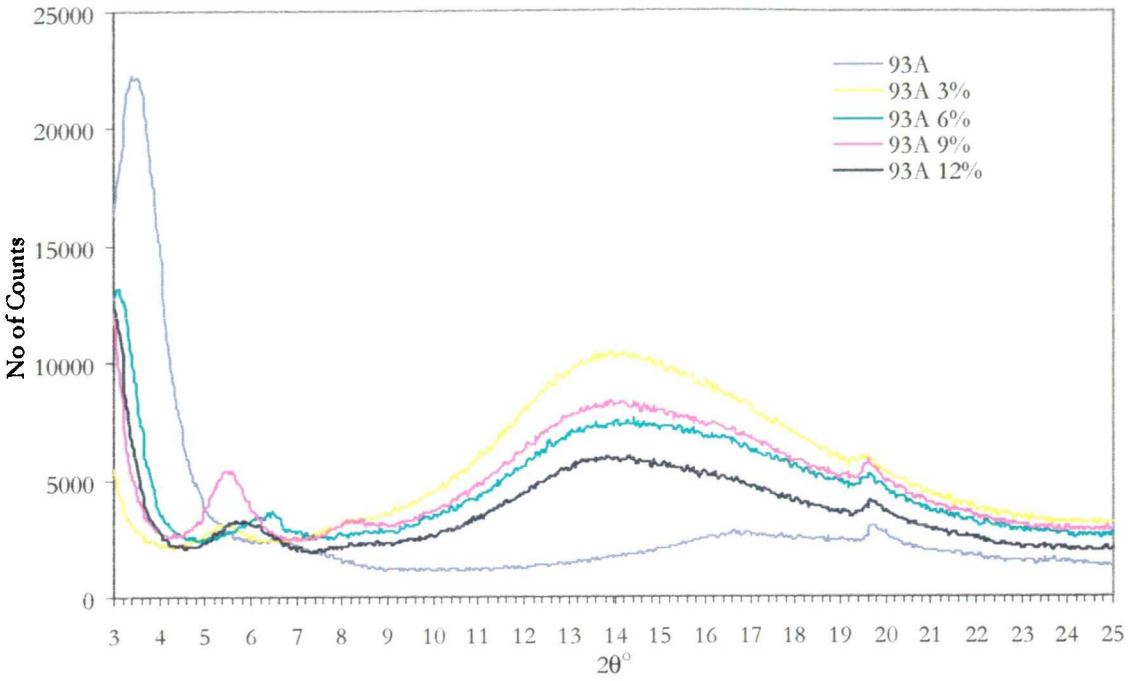


Figure 4.15: XRD Patterns of Cloisite 93A and its 3wt% 6wt%, 9wt% and 12wt% Composites.

This peak, since its position is constant, also verifies that the movement of the other peaks that occur between 2θ = 3° and 2θ ≈ 11° are not measurement effects but real changes in the clays' intergallery distances. It is possible by examination of Figures 4.13 and 4.15 to confirm that the maxima which are only partly visible at the beginning of most XRD patterns are caused by X-rays diffracted by the 001 plane of the clay platelets and not by undiffracted X-rays; since the peak of the maxima is visible in both the 6wt% Cloisite 10A composite, on Figure 4.13, and the 6wt% Cloisite 93A composite XRD pattern, on Figure 4.15.

It should also be noted that in Table 4.3 the value given for the d_{001}-spacing of the 3wt% Cloisite 25A composite is in error, since a d_{001} value of 28.48Å relates to a 2θ value of between 2θ = 3.12° and 2θ = 3.08° thus a peak would be visible on Figure 4.14 but there is no peak at this value. Thus this d_{001}-spacing can be considered an

underestimation. This error is due to the uncertain position of the 002 peak which for the 3wt% Cloisite 25A composite XRD pattern is very indistinct.

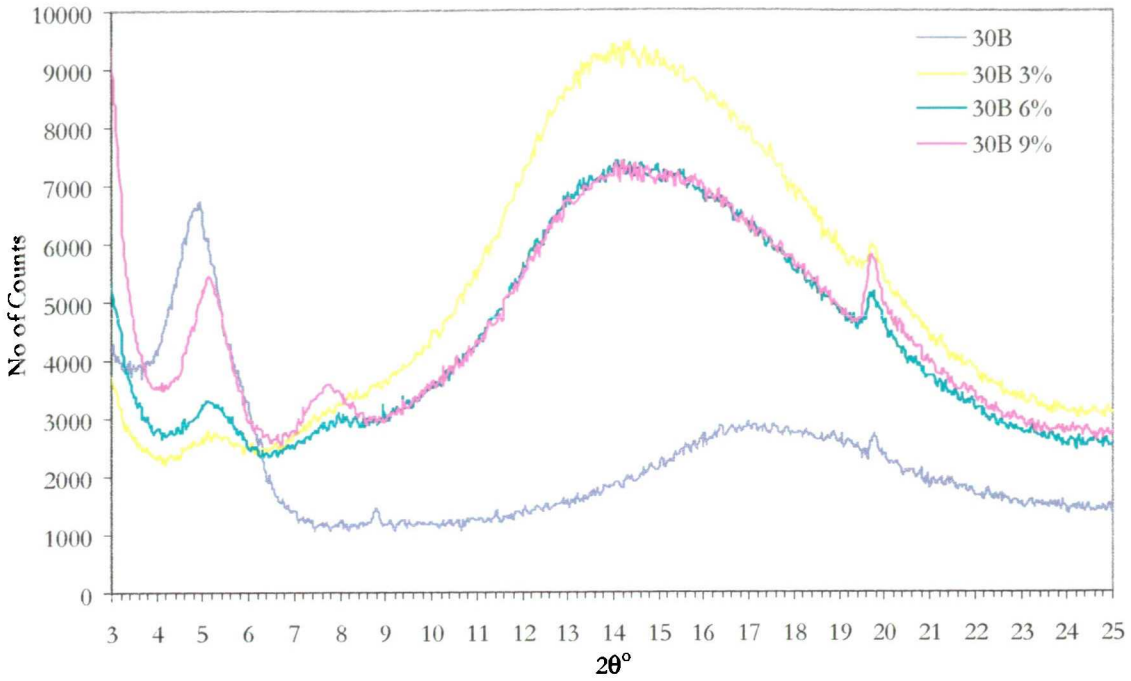


Figure 4.16: XRD Patterns of Cloisite 30B and its 3wt%, 6wt% and 9wt% Composites.



Figure 4.17: Photograph of 1wt% Composite.

From Figures 4.13 to 4.16 it can be concluded that the microstructures of all the composites formed are of the intercalated nanocomposite type.

Figure 4.13 shows the XRD patterns of Cloisite 10A and its 3, 6 and 9wt% composites with PMMA. From Figure 4.13 and Table 4.3 it can be concluded that the Cloisite 10A composite with the smallest d-spacing is the 6wt% composite. The d_{001}-spacings given in Table 4.3 for the 3wt% Cloisite 10A composite are likely to be an underestimation since the 002 peak of the 3wt% composite that can be seen on Figure 4.13 is difficult to define as it appears to be more of a shoulder to the beginnings a of broad 001 peak rather than a separate peak. Thus the d_{001}-spacing is likely to be similar to the 9wt% composites' d_{001}-spacing. According to Table 4.3 for Cloisite 10A the 9wt% composite has the largest d-spacing. However from Figure 4.13 it can be seen that both the 3wt% and 6wt% composites have more clay platelets at higher d-spacings than the 9wt% since neither of these XRD patterns have 003 peaks, and the intensity and sharpness of their 002 peaks is less than that of the 002 peak in the XRD pattern of the 9wt% composite. It is expected that the intensity of the peaks should decrease with decreasing clay content since the peaks are due to the clay platelets diffracting the X-rays, thus less clay gives fewer diffracted X-rays and so the peak intensity decreases. However the extent of the decrease is greater than would be expected for the decrease in clay content and the disappearance of the 003 peak in the 6wt% and 3wt% composite XRD patterns cannot be accounted for by this. This decrease in the intensity of the 002 peak and disappearance of the 003 in lower clay percentage loadings occurs in all of the composites fabricated, independent of d-spacing, as can be seen in Figures 4.13 to 4.16. From this it can be concluded that an effect of low clay percentage loading is that more clay platelets achieve the d_{001}-spacing whereas with higher percentage loadings fewer clay platelets achieve the d_{001}-spacing hence the appearance of the 003 peak and the increase in intensity of the 002 peak.

An expected effect of increasing the clay percentage loading was for the d_{001}-spacing to decrease as there would be less space for expansion of the clay galleries when more clay platelets are present in the same amount of polymer. However, from Table 4.3, it can be concluded that for this particular system either this effect does not occur, as in the

organoclay Cloisite 30B, or the effect occurs but is small, as in Cloisite 25A (a decrease of 0.22Å in going from 6wt% to 9wt% Cloisite 25A). With this system the d_{001}-spacing (the gallery spacing) appears from Table 4.3 to reach a maximum spacing relatively independent of clay loading. This is clearly demonstrated in Figure 4.16 where the only difference between the 002 peaks is their intensity, their positions coincide with one another. This indicates that this d-spacing is the maximum achievable for this particular system with this particular organoclay. Thus it can be concluded that for this system with the organoclays and clays tried that the d_{001}-spacing (the maximum gallery spacing) is independent of clay percentage loading over the range investigated and is more governed by the thermodynamics of mixing. In addition, for this system the thermodynamics of mixing appears to favour the formation of intercalated nanocomposite microstructures rather than exfoliated nanocomposite microstructures.

4.2.4 Confirmation of X-Ray Diffraction Results using Transmission Electron Microscopy

Introduction

The microstructural results already presented in this chapter, obtained from the analysis of the X-ray diffraction data for PMMA-organoclay composites with various organoclay loadings, will be verified in this section by the examination of transmission electron micrographs of a selection of the composites. A selection of composites were chosen to be examined by transmission electron microscopy (TEM) since both sample preparation and use of the TEM were complex and expensive. Also under an electron beam PMMA decomposes readily, hence the amount of time spent in a specific area of a sample was limited and areas near to the edges of the sample sheets could not be viewed as the electron beam damage caused the sample sheets to curl in on themselves.

The Cloisite 93A 3wt%, 6wt% and 9wt% composites were examined as well as the 3wt% Cloisite 25A composites using this technique. In the transmission electron micrographs regions of high density material appear darker than regions where the density is lower. This is because in the high density regions more electrons are

scattered by the material, and thus less are transmitted through the material to the detector, than in low density regions. Thus in the transmission electron micrographs presented here the clay particles and platelets appear as dark regions, due to their high density, whilst the PMMA (since it has a lower density than clay) appears as the lighter regions.

It should be noted that in general the data from analysis of X-ray diffraction patterns is considered to be more representative than data from transmission electron micrographs. The reason for this is that transmission electron micrographs typically cover an area of 385nm by 635nm and the sample sheets are between 70 to 100 nm thick. Whereas in X-ray diffraction the X-ray beam spot size is approximately 1cm^2 and 50% of the beam can be calculated[93] to penetrate to a depth of more than 90 μm. Typically clay particles before mixing have a diameter of approximately 10μm and an aspect ratio of approximately 4[94]. Thus it can be safely assumed that an XRD scan would collect information from more clay particles than can be accommodated in a transmission electron micrograph. However, transmission electron microscopy is still very useful as it can be used when the 001 peak of the microstructure is beyond the limit of the diffractometer, and to distinguish between exfoliated and delaminated nanocomposite microstructures.

Transmission Electron Micrographs of the Composites

Figure 4.18 and 4.19 present the transmission electron micrographs of the 3wt% Cloisite 25A and 3wt% Cloisite 93A composites respectively. From these figures it can be concluded that polymer is present in the clay galleries i.e. the composites possess an intercalated nanocomposite microstructure as discussed below. However a few disassociated clay platelets can be seen, and thus the extent of intercalation of polymer in the clay galleries for the composites is variable. For the 3wt% Cloisite 25A composite see Figure 4.18 it can be found by measurement that the average spacing of the clay platelets is approximately 44.9Å (4.49 nm). This is somewhat larger than the d-spacing value of 28.5Å obtained using XRD, as shown in Table 4.3.

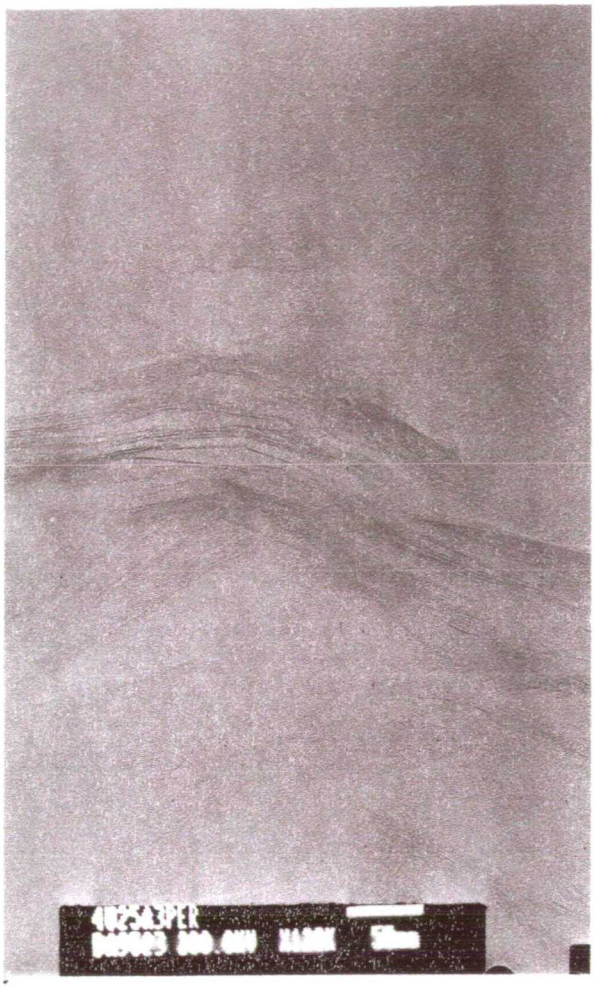


Figure 4.18: Transmission Electron Micrograph of a PMMA-3wt% Cloisite 25A Composite. (Note the scale bar represents 50nm (500Å)).

It has already been argued that the value found from the XRD analysis is deceptively low and likely to be in error since the 001 peak is not visible and the 002 peak is not distinct. As well as this, the exact shape of the 001 peak is unknown since it occurs beyond the resolution of the X-ray diffractometer. However, the 001 peak is a *00l* basal reflection, rather than an *hk* diffraction band, and thus will be symmetrical about its centre[95]. The 001 peak of the 3wt% Cloisite 25A composites (as can be seen in Figure 4.20) commences at $2\theta = 4.20°$ (21Å) and has not reached its apex at $2\theta = 3°$, thus is a relatively broad peak that would be expected to include the d-spacing of 44.9Å observed in the micrographs at $2\theta = 1.965°$.

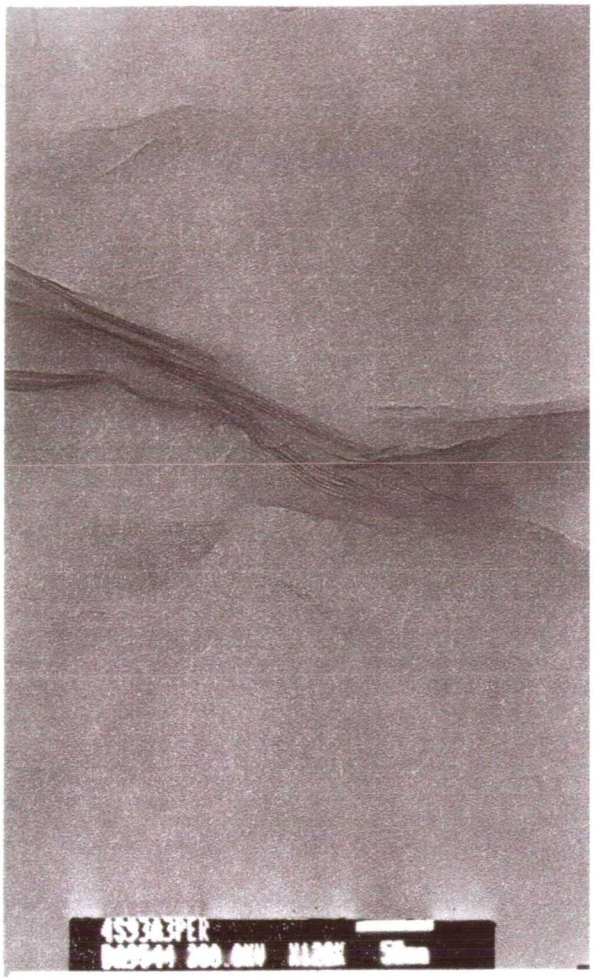


Figure 4.19: Transmission Electron Micrograph of a PMMA-3wt% Cloisite 93A Composite. (Note the scale bar represents 50nm (500Å)).

Using Figure 4.19 and other transmission electron micrographs, the average clay gallery spacing for the 3wt% Cloisite 93A can be found to be approximately 48.8 Å (4.88nm). This value, along with the value found for the 3wt% Cloisite 25A composite, shows good agreement with the values found from XRD taking into account that the sample area under examination using the TEM is only a tiny fraction of the sample area under examination using XRD.

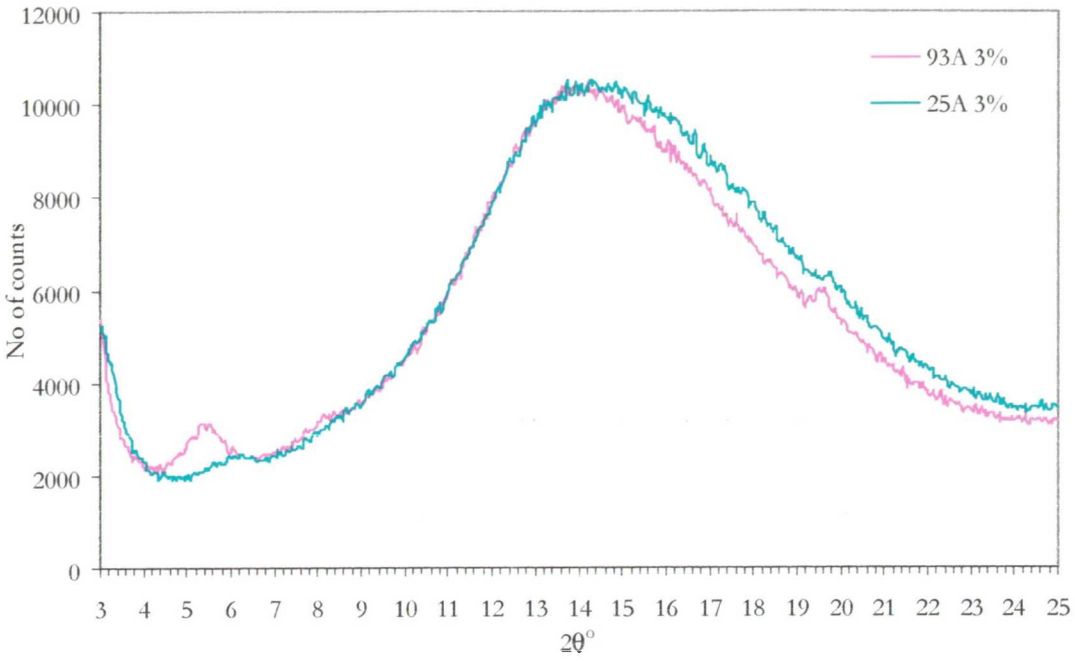


Figure 4.20: XRD Patterns of a PMMA-3wt% Cloisite 25A Composite and a PMMA-3wt% Cloisite 93A Composite.

Figure 4.21 presents two transmission electron micrographs of composites containing 6wt% of Cloisite 93A. It can be seen again in Figure 4.21 that polymer has entered the clay galleries, thus the microstructure formed is that of an intercalated nanocomposite. In these micrographs there are a few semi-dark regions that can be concluded to be disassociated clay platelets due to the abruptness of the boundaries of these regions. From these micrographs an average clay gallery spacing of approximately 28Å (2.8nm) is found. This value agrees well with the XRD value of 28.3 Å, as shown in Table 4.3.

Figure 4.22 presents two transmission electron micrographs of 9wt% Cloisite 93A composites. From these micrographs it can be concluded again that there is polymer between the clay platelets, thus the microstructure is that of an intercalated nanocomposite. It can also be seen that the extent of the intercalation is very varied. However, from comparison with the 3wt % micrographs, see Figure 4.19, for the 9wt% composites the extent of intercalation tends to be smaller than for the 3wt% composites. From the micrographs presented in Figure 4.22 an average clay gallery spacing of approximately 27Å (2.7nm) is found. This value is somewhat smaller than

the value of 32Å calculated from the 002 peak using XRD. However, if Figure 4.23 showing the XRD trace of Cloisite 93A 9wt% is examined, it can be seen that 27Å (2θ = 3.26°) is well within the 001 peak. Also it must be noted that only a small fraction of sample can be examined by TEM whereas XRD can examine a much greater area of specimen.

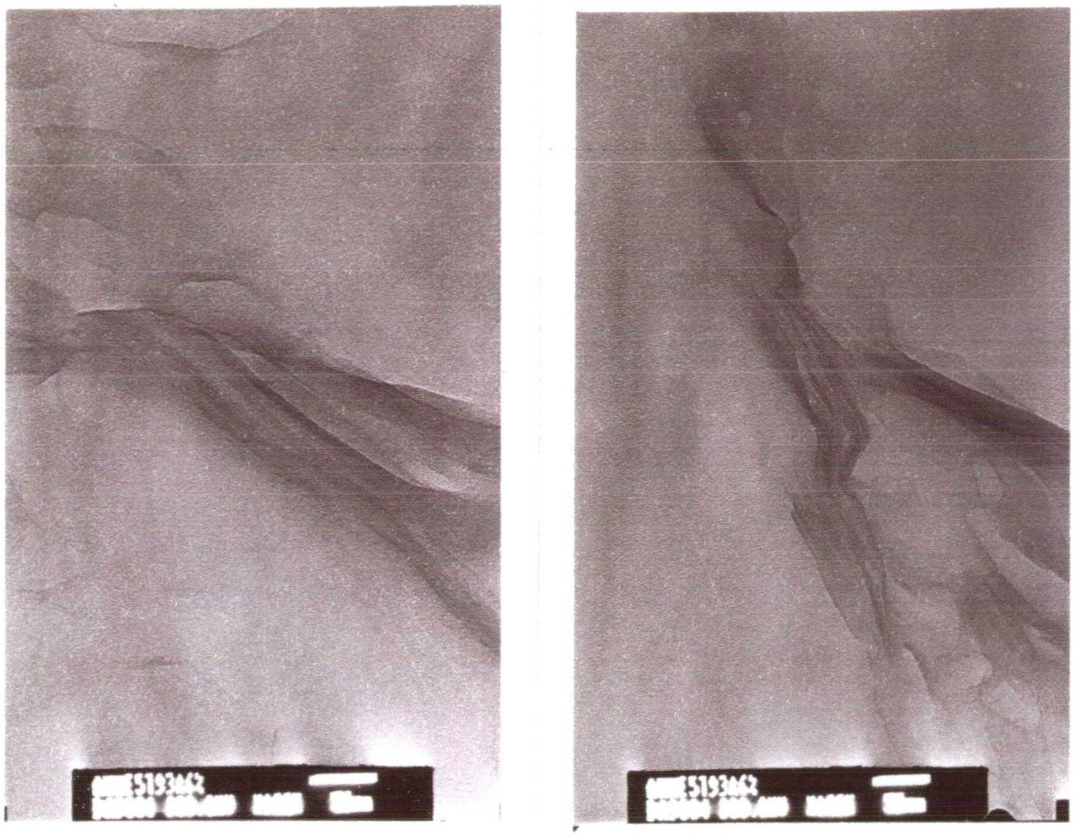


Figure 4.21: Transmission Electron Micrographs of a PMMA-6wt% Cloisite 93A Composite. (Note the scale bar represents 50nm (500Å)).

Thus the micrographs shown in Figures 4.18, 4.19, 4.21 and 4.22 confirm the X-ray diffraction analysis results, that the composites formed all possess an intercalated nanocomposite microstructure. The micrographs also confirm that as the percentage loading increases then the proportion of clay platelets with large extents of intercalation decreases.

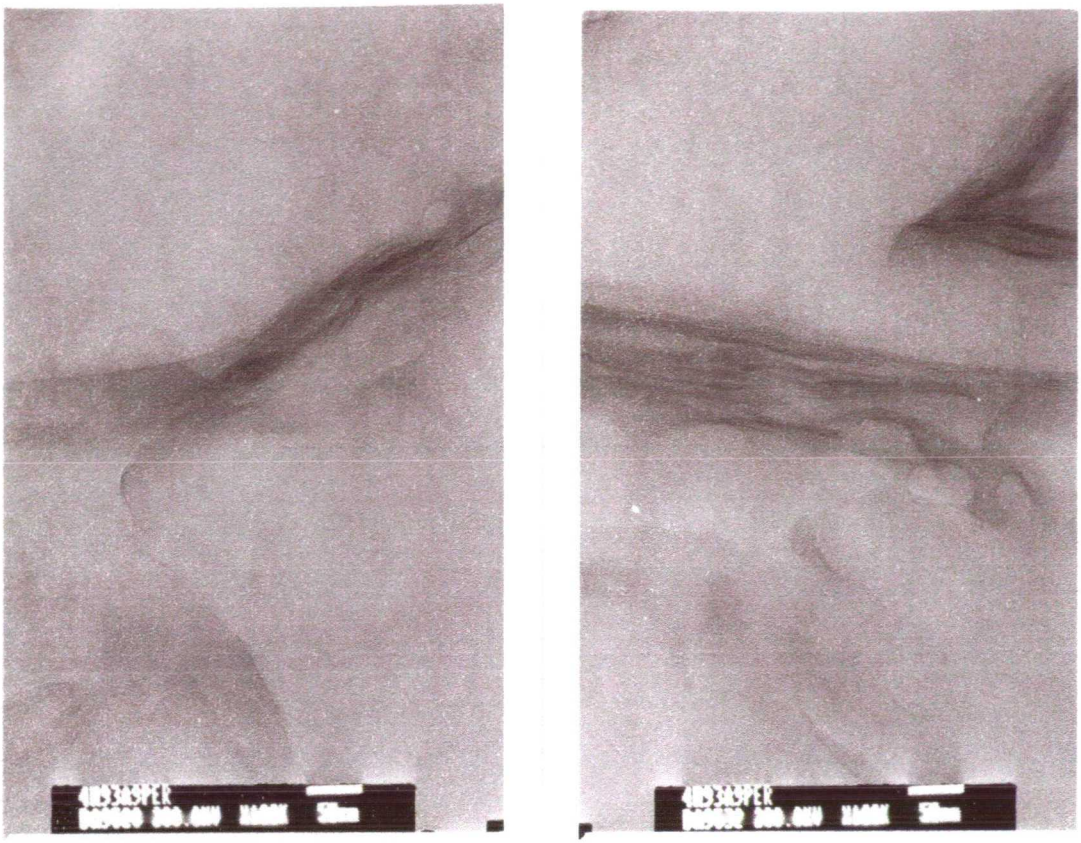


Figure 4.22: Transmission Electron Micrographs of a PMMA-9wt% Cloisite 93A Composite. (Note the scale bar represents 50nm (500Å)).

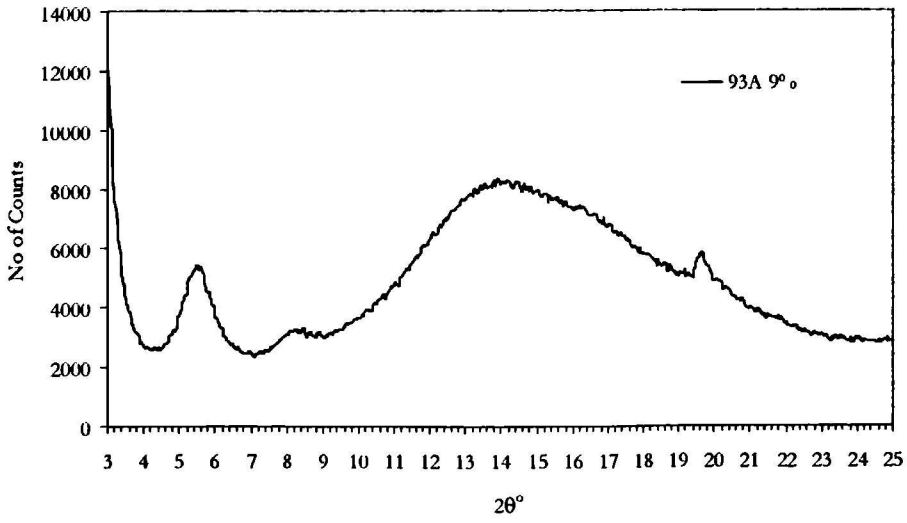


Figure 4.23: XRD Pattern of a PMMA-9wt% Cloisite 93A Composite.

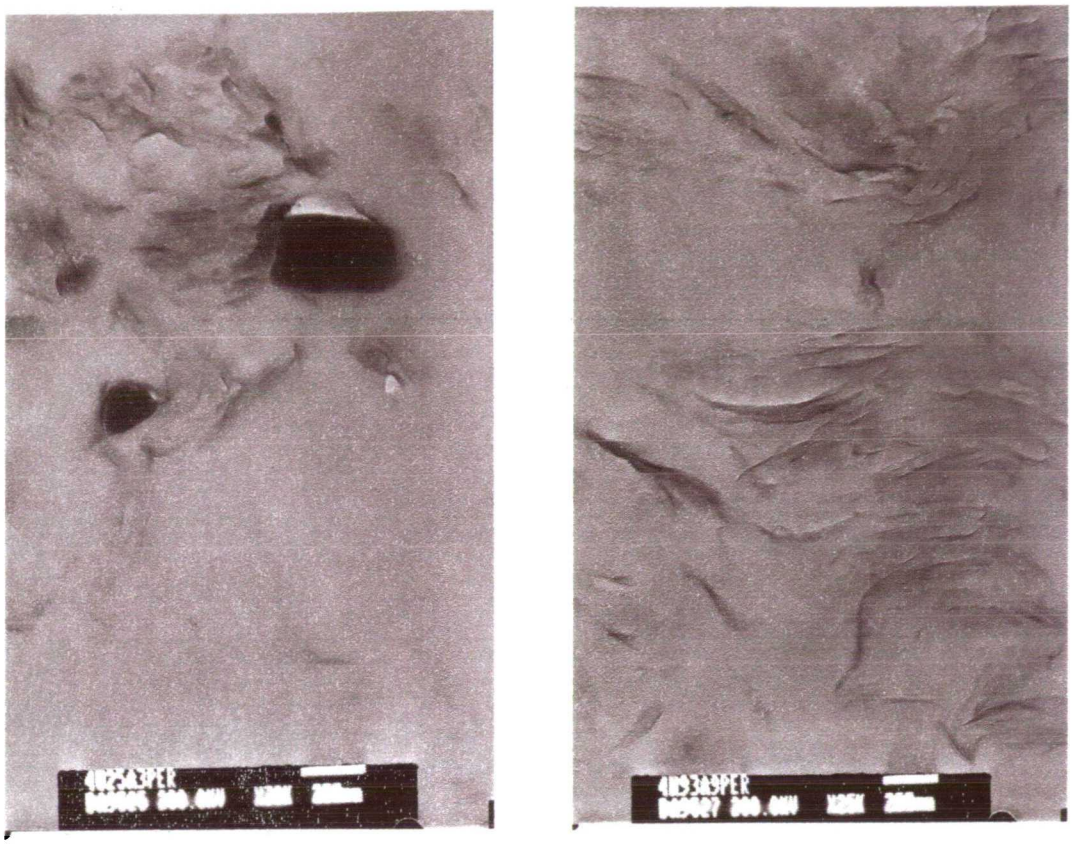


Figure 4.24: Transmission Electron Micrograph of a 3wt% Cloisite 93A Composite showing Particle Distribution. (Note the scale bar represents 500nm (5000Å)).

Figure 4.24 demonstrates clearly two points. (Note that the very dark region running diagonally through the micrograph is a fold in the ultra-microtomed specimen sheet.) Firstly the material can be said to be reasonably homogenous since the clay particles are quite evenly distributed. Secondly it can be seen that although the clay platelets are most certainly intercalated with polymer, the clay particles still remain agglomerated but are less dense due to the polymer intercalation.

Using Figure 4.25 it can be concluded that clay particle size can vary quite extensively. For example, in Figure 4.25(a) two face-on clay particles can be seen, the larger particle

is approximately 340nm by 230nm whereas the smaller particle at its widest points is 160nm by 120nm.



(a) (b)

Figure 4.25: Transmission Electron Micrographs of (a) 3wt% Cloisite 25A Composite and (b) 9wt% Cloisite 93A Composite, showing Clay Particle Size and Aspect Ratio.
(Note the scale bar represents 200nm (2000Å)).

Figure 4.25(b) can be used to give a guide to the range of aspect ratios typical for these composites by measuring the thickness and length of the clay particles. The range found from this figure is from approximately 7.5 to 10. These aspect ratios are relatively low compared to those mentioned in the literature[7] this is in part expected since the microstructures achieved here are not those of an exfoliated nanocomposite. The aspect ratio of a particle is defined as the length (diameter) of the particle divided by its thickness. Hence, for an intercalated microstructure, as achieved in these composites, the aspect ratio of the particles would decrease as the length (diameter) of the particles

would remain constant and the thickness of the particles would increase. As previously stated the aspect ratio of these particles in the unmixed state is 4. The range of aspect ratios calculated from Figure 4.25(b) is actually greater than this not less. This revelation leads to two possible conclusions, firstly that upon mixing the particles break up or secondly that the particles in Figure 4.25(b) used to calculate aspect ratio were not complete particles but delaminated parts of a particle.

4.2.5 Effect of Choice of Polymerisation Initiator

Through the published findings of many studies it has been agreed that the choice of polymerisation initiator/curing agent has a significant effect on the microstructure of the composites produced as discussed in Chapter 2. For the majority of this study the initiator used to produce the composites was 2,2-azo-bis-isobutyronitrile, AIBN. However, to investigate the effect of initiator choice on the microstructure of the final composite two additional initiators were selected. These initiators, lauroyl peroxide and trigonox 23, were selected based upon the advice given by both Dr Gordon Seeley[96] (ICI Strategic Technology Group) and Jon Hickey[97] (Cambridge University).

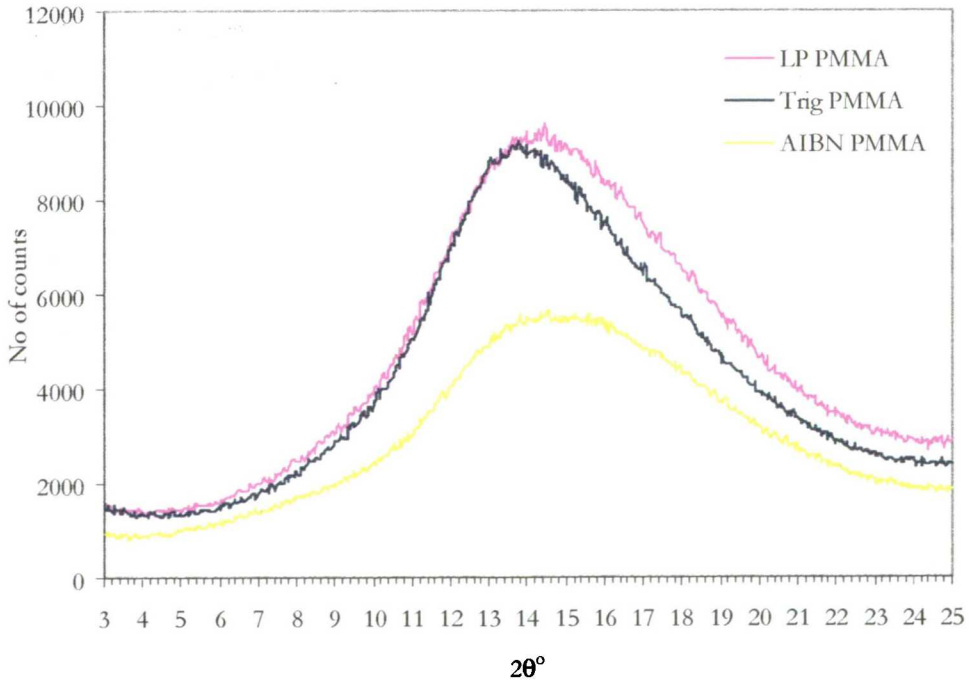


Figure 4.26: XRD Patterns of PMMA Initiated with AIBN, Lauroyl Peroxide and Trigonox 23.

The microstructure of the composites produced using these initiators was compared to the microstructure of composites produced using AIBN as the polymerisation initiator. The XRD patterns of lauroyl peroxide initiated, trigonox 23 initiated, and AIBN initiated PMMA are shown in Figure 4.26. It can be concluded that changing the polymerisation initiator has no effect on the microstructure of the PMMA formed since neither the position of the peak or its shape have altered. This was as expected since changing the polymerisation initiator only alters the end groups of the polymer chains.

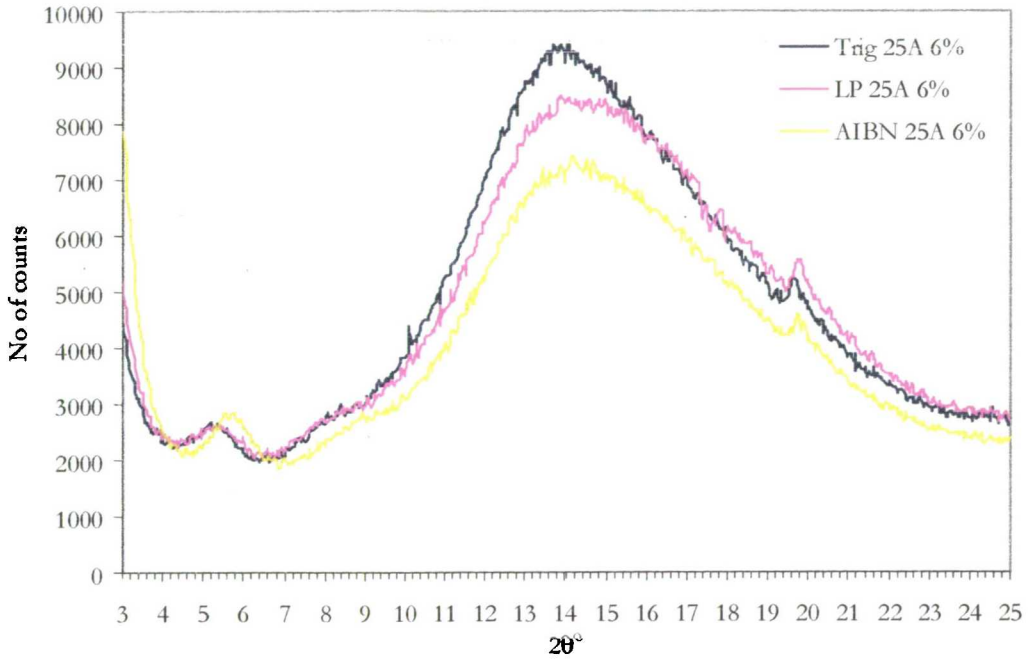


Figure 4.27: XRD Patterns of AIBN, Lauroyl Peroxide and Trigonox 23 Initiated PMMA-Cloisite 25A 6wt% Composites.

The effect of choice of polymerisation initiator on the composite microstructure was investigated using two organoclays - Cloisite 93A and Cloisite 25A. These were chosen as it was considered that they had quite different surfactants. Composites were formed using 3wt%, 6wt% and 9wt% of the appropriate organoclay (note that no composites using trigonox 23 as the initiator with 3wt% organoclay were produced due to the limited supply of trigonox 23). The XRD patterns of the composites using Cloisite 25A 6wt% and Cloisite 93A 6wt% are shown in Figure 4.27 and Figure 4.28 respectively.

These data are summarised in Table 4.4, which contains the measurable 001 and 002 spacings of the composites. Note that most of the 001 peaks of the composites were beyond the 3° limit of the diffractometer, except for the 6wt% Cloisite 93A composite initiated with AIBN. Also included in Table 4.4 are 001 spacings calculated assuming that the 001 spacing is twice the 002 spacing, as shown in Equation 4.3.

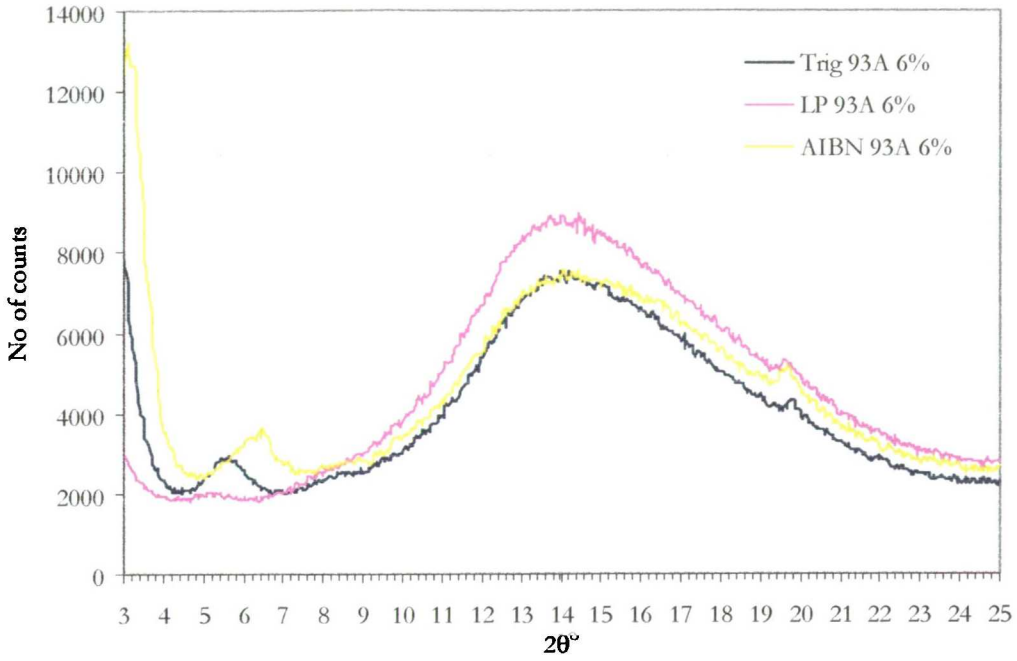


Figure 4.28: XRD Patterns of AIBN, Lauroyl Peroxide and Trigonox 23 Initiated PMMA-Cloisite 93A 6wt% Composites.

Figures 4.27 and 4.28 show that all of the d-spacings for the composites formed exceed those of the pristine organoclays. Thus all the composites formed possess an intercalated nanocomposite microstructure. From Figure 4.27 it could be concluded that with 6wt% of Cloisite 25A using either lauroyl peroxide or trigonox 23 would produce a composite with d-spacings exceeding those when using AIBN as a polymerisation initiator.

The same trend of a larger d-spacing from initiating by lauroyl peroxide and trigonox 23 than for AIBN, is seen for the 6wt% Cloisite 93A data, as shown in Figure 4.28. The greatest d-spacings of 34.5Å are achieved with 6wt% Cloisite 93A when lauroyl peroxide is used as the initiator. This can be said since firstly the 002 peak is weak in

intensity indicating that there are few platelets at this spacing. Secondly the gradient of the 001 peak of the lauroyl peroxide initiated composite is less steep than that of both the AIBN and trigonox 23 initiated materials. This indicates that the 001 peak position is at the lowest angle for the lauroyl peroxide 6wt% Cloisite 93A composite.

Table 4.4: D-spacing of 6wt% Cloisite 25A and Cloisite 93A Composites Initiated with either AIBN, Lauroyl Peroxide or Trigonox 23.

Spacing, Å	Lauroyl Peroxide		Trigonox 23		AIBN	
(2θ°)	25A 6%	93A 6%	25A 6%	93A 6%	25A 6%	93A 6%
001	UV	UV	UV	UV	UV	28.3 (3.12)
002	16.6 (5.32)	17.25 (5.12)	16.47 (5.36)	15.66 (5.64)	15.77 (5.6)	13.63 (6.48)
Calculated 001	33.20	34.50	32.94	31.32	31.54	27.26

Note. Calculated 001 data used 002 data and Equation 4.3, UV: unable to view.

From the d-spacings listed in Table 4.4 it is possible to conclude that using lauroyl peroxide as the polymerisation initiator produces composites with intercalated nanocomposite microstructures that have larger d-spacings than composites formed with either AIBN or trigonox 23. This was a little unexpected as it was thought that the composites with the largest d-spacings would have been initiated using trigonox 23 since it was liquid in form, thus would have dispersed readily in the liquid monomer-clay solution, and could enter the clay galleries. By contrast lauroyl peroxide was in flake form and AIBN in powder form hence they would not readily enter the galleries between the clay platelets. As well as this it was expected that the largest d-spacing would occur in the trigonox 23 composites as this is a more volatile compound than either lauroyl peroxide or AIBN (which both undergo thermolysis at 60°C unlike the 40°C that trigonox 23 does) thus it was believed a favourable balance could be struck between internal and external clay gallery polymerisation rate. It appears that the mixing procedure used may influence the d-spacing. The AIBN used in this work was in a fine powder form and was added straight to the monomer-clay and allowed to dissolve over a 3 hour time period as it was considered that its dissolution would be unhindered by

the clay particles. As trigonox 23 is very volatile it was only given 20 minutes on the rollers whereas both the lauroyl peroxide mixture and the AIBN mixtures were given 3 hours. Hence the resulting d-spacing may be lower than originally expected. The lauroyl peroxide used in this work came in the form of flakes with an average diameter of a few millimetres. So that their dissolution was unhindered by the clay particles approximately 30ml of monomer solution was set aside and the lauroyl peroxide flakes were dissolved in this for 2 hours. This lauroyl peroxide-monomer solution was added to the monomer-clay solution and put on to the rollers for 3 hours to allow mixing and the release of any trapped air. Thus the lauroyl peroxide solution was afforded the largest time period to work its way into the clay galleries and thus increasing the probability of the lauroyl peroxide initiating polymerisation in the clay galleries. Hence this gives the largest d-spacing.

System Tuning: Surfactant and Initiator

The XRD patterns of both 6wt% and 9wt% of Cloisite 25A initiated by both lauroyl peroxide and trigonox 23 are shown in Figure 4.29. Figure 4.30 shows the XRD patterns of lauroyl peroxide initiated and trigonox 23 initiated 6wt% and 9wt% Cloisite 93A composites. From these figures it can be concluded that the organoclay Cloisite 25A achieves larger d-spacings at both 6wt% and 9wt% when trigonox 23 is used to initiate polymerisation rather than lauroyl peroxide. Conversely the organoclay Cloisite 93A achieves larger d-spacings at both 6wt% and 9wt% when lauroyl peroxide is used to initiate polymerisation rather than trigonox 23. This indicates that to achieve an exfoliated nanocomposite microstructure for this particular form of PMMA requires very fine tuning of either the clay surfactant to the polymerisation initiator.

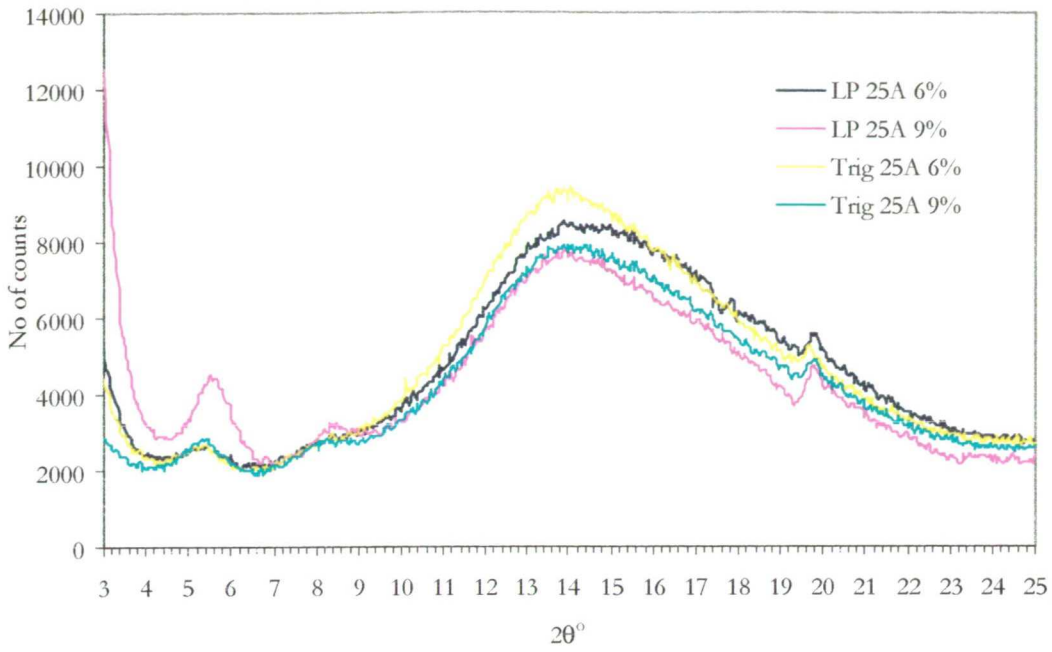


Figure 4.29: XRD Patterns of both Lauroyl Peroxide and Trigonox 23 Initiated 6wt% and 9wt% Cloisite 25A Composites.

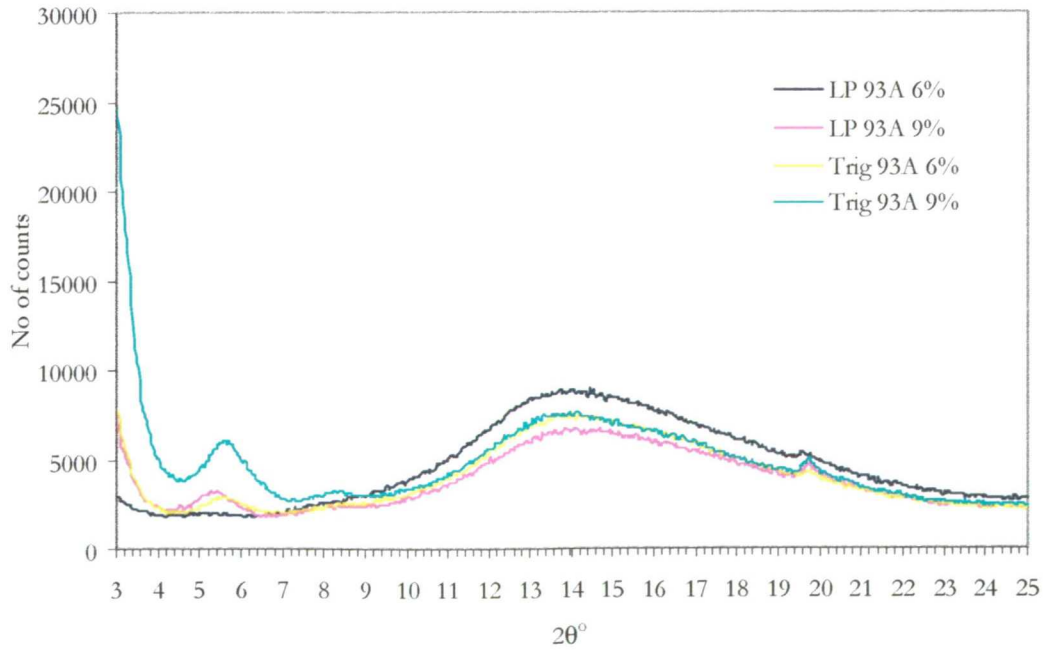


Figure 4.30: XRD Patterns of both Lauroyl Peroxide and Trigonox 23 Initiated 6wt% and 9wt% Cloisite 93A Composites.

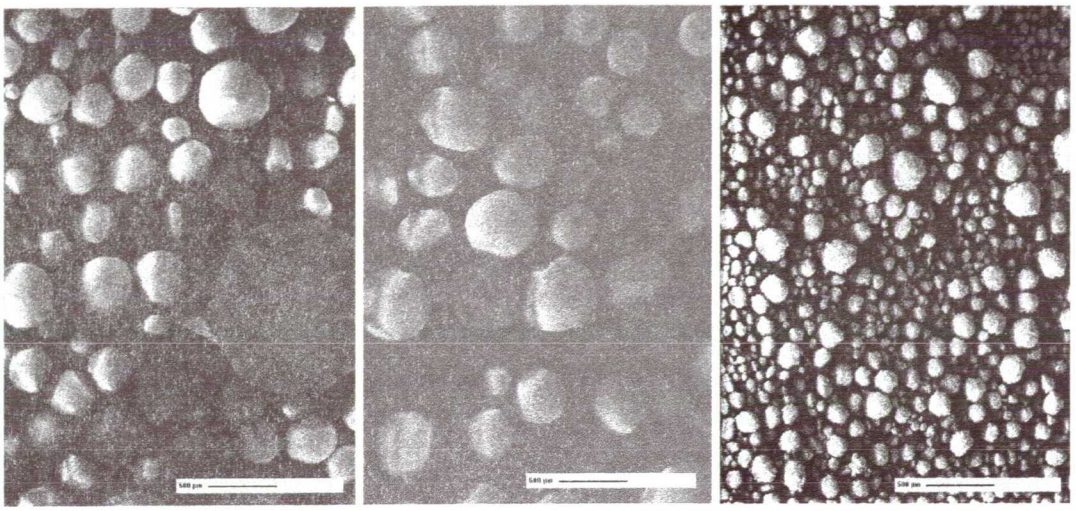
4.3 Microstructure of Rubber Toughened Composites

Two different approaches were used to produce a rubber toughened form of the PMMA under investigation. The first approach used a solid rubber, hypalon (a chlorosulfonated polyethylene), as the toughening agent. The rubber was dissolved into the monomer solution and subsequently the solution was polymerised. This method was unsuccessful in that once dissolved the rubber would precipitate out into a single large rubber mass before the solution had a chance to polymerise. When the solution was successfully polymerised a similar effect was found to happen in the solid where the rubber would phase separate not into micron-sized discrete particles but into large volumes of rubber.

The other approach involved the use of pre-formed core-shell particles as the toughening agent. Briefly, core-shell particles are multi-layer particles, with typically 2, 3 or 4 layers. The layers alternate from a rubbery polymer, such as poly[(n-butyl acrylate)-co-styrene], to a glassy polymer, typically PMMA is used, with the outer layer of the core-shell particle always being of the glassy polymer. For a more detailed description of core-shell particles see Section 2.8 of Chapter 2. This approach was immediately successful at producing useable samples. Thus in light of this the solid rubber approach was abandoned and the work continued using the core-shell particles approach. Toughened PMMA was formed with three different core-shell particles, two obtained from the Lucite International production line (XC42 and XC44) and one chosen, on advice, from the Rohm & Haas range of impact modifiers (KM355). All three of these particles produced homogenous toughened PMMA.

The micrographs in Figure 4.31, from scanning electron microscopy, show each of the core-shell particles before being added to the monomer. Unfortunately however since the particles are aggregated when in this state Figure 4.31 gives a deceptive idea of particle size (of between 60μm and 500μm as shown in Figure 4.31). For a more realistic particle size the fracture surfaces of PMMA containing these core-shell particles were examined for particles on the surface. Figure 4.32 shows micrographs from different areas of a sample containing 5wt% of KM355 core-shell and shows that the

particle size does vary quite widely but is significantly smaller than those implied from Figure 4.31.



(a) (b) (c)

Figure 4.31: Scanning Electron Micrographs of the Core-Shell Particles used in this Work (a) XC42 (b) XC44 and (c) KM355. (Note the scale bar represents 500μm).

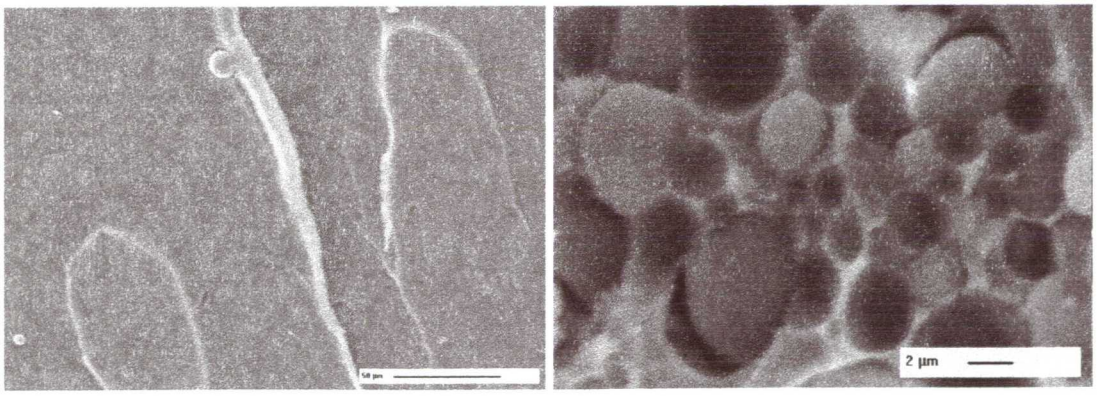


Figure 4.32: Scanning Electron Micrographs of the Fracture Surfaces of a 5wt% KM355-PMMA Composite. (Note the scale bars represents 50μm and 2μm respectively and micrographs from two different areas of the same sample).

It was expected that the presence of core-shell particles within the PMMA would have no effect on the amorphous nature of the PMMA's XRD pattern since the core-shell particles cannot form part of the polymer chains. Figure 4.33, showing the XRD

patterns of PMMA, PMMA-XC42, PMMA-XC44 and PMMA-KM355, confirms this expectation as the shape and position of the PMMA peak does not alter.

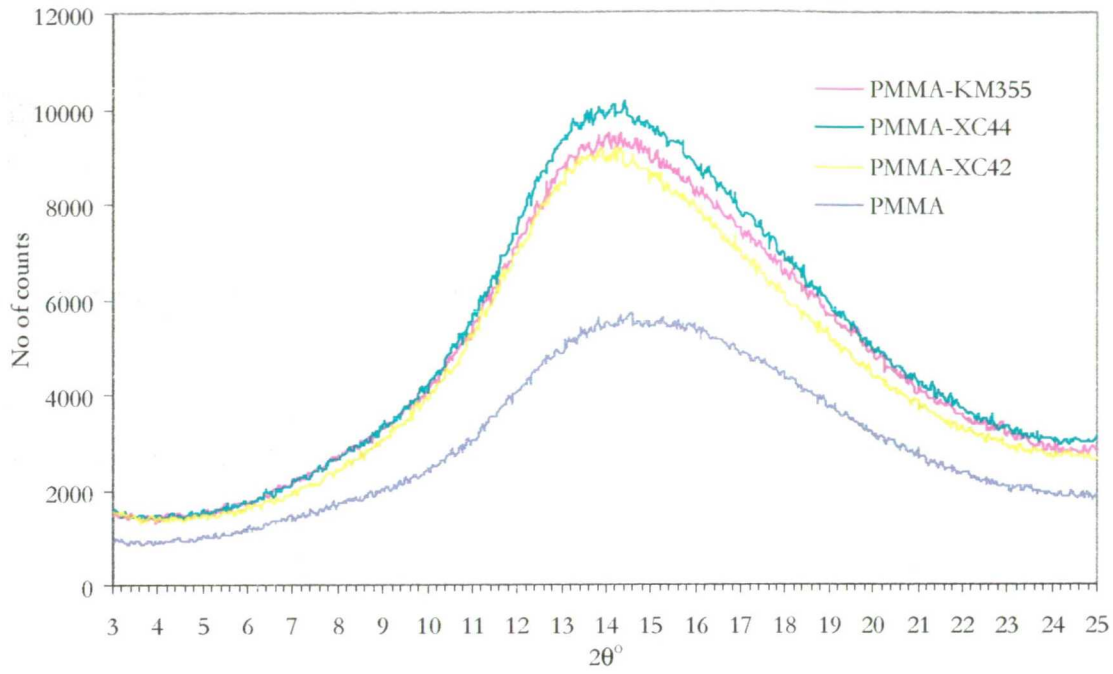


Figure 4.33: XRD Patterns of PMMA, PMMA-5wt%KM355, PMMA-5wt%XC42 and PMMA-5wt%XC44.

Toughened PMMA-clay composites were fabricated using 5wt% of core-shell particles and 6wt% Cloisite 25A. The core-shell loading of 5wt% was chosen since it was noted when the toughened PMMA was fabricated that a sharp increase in viscosity of the monomer solution occurred upon the addition of 5wt% of core-shell particles. Thus it was concluded that, at any greater loading of core-shell particles, the toughened PMMA-clay system would become unprocessable. Cloisite 25A was chosen as the organoclay as it always combined well with PMMA and there was a ready supply of this material.

Each of the core-shell particles was used to fabricate toughened PMMA-Cloisite 25A composites. The XRD patterns of these toughened composites, of PMMA-Cloisite 25A 6wt% and of Cloisite 25A are shown in Figure 4.34. (Note that Figure 4.35 shows

the same XRD patterns as in Figure 4.34 except that the XRD pattern of Cloisite 25A has been removed so as to aid interpretation.) Table 4.5 gives the d-spacings of the toughened PMMA-Cloisite 25A composites as well as those of PMMA-Cloisite 25A 6wt% composite.

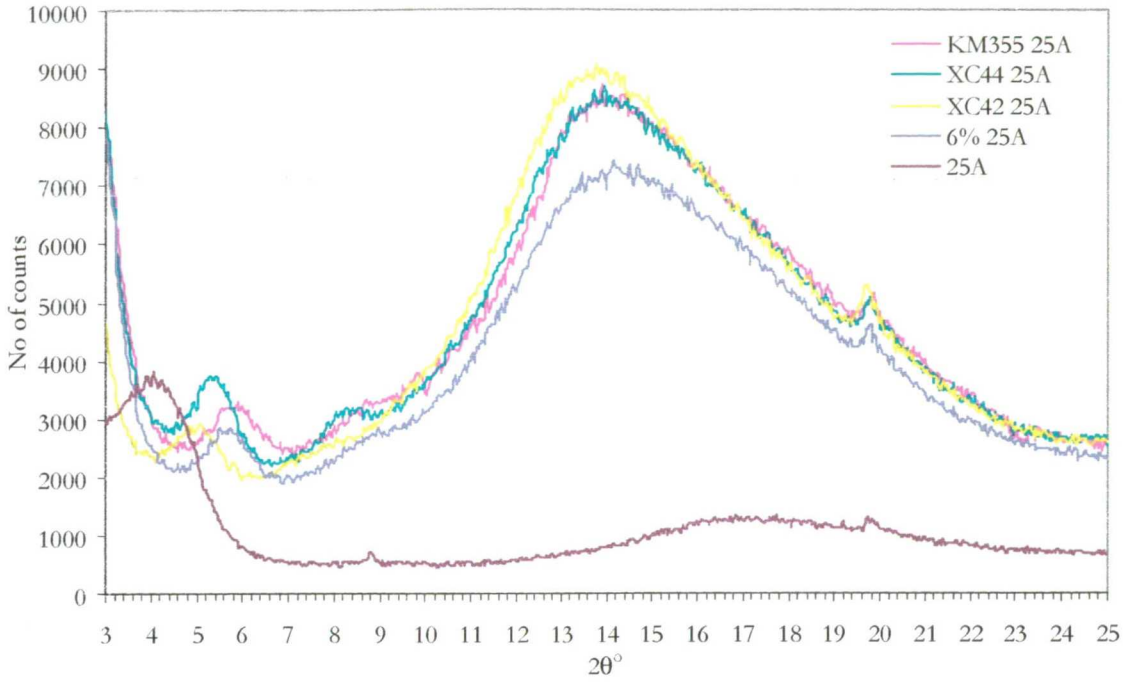


Figure 4.34: XRD Patterns of Cloisite 25A, its 6wt% Toughened Composites and of a PMMA-6wt% Cloisite 25A Composite.

Firstly it can be seen from the constant position of the peak representing the 020 plane at $2\theta \approx 19.7°$ in all the XRD patterns in Figures 4.34 and 4.35 that the variations in the XRD patterns of the composites between $2\theta = 3°$ and $2\theta \approx 10°$ are not due to measurement effects but are real differences in microstructure. Secondly, Figure 4.34 demonstrates clearly that although none of the composites formed have an exfoliated nanocomposite microstructure (i.e. no peaks in the $2\theta < 10°$ range), the position of all the composite 001 peaks are greater than $2\theta = 3°$ and also greater than $2\theta = 4.04°$, the position of the 001 peak in Cloisite 25A. Thus it can be said that all the composites formed have an intercalated nanocomposite microstructure with d-spacings greater than 29.43Å ($2\theta = 3°$).

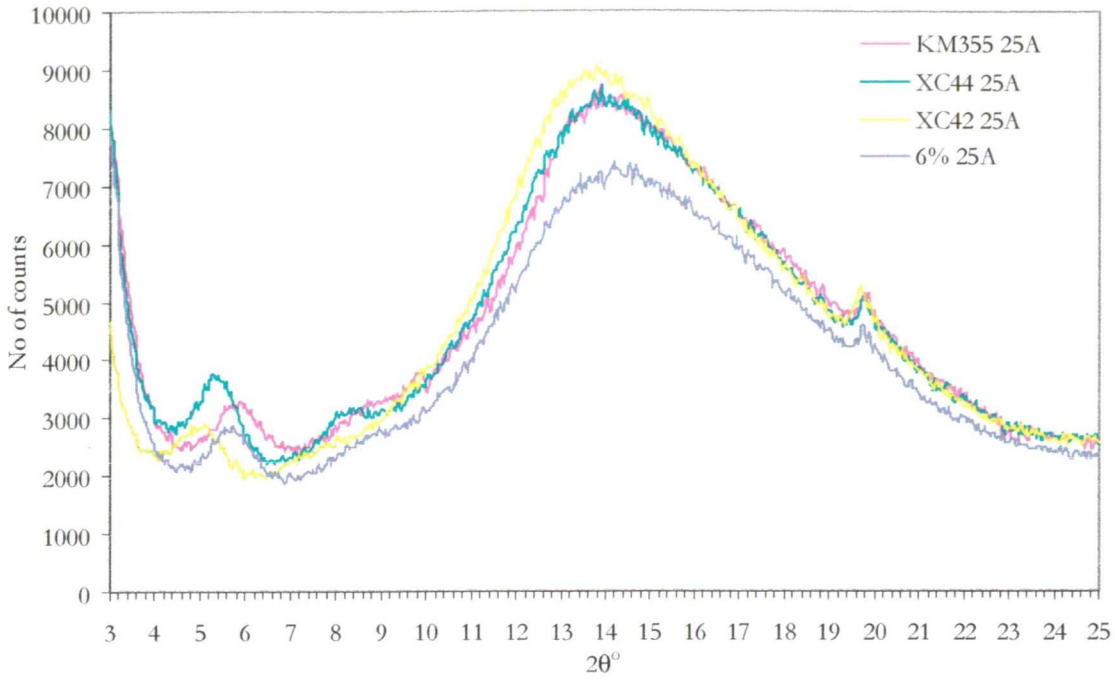


Figure 4.35: XRD Patterns of a PMMA-6wt% Cloisite 25A Composite and Toughened PMMA-6wt% Cloisite 25A Composites.

Table 4.5: D-spacings of Toughened PMMA-6wt% Cloisite 25A Composites and of a PMMA-6wt% Cloisite 25A Composite.

Cloisite 25A 6wt% Composite With	d-spacings, Å (2θ,°)			
	001	002	003	Calculated 001
PMMA	UV	15.44 (5.72)	NA	30.88
5wt% XC42	UV	17.38 (5.08)	NA	34.76
5wt% XC44	UV	16.11 (5.48)	10.42 (8.48)	32.22
5wt% KM355	UV	15.02 (5.88)	NA	30.04

Note: UV - unable to view, NA – not apparent.

Using Figure 4.35 and Table 4.5 it is apparent that all the toughened composites have larger d-spacings than the PMMA-Cloisite 25A 6wt% composite apart from the composite formed with the KM355 core-shell particles. The KM355 composite

appears from Figure 4.35 to have a d-spacing that is marginally smaller than or identical to the PMMA-Cloisite 25A 6wt% composite.

From Table 4.5 it can be seen that the toughened composite with the greatest d_{001}-spacing used XC42, with d_{001}= 34.8Å, followed by that using XC44 with a d_{001}-spacing of d_{001}= 32.2Å. With these two toughened composites it can be concluded that the increase in their d-spacings over those of the PMMA-Cloisite 25A 6wt% is due to the dramatic increase in viscosity of these toughened composites conveying the shear stress induced by the impeller to the clay particles more effectively. However, it can be seen from Figure 4.35 that the toughened composite formed with KM355 has more or less the same d-spacing as the PMMA-Cloisite 25A 6wt% composite. In light of this finding, and in combination with the average sizes of the different core-shell agglomerates shown in Figure 4.31, it can be concluded that a very fine balance must be struck with the percentage loading of core-shell particles to achieve the largest d-spacing possible and that the core-shell particle size must be taken into account. From Figure 4.31 it can be seen that the agglomerates found in KM355 are finer than those found in either XC42 or XC44. Thus for the same weight percent there would be more core-shell particles in a sample of KM355 than in a sample of either XC42 or XC44. Thus an explanation for the KM355 composite having smaller d-spacing than either composites formed with XC42 or XC44 is that, although the clay particles do experience a greater shearing force caused by the increase in viscosity, but for the case of KM355 the increase in viscosity is so great that any increase in shear forces is negated. This leaves only the thermodynamics of the system to drive the polymer into the clay galleries. Thus the d-spacing of the KM355 composite is more or less the same as that of the PMMA-Cloisite 25A 6wt%.

4.4 Repeatability of Microstructure Results

The repeatability of the microstructure results has been investigated for both the PMMA-clay system and the toughened PMMA-clay system. In each case the XRD patterns were taken for two different sample plates that had identical compositions and had undergone the same method of fabrication but had been fabricated on different

days from different PMMA batches. Figure 4.36 contains the XRD patterns of two composites, sample 1 and sample 2, that were both 3wt% Cloisite 93A composites initiated with AIBN. It can be seen from Figure 4.36 that the 002 peaks coincide. The XRD pattern for sample 2 between $2\theta \approx 13°$ and $2\theta \approx 22°$ is noisy. However this section of the pattern is caused by the amorphous polymer and since its general shape and position do not change the noise can be safely ignored.

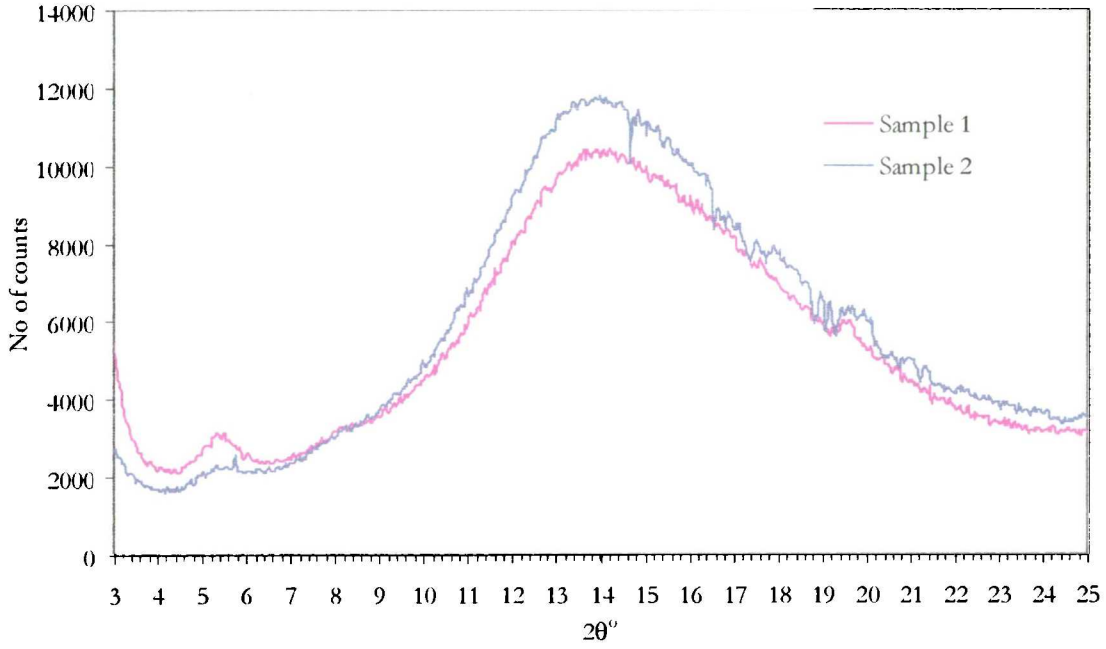


Figure 4.36: Replicate XRD Patterns of PMMA-3wt% Cloisite 93A Composites.

Figure 4.37 shows the XRD patterns of two replicate composites formed with XC44 as the toughening agent and 6wt% Cloisite 25A as the organoclay. Here the 002 maxima can be seen to coincide with the peaks of the maxima being only slightly offset. The difference in the 002 maxima peak position is 0.61Å, which is less than a 5% difference between the positions. Thus for both the toughened and the untoughened PMMA-clay systems the microstructure results can be considered to be repeatable within experimental error.

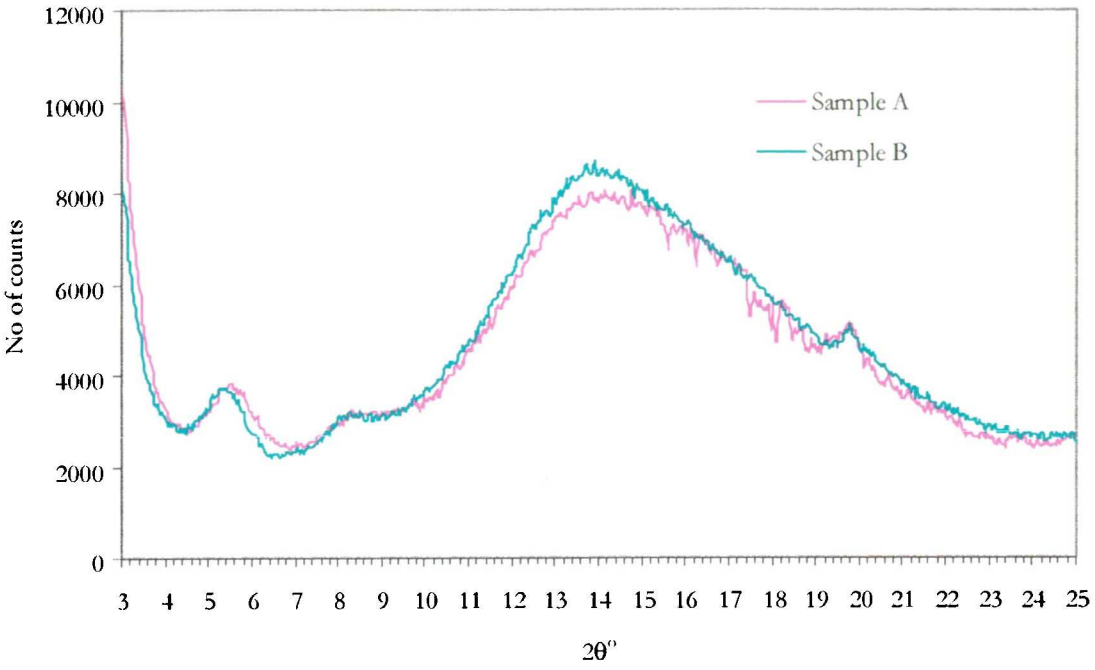


Figure 4.37: Replicate XRD Patterns of Toughened PMMA-Cloisite 25A 6wt% Composites.

4.5 Concluding Remarks

The data presented in this chapter leads to several conclusions about the effect of processing variables on the formation of nanocomposite microstructures. It was found that for the particular system of polymer and clay that so long as the organoclay used had been surface treated with a relatively polar surfactant the microstructure of the composites formed were that of intercalated nanocomposites. Evidence was also found to support the proposition that for each PMMA-organoclay system there was a maximum intergallery spacing that could be achieved. As well as this, the effect of increasing clay content on the microstructure formed was shown to be that the proportion of clay platelets achieving the maximum intergallery spacing decreased. The microstructural data on the toughened PMMA-clay composites showed that the effect of increased viscosity, caused by the presence of core-shell particles, on the intergallery spacing was two fold i.e. at the ideal viscosity shearing forces are transferred to the clay

particles causing the galleries to expand past the maximum achieved through thermodynamics, at too low a viscosity the shear forces are not great enough to overcome the viscosity thus the clay galleries expand to the maximum intergallery spacing achievable through thermodynamics.

The effect of these microstructure results on the physical properties (glass transition temperature, viscoelastic properties and thermal stability) of the composites formed are discussed in Chapter 5.

Chapter 5

Results - Physical Properties

5.0 Introduction

In this chapter the results from the various experiments performed to determine some of the physical properties of the nanocomposites are presented. However, now so as to refresh the reader's memory, the relevant observations from the microstructure chapter, Chapter 4, will be touched upon briefly. Firstly all the composites successfully prepared possessed an intercalated nanocomposite microstructure. The extent of the intercalation varied with each organoclay type, each organoclay appearing to have a maximum d-spacing that is relatively independent of certain processing variables such as the mixing time. Secondly it was observed that the major effect of variation of the clay percentage loading was that the proportion of clay platelets achieving the maximum d-spacing for the organoclay in this system decreased with increasing clay loading.

The properties of the nanocomposites that are presented and examined here are the glass transition temperature, the storage modulus, and the thermal stability. The glass transition temperature and the storage modulus were both investigated using dynamic mechanical thermal analysis. Thermogravimetric analysis was used to examine the thermal stability of the nanocomposites formed.

5.1 Dynamic Mechanical Thermal Analysis Results

5.1.1 Effect of Nanocomposite Formation

Glass Transition

The effect of nanocomposite formation on the glass transition temperature has been investigated using dynamic mechanical thermal analysis (DMTA), one of the two possible methods of examining the glass transition region mentioned in section 2.6.2. The other method mentioned, differential scanning calorimetry (DSC) was tried, but no discernable change in gradient was found at normal heating rates of 10-20°C/min. At faster heating rates, 50°C/min, (DSC becomes more sensitive the faster the heating rate) changes in gradient, which indicate the glass transition temperature, were only discernable to the well-trained eye. These difficulties resulted in the DMTA method being favoured over the DSC method.

DMTA testing was performed using a Combined 300°C Rheometric Scientific DMTA. For each of the composites formed at least three testing bars were used. The best testing conditions for these composites were found to be a strain setting of 1 (other strain settings were used but the specimens and the test data showed signs of plastic deformation at higher strain settings), a heating rate of 2°C/min and two testing frequencies of 10Hz and 1Hz. (Tests were run initially with three testing frequencies, 10Hz, 1Hz and 0.1Hz since it was originally desired to examine the effect of nanocomposite formation on activation energy. However it was found that too few data points were being taken to accurately determine either the glass transition temperature or the activation energy.) The glass transition temperature, T_g, was taken as being the peak of the tan δ curve.

The first testing bar of each sample was tested twice and the second testing bar was tested either once, if the first test run of the second testing bar coincided with the first run of the first testing bar, or twice if it did not. The bars were tested twice since the first run could be unreliable as the peaks were poorly defined, whereas the second run

was always reliable as the peaks were narrow and well-defined, see Figure 5.1 and 5.2. This is thought to be due to some slight post-curing of the samples.

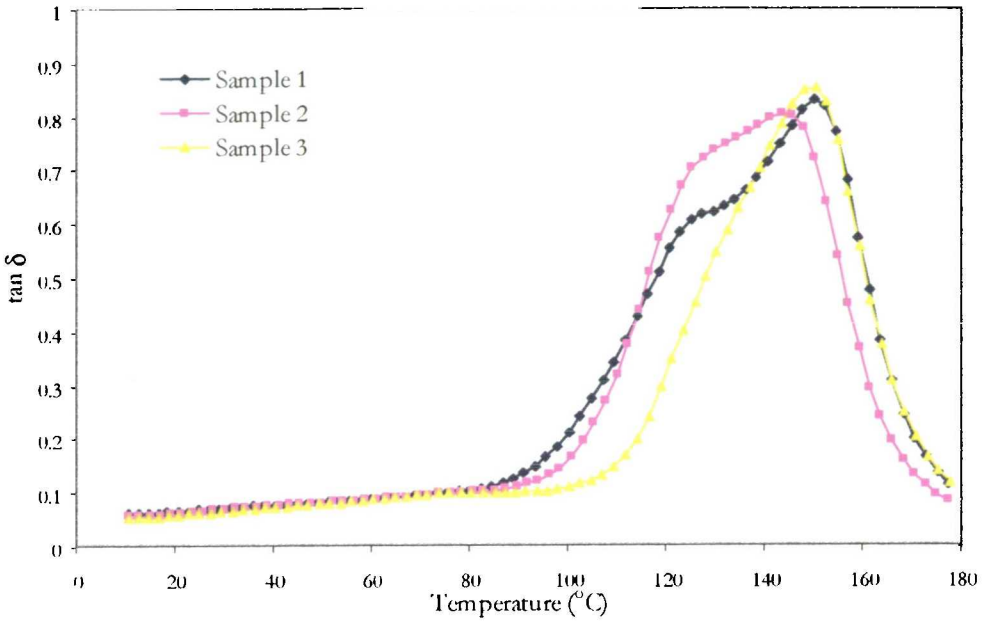


Figure 5.1: The First Test Runs of Three Testing Bars of the same Specimen (3wt% Cloisite 10A).

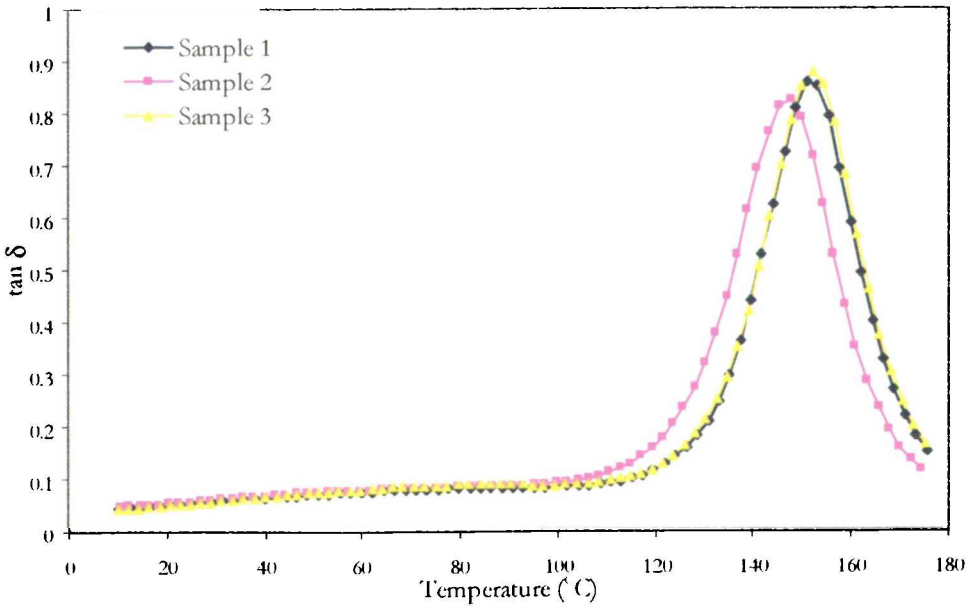


Figure 5.2: The Second Test Runs of Three Testing Bars of the same Specimen (3wt% Cloisite 10A).

As well as this the glass transition temperature measured on the second run was always found to be significantly greater (6°C or more) than the glass transition temperature of the first test run of the bar. Table 5.1 lists the glass transition temperatures, T_g, for a testing bar of PMMA-Cloisite 25A 3wt% nanocomposite that was tested three times.

Table 5.1: Glass Transition Temperature, T_g, of PMMA-Cloisite 25A 3wt%.

	T_g (°C)	
Run No	10Hz	1Hz
1	118.28	110.4
2	128.28	118.28
3	130.1	122.24

From Table 5.1 it can be seen that no significant change in T_g occurs between run number 2 and 3. This was consistent for other samples tested three times. Thus it was considered that the value for T_g after the sample had been tested twice was sufficiently accurate to use. Table 5.1 also shows the viscoelastic nature of the nanocomposite with the T_g found from the 1Hz data being lower than the T_g found from the 10Hz data. This was as expected since it is a polymeric composite. The DMTA data presented in this study is taken from the 10Hz test data unless stated otherwise.

Figure 5.3 shows the variation of the glass transition temperature with percentage clay loading. From this Figure it is clear that the addition of the clay to PMMA does affect the glass transition temperature of the composite formed. The broken line on Figure 5.3 represents the T_g of PMMA (149.1°C) and is shown for comparison purposes. It is apparent from Figure 5.3 that the general trend for all the composites is for the T_g to decrease in comparison with the T_g of PMMA except for Cloisite 10A 3wt%, 6wt% and Cloisite 93A 6wt% composites. The most significant decreases occur for the composites with 3wt% loading of clay, and also for those fabricated using Cloisite 25A.

This decrease in T_g was unexpected since other studies mentioned in Chapter 2 have consistently found that upon the addition of clay to a polymer system the T_g of the resulting composite is greater than the polymer's. The decrease in T_g, when compared

to PMMA's T_g, is the result of a combination of effects since the decrease in T_g for the 6wt% composites is less than for the 3wt% composites. It would have been expected for the T_g to decrease further upon increasing clay content if the decrease in T_g was caused solely, for example, by the plasticisation of the polymer matrix by the clay's surfactants. This however does not occur.

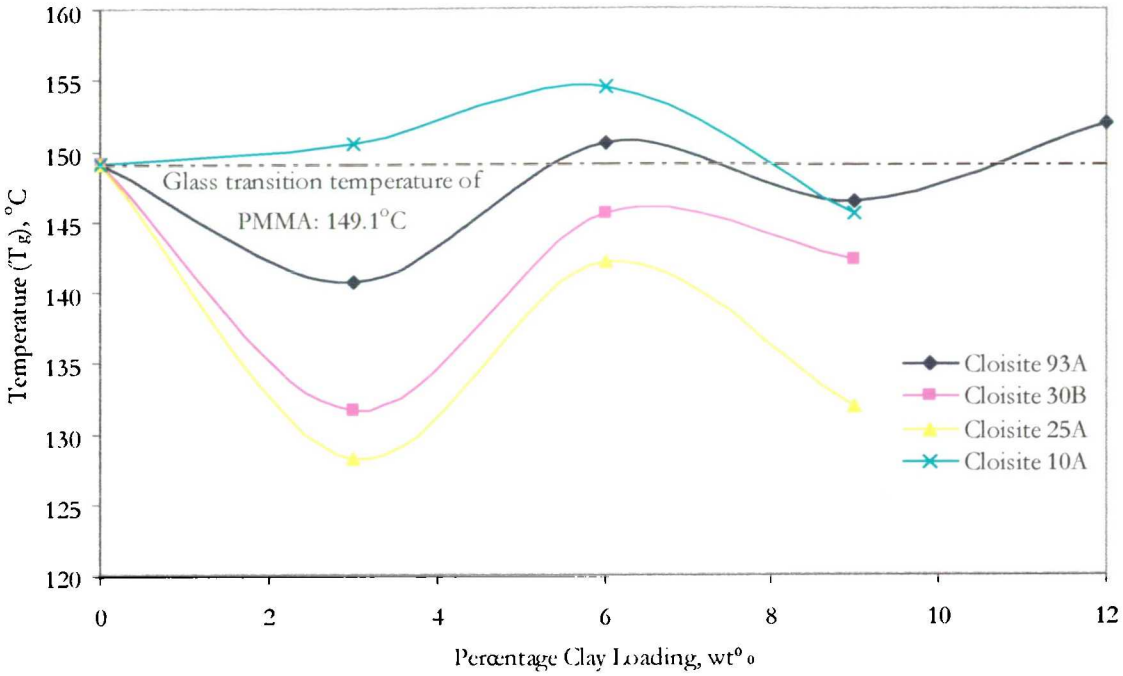
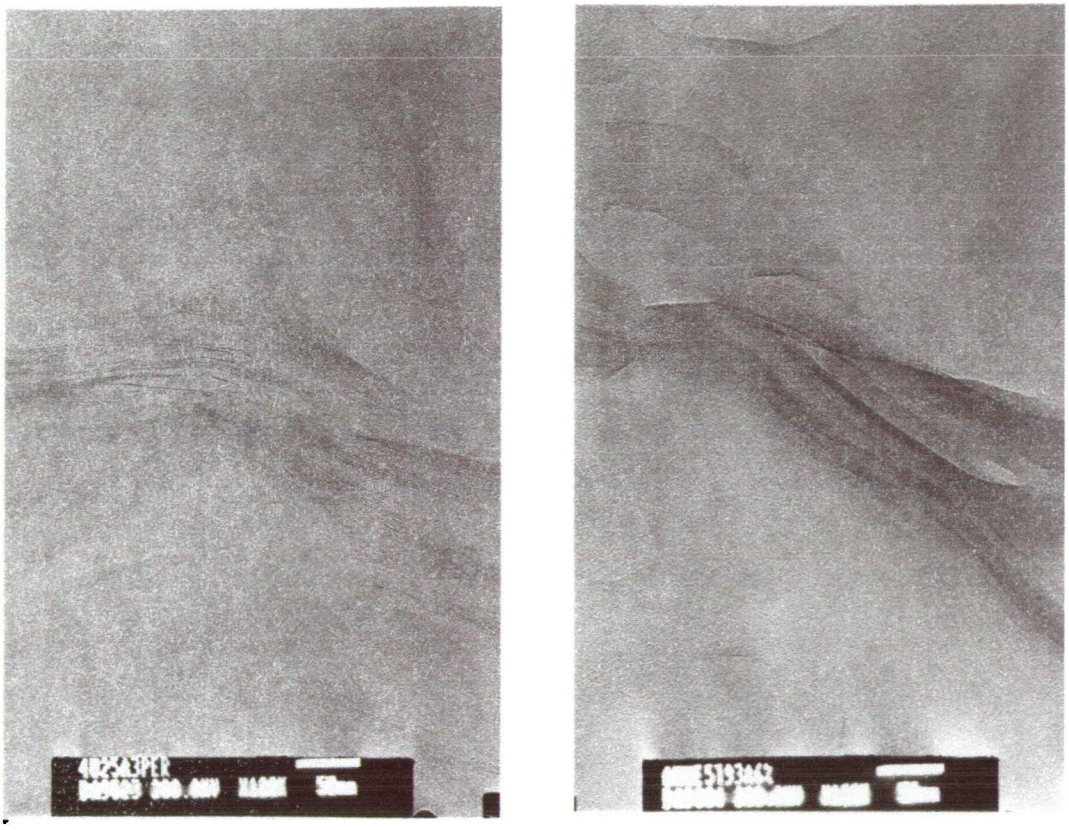


Figure 5.3: Variation of Glass Transition Temperature with Percentage Clay Loading for the Organoclays used. (Note the broken line represents the T_g of PMMA: 149.1°C)

The decrease in the T_gs of the composites in comparison to PMMA's T_g can be explained by combining the two opposing effects of matrix plasticisation by the clay's surfactant and the reinforcing/confining effect of the clay particles in the matrix.

Using the microstructure results in Chapter 4 it can be seen that as the percentage content of clay increases then the number of clay platelets achieving the maximum d-spacing for that specific clay in this system reduces. It can also be seen from transmission electron micrographs that clay platelets are more flexible when the stack that they are included in is expanded, i.e. with a large intergallery spacing, than when the intergallery spacing is smaller. This effect can be seen in Figure 5.4 (also Figures 4.18 &

4.19), showing TEMs of a Cloisite 25A 3wt% composite and a Cloisite 93A 6wt% composite, where the clay platelets in the 3wt% composite (Figure 5.4(a)) can be seen to be bending. Thus it can be concluded that the larger the intergallery distance the less reinforcing/confining effect provided by the clay particles. Thus in the 3wt% composite the presence of the plasticising surfactant is not opposed as effectively by the clay particles because of the large proportion of clay platelets at larger spacings thus the T_g of the composites decreases in comparison to PMMA's T_g.



(a) (b)

Figure 5.4: Transmission Electron Micrographs of (a) a Cloisite 25A 3wt% Composite and (b) a Cloisite 93A 6wt% Composite.

In the 6wt% composites, although the surfactant content does increase the balance is somewhat redressed because the proportion of clay platelets at the maximum spacing for the clay is reduced. Hence the clay particles are stiffer and confine the polymer

chains more effectively, increasing the T_g of the 6wt% composites compared to the 3wt% composites.

In the 9wt% composites the balance is tipped again somewhat in favour of the plasticising surfactant. This is since the proportion of the clay platelets at the maximum spacing has decreased again, thus there are less polymer chains in the clay platelets, i.e. although the chains in the clay intergallery are more confined in the 9wt% composites than in the 6wt% there are less chains present and so their effect of increasing T_g is reduced. Hence the increase in the surfactant content is not as effectively combated, allowing the T_g of the 9wt% composites to decrease in comparison with the 6wt% composites.

It was noted earlier that the Cloisite 10A 3wt% and 6wt% composites have T_gs that are greater than the T_g of PMMA. The organoclay Cloisite 10A is dissimilar to the other organoclay on two points. Firstly the concentration of surfactant is much greater than that of the other clays (125meq/100g for Cloisite 10A compared with between 90 to 95 meq/100g). Secondly as can be seen from Figure 5.5 (which shows Cloisite 10A's surfactant) that the surfactant contains a ring group which none of the other clay surfactants do.

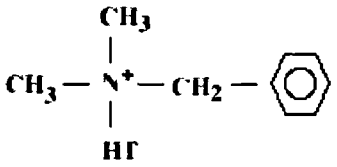


Figure 5.5: The Surfactant of Cloisite 10A[91].

It is possible that a combination of both the bulkiness and concentration of this surfactant, along with the comparatively small maximum d-spacing achievable in this system, confines the polymer chains much more rigidly than for the other clays. Hence instead of the matrix plasticisation dominating the effect on T_g it is the amount of confinement that does, thus the T_g of the Cloisite 10A 3wt% and 6wt% increases compared with PMMA's T_g.

Storage Modulus

The data from the dynamic mechanical thermal analysis (DMTA) performed to investigate the glass transition temperature of the composites formed can be used to probe the storage modulus (one of the two dynamic moduli) of the composites as well. The results presented here, as in the previous section on the effect of nanocomposite formation on the glass transition temperature of the composite, are from the 10Hz data of the second testing run of each specimen. The storage modulus of a polymer (or a polymer composite), as discussed in section 2.6.2, decreases greatly (from GPa to MPa) with increasing temperature as the polymer goes through its glass transition temperature and into its rubbery region. A typical plot of the logarithm of the storage modulus against temperature for PMMA and a PMMA-clay composite produced during this project is presented in Figure 5.6 and shows this behaviour. The storage modulus at 20°C (in the glassy region) and at 160°C (in the rubbery region) for PMMA and for the various PMMA-clay composites produced are shown in Table 5.2, which also contains the glass transition temperatures for PMMA and the composites.

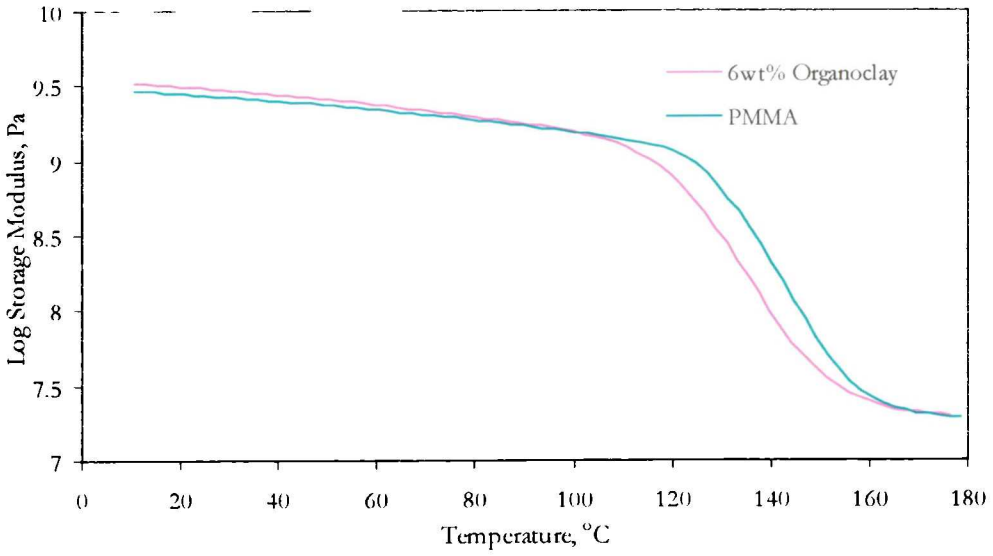


Figure 5.6: Typical Plot of the Logarithm of the Storage Modulus against Temperature for PMMA and a PMMA-clay Composite.

Table 5.2: DMTA Data for PMMA and its Composites.

	PMMA	Cloisite 93A				Cloisite 30B			Cloisite 25A			Cloisite 10A		
		3%	6%	9%	12%	3%	6%	9%	3%	6%	9%	3%	6%	9%
Storage Modulus at 20°C, GPa	2.79	2.43	3.35	2.47	2.61	2.60	3.12	2.44	2.34	3.14	2.65	3.02	3.18	2.14
Storage Modulus at 160°C, MPa	26.07	18.21	37.84	29.84	44.93	21.86	23.15	31.44	19.63	24.2	19.63	33.93	40.11	30.77
T_g, °C	149.1	140.7	150.4	146.4	152.0	131.7	145.6	142.3	128.3	142.1	131.9	150.5	154.4	145.6

From Table 5.2 it can be seen that the storage modulus, both in the glassy region and in the rubbery region, is not significantly affected by the clay adopting an intercalated nanocomposite microstructure in the PMMA. In the glassy region the storage modulus of the composites varies by approximately ±20% of the storage modulus of PMMA in the glassy region. In the rubbery region the storage modulus varies by approximately +70% to –30% of the storage modulus of PMMA in the rubbery region. From this it can be concluded that the data confirms the proposition in the literature that although the formation of a nanocomposite does affect the storage modulus of the composite both in the glassy region and in the rubbery region it is however the rubbery region's storage modulus that is affected more[51]. This is to be expected, as when in the rubbery region the modulus of the clay is in the order of GPA compared to that of the PMMA which is in the order of MPa. However, in the glass region both moduli are in the order of GPa, hence the effect of the clay addition is less.

The storage modulus data at 20°C and at 160°C that appear in Table 5.2 are presented in graphical form in Figures 5.7 and 5.8 respectively. The variation of the storage modulus with percentage clay loading at 20°C presented in Figure 5.7 varies in a similar manner to the variation of T_g with percentage clay loading shown in Figure 5.3 (page 147). The explanation of this variation in the storage modulus at 20°C with percentage clay loading can also be explained by a similar argument to that used on the variation of T_g with percentage clay loading. There is a balance of the matrix plasticisation by the surfactant and the reinforcing/confining effect of the clay particles except there is an additional factor to be added to the balance. The additional factor is crosslink density, it has been shown for highly crosslinked polymer systems that the presence of clay severely reduces the amount of crosslinking that occurs and the properties of the composite compared to the pristine polymer are consequently reduced[98].

Although the system under investigation here is not highly crosslinked the presence of clay in the polymer could still reduce the crosslink density. Thus in the 3wt% composite systems, where the largest proportion of clay platelets are at their maximum spacing, the most interference with crosslinking occurs. In addition the plasticisation of

the matrix caused by the surfactant is not completely compensated for by the reinforcing/confining effect of the clay particles.

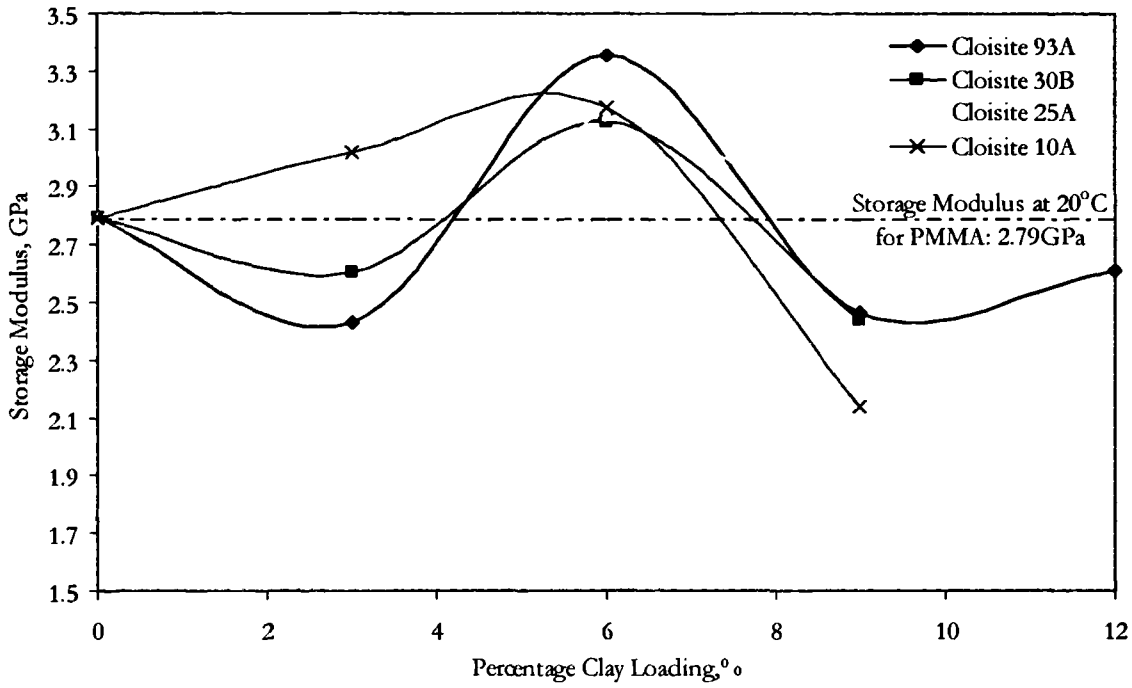


Figure 5.7: Storage Modulus at 20°C versus Clay Loading, for PMMA and Composites.

From Figure 5.7 it can be seen that the balance between crosslinking, plasticisation and reinforcement is at its optimal level for increasing the storage modulus in the glassy region at a percentage clay loading of 6wt% for all the clays used.

Again, as in Figure 5.3, it can be distinctly seen in Figure 5.7 that with composites containing Cloisite 10A there is no initial drop in storage modulus at 20°C again here it is suggested that this difference in behaviour is caused by both the much greater concentration of surfactant and also by the presence of a ring group in the surfactant possibly reducing the surfactant's plasticising effect.

In Figure 5.8 it can be seen that the variations of storage modulus at 160°C do not exactly mirror those seen in Figure 5.7 but are reasonably similar. Unlike for the storage modulus at 20°C it cannot be said that for all the clays the optimum percentage clay loading is 6wt%. Figure 5.8 shows that the storage modulus at 160°C for Cloisite

30B appears to increase with increasing clay content. However for the other clays trends similar to those in the storage modulus at 20°C can be seen at 160°C, this is as would be expected since the material has not changed.

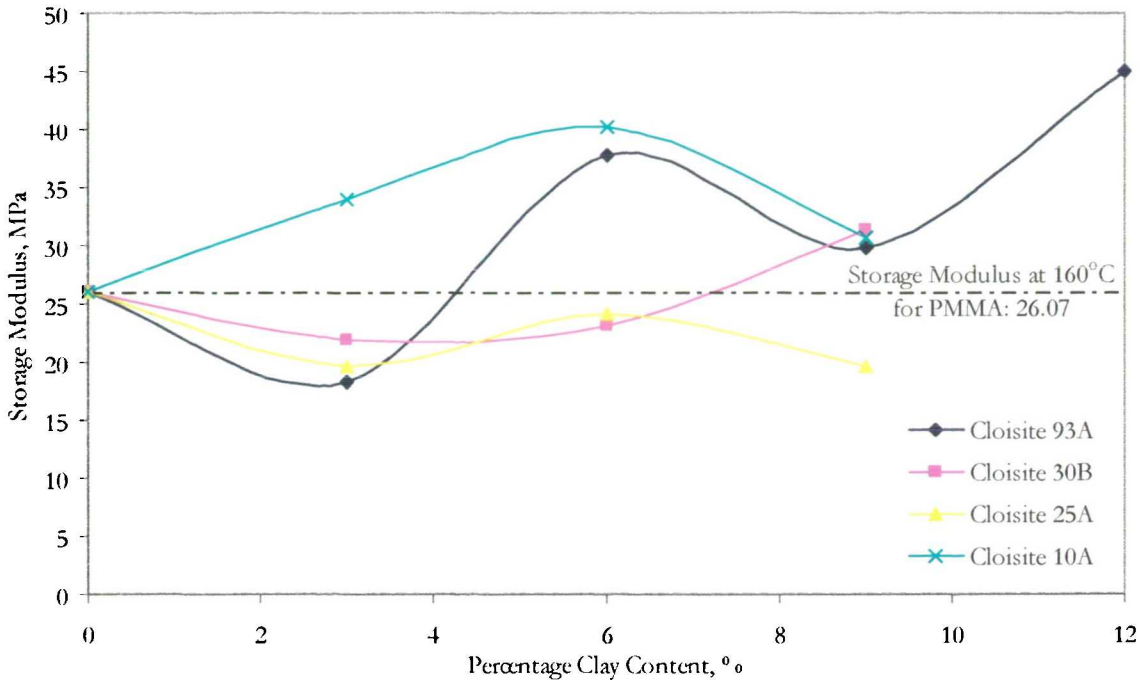


Figure 5.8: Storage Modulus at 160°C versus Clay Loading for PMMA and Composites.

5.1.2 Effect of Choice of Polymerisation Initiator

Glass Transition

In Chapter 4 the effect of the different polymerisation initiators on the composite microstructure was investigated. The initiators used during this investigation were 2,2-azo-bis-isobutyronitrile (AIBN) (this can be considered as the control initiator), lauroyl peroxide (LP) and trigonox 23 (Trig). It was found that when using Cloisite 25A or Cloisite 93A as the organoclay, and initiated with either lauroyl peroxide or trigonox 23, composites with an intercalated nanocomposite microstructure with d-spacings exceeding those of the AIBN initiated composites were produced.

In this section the glass transition temperatures, T_gs, of these composites are investigated using data obtained by DMTA. The testing conditions for these experiments were the same as those previously detailed in section 5.1.1. As discussed previously the data presented here are taken from the 10Hz data of the second test run.

The T_gs of PMMA initiated with either AIBN, lauroyl peroxide or trigonox 23 are presented in Table 5.3. Also included in the table are the respective T_gs of the Cloisite 25A and Cloisite 93A composites. Note that the T_g for the 6wt% Cloisite 25A lauroyl peroxide composite is missing since all the samples for this composite broke in the DMTA jaws, and also that due to the limited supply of trigonox 23 only 6wt% and 9wt% composites were fabricated using this initiator.

From Table 5.3 it can clearly be seen that the alteration of the polymerisation initiator has very little effect on the T_g of the plain PMMA. The minor differences that do occur can be accounted for by the usual factors that affect T_g, e.g. a minor increase in free volume caused by the configuration and size of end groups for instance. From this it can be concluded that any variation in the composites' T_g is due to the presence of the organoclay and its adopted microstructure in the polymer.

Table 5.3: The Glass Transition Temperatures of PMMA Initiated with either AIBN, Lauroyl Peroxide (LP) or Trigonox 23 (Trig) and their respective Cloisite 25A and Cloisite 93A Composites.

	T_g Cloisite 25A Composite, °C			T_g Cloisite 93A Composite, °C		
% Clay Loading	AIBN	LP	Trig	AIBN	LP	Trig
Plain	149.14	143.62	149.3	149.14	143.62	149.3
3wt%	128.28	142.5	-	140.68	153.42	-
6wt%	142.08	-	156.04	150.44	155.6	157.92
9wt%	131.94	145.88	142.46	146.35	152.6	158.52

Table 5.3 shows clearly that the presence of the organoclay in the composites initiated with lauroyl peroxide or trigonox 23 does not affect the T_g of those composites as

greatly as the presence of organoclay does for the AIBN initiated composites, particularly when Cloisite 25A is the organoclay. Table 5.3 also reveals that the presence of Cloisite 25A in the lauroyl peroxide or trigonox 23 initiated composites has very little, if any, effect on the composite T_g. It is apparent from Table 5.3 that the presence of Cloisite 93A has slightly more effect on T_g (compared to the Cloisite 25A). The variation in the T_gs of the Cloisite 93A composites initiated with lauroyl peroxide or trigonox 23 indicate that the balance of surfactant plasticisation and polymer chain confinement present in the AIBN initiated composites is active in these composites as well. However the balance seems less tipped in favour of the surfactant plasticisation of the matrix and more towards confinement.

Storage Modulus

As well as being used to examine any variations in the glass transition temperature, the data obtained through DMTA testing is also used to examine any variations in the storage modulus (one of the two dynamic moduli) of these composites. The data presented here as before is taken from the 10Hz data of the second test run. Tables 5.4(a) and (b) present the storage moduli below T_g in the glassy region (storage modulus at 20°C) and above T_g in the rubbery region (storage modulus at 160°C), as well as the glass transition temperature for PMMA initiated with either AIBN, lauroyl peroxide or trigonox 23 and their respective Cloisite 25A and Cloisite 93A composites.

Firstly considering the effect of different initiators on the storage modulus of various PMMAs formed. Table 5.4 makes plain that, for the polymerisation initiators tried, altering the polymerisation initiator has only a small, if any, effect on the storage modulus at 20°C (in the glassy region) whilst the storage modulus at 160°C is slightly more affected. However this is only to be expected since at 160°C the chain sections are more mobile, thus it is probable that end group size and configuration would affect the properties of the polymer more at this elevated temperature.

Table 5.4(a): Cloisite 93A, DMTA Data for PMMA and Composites.

Clay Loading	Storage Modulus at 20°C, GPa			Storage Modulus at 160°C, MPa			T_g, °C		
	AIBN	LP	Trig	AIBN	LP	Trig	AIBN	LP	Trig
Plain	2.79	2.43	2.87	26.07	20.04	22.56	149.1	143.6	149.3
3wt%	2.43	3.60	-	18.21	44.82	-	140.7	153.4	-
6wt%	3.35	3.00	2.79	37.84	39.44	51.55	150.4	155.6	157.9
9wt%	2.47	3.08	2.58	29.84	44.04	51.31	146.4	152.6	158.5

Table 5.4(b): Cloisite 25A, DMTA Data for PMMA and Composites.

Clay Loading	Storage Modulus at 20°C, GPa			Storage Modulus at 160°C, MPa			T_g, °C		
	AIBN	LP	Trig	AIBN	LP	Trig	AIBN	LP	Trig
Plain	2.79	2.43	2.87	26.07	20.04	22.56	149.1	143.6	149.3
3wt%	2.34	2.66	-	19.63	27.44	-	128.3	142.5	-
6wt%	3.14	-	2.79	24.2	-	40.48	142.1	-	156.0
9wt%	2.65	3.18	2.87	19.63	34.69	25.68	132.0	145.9	142.5

Examining Tables 5.4 (a) and (b) reveals several points. Firstly, for all the trigonox 23 composites the storage modulus at 20°C is barely affected by the organoclay or by the organoclay percentage loading. Secondly, the presence of an intercalated nanocomposite microstructure has more of a net positive effect when the polymerisation initiator is not AIBN. Also that for the storage modulus at 20°C the best results are achieved from the composites initiated by lauroyl peroxide and containing Cloisite 93A. However it should be noted after the initial increase in the storage modulus at 20°C the addition of further clay has very little effect. Considering the storage modulus at 160°C, the presence of organoclay for both lauroyl peroxide or trigonox 23 causes an increase in storage modulus. Again it is the composites formed with Cloisite 93A that have the largest increase. It is apparent that the variations in storage modulus are almost parallel to the variations that occur in the glass transition temperature. Thus the balance between the matrix plasticisation by the surfactant and the confinement/reinforcement effect of the clay platelets is also occurring here.

5.1.3 Effect of Core-Shell Addition

Glass Transition

The effects of the formation of a nanocomposite microstructure on the glass transition temperature of toughened PMMA-clay composites was investigated using the same technique of dynamic mechanical thermal analysis that was used for the PMMA-clay composites. For each composite three testing bars were machined, at least two of which were tested and both bars that were used underwent three test runs each. The data tabulated here is the mean of the values taken from the 10Hz second test run data. The 10Hz data are used so as to be consistent with the PMMA-clay data already presented here. The data is taken from the second test run of the testing bars as it was found that the third run data was not comparable either between test runs or testing bars, see Figure 5.9.

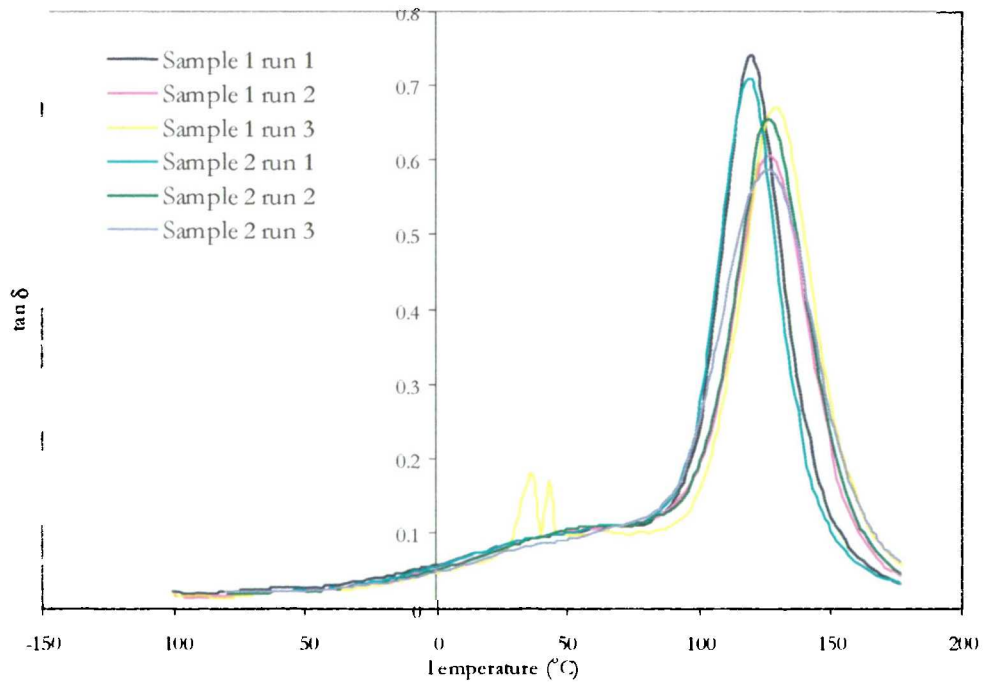


Figure 5.9: Variation of Tan δ with Temperature for PMMA KM355 5wt% (10Hz).

The frequencies, strain setting and heating rate used remained the same as for the PMMA-clay composites. However, the temperature range was altered to -80°C to 180°C so as to catch the glass transition temperature of the core-shell particles. Table

5.5 details the T_g results found from the DMTA testing of the toughened PMMA and the toughened PMMA-clay composites. Also included in the table for comparison purposes are the T_g of PMMA and PMMA-Cloisite 25A 6wt% o. It should be noted that the toughened PMMA was fabricated with 5wt% o of core-shell particles and that the toughened PMMA-clay composites were fabricated with 5wt% of core-shell particles and 6wt% o of Cloisite 25A.

Table 5.5: The Glass Transition Temperature of Toughened and Untoughened PMMA and their Cloisite 25A 6wt% o Composites.

	T_g, °C	
	No Clay	25A 6wt%
PMMA	149.14	142.08
5wt% KM355	127.21	155.02
5wt% XC42	147.24	125.24
5wt% XC44	147.14	143.09

Firstly by examining the "No Clay" T_g column it is clear that PMMA-KM355 has the lowest T_g of the toughened PMMA's, and that the presence of the XC42 and XC44 in the PMMA has very little effect on the T_g of the toughened PMMA formed. This can also be seen from Figure 5.10 which presents the tan δ curves for the second test run of PMMA, PMMA-XC42, PMMA-XC44 and PMMA-KM355. From this figure it is also apparent that no rubber T_g (a peak in the -50°C to 0°C region) is visible. This was not unexpected since the rubber component of the core-shell particles is inside the particles, i.e. the rubber is surrounded by a layer of PMMA.

The behaviour of the PMMA toughened with KM355 is unexpected. It can be partially explained if the fracture surfaces of samples of the toughened PMMAs are examined using a scanning electron microscope. Figures 5.11, 5.12 and 5.13 show the fracture surfaces of PMMA-XC42, PMMA-XC44 and PMMA-KM355 respectively at the same magnification. Note that unless otherwise stated direction of crack propagation is from the top of the micrograph to the bottom. From these figures it can be stated that in

appearance the fracture surfaces of PMMA-XC42 and XC44 are very similar to each other and quite dissimilar to the fracture surface of PMMA-KM355.

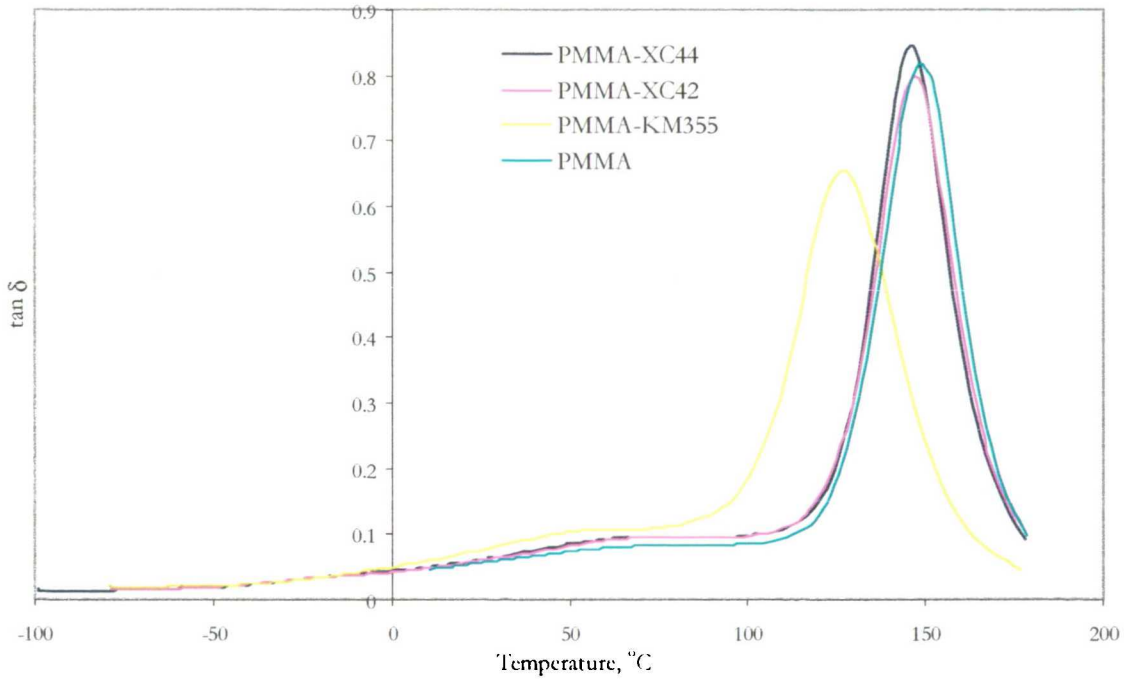


Figure 5.10: The Tan δ Curves for Toughened PMMA and PMMA (2nd run, 10Hz).

From the fracture surface of PMMA-KM355 (Figure 5.13), PMMA-KM355 appears to have two phases shown by the light and dark areas on the figure. There are however definitely particles and signs of particles (holes) on the figure as well. Figure 5.14 is a close up of a different area of the same PMMA-KM355 fracture surface as in Figure 5.13. On Figure 5.14 the light and dark areas are still visible along with several holes, which once contained particles, and a debonded particle. It is clear that these holes are due to the core-shell particles because they are not seen on the micrographs of the non-toughened PMMA.

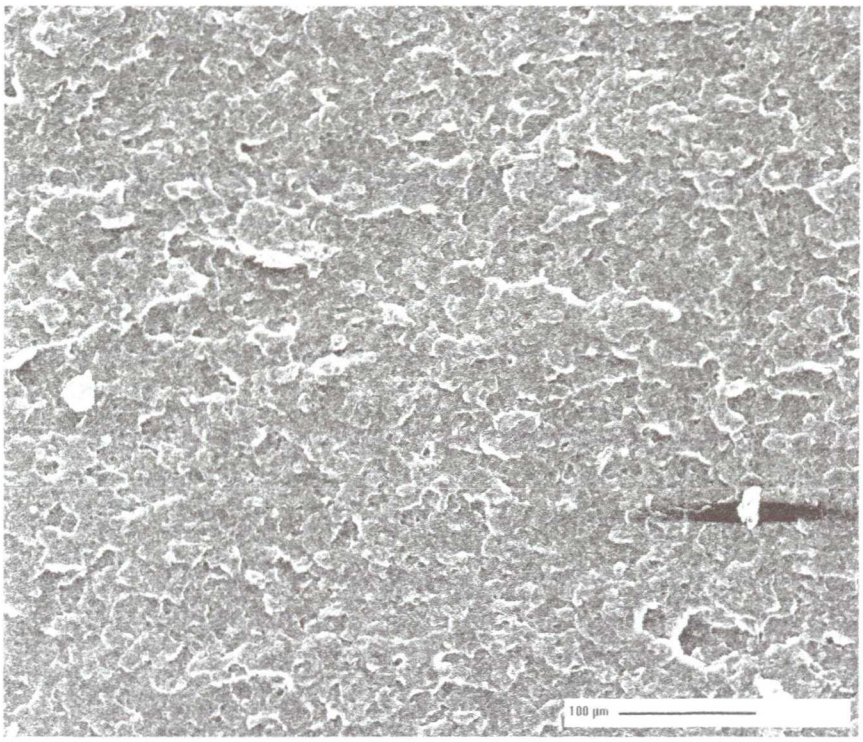


Figure 5.11: Scanning Electron Micrograph of the Fracture Surface of PMMA-XC42.

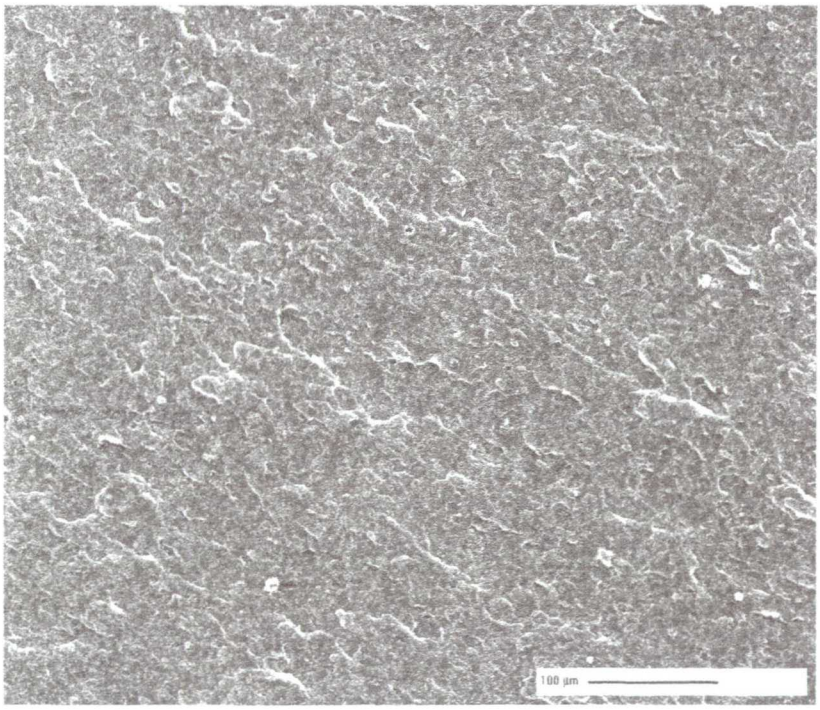


Figure 5.12: Scanning Electron Micrograph of the Fracture Surface of PMMA-XC44.

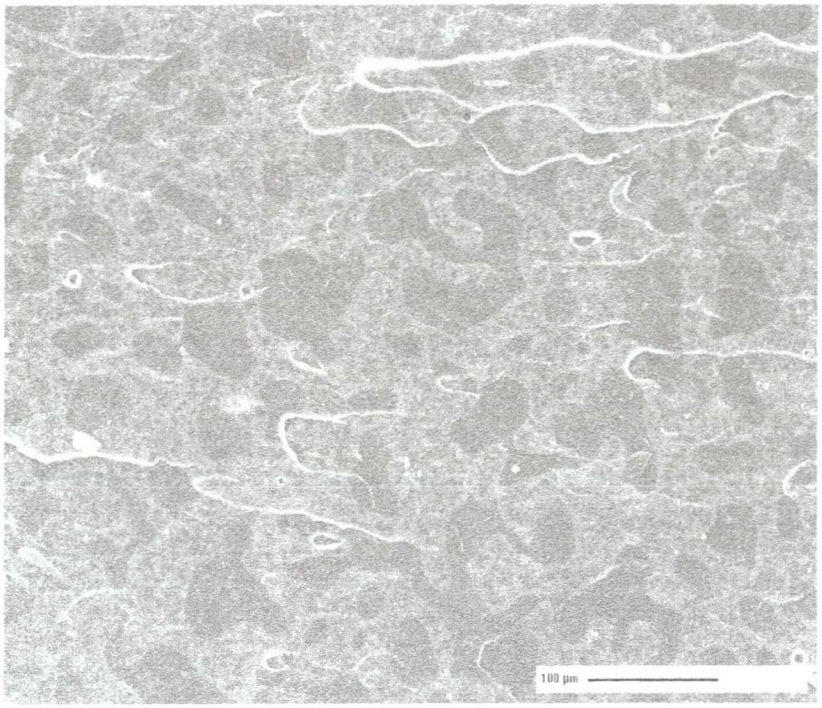


Figure 5.13: Scanning Electron Micrograph of the Fracture Surface of PMMA-KM355.

(Note crack propagation is from left to right.)

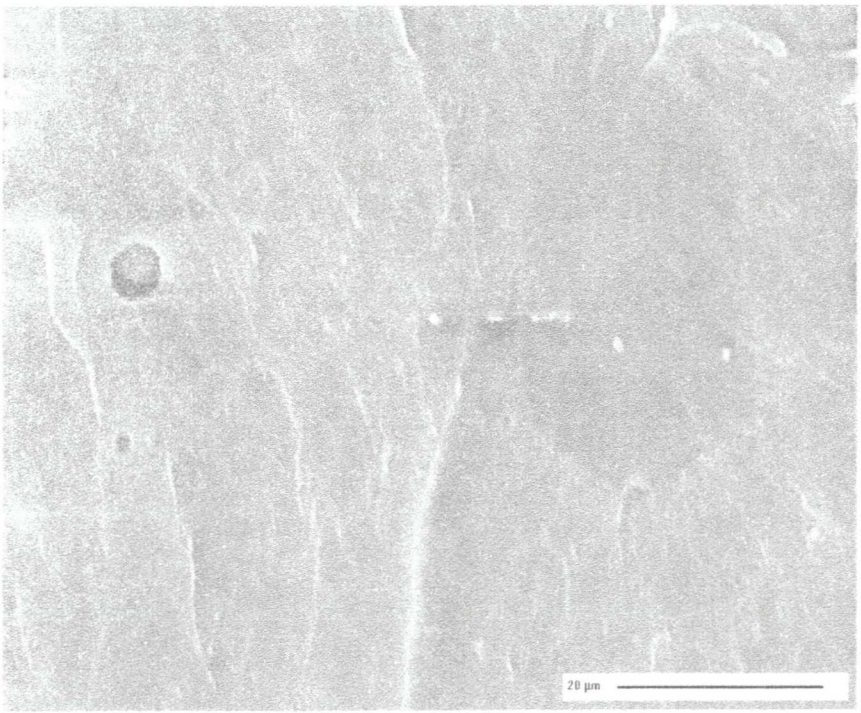


Figure 5.14: Scanning Electron Micrograph of the Fracture Surface of PMMA-KM355.

(Note crack propagation is from top to bottom.)

The phase separation visible in Figures 5.13 and 5.14 is possibly the cause of the dramatic drop in the T_g. The origin of this second phase is somewhat puzzling since the second phase cannot originate from the core-shell particles as the particles cannot partake in the polymerisation and also there are core-shell particles visible on the fracture surfaces.

Table 5.5 shows that both the T_g of PMMA-XC42 and PMMA-XC44 decrease slightly, by 1.9°C and 2°C respectively, these minor decreases are most probably the result of increased free volume caused by the inclusion of core-shell particles.

Table 5.6 has the same T_g results as those shown in Table 5.5, however the calculated d_{001}-spacings for the composites formed are also included.

Table 5.6: T_g Results for PMMA, Toughened PMMA and their Clay Composites.

	T_g, °C		Calculated
	No Clay	25A 6wt%	d_{001}-spacing, Å
PMMA	149.14	142.08	30.88
5wt% KM355	127.21	155.02	30.04
5wt% XC42	147.24	125.24	34.76
5wt% XC44	147.14	143.09	32.22

Note: d_{001}-spacing calculated from measured d_{002}-spacing.

From Table 5.6 it can be stated that the toughened PMMA-Cloisite 25A 6wt% composite with the highest T_g is KM355. This composite is also the only one whose T_g has increased upon the addition of clay when compared to the pristine toughened PMMA. From Table 5.6 it can also be stated that the T_g of the XC42-clay composite decreases the most, 22°C, and it is the lowest. The table also shows that this composite has the largest d_{001}-spacing of 34.8Å.

Figure 5.15 shows the fracture surface of the PMMA-KM355-Cloisite 25A 6wt% composite. Comparing Figures 5.13 and 5.15 it can be seen that the phase separation

that has occurred in the fracture surface shown in Figure 5.13 has not occurred in the fracture surface shown in Figure 5.15. It can be concluded from Figure 5.15 that the presence of clay in the system prevents the phase separation occurring. The increase in T_g seen in the KM355 toughened PMMA-clay composite can be argued to be due to both the absence of the phase separation and also the relatively tight confining of the polymer by the clay particles, this composite had the smallest d_{001}-spacing for the Cloisite 25A 6wt% composites.

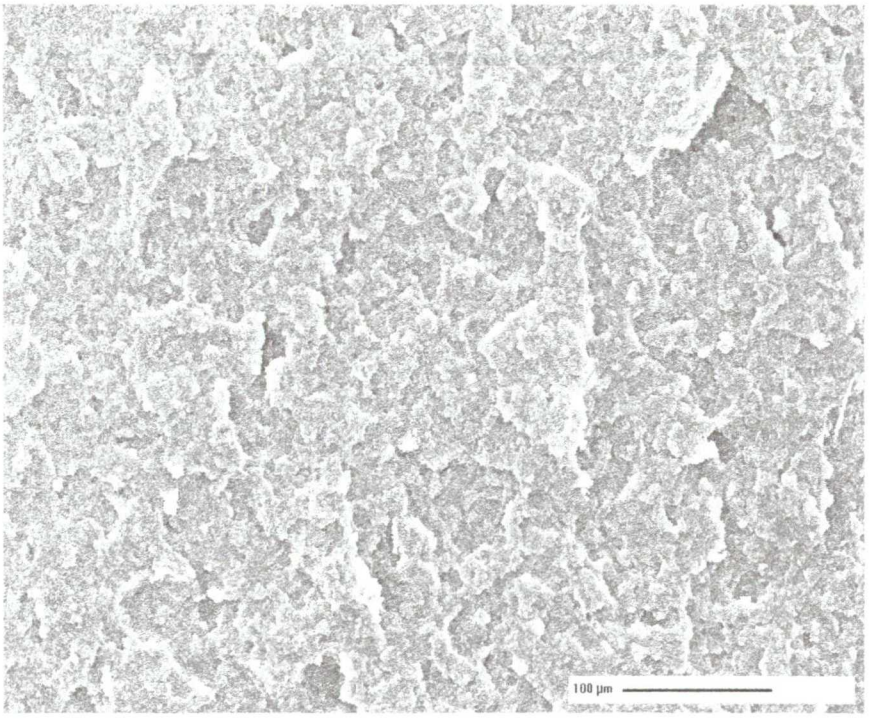


Figure 5.15: Scanning Electron Micrograph of the Fracture Surface of KM355 toughened PMMA-Cloisite 25A 6wt% Composite. (Note crack propagation is from top to bottom.)

The XC42 toughened PMMA-Cloisite 25A 6wt% composites possess the largest d_{001}-spacing of all the 6wt% Cloisite 25A composites fabricated during this study. This indicates that firstly more of the surfactant is exposed to the polymer than in the untoughened PMMA-Cloisite 25A composite, which has a smaller d_{001}-spacing. Secondly the clay particles are not as stiff since they are not as compressed as in the PMMA-Cloisite 25A 6wt% composite and thus do not provide such a reinforcing effect

as the clay particles in the PMMA-Cloisite 25A 6wt% composite. Hence the balance struck between the plasticising effect of the surfactant and the reinforcing effect of the clay platelets is tipped towards the plasticising surfactant so causing a large drop in the T_g of the XC42 toughened PMMA-Clay composite.

From Table 5.6 it is apparent that the toughened PMMA-Cloisite 25A 6wt% composite with the most similar T_g to the PMMA-Cloisite 25A 6wt% composite has been formed using the XC44 core-shell particles. Also from Table 5.6 it is clear that the XC44 toughened PMMA-Cloisite 25A 6wt% composite has a larger d_{001}-spacing than the untoughened PMMA-Cloisite 25A 6wt% composite. This larger d_{001}-spacing, using the plasticising/reinforcement balance argument, would imply a lower T_g than that found. However, if the XRD patterns of the toughened PMMA-Cloisite 25A 6wt% composite and the PMMA-Cloisite 25A 6wt% composite are compared, as shown in Figure 5.16, it can be seen that the toughened XRD pattern contains a 003 peak. The presence of this peak in the XRD pattern indicates that the proportion of clay platelets at the maximum d_{001}-spacing in the toughened-clay composite is less than in the untoughened-clay composite whose XRD pattern does not contain a 003 peak. Thus the reinforcing effect of the clay platelets in the toughened composite is larger than first thought, hence combating the effect of the surfactant more effectively, and thus giving the value of T_g found.

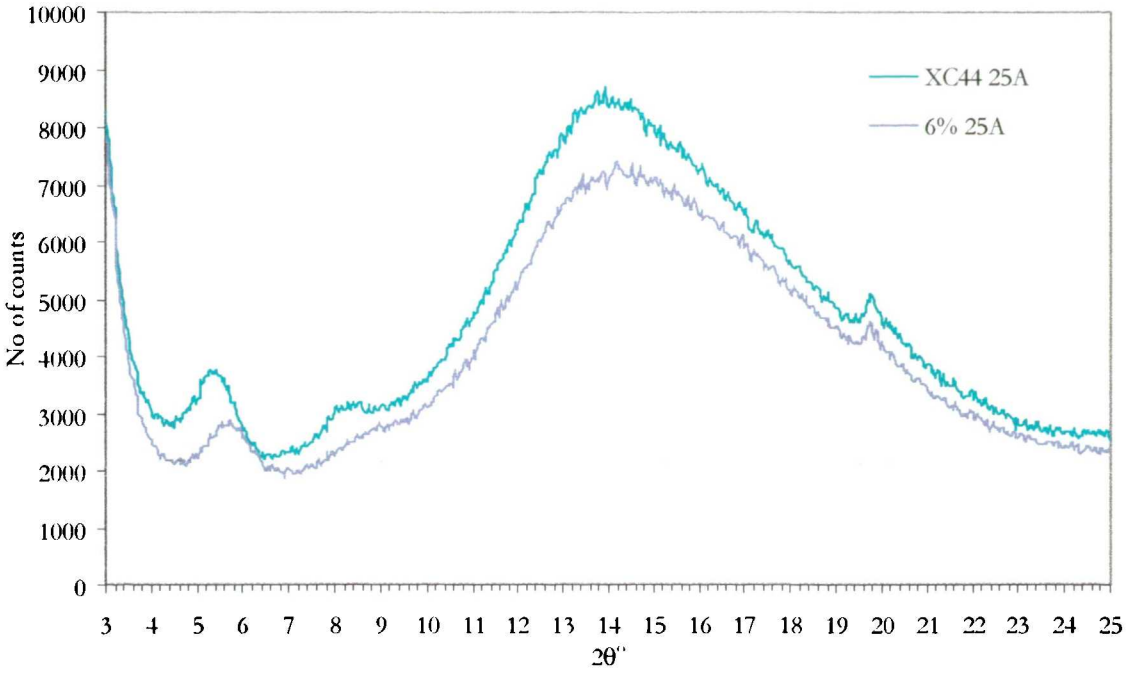


Figure 5.16: XRD Patterns of XC44 toughened PMMA-6wt% Cloisite 25A and PMMA-6wt% Cloisite 25A Composites.

Storage Modulus

The DMTA data that was obtained to examine the effect of the nanocomposite formation on the T_g of toughened PMMA-clay composite was also used to examine if a nanocomposite microstructure would cause any variation in the storage modulus of the composites. The testing conditions used were those mentioned in the previous section and again the data was taken from the 10Hz second test run data. Figure 5.17 presents a typical plot of the logarithm of the storage modulus against temperature for a toughened PMMA and its clay composite.

In the figure the storage modulus, as expected, can be seen to drop (by two orders of magnitude) as T_g is approached and passed through. This behaviour occurs for all polymers and for all the toughened PMMAs and their composites produced for this project.

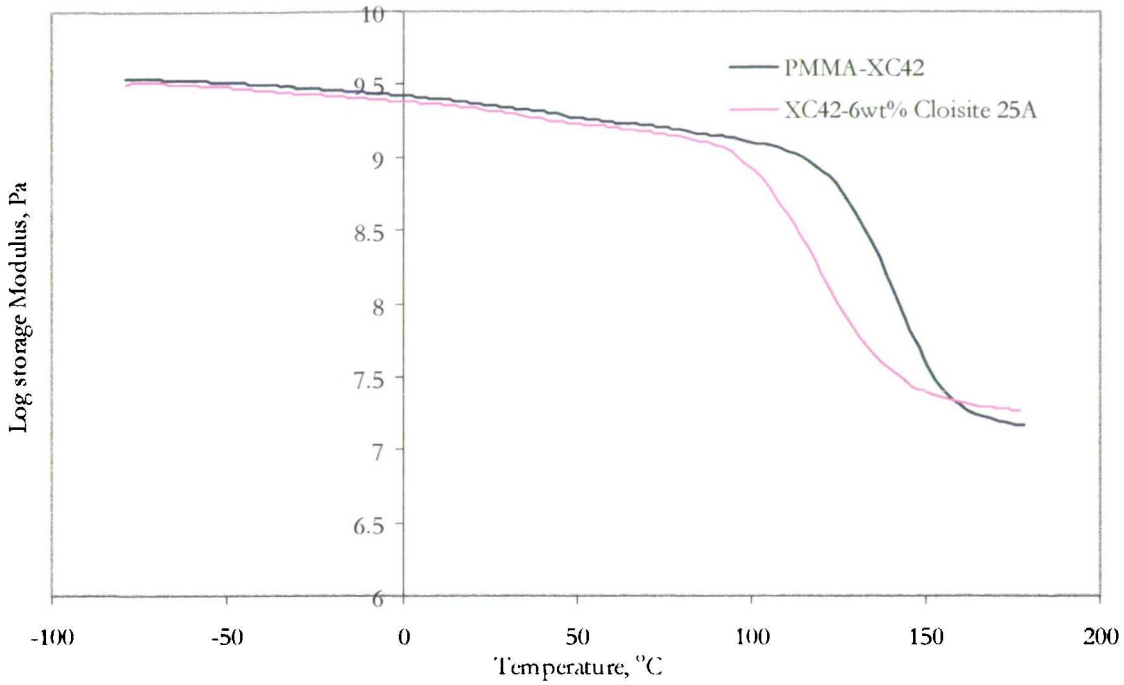


Figure 5.17: Typical Plot of the Logarithm of the Storage Modulus against Temperature for a Toughened PMMA (PMMA-XC42) and a Toughened PMMA-clay Composite.

Presented in Table 5.7 are the storage moduli at 20°C and 160°C and the T_gs of the toughened PMMAs and their composites. Also included for comparison purposes are the data on PMMA and its 6wt% Cloisite 25A composite. In Table 5.7 the storage modulus at 20°C represents the storage modulus of the material in the glassy region, and at 160°C represents the storage modulus of the material in the rubbery region.

From Table 5.7 it can be seen that the addition of any core-shell particle caused a relatively large drop in storage modulus both in the glassy and rubbery regions. This is not unexpected since core-shell particles are effectively pre-formed rubbery particles. The particularly large drop in storage modulus, approximately a 30% drop both at 20°C and 160°C, upon the addition of KM355 type core-shell particles can be considered to be due to the phase separation as seen in the scanning electron micrograph of the

fracture surface (presented in Figure 5.18). This also accounts for the reduction in the toughened PMMA's T_g compared to the untoughened PMMA's T_g.

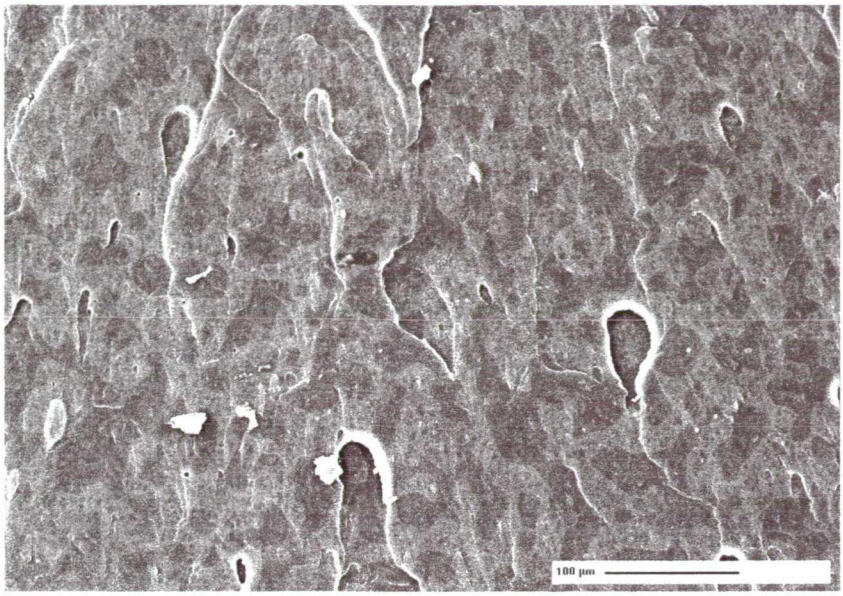


Figure 5.18: Scanning Electron Micrograph of the Fracture Surface of PMMA-KM355.

Table 5.7: DMTA Data for PMMA, Toughened PMMA and Composites.

	PMMA		KM355-PMMA		XC42-PMMA		XC44-PMMA	
	Plain	25A6%	Plain	25A6%	Plain	25A6%	Plain	25A6%
Storage Modulus at 20°C, GPa	2.79	3.14	1.89	2.41	2.23	2.22	2.28	2.06
Storage Modulus at 160°C, MPa	26.07	24.2	18.50	53.53	19.63	21.40	23.28	19.59
T_g, °C	149.1	142.1	127.2	155.0	147.6	125.2	147.1	143.1

In Table 5.7 it can be seen that for the KM355-Cloisite 25A composite these reductions in storage moduli are partly recovered in the glassy region and totally recovered in the

rubbery region. This again is caused by the phase-separation. The phase-separation that occurs in the KM355-PMMA does not occur in the composite with Cloisite 25A. Thus it can be concluded that the addition of clay interfered with the phase-separation.

However, the losses in the storage modulus for PMMA-XC42 and PMMA-XC44 are not recovered upon the addition of clay to the system. For XC42 it can be concluded that any gains made by the addition of clay to the system are negated by two mechanisms. Firstly by the surfactant also added, and secondly the XC42-6wt% Cloisite 25A composite achieved the largest d-spacing of all the 6wt% composites fabricated, thus the lack of rigidity caused by the expanded state of the clay platelets. The storage modulus results of the XC44-6wt% Cloisite 25A composite show very similar trends to the glass transition temperature results, thus can be explained by the same balance between matrix plasticisation due to the surfactant and the confinement/reinforcing effect of the clay particles

5.2 Thermal Stability

5.2.1 Introduction

In this section the results of experiments investigating the effects of nanocomposite formation on the thermal stability of the thermosetting PMMA will be presented. The thermal stability was investigated using thermogravimetric analysis, TGA. Experiments were run both in air and in Argon. However, when the experiment was performed in air oxidation of the sample occurred. This was highly exothermic, increasing the measured temperature by up to 75°C. This distorts the heating rate, see Figure 5.19, making interpretation of the results difficult as the heating rate and temperature differ between samples at this point. This effectively invalidates the data in air. In an Argon environment, although some oxidation does occur due to the oxygen located in the polymer chains, the amount is small, and hence the heating rate is unaffected. Hence the results presented below are taken from the experiments performed in argon only.

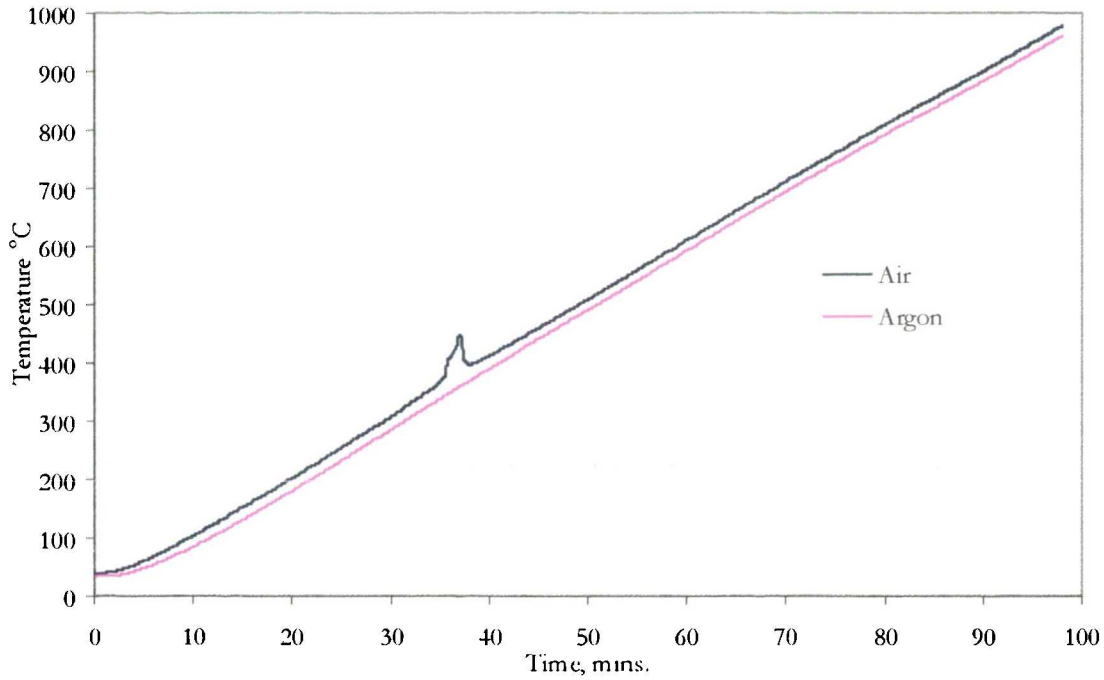


Figure 5.19: Measured Temperature versus Time for TGA of PMMA-clay Composites Tested in Air and in Argon.

5.2.2 Thermal Stability of Organoclays

For the purposes of this investigation, the onset temperature (the temperature at which thermal decomposition commences) was defined as the temperature at which the sample had lost 10% of its mass, since clays typically have a few percent of moisture as well as for the organoclays there is possibly some free surfactant. The thermal stability of the organoclays was first investigated to ensure that the post-cure of the composites did not adversely affect the organoclay's surfactant, and to assess the montmorillonite content of the composites. Figure 5.20 shows the TGA traces for montmorillonite and all the organoclays successfully used in this project.

In Figure 5.20 the initial weight loss, between 0-100°C, shown by all the clays can be seen to be caused mostly by the loss of water. This can be concluded since montmorillonite, an unmodified clay mineral (and the clay mineral on which all the organoclays used are based), also shows weight loss in this area. Since there is no surfactant to lose, this can only be accounted for by the loss of water. It should also be

noted that since this montmorillonite is unmodified it is more hydrophilic than the organoclays thus will have absorbed more atmospheric water.

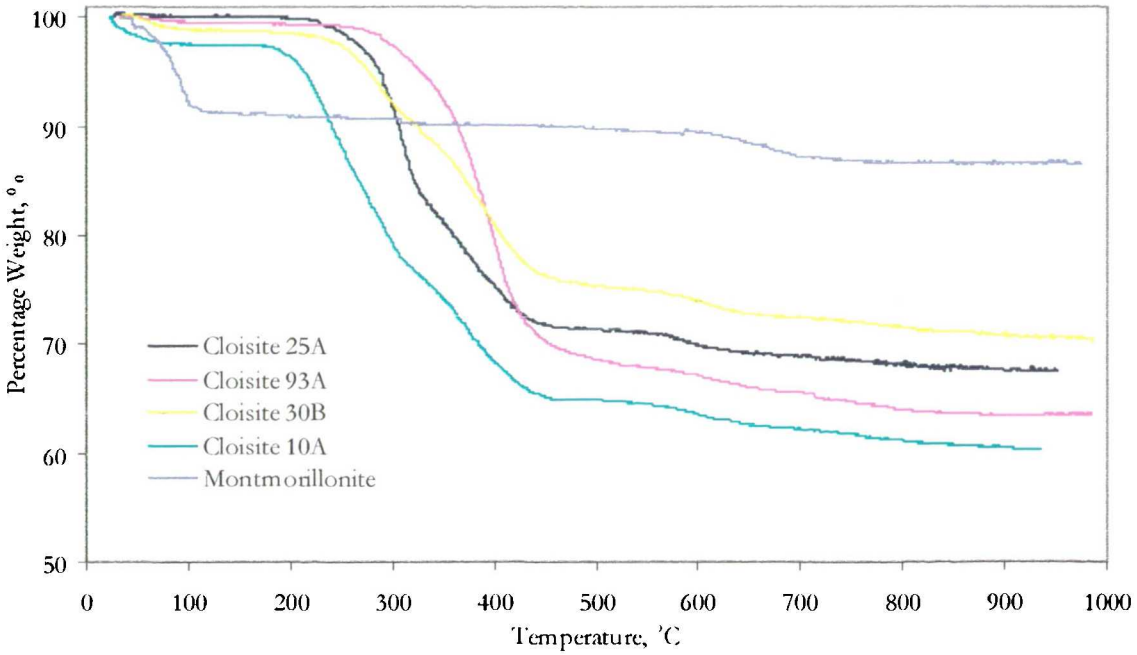


Figure 5.20: TGA Traces of Montmorillonite and the Organoclays Successfully Used in this Project.

The weight losses that occur in the region beyond 100°C for the organoclays can be concluded to be due to the surfactants decomposing since the TGA trace for montmorillonite in this region shows no further weight losses until between 600-700°C. The data for the organoclays shown in Figure 5.20 are summarised in Table 5.8 which details the onset temperature, plus the temperature when the organoclay has lost 20% of its mass, the weight loss that occurs between 0-130°C and the percentage weight loss on ignition of the organoclays. Also included are the manufacturer's data on both surfactant concentration and, for the purposes of comparison, on the percentage weight loss on ignition.

Table 5.8: TGA Data for Organoclays, Plus Percentage Weight Loss on Ignition from reference 91. (Note the post cure temperature used in the present work was 120°C.)

	Surfactant Concentration, meq/100g	Onset Temp., °C	Temp. at 20% Weight Loss, °C	°oWeight Loss between 0-130°C	°o Weight Loss on ignition	
					Exp	Manu
Cloisite 93A	90	364.5	398.6	0.46	36.51	40
Cloisite 30B	90	325.6	407.5	1.07	29.87	30
Cloisite 25A	95	305.9	359.8	0	32.48	34
Cloisite 10A	125	240.3	295.8	2.55	39.74	39

Note. Onset temperature occurs at 10% weight loss.

Exp: measured in present work. Manu: manufacturers data.

It can be plainly seen from both Figure 5.20 and Table 5.8 that the most thermally stable organoclay is Cloisite 93A with an onset temperature of 364°C. Also it can be concluded that Cloisite 10A is the most thermally unstable of the organoclays investigated with an onset temperature of 240°C. It can be seen that the onset value for Cloisite 10A is much lower than that of Cloisite 25A, the clay with the second lowest onset temperature of 305°C (a 65°C increase on Cloisite 10A's onset temperature). Table 5.8 also shows that Cloisite 10A has a much higher surfactant concentration (125meq/100g) than the other clays. Montmorillonite, the clay upon which all these organoclays are based, has a cation concentration of approximately 90meq/100g[20, 91]. Hence Cloisite 10A has a large excess of surfactant. It is this large excess of surfactant that causes Cloisite 10A to degrade more readily.

Examining Figure 5.20 it can be stated that the degradation of the surfactant occurs within the temperature range of 200°C to 450°C for all the organoclays used. It can be concluded from this, along with the data shown in the percentage weight loss between 0-130°C column of Table 5.8, that the organoclays are not degraded by the maximum post cure temperature of 120°C. The weight loss that does occur in the temperature range of 0-130°C ties in with the data given by the manufacturer that the organoclays contain less then 2°o moisture. (Note that although Cloisite 10A does have a percentage

weight loss in excess of 2% in this temperature range, the weight loss is still due to water coming off since in Figure 5.20 the percentage weight can be seen to be constant after 100°C up to 200°C.) In Figure 5.20 it is clear from the changes in the gradient of the traces that Cloisite 30B, Cloisite 25A and Cloisite 10A all degrade in two stages whereas Cloisite 93A degrades in one stage. A possible cause of this difference in degradation behaviour could be the presence of two hydrogenated tallow groups in the Cloisite 93A surfactant instead of one as for the other organoclays. The two stages of decomposition can be seen most distinctly in Cloisite 25A which has a very rapid weight loss in the first stage then in the second stage this rate reduces (the trace becomes less steep). This reduction in the decomposition rate could be due to the collapse of the clay galleries restricting the thermal motion of the surfactant, thus slowing the rate of decomposition. Table 5.8 shows good agreement between the manufacturer's percentage weight loss on ignition values and those found experimentally. Since this was the case it was decided to use the manufacturer's values to calculate the montmorillonite content added to the PMMA to form the various composites.

5.2.3 Effect of Nanocomposite Formation

TGA experiments were performed on the 3wt% , 6wt% and 9wt% PMMA (AIBN initiated) composites of all the organoclays, as well as on PMMA. The TGA traces for the 3wt% , 6wt% and 9wt% composites are compared to PMMA's TGA trace in Figures 5.21, 5.22 and 5.23 respectively.

From these Figures it is apparent that the main decomposition stage occurs in the same temperature range, 360-460°C for all the composites and for the PMMA. Indicating that this is the temperature range in which the polymer decomposes, this conclusion is supported by the negligible change in percentage weight that occurs in the PMMA TGA trace after 460°C. It is also clear from Figure 5.21 and 5.22 that Cloisite 93A produces the most thermally stable composites for 3wt% and 6wt%. This is somewhat expected in light of Cloisite 93A being the most thermally stable clay. Table 5.9 demonstrates that most of the composites formed have higher onset temperatures than

PMMA. The table also confirms what is shown in Figures 5.21, 5.22 and 5.23, that at 3wt% and 6wt% loading of clay composites formed with Cloisite 93A are the most thermally stable of the composites whilst at 9wt% it is Cloisite 30B that produces the most thermally stable composite.

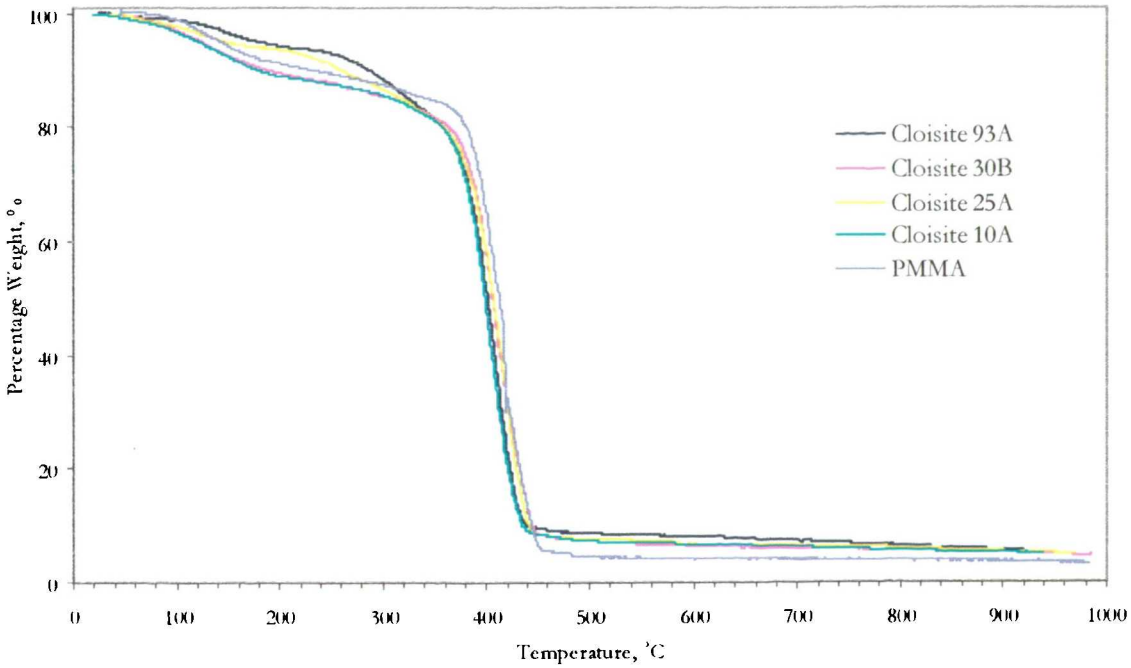


Figure 5.21: TGA Traces of PMMA and its 3wt% Clay Composites.

It can be seen from Table 5.9 that at 3wt% of clay, Cloisite 30B and Cloisite 10A produce composites with onset temperatures lower than that found for PMMA. Also, from closer examination of the onset temperatures for Cloisite 30B, a trend becomes apparent of increasing onset temperature, thus thermal stability, with increasing clay content. A similar trend occurs in Cloisite 10A, although after the large initial increase in onset temperature at 6wt% the increase on addition of 9wt% of Cloisite 10A is a lot less (see Figure 5.24 showing the variation of the composites onset temperature). From Figure 5.24 it is clear that for Cloisite 25A the onset temperature remains fairly stable with increasing clay content.

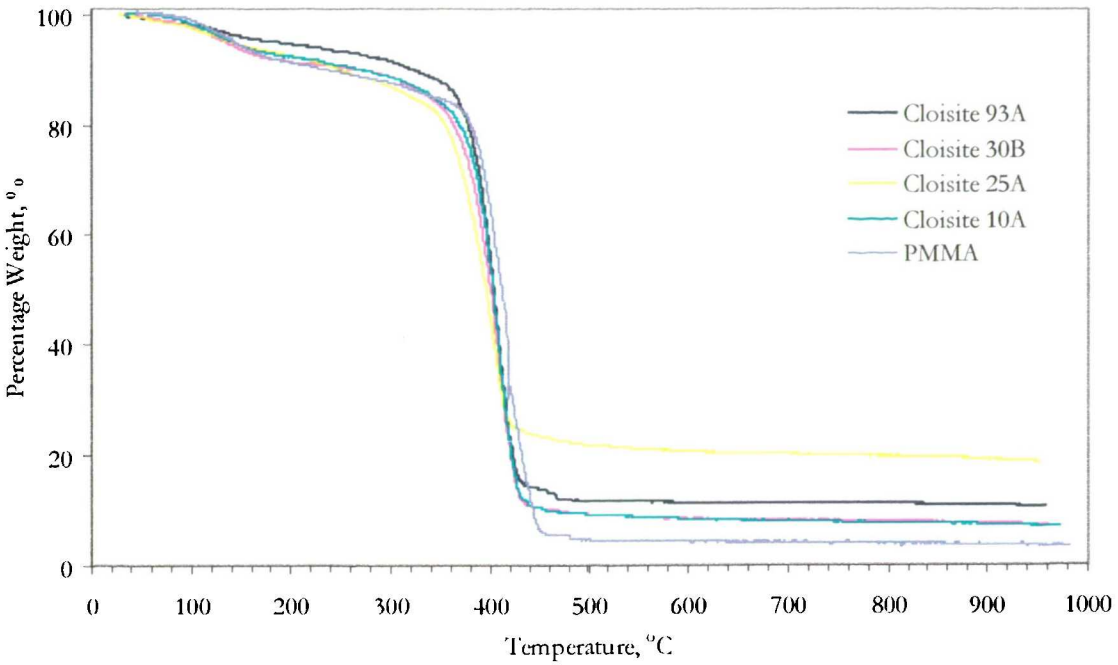


Figure 5.22: TGA Traces of PMMA and its 6wt% Clay Composites.

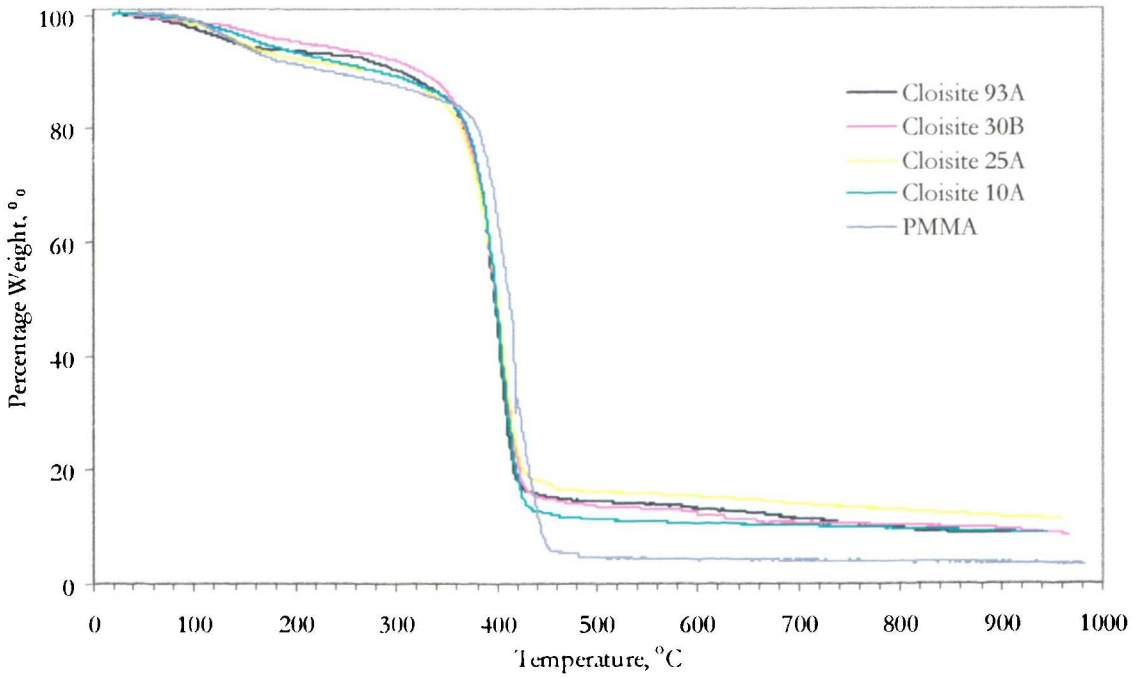


Figure 5.23: TGA Traces of PMMA and its 9wt% Clay Composites.

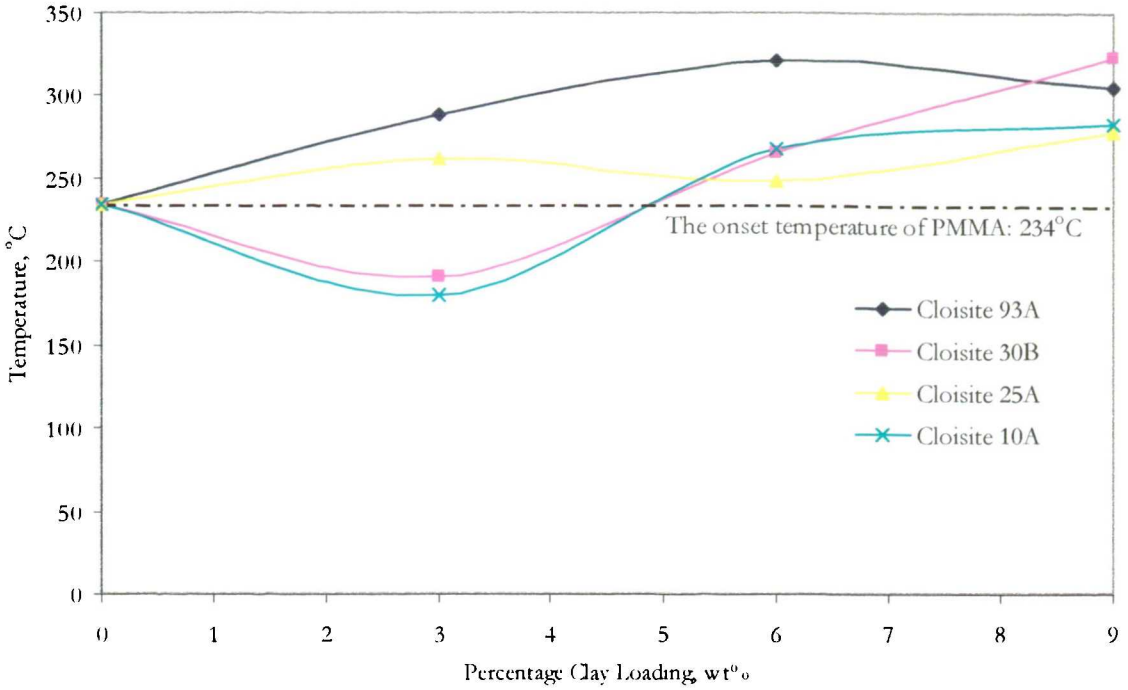


Figure 5.24: Variation of Onset Temperature of Composites with Percentage Clay Loading for the different Organoclays. (Note that the broken line denotes the onset temperature of PMMA, 234°C).

From the data presented in Table 5.9 perhaps the most significant point is that on the residual matter leftover once the TGA test is complete. It is clear that the composite with the largest percentage residual matter is the Cloisite 25A 6wt% composite.

Table 5.10 lists the montmorillonite content calculated from the manufacturer's data (the expected residual from the composite once the PMMA residual has been taken into account) and the experimentally found montmorillonite fraction of the composite residual, i.e. for a 3wt% clay composite, the composite residual will contain 97% PMMA residual, termed in this table the montmorillonite residue % experimental.

Table 5.9: TGA Data for PMMA and its Clay Composites.

	PMMA	Cloisite 93A			Cloisite 30B			Cloisite 25A			Cloisite 10A		
		3%	6%	9%	3%	6%	9%	3%	6%	9%	3%	6%	9%
Temperature at 5% Weight Loss, °C	142.5	179.0	187.6	143.5	125.5	134.2	208.8	149.3	141.0	149.0	122.2	141.9	167.8
Onset Temperature, °C	234.5	288.3	320.9	305.2	190.6	265.0	324.0	262.0	248.2	279.0	179.9	268.5	283.4
Temperature at 50% Weight Loss, °C	411.8	400.5	403.7	397.5	405.6	399.9	399.3	406.9	395.7	400.1	398.6	402.9	399.6
Residual Matter, %	3.20	5.29	10.58	8.92	4.79	7.25	8.55	4.98	18.71	11.37	4.90	6.99	8.67

Note: Onset Temperature is at 10% weight loss

Table 5.10: Predicted and Experimental Montmorillonite Residue (i.e. with expected residual PMMA subtracted).

	3wt% MMT Residue%		6wt% MMT Residue%		9wt% MMT Residue%	
	Exper.	Predicted	Exper.	Predicted	Exper.	Predicted
Cloisite 93A	2.19	1.80	7.57	3.60	6.01	5.40
Cloisite 30B	1.68	2.10	4.24	4.20	5.64	6.30
Cloisite 25A	1.88	1.90	15.70	3.96	8.46	5.94
Cloisite 10A	1.80	1.83	3.98	3.66	5.76	5.49

Note: MMT is an abbreviation for Montmorillonite.

By examining Table 5.10 several points become apparent. Firstly, for the 3wt% composites the experimental montmorillonite residue is not significantly different from the calculated montmorillonite content. The small variations that do occur can be accounted for by slight inhomogeneities of the specimens, thus the residue can be thought of as being only montmorillonite. Secondly, the values of the montmorillonite residue for all the Cloisite 30B and Cloisite 10A composites compare well with the montmorillonite content values. Finally the experimental montmorillonite residue for the 6wt% Cloisite 93A and for the 6wt% and 9wt% Cloisite 25A are significantly larger than the predicted montmorillonite content values. This is especially true for the Cloisite 25A 6wt% which gave the largest experimental montmorillonite content found and is four times greater than the calculated montmorillonite content. These variations in experimental and predicted montmorillonite residue as seen for 6wt% Cloisite 93A, 6wt% Cloisite 25A and 9wt% Cloisite 25A cannot be accounted for by inhomogeneity in the sample but must be a large amount of residual char. From the literature it is clear that some residual char should be expected since the clay platelets protect the polymer and prevent complete degradation.

Figures 5.22 and 5.23 reveal that the thermal stability of none of these composites differs greatly from the thermal stability of the other composites. It can also be seen from Table 5.11 showing the d-spacings for all the composites that underwent TGA testing, the values in italics have been calculated using the 002 peak position, that the d-spacings for the composites are all approximately equal. Hence it appears that the

differences in thermal stability cannot be accounted for by the variations in the measured d-spacings.

Table 5.11: D-spacing Measured using XRD for the Composites.

	D001-spacing, Å		
	3wt%	6wt%	9wt%
Cloisite 10A	*30.88*	28.66	*32.22*
Cloisite 25A	*28.48*	*31.54*	*31.32*
Cloisite 93A	*32.7*	28.30	*31.98*
Cloisite 30B	*34.48*	*34.48*	*34.48*

However if the thermal degradation and stability of the organoclay Cloisite 25A is examined two plausible explanations are revealed. The first can be seen in Figure 5.20 showing the thermal degradation of the organoclays. From this figure it can be seen that Cloisite 25A degrades in two stages. The first stage of this degradation is very steep, the steepest of all the organoclays. The second stage becomes more shallow and similar to the other organoclays. It can be concluded that the first stage of the degradation is very rapid and it is also reasonable to assume that the thermal degradation of the surfactant (and in the case of the composites the polymer and surfactant) commences at the edges of the clay platelets. Hence these edges would then be unsupported and would be likely to collapse hence protecting the surfactant/polymer resident in the centre of the clay particle. This results in the shallower second stage of thermal degradation seen in Figure 5.20. This effect does however appear to be very sensitive to clay loading as at 3wt% Cloisite 25A it does not occur, possibly due to there being too little clay present to act as an effective barrier and at 9wt% the effect does occur but to a lesser extent.

The other plausible explanation presents itself from Figure 5.20 and the TGA data from the organoclays. Between 0-130°C Cloisite 25A has no mass loss and Cloisite 93A has a mass loss of 0.46% whereas Cloisite 30B has a mass loss of 1.07% and Cloisite 10A has a mass loss of 2.55%. From this it can be concluded that both Cloisite

25A and 93A are "dry", i.e. contain no water, whereas Cloisite 30B and Cloisite 10A are comparatively "wet". The water present in Cloisite 30B and 10A would turn to steam at 100°C, expanding rapidly and forcing the clay particles to break up. In the composite this may destroy the microstructure and any protection given to the polymer by the clay. However, with Cloisite 25A there is no water and very little in Cloisite 93A, and hence no steam to break up the clay particles and destroy the microstructure.

From the TGA data presented here it can be concluded that these composites show potential as char forming materials but are sensitive to the organoclay used and its percentage loading.

5.3 Concluding Remarks

The data presented in this chapter have lead to several conclusions on the effect of nanocomposite formation on some of the physical properties of the composites formed. The physical properties of the composites investigated were the glass transition temperature and the storage modulus using dynamic mechanical thermal analysis (DMTA) and the thermal stability using thermogravitmetric analysis (TGA). The DMTA data presented in this chapter led to the conclusion that the effect of nanocomposite formation on the glass transition temperature varied due to a delicate balance between the organoclay's surfactant plasticising the polymer matrix and the stiffening/confining effect of the clay particles. This balance was also seen to be active for the storage modulus of the composites. The effect of nanocomposite formation on the storage modulus was greater in the rubbery region as expected. The TGA data presented lead to the conclusion that several of the composites showed excellent potential as char forming materials in particular those formed using Cloisite 25A as the organoclay. The data revealed also that the thermal stability of the composites compared to the pristine polymer was generally increased.

The effect of the microstructural results presented in Chapter 4 on the mechanical properties of the composites are discussed in Chapter 6. The mechanical properties

investigated were the Young's modulus, tensile strength, fracture toughness and fracture energy.

Chapter 6

Results – Mechanical Properties

6.0 Introduction

In this chapter the results from various experiments conducted to investigate the mechanical properties of the nanocomposites are presented. So as to aid the reader the relevant observations from both the microstructure chapter, Chapter 4, and the physical properties chapter, Chapter 5, will be briefly recalled now. Firstly in Chapter 4 it was concluded that all the composites successfully formed possessed an intercalated nanocomposite microstructure. The extent of the intercalation varied with each organoclay type, each organoclay appearing to have a maximum d-spacing that is relatively independent of certain processing variables such as mixing time. Secondly it was observed that the major effect of variation of the clay percentage loading was that the proportion of clay platelets achieving the maximum d-spacing for the organoclay in this system decreased with increasing clay loading. In Chapter 5 it was found that the effect of nanocomposite formation on the glass transition temperature varied due to a delicate balance between the organoclay's surfactant plasticising the polymer matrix and the stiffening/confining effect of the clay particles. This balance was also seen to be

active for the storage modulus of the composites. The effect of nanocomposite formation on the storage modulus was greater in the rubbery region as expected.

The properties of the nanocomposites that are presented and examined here are the Young's modulus, the tensile strength, the fracture toughness and the fracture energy. The Young's modulus and the tensile strength were both investigated using tensile tests. Compact tension geometry fracture tests were used to examine the fracture toughness and fracture energy of the nanocomposites formed. The fracture mechanisms were also investigated using scanning electron microscopy. The final section of this chapter compares the experimental results for Young's modulus, tensile strength and fracture energy to those predicted from several theoretical models.

6.1 Tensile Properties

6.1.1 Effect of Nanocomposite Formation

Tensile tests were conducted so as to examine the effect that the formation of a nanocomposite has on the tensile properties of PMMA-clay composites, compared with the tensile properties of the PMMA used. For each of the compositions three or more dog-bone shaped specimens were machined. (Note that PMMA-3wt% Cloisite 25A and PMMA-3wt% Cloisite 93A were two exceptions to this as these composite plates proved very difficult to machine as they had a tendency to fracture even at low cutting speeds, and thus none were successfully machined.) All the tensile tests were conducted at room temperature. At least three specimens of each composition were tested on an Instron 5584 at a crosshead speed of 1mm/min using a 150kN load cell. Since some tensile properties (e.g. tensile strength) are severely affected by the quality of the surface finish it was decided to assess the effect of nanocomposite formation on the tensile properties of the composites using Young's modulus as this property is relatively unaffected by surface finish. The Young's modulus and the tensile strength were recorded for each specimen, then the mean and the standard deviation of each were calculated. The tensile strength of the composites will only be briefly mentioned

here as it is vulnerable to surface finish defects. It is expected that there will be an increase in the composite Young's modulus caused by the presence of the clay, since the clay has a higher Young's modulus (~170GPa) than the polymer (~3GPa).

The results of the tensile tests (Young's modulus and tensile strength) performed and the storage modulus at 20°C of the composites appear in Table 6.1. The storage modulus at 20°C of the composites found from dynamic mechanical thermal analysis (DMTA) are included so any differences between the effect of nanocomposite formation on the dynamic (storage) and static (Young's) modulus can be noted. Figure 6.1 presents the Young's modulus data in graphical form. Figure 6.1 also includes the error bars for the Young's modulus based on one standard deviation from the mean value. From Figure 6.1, it can be seen that most of the results have small error bands (standard deviations) apart from the 6wt% Cloisite 10A result, which is unusually high, that has a comparatively large error band so it can be concluded that this result must be treated with caution.

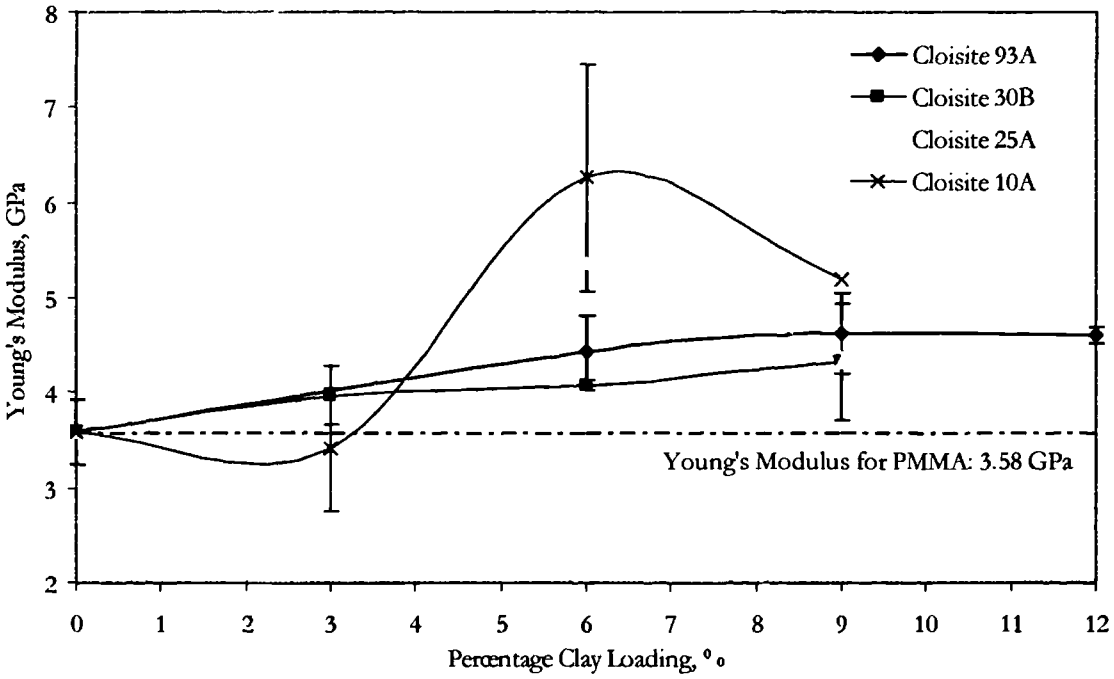


Figure 6.1: Young's Modulus of PMMA and PMMA-clay Composites. (Error bars are ±1 standard deviation.)

Table 6.1: The Tensile Test Data and the Storage Modulus at 20°C for PMMA and its Composites.

	PMMA	Cloisite 93A				Cloisite 30B			Cloisite 25A			Cloisite 10A		
		3%	6%	9%	12%	3%	6%	9%	3%	6%	9%	3%	6%	9%
Young's Modulus, GPa	3.58	-	4.43	4.62	4.6	3.97	4.08	4.33	-	5.36	4.34	3.41	6.26	5.20
Tensile Strength, MPa	79.9	-	49.0	36.8	42.4	59.8	33.2	30.4	-	35.2	26.4	41.5	26.2	14.8
Storage Modulus at 20°C, GPa	2.79	2.43	3.35	2.47	2.61	2.60	3.12	2.44	2.34	3.14	2.65	3.02	3.18	2.14

Note that for the 9wt% Cloisite 10A due to premature failure of the specimens only one of the three specimens gave a Young's modulus value, thus the error bar for the point is missing.

By examining Table 6.1 and Figure 6.1 several points become clear. Firstly in general the Young's moduli of the PMMA-clay composites are greater than that of the pristine PMMA. As well as this the extent of the increase in Young's modulus varies with organoclay type and loading. The 6wt% Cloisite 10A composite has the highest value for Young's modulus, however this result must be treated with caution due to its large error band (± 1.20 GPa). Therefore the composite with the next highest value for Young's modulus is the 6wt% Cloisite 25A composite at 5.36 GPa. This result is more credible than that for the 6wt% Cloisite 10A composite as from Figure 6.1 it can be seen that the error band is not large (± 0.40 GPa).

Secondly, Figure 6.1 shows that as the percentage clay loading increases so too does the Young's modulus (Cloisite 10A also follows this trend if the 6wt% value is considered as an error). In general the increase in Young's modulus with percentage clay loading can be said to be small compared to the initial increase seen upon the addition of clay. From these points it can be concluded that the addition of organoclay and the microstructure it adopts affects the Young's modulus of the composites. It can be concluded that the greater the proportion of clay platelets at the widest d-spacings the greater the increase in Young's modulus. This can be concluded from the microstructural results in Chapter 4 point to the proportion of clay platelets assuming the widest d-spacing decreasing as the percentage clay loading increases. The results here show the rate of the increase in Young's modulus decreasing with increasing percentage clay loading i.e. increasing the content of clay platelets not at the widest spacing achievable for that particular clay.

Thirdly, considering the tensile strength of the composites. Table 6.1 and Figure 6.2 show the effect of the addition of the clay and the effect of the proportion of clay platelets at the maximum spacing decreasing (increasing the percentage clay loading decreases the proportion of clay platelets at the maximum d-spacing) on the tensile

strength. From Figure 6.2 it is clear that the addition of clay is detrimental to the tensile strength of the composite formed. This is in part expected since even when composites are formed using silica spheres as the filler particles the tensile strength of the composite decreases[99, 100]. Thus it is expected when comparatively sharp-edged clay particles are used to form composites that they act as flaws and the tensile strength of the composite decreases. The decrease in tensile strength shown in the data also suggests that the clay particles are not well bonded into the matrix, thus allowing the particles to act as flaws. During the tensile test it was noted that as the percentage clay loading increased so too did the number of premature failures, the worst specimens for premature failure were those fabricated from 9wt% Cloisite 10A composite. The probable cause of these premature failures is the clay particles close to the surface acting as flaws. From this and the data presented in Figure 6.2 it can be concluded that the effect of increased clay content is to increase the number of flaws and consequently cause a reduction in tensile strength.

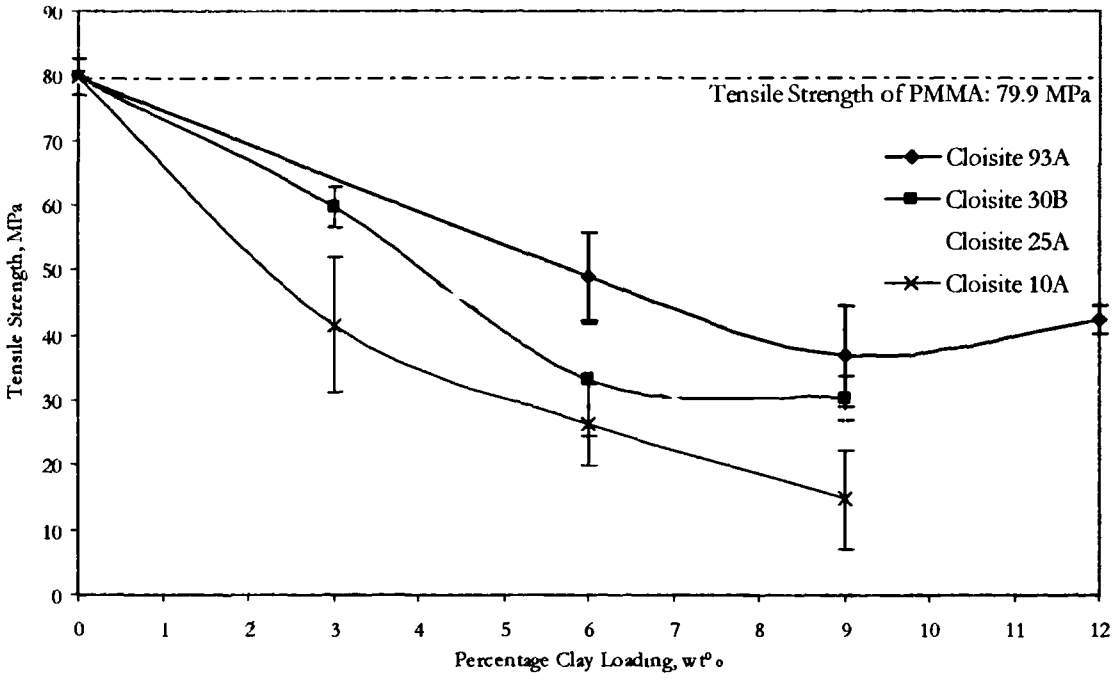


Figure 6.2: Tensile Strength of PMMA and PMMA-clay Composites. (Error bars are ±1 standard deviation.)

Finally Table 6.1 with the aid of Figures 6.1 and 6.3 demonstrates that the effect of nanocomposite formation on the dynamic (storage) modulus is different to the effect on the static (Young's) modulus. In this comparison of dynamic to static moduli it is not the absolute values of each that are being compared (since the dynamic mechanical thermal analysis method of measuring the storage modulus is not particularly accurate) but the trends that can be seen that are being compared. Comparing Figures 6.1 and 6.3 it can be seen that for the static (Young's) modulus there is little fluctuation occurring with increasing clay content whereas for the dynamic (storage) modulus there are quite significant fluctuations. This suggests that the dynamic modulus is greatly affected by the balance between matrix plasticisation by the surfactant and the polymer chain confinement/reinforcement provided by the clay particles that exists for these composites.

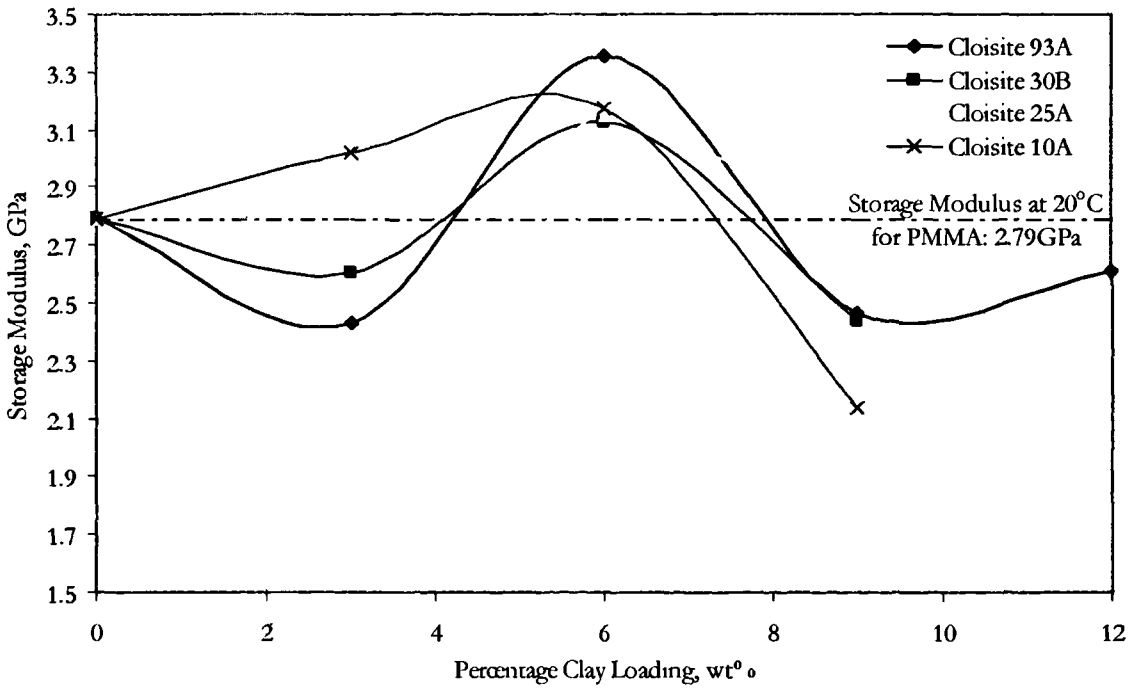


Figure 6.3: Storage Modulus at 20°C of PMMA and PMMA-clay Composites.

6.1.2 Effect of Choice of Polymerisation Initiator

The tensile test data presented here investigates the changes in tensile properties brought about by the effects of different polymerisation initiators on the microstructure of the polymer-clay composites. The polymerisation initiators used were 2,2-azo-bis-isobutyronitrile (AIBN, as a control), lauroyl peroxide and trigonox 23. The two organoclays used to form the polymer-clay composites were Cloisite 25A and Cloisite 93A. The microstructural results presented in Chapter 4 found from X-ray diffraction that no matter which initiator was used the composites produced had an intercalated nanocomposite microstructure. It was also concluded from the results that composites produced using lauroyl peroxide as the polymerisation initiator and Cloisite 93A as the organoclay had the largest gallery spacing, and those formed using AIBN as the initiator (no matter which organoclay was used) possessed the smallest gallery spacings. The tensile tests were performed as detailed in Chapter 3 and in section 6.1.1.

Table 6.2(a): Cloisite 93A, Tensile Data for PMMA and Composites.

	Young's Modulus, GPa			Tensile Strength, MPa			Storage Modulus at 20°C, GPa		
	AIBN	LP	Trig	AIBN	LP	Trig	AIBN	LP	Trig
Plain	3.58	3.9	4.68	79.92	72.11	65.17	2.79	2.43	2.87
3wt%	-	4.67	-	-	60.13	-	2.43	3.60	-
6wt%	4.43	4.34	4.58	48.93	58.33	32.7	3.35	3.00	2.79
9wt%	4.62	6.0	3.62	36.77	52.42	51.13	2.47	3.08	2.56

Table 6.2(b): Cloisite 25A, Tensile Data for PMMA and Composites.

	Young's Modulus, GPa			Tensile Strength, MPa			Storage Modulus at 20°C, GPa		
	AIBN	LP	Trig	AIBN	LP	Trig	AIBN	LP	Trig
Plain	3.58	3.9	4.68	79.92	72.11	65.17	2.79	2.43	2.87
3wt%	-	4.69	-	-	56.89	-	2.34	2.66	-
6wt%	5.36	3.66	5.40	35.19	42.06	50.74	3.14	-	2.79
9wt%	4.34	4.69	4.36	26.39	32.57	33.05	2.65	3.18	2.87

Table 6.2(a) presents the tensile test data (Young's modulus and tensile strength) for the PMMA initiated with AIBN, lauroyl peroxide or trigonox 23 and their respective Cloisite 93A composites. Table 6.2(b) presents this data for the composites formed with Cloisite 25A as the organoclay. Included in these tables as well are the storage moduli at 20°C for the composites, acquired using dynamic mechanical thermal analysis, thus enabling an assessment of whether the formation of a nanocomposite microstructure has the same effect on the static (Young's) modulus as on the dynamic (storage) modulus.

It can be seen in either table that the effect of altering the polymerisation initiator on the Young's modulus of the pristine polymer is an apparent increase in Young's modulus. Since in this case nothing is being added to the polymer it can only be assumed that the change in polymerisation initiator has caused a subtle change in the microstructure of the polymers. This is undetectable using X-ray diffraction since the polymers formed are still thermoset and thus will still be amorphous in nature. It is probable that the change of polymerisation initiator could vary the degree of crosslinking which would in turn stiffen (if the crosslink density was to increase) or soften (if the crosslink density decreased) the matrix. This suspicion can be either confirmed or be denied by the examination of the glass transition temperatures of these polymers, if the crosslink density has increased causing the Young's modulus to increase, it will also have caused the glass transition temperature of the polymer to increase. Table 6.3 presents the glass transition temperatures for these polymers. It can be seen that there is hardly any increase in the glass transition temperature of the polymers. From this it can be concluded that the crosslink density is unchanged between the PMMAs. Also included in Table 6.3 are the mean values and the standard deviations for the Young's modulus experimental data. By closer examination of the standard deviations it can be seen that they overlap, and thus the Young's moduli of the pristine polymers can be considered to be the same within experimental error. In Table 6.2(a) the Young's modulus value for lauroyl peroxide initiated PMMA-9wt% Cloisite 93A is noticeably larger than the other lauroyl peroxide initiated Cloisite 93A

composites. The result also has a standard deviation of 1.20 GPa. It is in light of these facts that it is considered prudent to treat this result with caution

Table 6.3: The Glass Transition Temperature, T_g, Young's Modulus and Standard Deviation of Young's Modulus of the Various PMMAs.

	AIBN-PMMA	LP-PMMA	Trig-PMMA
T_g, °C	149.1	143.6	149.3
Young's Modulus, GPa	3.58	3.9	4.68
Standard Deviation of Young's Modulus, GPa	0.34	0.67	0.82

It is clear from Tables 6.2(a) and (b) that the effect of the addition of clay on the tensile strength of the composites is to cause a reduction in tensile strength no matter which initiator is used. This is in part expected since the clay particles can act as flaws in the polymer.

Examining the results for the Young's modulus of the lauroyl peroxide composites it can be concluded that the effect of the addition of clay is to increase the Young's modulus of the composite compared to the pristine polymer. This is expected for two reasons. Firstly the Young's modulus of clay is much larger than that of the polymer, and thus it is expected that the composites' modulus should increase. Secondly a proportion of the polymer is confined both around the clay particles and between the clay platelets. This proportion of polymer, due to its proximity to the clay, has a greater Young's modulus than the polymer far from the clay surfaces, see section 2.6.1 of Chapter 2. It is also noted that as the percentage clay loading increases the Young's moduli of the lauroyl peroxide composites decrease slightly. It is known from Chapter 4 that as the percentage clay content increases the proportion of the clay platelets at the larger d-spacings decreases, thus the proportion of polymer confined within the clay particles reduces. Hence the Young's modulus of the composite is less than that of composites where the proportion of clay platelets at larger d-spacings is greater.

From examination of the tables it appears that for the trigonox 23 initiated composites a somewhat different mechanism is at work since the Young's modulus decreases when clay is added. Table 6.4 details the Young's moduli and standard deviation for these trigonox 23 initiated composites.

Table 6.4: Young's Modulus and Standard Deviation of Young's Modulus for Trigonox 23-PMMA and its Composites.

	Plain	Cloisite 93A		Cloisite 25A	
		6%	9%	6%	9%
Young's Modulus, GPa	4.68	4.58	3.62	5.40	4.36
Standard Deviation of Young's Modulus, GPa	0.82	0.67	0.51	0.94	1.04

It can be seen from Table 6.4 that any fluctuations in the Young's modulus for the trigonox 23 initiated composites are within experimental error of the Young's modulus of the trigonox 23 initiated PMMA's Young's modulus. Thus it can be concluded that the addition of clay for these composites has no significant effect on Young's modulus.

Using Tables 6.2(a) and (b) some similar trends can be seen between the dynamic (storage) modulus and the static (Young's) modulus of the PMMA and its composites.

6.1.3 Effect of Core-Shell Addition

Tensile tests were performed on the rubber toughened PMMA's and their composites as with the untoughened PMMA so as to investigate any effects that the formation of nanocomposite microstructures had on tensile properties of the rubber toughened composites compared with the rubber toughened PMMA's.

The tensile specimens were cut and tests were performed in the same manner as previously detailed in Chapter 3 and in section 6.1.1. The Young's modulus is as before used to assess the tensile properties of the specimens.

Table 6.5 details the Young's modulus, tensile strength and the storage modulus at 20°C (found from DMTA) for PMMA and for the core-shell toughened PMMA. It is expected that the Young's modulus of the toughened PMMAs should decrease as the addition of core-shell particles can be considered a rubbery addition.

Table 6.5: Tensile Data (Including Storage Modulus at 20°C) for PMMA and Core-Shell Toughened PMMA.

	Young's Modulus, GPa	Tensile Strength, MPa	Storage Modulus at 20°C, GPa
PMMA	3.58	79.92	2.79
PMMA-5% KM355	2.51	48.16	1.89
PMMA-5% XC42	3.32	54.67	2.23
PMMA-5% XC44	3.22	51.72	2.28

Table 6.5 demonstrates that as expected the Young's moduli of the core-shell toughened PMMA decrease compared to PMMA. It also illustrates that the dynamic (storage) and static (Young's) moduli show the same trend, i.e. the moduli decrease upon the addition of core-shell particles, when no clay is present.

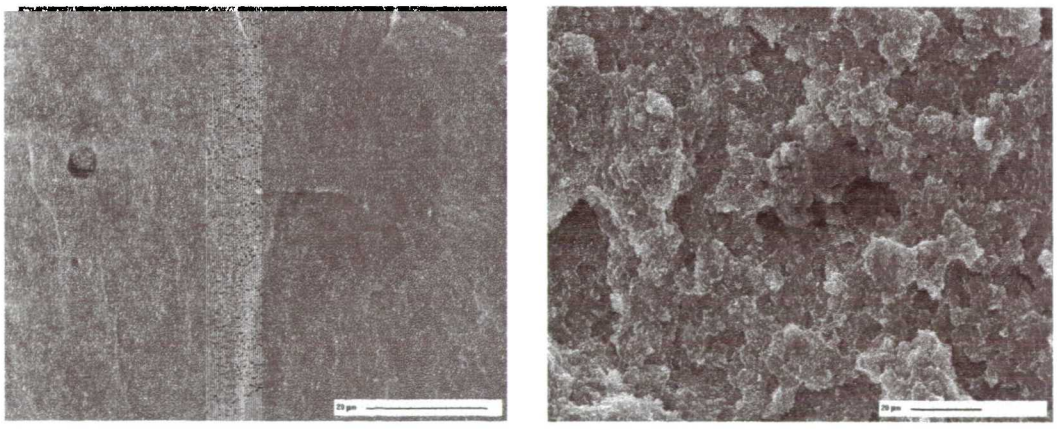
Table 6.6 presents the Young's moduli, tensile strength and storage modulus at 20°C of the toughened PMMA's and their respective 6wt% Cloisite 25A composites, included for comparison is the data on PMMA and its 6wt% Cloisite 25A composite.

Table 6.6: Tensile Data (Including Storage Modulus at 20°C) for PMMA, Core-Shell Toughened PMMA and their 6wt% Cloisite 25A Composites.

	PMMA		PMMA-KM355		PMMA-XC42		PMMA-XC44	
	Plain	6% 25A	Plain	6% 25A	Plain	6% 25A	Plain	6% 25A
Young's Modulus, GPa	3.58	5.36	2.51	3.67	3.32	3.04	3.22	3.36
Tensile Strength, MPa	79.92	35.19	48.16	37.52	54.67	34.09	51.72	40.58
Storage Modulus at 20°C, GPa	2.79	3.14	1.89	2.41	2.23	2.22	2.28	2.06

Examining Table 6.6 reveals that the Cloisite 25A 6wt% composite with the greatest Young's modulus is the untoughened PMMA composite. It also reveals that in general as expected upon the addition of clay into the systems the Young's moduli of the composites formed increase. The extent of the increase is variable and for the composites formed using XC42 or XC44 as the core-shell particles any variation in Young's modulus is small (between 4% and 8%). The largest increase in the Young's modulus of the toughened composites is for the PMMA KM355 6wt% Cloisite 25A composite (an increase of 48%).

However, the cause of this increase cannot be claimed to be due to the addition of clay alone. This increase, as for the dramatic rise in the glass transition temperature of the PMMA-KM355 6wt% Cloisite 25A composite (28°C increase), is believed to be caused mainly by the absence of a second phase (that is separate from the core-shell particles) seen in the toughened polymer (PMMA-5wt% KM355) but not seen in the toughened polymer-clay composite (PMMA-5wt% KM355-6wt% Cloisite 25A). Figure 6.4 presents the scanning electron micrographs of (a) the fracture surface of a PMMA-5wt% KM355 specimen and (b) the fracture surface of a PMMA-5wt% KM355-6wt% Cloisite 25A specimen.



(a) (b)

Figure 6.4: Scanning Electron Micrographs of (a) the Fracture Surface of a PMMA-5wt% KM355 Specimen and (b) the Fracture Surface of a PMMA-5wt% KM355-6wt% Cloisite 25A Specimen.

Table 6.6 shows again that the effect of the presence of clay in the matrix, both toughened and untoughened, on the tensile strength on the composite formed is to reduce the tensile strength of the composite compared with that of the matrix. The reason for this shall be discussed later in section 6.2.3 dealing with the fracture toughness of these toughened composites. However, it can be said based on the evidence presented thus far there are no synergistic effects occurring in the composites between the core-shell particles and the clay particles.

6.2 Fracture Properties

6.2.1 Effect of Nanocomposite Formation

Introduction

The fracture properties, fracture toughness and fracture energy, of the composites formed were investigated to establish what effect the nanocomposite microstructure has on the fracture properties. The results of experiments performed to investigate this are presented in this section.

In general it is expected that when well distributed, rigid, impenetrable particles are added to a polymer that the fracture properties of the composite should be improved compared to the pristine polymer[94]. Indeed, the Faber-Evans model implies that as the aspect ratio of these particles increases so too would the fracture energy of the composites formed, see Figure 6.5. Thus this indicates that a composite with an exfoliated nanocomposite microstructure should have an improved fracture energy compared to both the pristine polymer and a conventionally filled composite (macrocomposite). Although the fracture properties of the composites with nanocomposite microstructures have not yet been extensively studied, the work that has been published has not shown this to be the case[94, 17].

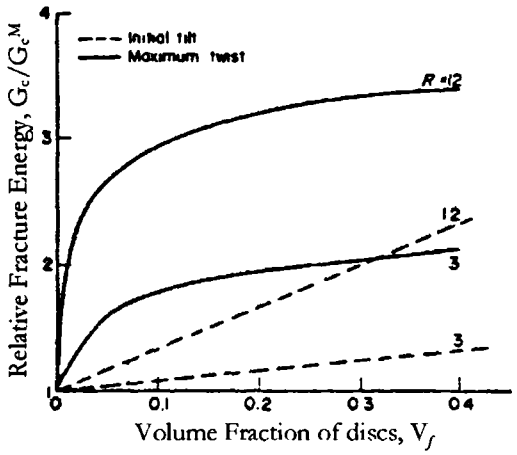


Figure 6.5: Relative Fracture Energy Predictions for Initial Tilt and for Maximum Twist based on Crack Deflection Model for Disc-shaped Particles of two Aspect Ratios (R)[77].

The fracture properties of the PMMA-clay composites formed were investigated using a fracture mechanics approach. Compact tension tests were used, and Figure 6.6 shows the general geometry of the specimens. The tests were performed in accordance with ISO13586[88] on a 5584 Instron testing machine at standard room temperature and humidity. The specimens were machined from plates, and two different sizes of specimens were used. The "large" (60mm by 62.5mm) specimens were replaced by the "small" (24.5mm by 25.5mm) specimens to allow more test specimens to be produced from the specimen plates, and enable the repeatability of the experimental data to be verified. Note that the data from both sizes of test specimen was found to be identical within experimental error. The machined notch was in all cases sharpened by tapping a natural crack into the tip of the notch with a razor blade. Note that a fresh razor blade was used for each specimen tested.

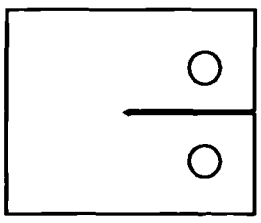


Figure 6.6: Schematic of a Compact Tension Specimen.

A minimum of three specimens were tested for each composite composition. For each test specimen the fracture toughness was recorded. The results presented here are the mean values of these data. The mean values of fracture toughness, K_c, and the experimentally measured mean values of Young's modulus, E, were used to calculate the fracture energy, G , using equation 6.1. The value of Poisson's ratio used was 0.35.

$$G_c = \frac{K_c^2(1-\nu^2)}{E} \qquad \text{....Equation 6.1}$$

where ν is Poisson's ratio.

Fracture Toughness

Before the fracture toughness, K_c, results are presented it must be stated that all the specimens tested failed in an unstable manner, i.e. by rapid crack propagation. Hence the fracture toughness results presented are only initiation values since the specimens had completely failed before the crack arrested in all cases. Table 6.7 presents the fracture toughness and fracture energy of PMMA and the various PMMA-organoclay composites. The Young's modulus values used to calculate the fracture energy are also included in this table.

It is clear from Table 6.7 that, unlike previously reported studies using epoxies and unsaturated polyesters by Kinloch and Taylor [94] and by Kornmann[22, 49], the addition of clay to this form of PMMA has a detrimental effect on the fracture toughness and energy of the composites when compared to pristine PMMA. It is also clear that as the percentage loading of the composite increases the fracture toughness decreases. Figure 6.7 presents the fracture toughness data in Table 6.7 in graphical form so as to make apparent any trends.

From both Figure 6.7 and Table 6.7 it can be concluded that the composites with consistently the highest values of fracture toughness are those formed using Cloisite 93A as the organoclay. Examination of Figure 6.7 reveals that for the 3wt% composites the greatest decrease in fracture toughness occurs for the composite formed using

Cloisite 10A. A closer examination of the Cloisite 10A composite data reveals that after this initial severe decrease there is little change in the fracture toughness upon the addition of more clay. This behaviour differs slightly from that of the composites formed using either Cloisite 25A or Cloisite 30B as the organoclay. As with these composites the fracture toughness continues to decrease significantly with increasing clay content. The composites formed using Cloisite 93A as the organoclay can also be said to follow this trend of decreasing fracture toughness with increasing percentage clay loading only that the decrease in fracture toughness is not as rapid.

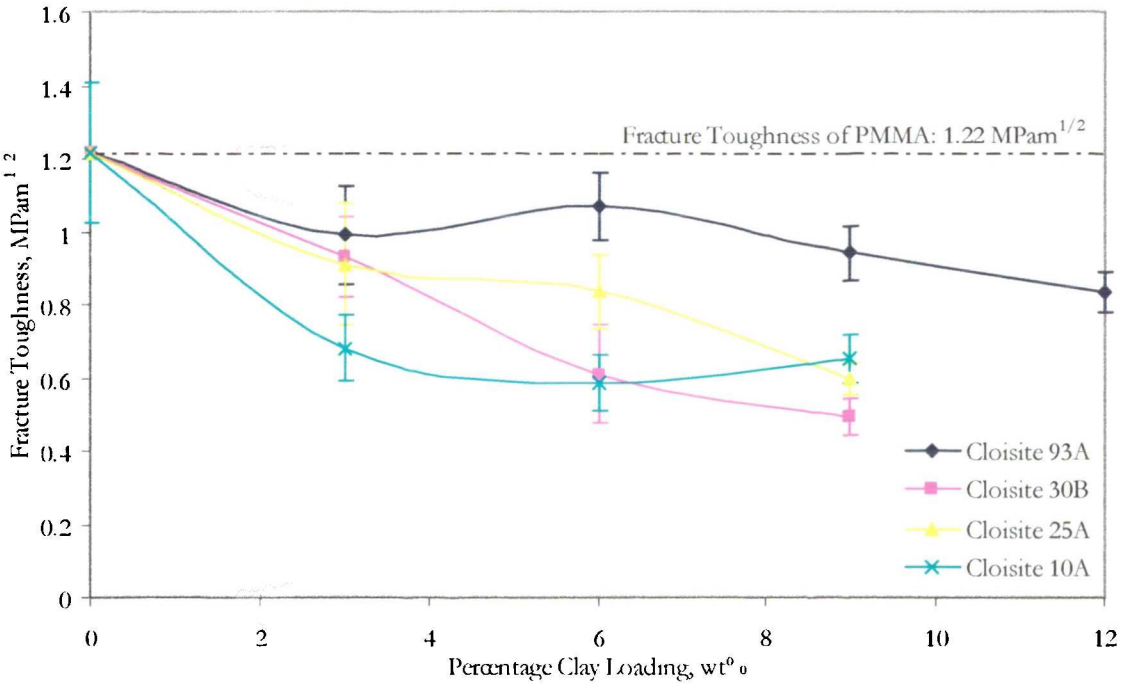


Figure 6.7: Fracture Toughness of PMMA and PMMA-clay Composites. (Error bars are ±1 standard deviation.)

Table 6.7: Fracture Data for PMMA and its Composites.

	PMMA	Cloisite 93A				Cloisite 30B			Cloisite 25A			Cloisite 10A		
		3%	6%	9%	12%	3%	6%	9%	3%	6%	9%	3%	6%	9%
Fracture Toughness, $MPam^{1/2}$	1.22	0.99	1.07	0.94	0.83	0.93	0.61	0.50	0.91	0.84	0.60	0.68	0.59	0.65
Fracture Energy, J/m^2	363.0	-	226.8	167.8	132.1	192.4	80.1	49.7	-	114.5	72.2	119.9	48.3	71.3
Young's Modulus, GPa	3.58	-	4.43	4.62	4.6	3.97	4.08	4.33	-	5.36	4.34	3.41	6.26	5.20

It is known from Chapter 4 that all these composites possess an intercalated nanocomposite microstructure. Thus it can be concluded from the definition of an intercalated nanocomposite that the clay particle platelets maintain their registry, but that the particles are now more expanded. Hence from the decrease in the fracture toughness of the composite compared to the pristine PMMA, it can be concluded that the particles act not to relieve constraint and help the matrix to yield, but as flaws in the matrix. The tensile strength data presented in section 6.1.1 confirms this as it too shows the composite performance decreasing compared to the pristine PMMA. From this data it is possible to conclude that the mechanisms governing fracture toughness occur on the macro/micro-scale rather than on the nano-scale.

Figure 6.8 presents the fracture energy, G_c, data calculated using equation 6.1. In this figure it can be seen that all the composites have fracture energies lower than that of the pristine PMMA and that the fracture energy of the Cloisite 93A composites does not decrease as rapidly as for the other organoclays used.

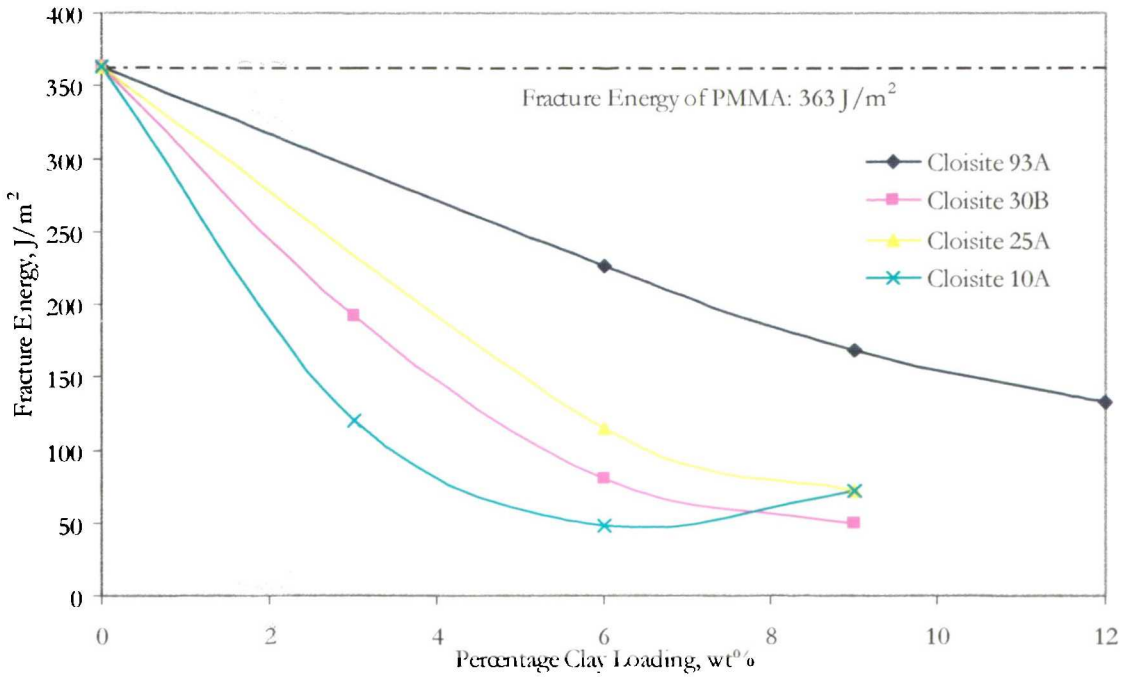


Figure 6.8. Fracture Energy of PMMA and PMMA clay Composites.

Toughening Mechanisms

Often through close examination of the fracture surfaces it is possible to determine the toughening mechanisms (in this case weakening mechanisms) that are in action. To this end a selection of composite and PMMA specimens had their fracture surfaces examined using a scanning electron microscope. The micrographs presented here are representative of a number of samples. It should be noted that PMMA decomposes rapidly under an electron beam, and hence focused, high magnification micrographs are difficult to achieve. The micrographs presented in Figures 6.9, 6.10 and 6.11 show the fracture surface of PMMA. As expected the fracture surface of PMMA is relatively smooth and glassy, with few features visible. This is typical of the fracture surfaces of crosslinked thermosets[101]. The features that can be seen on Figure 6.9 are termed river or feather markings[102] and are caused by the crack deviating slightly from its original path (level). In Figure 6.10 the river markings can be seen again as the crack deviates. These features are commonly observed for stick slip failure[102] and are caused by the crack forking. This process of forking is where the crack divides into two branches before one of the branches arrests. The process occurs due to an excess of energy available due to the stick/slip nature of crack propagation. Note that unless otherwise stated the direction of crack propagation is from the top to bottom of the micrograph.

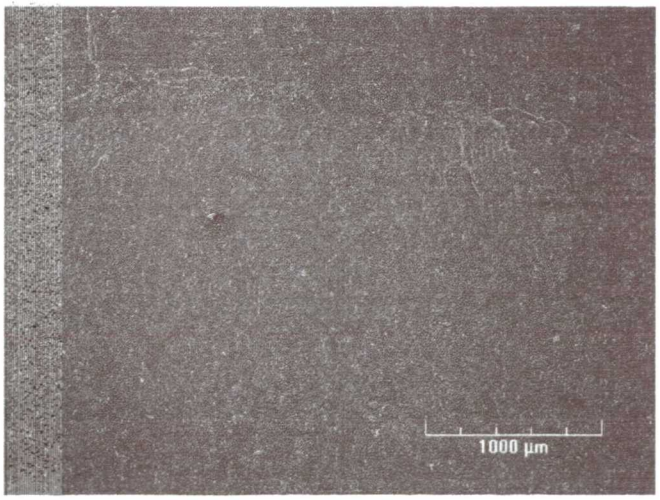


Figure 6.9: Micrograph of Fracture Surface of PMMA. (Note crack propagation is from top to bottom.)

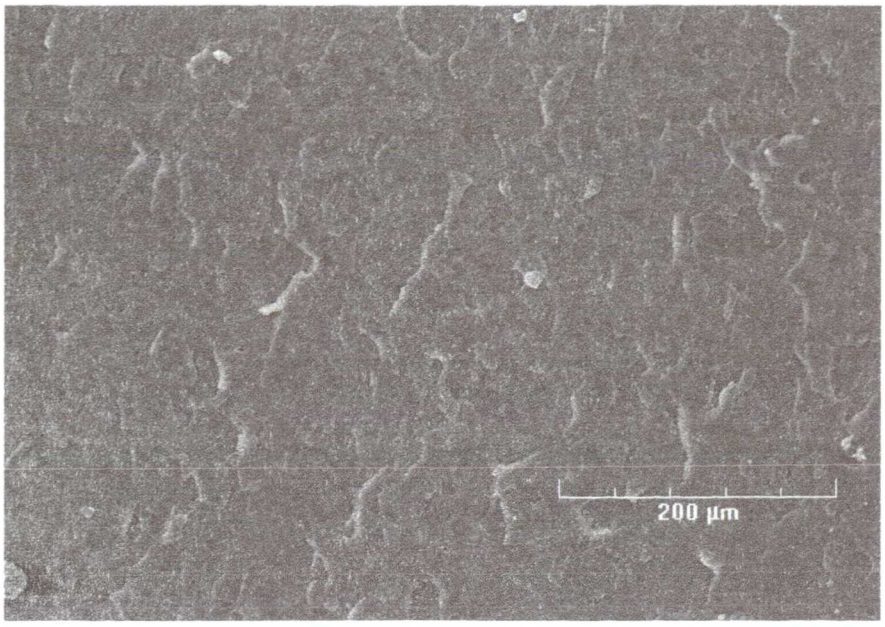


Figure 6.10: Micrograph of Fracture Surface of PMMA showing River Markings. (Note crack propagation is from top to bottom.)

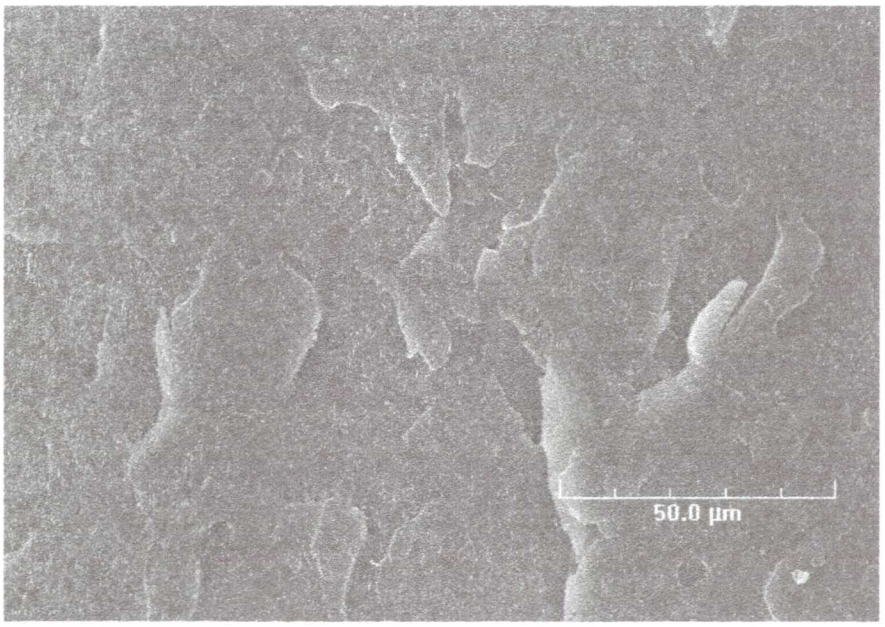


Figure 6.11: Micrograph of Fracture Surface of PMMA. (Note crack propagation is from top to bottom.)

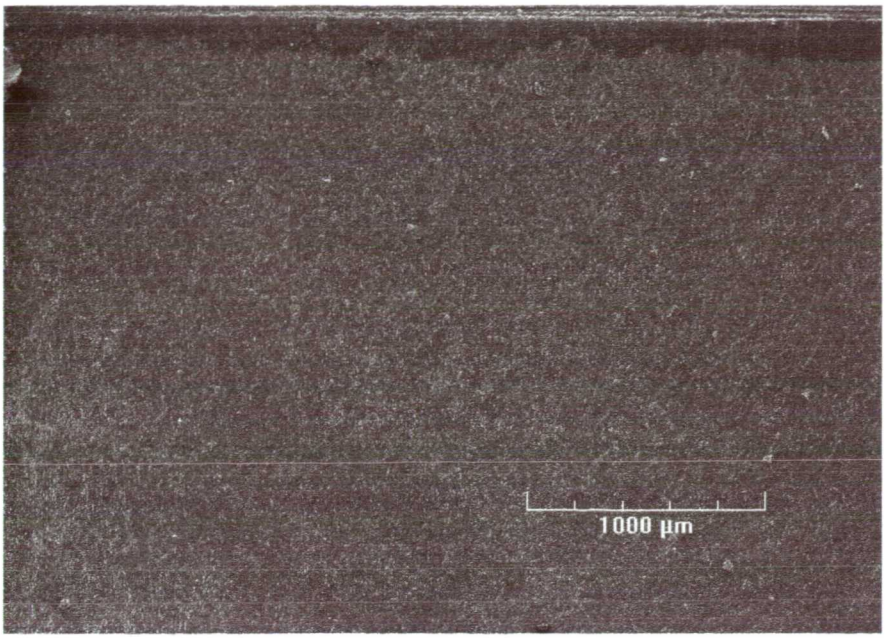


Figure 6.12: Micrograph of Fracture Surface of PMMA-6wt% Cloisite 25A Specimen.
(Note crack propagation is from top to bottom.)

Micrographs of the fracture surfaces of a PMMA-6wt% Cloisite 25A specimen are presented in Figures 6.12, 6.13 and 6.14. The micrographs featured in these figures are representative of all the fracture surfaces of the other composites, which are not shown here.

Even at low magnifications, see Figure 6.12, it is clear that the fracture surfaces of the composites are substantially rougher than those of the pristine polymer seen previously in Figures 6.9 to 6.11. The roughness seen in Figures 6.12, 6.13 and 6.14 would suggest that the fracture toughness of the composites should exceed that of the pristine polymer as additional energy will be dissipated due to the increased surface area and due to mode mixity of the crack propagation, as discussed in section 2.7.4. However, it can be postulated from Table 6.7 that this is not the case. It was observed during the tests that none of the specimens failed in a stable manner. The fracture surfaces of the composites suggest that had the failure been stable then the propagation values of

fracture toughness may have been greater than the initiation values of fracture toughness (i.e. those seen in Table 6.7).

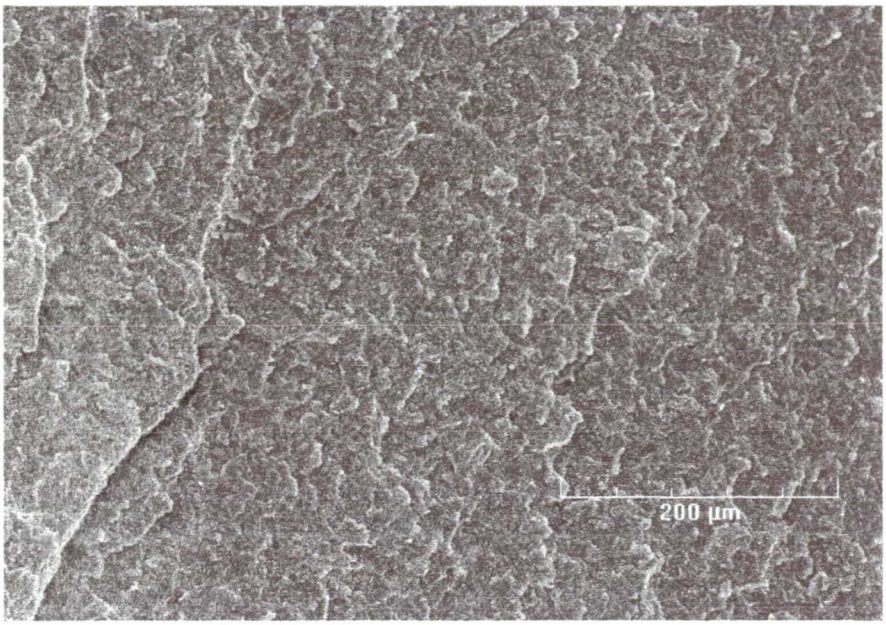


Figure 6.13: Micrograph of Fracture Surface of PMMA-6wt% Cloisite 25A Specimen.

(Note crack propagation is from top to bottom.)

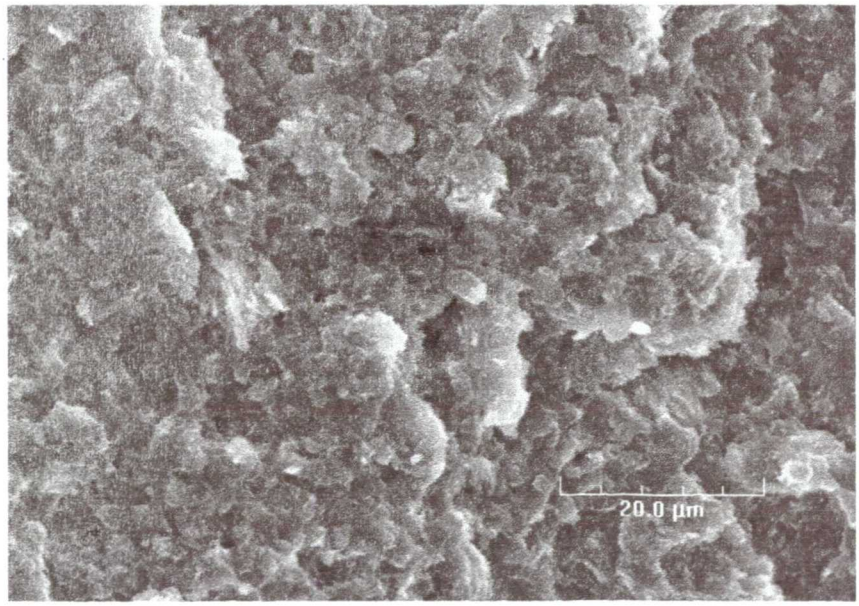


Figure 6.14: Micrograph of Fracture Surface of PMMA-6wt% Cloisite 25A Specimen.

(Note crack propagation is from top to bottom.)

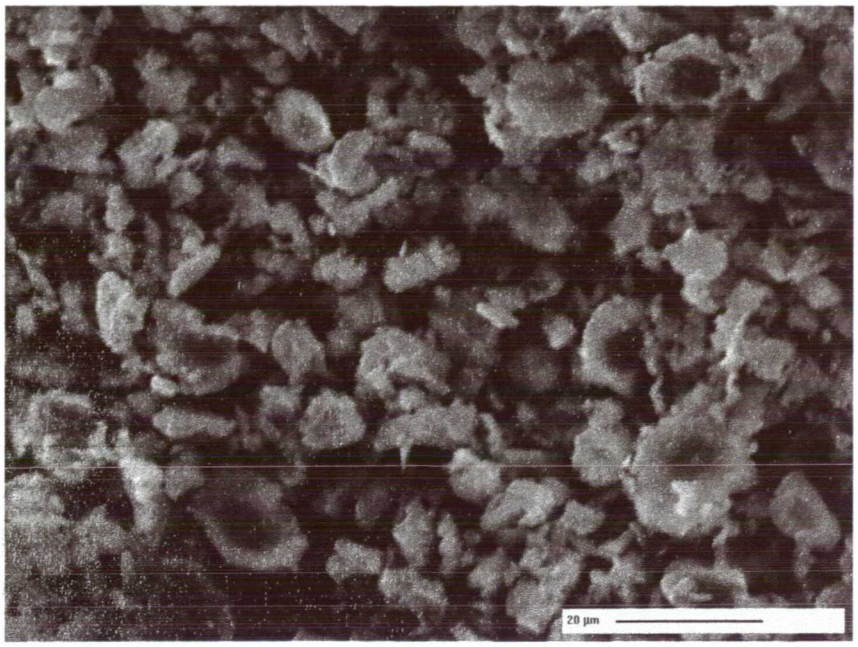


Figure 6.15: Micrograph of Cloisite 25A Particles Before Incorporation With PMMA.

For most particulate composites the particles are clearly visible in micrographs of the fracture surfaces[94, 101]. It can be seen by close examination and comparison of the micrograph of the fracture surface of a 6wt% Cloisite 25A composite, shown in Figure 6.14, with the micrograph in Figure 6.15, of Cloisite 25A before incorporation with PMMA, that the clay particles are difficult to identify in the fracture surface even at high magnification. It can be concluded that this is due to the intercalation of the clay in the polymer and the clay platelets' flexibility. Since in micrographs of other layered silicates composites that do not form intercalated microstructures with polymer, for example mica, the particles are clearly visible[94, 101] on the fracture surfaces as smooth flat platelets. In contrast, the platelets of the organoclay used in the present work will bend as shown in the transmission electron micrographs discussed in Chapter 4, and hence they are difficult to distinguish from the polymer matrix.

Previous work using mica in various thermoset matrices reported by Taylor and Kinloch[57], large increases in the measured toughness occurred due to debonding and plastic hole growth around the mica particles. These processes cannot be observed

here, although they would have been more obvious for stable failure rather than the stick-slip crack propagation that occurred in the present work.

Property Map

In most engineering applications the materials used are required to have a good property balance. One of the most critical property balances for all materials in determining their usage occurs between fracture toughness and Young's modulus. For example a material with a high Young's modulus but low fracture toughness finds few applications and vice versa. Figure 6.16 presents the property balance of fracture toughness and Young's modulus for PMMA and its composites. From Figure 6.16 it is clear to see that the Cloisite 93A composites have the best property balance between toughness and modulus. These data also show that the formation of nanocomposites using organoclay reduces fracture toughness but increases the modulus. However, the exact balance of properties is dependent on the organoclay used.

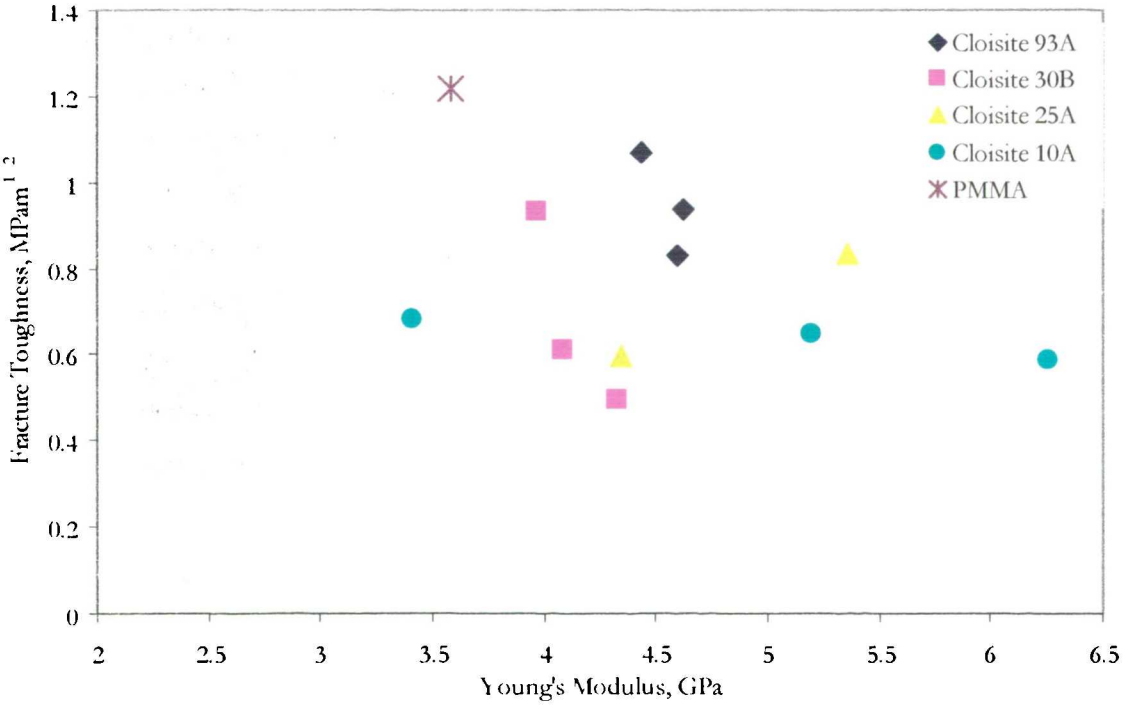


Figure 6.16: Property Map of Fracture Toughness versus Young's Modulus for PMMA and its Composites.

In conclusion it can be seen from the data presented here that the presence of an intercalated nanocomposite microstructure is detrimental to the fracture properties of PMMA, and that the presence of clay particles has no stabilising effect on the fracture of PMMA based composites.

6.2.2 Effect of Choice of Polymerisation Initiator

Fracture Toughness

The fracture data presented here probes the effects of microstructural changes brought about by the use of different polymerisation initiators on the fracture properties of the polymers and composites formed. Three polymerisation initiators, 2,2-azo-bis-isobutyronitrile (AIBN), lauroyl peroxide and trigonox 23, were used. Two organoclays, Cloisite 25A and Cloisite 93A, were used.

It has been seen from previously presented data that for the polymerisation initiators tried the microstructures formed all have been of the intercalated nanocomposite type. It was also seen that AIBN initiated composites possessed the smallest intergallery spacing and that the largest intergallery spacings were found in the lauroyl peroxide initiated Cloisite 93A composites.

The fracture toughness and fracture energy data of the various PMMAs and their composites are presented in Table 6.8(a) for the Cloisite 93A composites and in Table 6.8(b) for the Cloisite 25A composites. Also included in the tables are the Young's modulus data, used to calculate the fracture energy, and in italics the standard deviation of the fracture toughness. The fracture tests were carried in accordance with ISO13586[88] and at standard temperature and humidity.

Using these tables it can be seen that the pristine polymer initiated using AIBN has the largest value for fracture toughness and fracture energy. It is also clear that the general effect of adding clay into the systems is for the resulting composite to have reduced fracture toughness compared to the pristine polymer.

Table 6.8(a): Cloisite 93A, Fracture Data for PMMA and Composites.

	Fracture Toughness, $MPam^{1/2}$			Fracture Energy, J/m^2			Young's Modulus, GPa		
	AIBN	LP	Trig	AIBN	LP	Trig	AIBN	LP	Trig
Plain	1.22 *0.19*	1.16 *0.09*	0.89 *0.09*	363.0	302.8	147.1	3.58	3.9	4.68
3wt%	0.99 *0.14*	0.94 *0.04*	-	-	167.1	-	-	4.67	-
6wt%	1.07 *0.09*	0.94 *0.06*	0.92 *0.10*	226.8	177.8	163.0	4.43	4.34	4.58
9wt%	0.94 *0.07*	0.84 *0.06*	0.81 *0.05*	167.8	90.1	157.9	4.62	6.0	3.62

Table 6.8(b): Cloisite 25A, Fracture Data for PMMA and Composites.

	Fracture Toughness, $MPam^{1/2}$			Fracture Energy, J/m^2			Young's Modulus, GPa		
	AIBN	LP	Trig	AIBN	LP	Trig	AIBN	LP	Trig
Plain	1.22 *0.19*	1.16 *0.09*	0.89 *0.09*	363.0	302.8	147.1	3.58	3.9	4.68
3wt%	0.91 *0.17*	0.81 *0.07*	-	-	121.3	-	-	4.69	-
6wt%	0.84 *0.10*	0.71 *0.02*	0.77 *0.05*	114.5	119.1	95.5	5.36	3.66	5.40
9wt%	0.60 *0.04*	0.54 *0.04*	0.64 *0.04*	72.2	55.0	80.0	4.34	4.69	4.36

Comparing the Cloisite 93A composites (Table 6.8(a)) to the Cloisite 25A composites (Table 6.8(b)) several points can be made. Firstly, the use of Cloisite 25A as the organoclay is more detrimental to the resulting composites' fracture properties than the use of Cloisite 93A. Secondly, when Cloisite 25A is used the fracture toughness of the composites decreases with increasing percentage clay content. However when Cloisite 93A is used, after an initial decrease in fracture toughness upon the addition of the organoclay, the fracture toughness remains practically unchanged within experimental error as the percentage clay content is increased. This is particularly true for trigonox 23 Cloisite 93A composites. This is also reflected in these composites fracture energy values.

6.2.3 Effect of Core-Shell Addition

Fracture Toughness

The fracture properties, fracture toughness and fracture energy, of core-shell particle toughened PMMA-clay composites were investigated in order to establish two points. Firstly what effect the intercalated nanocomposites microstructure of the composites has on the fracture properties. Secondly to establish if there were any synergistic effects arising due to the interaction of the core-shell and clay particles. Compact tension experiments were conducted so as to investigate the fracture properties of the toughened PMMAs and their composites. The tests were conducted as detailed in section 3.2.4, in accordance with ISO13586[88] on a 5584 Instron testing machine at standard temperature and humidity. At least three specimens of each composite composition were tested and the fracture toughness recorded. The mean fracture toughness value for each composition was calculated from the experimental data. The mean fracture toughness and mean Young's modulus, found from previous tensile experiments, were used to calculated the fracture energy values. Table 6.9 presents the fracture toughness, fracture energy and Young's modulus of the toughened PMMA and of PMMA.

Table 6.9: Fracture Properties and Young's Moduli of PMMA and Core-Shell Toughened PMMA.

	Fracture Toughness, $MPam^{\frac{1}{2}}$	Fracture Energy, Jm^{2}	Young's Modulus, GPa
PMMA	1.22	363.1	3.58
PMMA-5% KM355	2.64	2444	2.51
PMMA-5% XC42	2.37	1480	3.32
PMMA-5% XC44	2.18	1298	3.22

It can be concluded from Table 6.9 that as expected that, compared to the pristine PMMA, the fracture toughness and fracture energy have significantly increased. This is to be expected since the addition of core-shell particles increases the amount of yielding possible for the polymer by firstly reducing the Young's modulus of the system and secondly making previously unavailable mechanisms such as particle debonding and

hole growth available to the polymer. The toughened PMMA with the highest fracture toughness is that formed using KM355 as the toughening agent. This toughened PMMA also has the lowest Young's modulus. This combination, high fracture toughness and low Young's modulus, leads to the comparatively very high fracture energy. From examination of scanning electron micrographs of the fracture surfaces of this toughened PMMA evidence of phase separation can be seen, Figure 6.17. It is suggested that part of the decrease in Young's modulus and increase in fracture toughness are caused by the phase separation seen in this toughened PMMA.

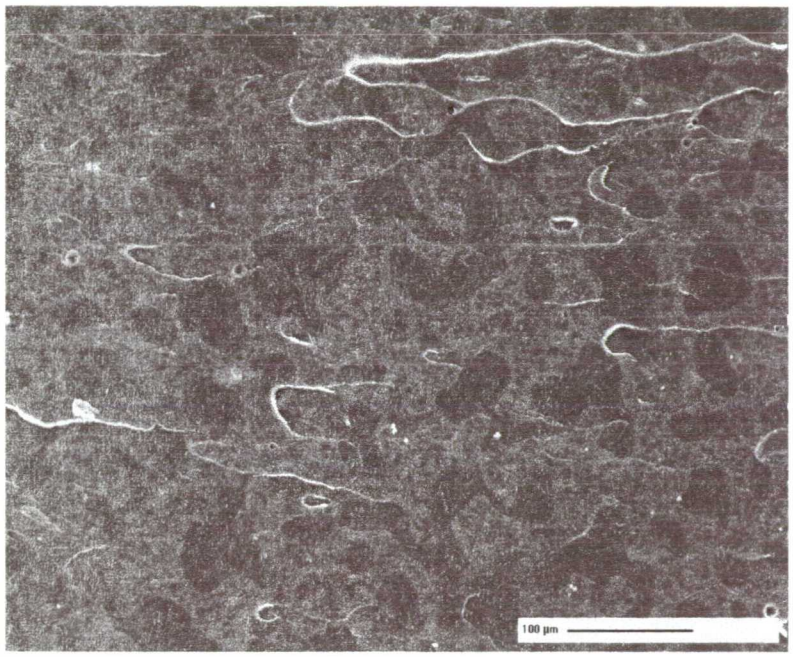


Figure 6.17: Scanning Electron Micrograph of the Fracture Surface of KM355 Toughened PMMA. (Note crack propagation is from left to right.)

The toughened PMMA-clay composites were fabricated using 5wt% core shell particles and 6wt% Cloisite 25A. All were found to have intercalated nanocomposite microstructures. The fracture properties and Young's modulus of the toughened PMMAs and their composites are tabulated in Table 6.10 along with the data for PMMA and its 6wt% Cloisite 25A composite.

Table 6.10: Fracture Properties and Young's Moduli of PMMA, Core-Shell Toughened PMMA and their 6wt% Cloisite 25A Composites.

	PMMA		PMMA-KM355		PMMA-XC42		PMMA-XC44	
	Plain	6%25A	Plain	6%25A	Plain	6%25A	Plain	6%25A
Fracture Toughness, $MPam^{1/2}$	1.22	0.84	2.64	0.91	2.37	0.53	2.18	0.73
Fracture Energy, Jm^{-2}	363.1	114.5	2444.0	199.9	1479.6	81.2	1298.1	225.4
Young's Modulus, GPa	3.58	5.36	2.51	3.67	3.32	3.04	3.22	3.36

From Table 6.10 it is apparent that the addition of clay to the toughened system is very detrimental to the fracture properties of the composites formed. This behaviour is similar to that for the untoughened system but is more pronounced, for example there is a 65% to 80% reduction in fracture toughness for the toughened system, compared with a 30% reduction (from 1.22 to 0.84 $MPam^{1/2}$) for the untoughened system. From this evidence it must be concluded that no synergistic effects are occurring between the core-shell particles and the clay. The fracture energy of the toughened composites also can be seen to decrease dramatically. This dramatic decrease, between 82% and 94% of the pristine toughened values, can be accounted for by the behaviour of both the Young's modulus, which increases, and the fracture toughness, which decreases.

From the evidence presented here it can be concluded that the clay particles act as flaws and so do not help increase the fracture performance of either the untoughened or toughened matrices.

Toughening Mechanisms

A selection of the fractured specimens were examined using a scanning electron microscope in order to determine what toughening mechanisms are in action. It should be noted that PMMA degrades rapidly under an electron beam, see Figure 6.18, thus preventing the examination of the fracture surfaces at very high magnifications.

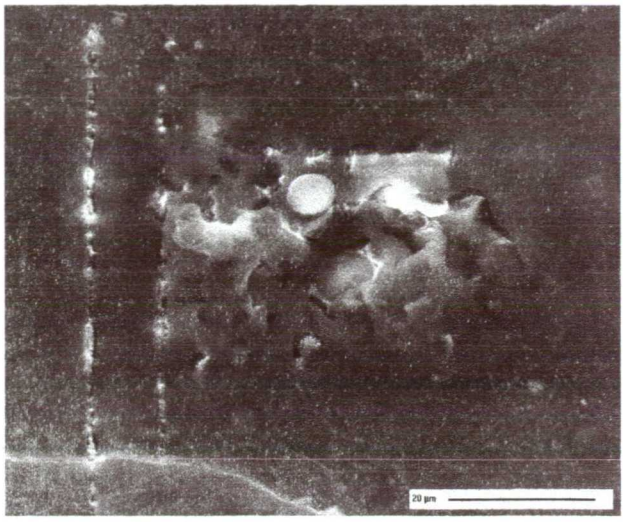


Figure 6.18: Scanning Electron Micrograph Demonstrating Electron Beam Damage.

The micrographs presented in Figures 6.19, 6.20 and 6.21 show the fracture surfaces of PMMA-5wt% XC42, PMMA-5wt% XC44 and PMMA-5wt% KM355 respectively. Figure 6.22 presenting a micrograph of the fracture surface of a PMMA specimen has also been included for comparison purposes.

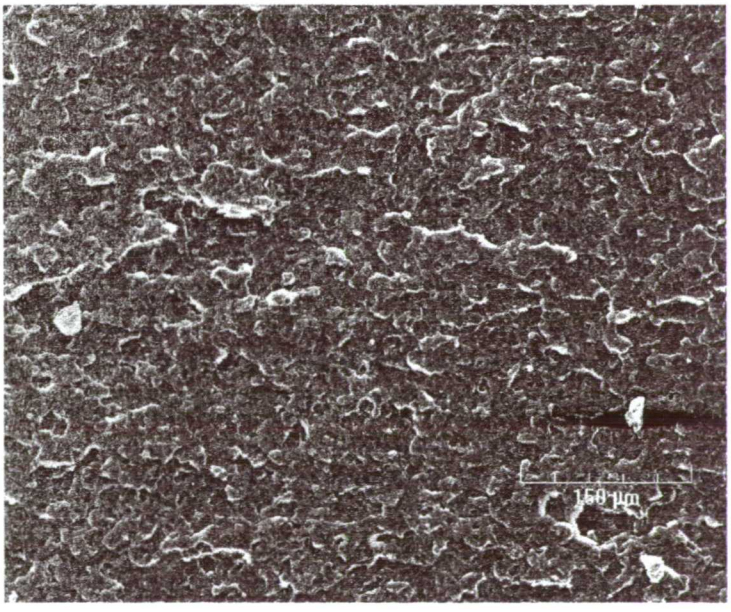


Figure 6.19: Scanning Electron Micrograph of the Fracture Surface of 5wt% XC42 Toughened PMMA. (Note crack propagation is from left to right.)

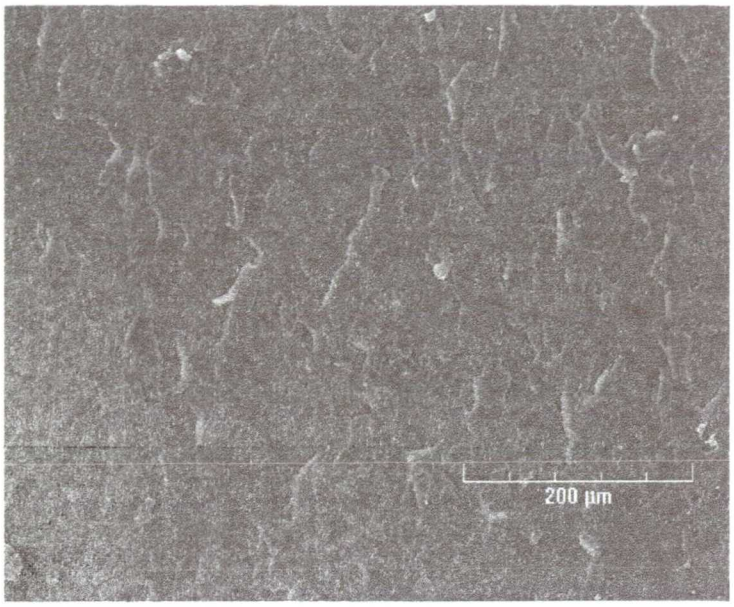


Figure 6.22: Scanning Electron Micrograph of the Fracture Surface of PMMA.

From the figures it can be seen that the fracture surfaces of PMMA-XC42, Figure 6.19, and PMMA-XC44, Figure 6.20, are very similar. It can be seen by comparison to Figure 6.22 that the surfaces are extremely rough compared to those of pristine PMMA. This surface roughness indicates that the propagating crack has had to alter its path frequently thus mixed mode fracture would have occurred increasing the energy required to cause the material to fracture. This is reflected in the increase that both materials show in fracture toughness and energy. It should be noted that due to the extent of the surface roughness in both these samples core-shell particles were difficult to find. Also, as shown in Figure 6.18, it was difficult to obtain good images of the particles due to the problems of polymer degradation when exposed to the electron beam.

In comparison to the fracture surfaces of PMMA-XC42 and PMMA-XC44 the fracture surfaces of PMMA-KM355 are relatively smooth and similar to those of PMMA (Figure 6.22). By closer examination of the fracture surfaces of PMMA-KM355 it is apparent that there are holes in the surface. Figure 6.23 presents two further micrographs of the fracture surfaces of PMMA-KM355.

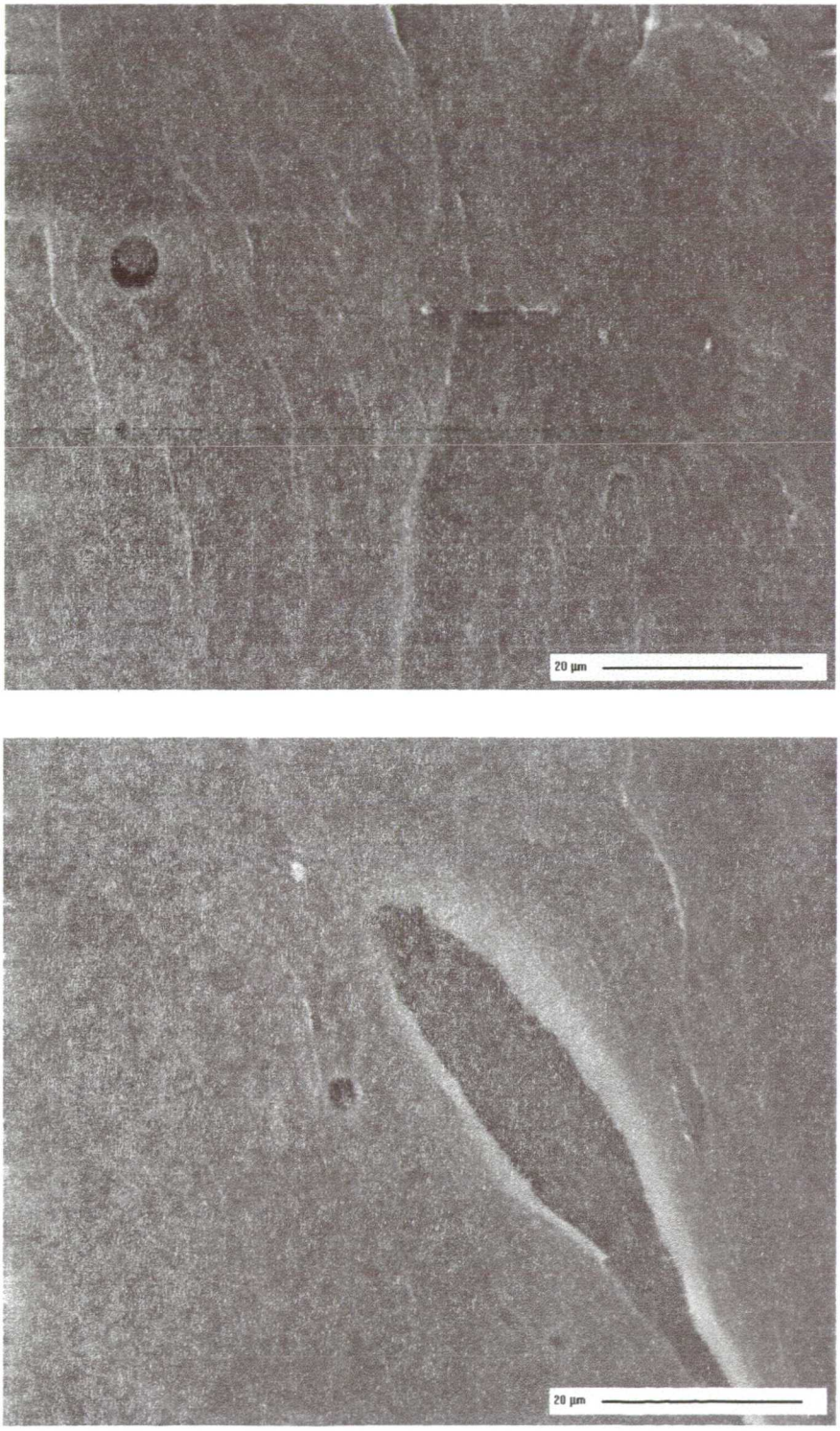


Figure 6.23: Scanning Electron Micrographs of the Fracture Surface of 5wt% KM355 Toughened PMMA.

In these micrographs it is clear to see that the holes are from debonded core-shell particles and it is also possible to see some hole growth about a core-shell particle. The processes of particle debonding and hole growth are mechanisms which can relieve the tri-axial stress state at the tip of the crack and instigate yielding in the area surrounding the crack front, thus causing the fracture toughness and energy to increase [82, 101]. It should also be noted that phase-separation, which can be seen in the fracture surfaces of PMMA-KM355 specimens, could play a part in increasing the fracture toughness and energy of the PMMA-KM355 specimens.

Figures 6.24, 6.25 and 6.26 present micrographs of the fracture surfaces of PMMA-XC42 6wt% Cloisite 25A, PMMA-XC44 6wt% Cloisite 25A and PMMA-KM355 6wt% Cloisite 25A respectively. A micrograph of the fracture surfaces of PMMA-6wt% Cloisite 25A included for comparison in Figure 6.27. Note that unless otherwise stated the direction of crack propagation is from the top to bottom of the micrograph.

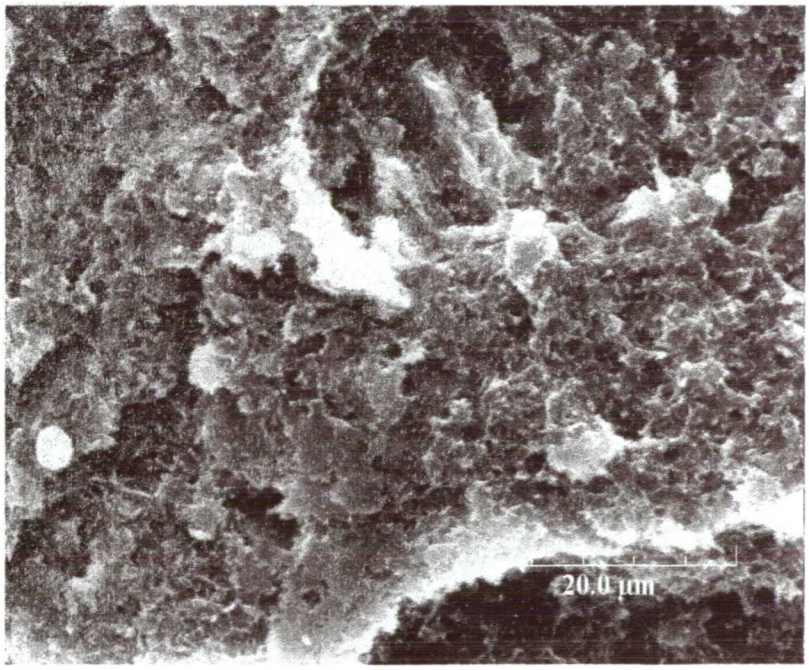


Figure 6.24: Scanning Electron Micrograph of the Fracture Surface of 5wt% XC42 Toughened PMMA-6wt% Cloisite 25A Composite.

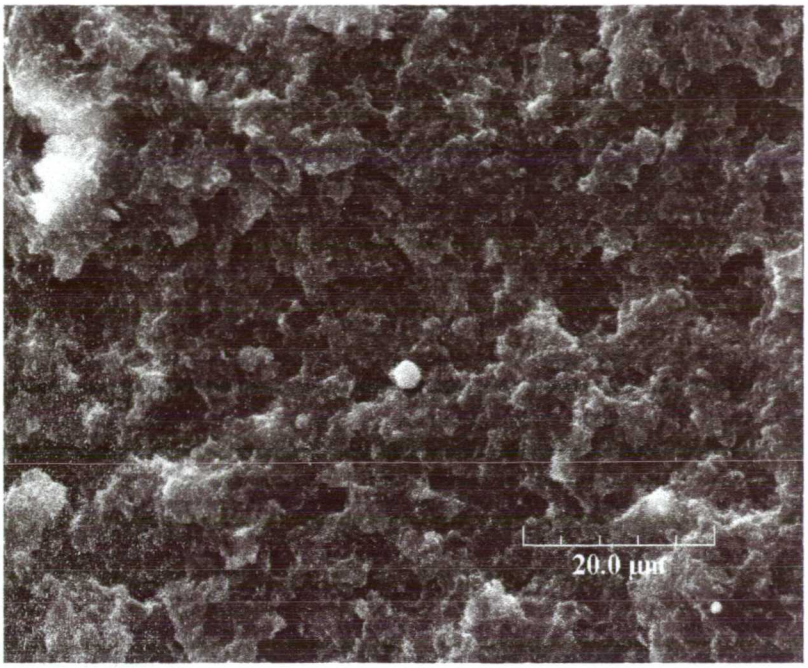


Figure 6.25: Scanning Electron Micrograph of the Fracture Surface of 5wt% XC44 Toughened PMMA-6wt% Cloisite 25A Composite.

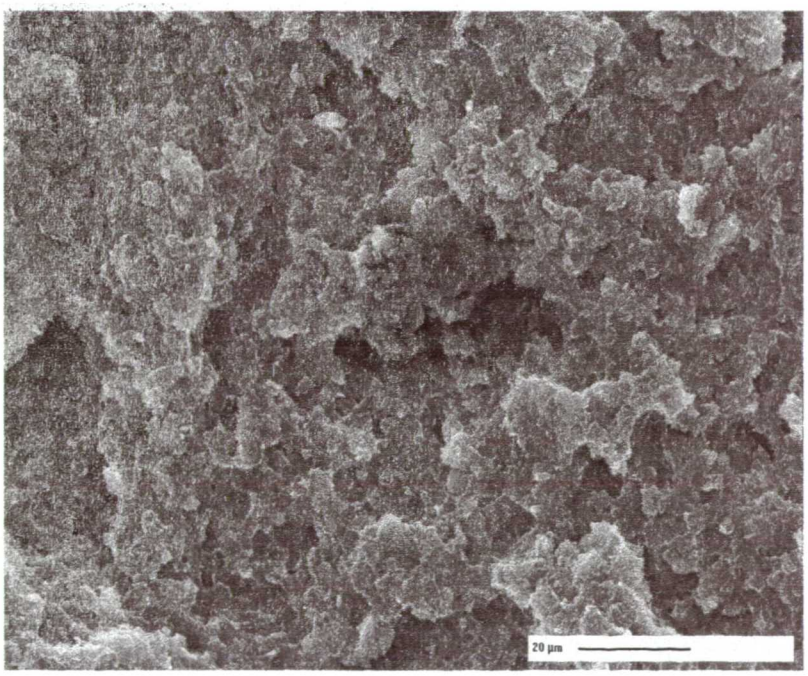


Figure 6.26: Scanning Electron Micrograph of the Fracture Surface of 5wt% KM355 Toughened PMMA-6wt% Cloisite 25A Composite.

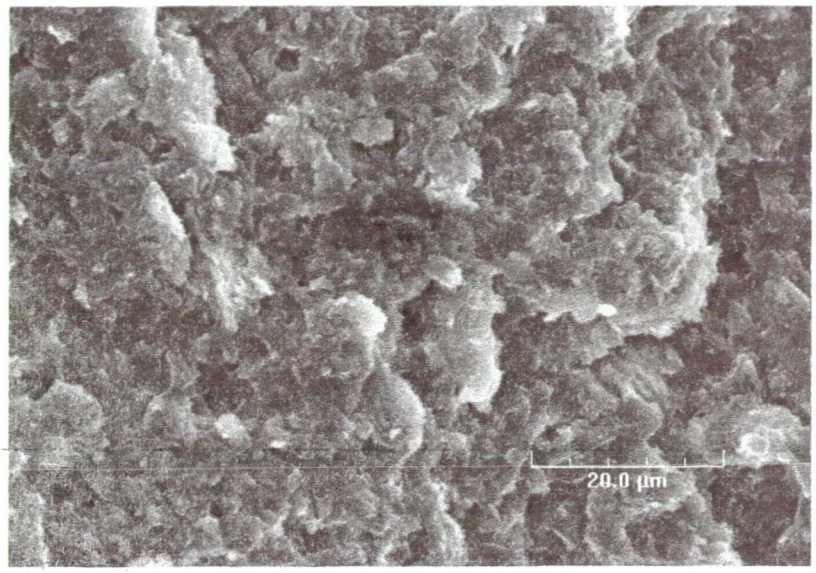


Figure 6.27: Scanning Electron Micrograph of the Fracture Surface of PMMA-6wt% Cloisite 25A Composite.

Firstly it can be seen that now all the fracture surfaces show considerable roughness indicating that the crack has travelled a tortuous route. Secondly, comparing Figures 6.21, 6.23 and 6.26 significant changes can be seen between the fracture surfaces of PMMA-KM355 with and without clay. Firstly there is a dramatic increase in surface roughness in the clay system compared to the pristine system. And secondly in the clay system there is no visible evidence of the phase separation seen in the pristine system. The absence of the phase separation in the clay system would partly explain some of the dramatic property changes seen with this system compared to the pristine KM355 system.

It can also been seen by comparison of Figure 6.28 (that presents a micrograph of the fracture surfaces of PMMA-5wt% XC42) to Figure 6.24 that the fracture surfaces of PMMA-XC42 6wt% Cloisite 25A are rougher than the pristine PMMA-XC42 fracture surfaces. This is also true for the XC44 system. This evidence would indicate that the toughened PMMA clay composites should have a higher value for fracture toughness than the pristine composite since the crack has apparently undergone mixed mode fracture. However, from the data presented earlier in Table 6.10 it is known that the

fracture toughness and energy of the composites reduces. From this it can be concluded that although at times the roughness of fracture surfaces can indicate high or low fracture toughness values, for these toughened PMMA-clay composites the fracture surface roughness is misleading.

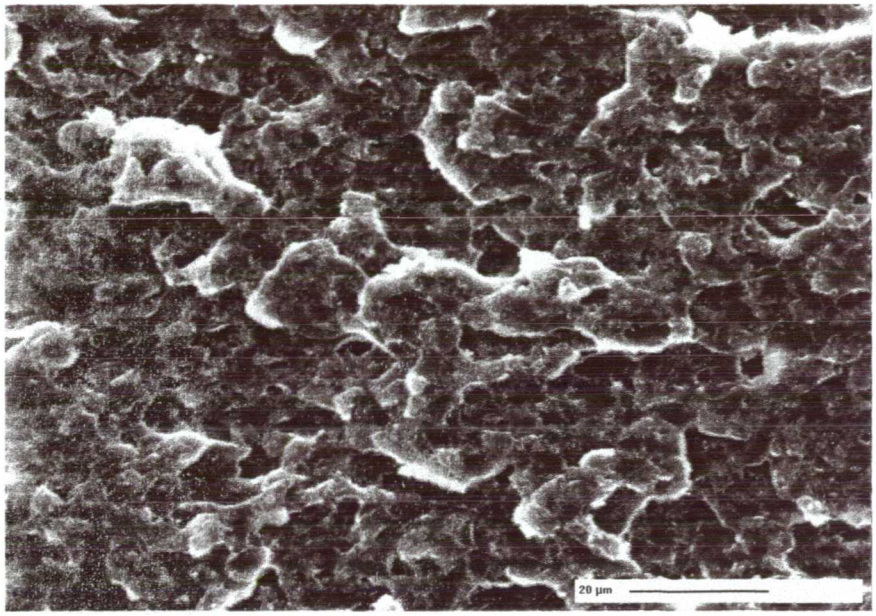


Figure 6.28: Scanning Electron Micrograph of the Fracture Surface of 5wt% XC42 Toughened PMMA. (Note crack propagation is from left to right.)

The micrographs presented here would suggest that the fracture properties of the composites would increase. This however is not the case. From this it can be concluded that the clay particles do act as flaws. These flaws (clay particles) then lead to premature failure of the specimens. It can also be seen that the presence of the clay particles reduces the effectiveness of the toughening mechanisms activated by the presence of the core-shell particles.

6.3 Comparison of Experimental Data to Theoretical Predictions

6.3.1 Introduction

Over the years many models have been developed to predict certain properties of particulate and fibre composites. In this section the experimental results for Young's modulus, tensile strength and fracture energy will be compared to various theoretical models to determine which, if any, of the currently developed models are applicable to particulate polymer composites that possess nanocomposite microstructures.

6.3.2 Young's Modulus

There are several theoretical models that can be used to predict the Young's modulus of a polymer composite. However, the theoretical models used here are "the rule of mixtures", "the Halpin-Tsai model" and "the Mori-Tanaka model". All these models assume that perfect bonding exists between the polymer matrix and the particles; that the particles are homogenously distributed in the polymer matrix; and that the Young's modulus of the surfactant is the same as that of the polymer matrix (thus the volume fraction of the clay is the volume fraction of the organoclay minus the volume fraction of the surfactant). Further details on these three models can be found in Section 2.7. The values taken for the matrix Young's modulus, E_m, of 3.58 GPa was that found from the tensile tests. The clay's Young's Modulus was taken to be that of montmorillonite (MMT), 172 GPa[94], since all the organoclays used in this work have been surface modified montmorillonites. The Poisson's ratio for the matrix was taken as 0.35 and for the clay as 0.25[94]. The value taken for the aspect ratio of the clay particles was 15. This is slightly larger than that found from transmission electron micrographs, shown in Chapter 4, however it has been frequently used in the literature. The Halpin-Tsai model used both the shape factor recommended by Halpin-Tsai (ζ=2w/t) and the shape factor recommended by van Es (ζ=2w/3t). The percentage weight of organoclay was converted to the percentage volume of montmorillonite using equation 6.2. Note that the density of the surfactant was assumed to be comparable to

that of the polymer and that the density of montmorillonite was taken from reference 91.

$$Volume\ MMT,\ \% = \frac{\%wt\ MMT \Big/ Density\ MMT}{\left(\%wt\ MMT \Big/ Density\ MMT\right) + \left(\%wt\ Polymer \Big/ Density\ Polymer\right)} \times 100$$

...Equation 6.2

Figure 6.29 presents the predicted relative modulus for the composites using the rule of mixtures, the Halpin-Tsai model, the van Es modified Halpin-Tsai model and the Mori-Tanaka model. Figure 6.29 also presents the normalised Young's modulus experimental data as well.

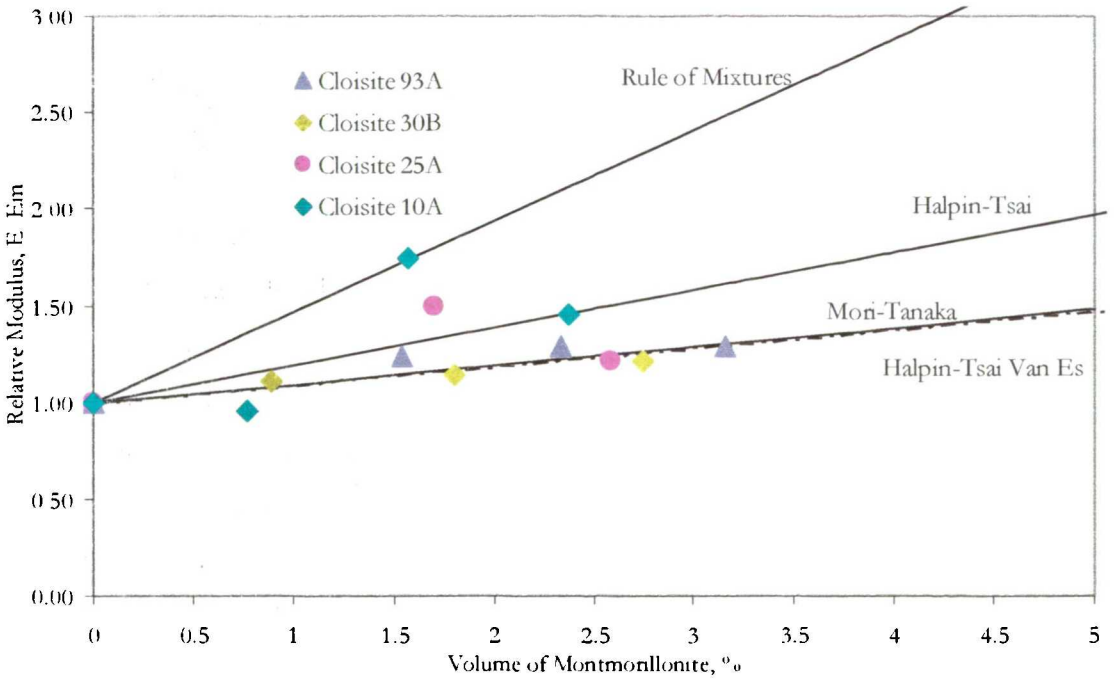


Figure 6.29: Experimental and Predicted Variation in Relative Modulus with Volume of Montmorillonite. (Models used: rule of mixtures, the Halpin-Tsai model, the van Es Modified Halpin-Tsai model and the Mori-Tanaka model.)

It can be seen that the values of relative modulus for both the van Es modified Halpin-Tsai model and the Mori-Tanaka model coincide, thus for clarity Figure 6.30, which

does not include the predicted relative moduli for the Mori-Tanaka model, has been included.

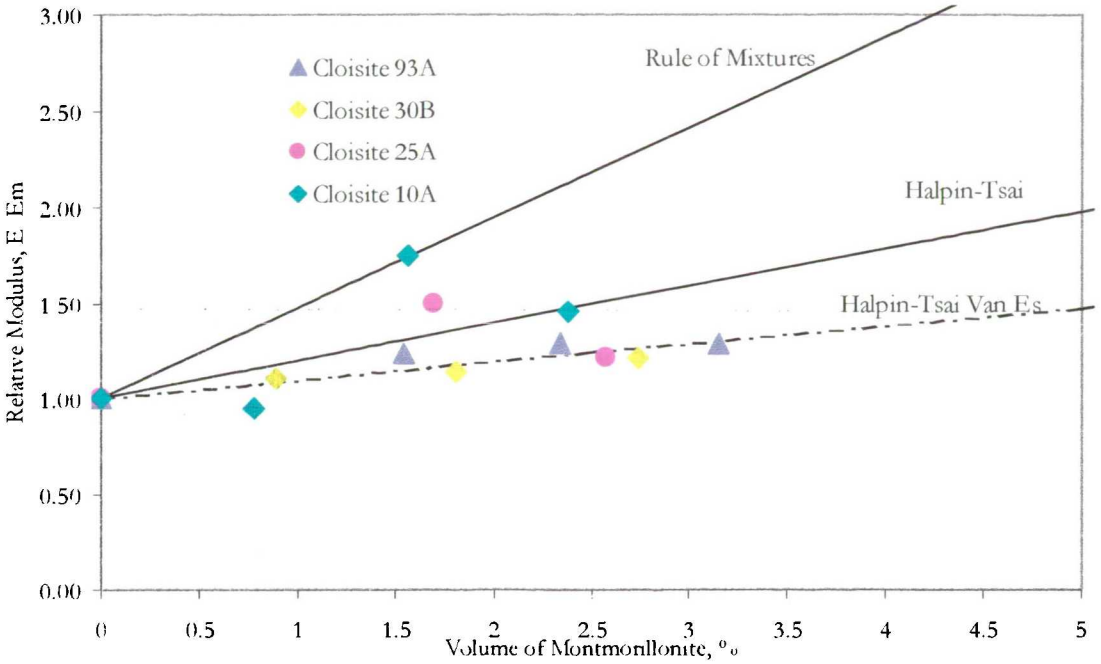


Figure 6.30: Experimental and Predicted Variation in Relative Modulus with Volume of Montmorillonite. (Models used: rule of mixtures, the Halpin-Tsai model, the van Es modified Halpin-Tsai model.)

From these figures it can be seen that most of the experimental data falls between the relative moduli predicted by the Halpin-Tsai and the Mori-Tanaka/van Es modified Halpin-Tsai models, and that the rule of mixtures over predicts the values of relative modulus. It is not unexpected that the Halpin-Tsai and Mori-Tanaka models predict the relative moduli of the composites more accurately than the rule of mixtures since these models take into account the shape of the filler particles by the inclusion of aspect ratio. From the figures it can be seen that most of the experimental data falls on or very near the Mori-Tanaka and the van Es modified Halpin-Tsai lines this is due to the models ability to describe the shape of the particles more accurately. Thus from the available data it can be concluded that either the van Es modified Halpin-Tsai model or the Mori-Tanaka model can be used with some confidence to predict the moduli of polymer-clay composites that possess an intercalated nanocomposite microstructure.

6.3.3 Tensile Strength

Again many models, the Sahu-Broutman model, the power law and the Leidner-Woodman model[103] to name but a few, have been developed to predict the tensile strength of particulate composites. Ahmed and Jones[103] conducted a review of several theoretical models for predicting the tensile strength of particulate composites. Figure 6.31 taken from the Ahmed and Jones review shows the relative tensile strength predictions from linear and power laws. From this figure it can be seen that the models predict that the relative tensile strength of the particulate composites will decrease with increasing filler volume fraction.

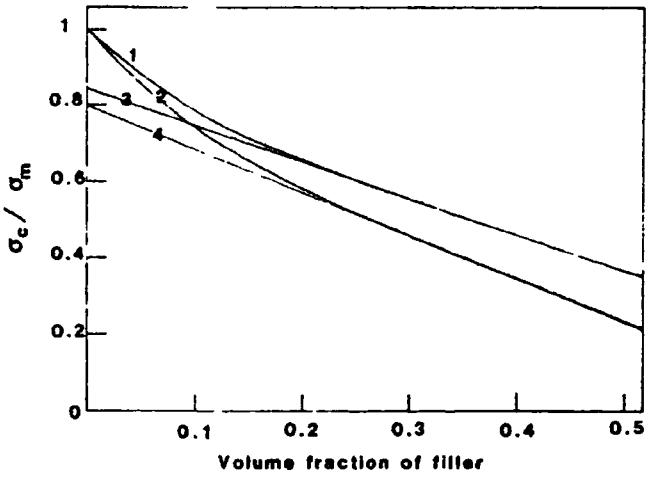


Figure 6.31: Comparison of Relative Strength Predicted from Linear and Power Laws[103]. (Curve 1 shows the Neilsen equation. Curve 2 is from the Nicolais and Narkis equation. Curves 3 and 4 are from the Piggott equation)

Figure 6.32 shows the normalised tensile strength data for the composites studied here. Comparing Figure 6.31 and 6.32 it can be concluded that the experimental data on tensile strength shows the tensile strength decreasing more rapidly with increasing clay content than that predicted by the models. Tensile strength is very dependant on the presence of surface flaws, it can be concluded from these results that the clay acts as sharp flaws and hence there is a rapid decrease in tensile strength.

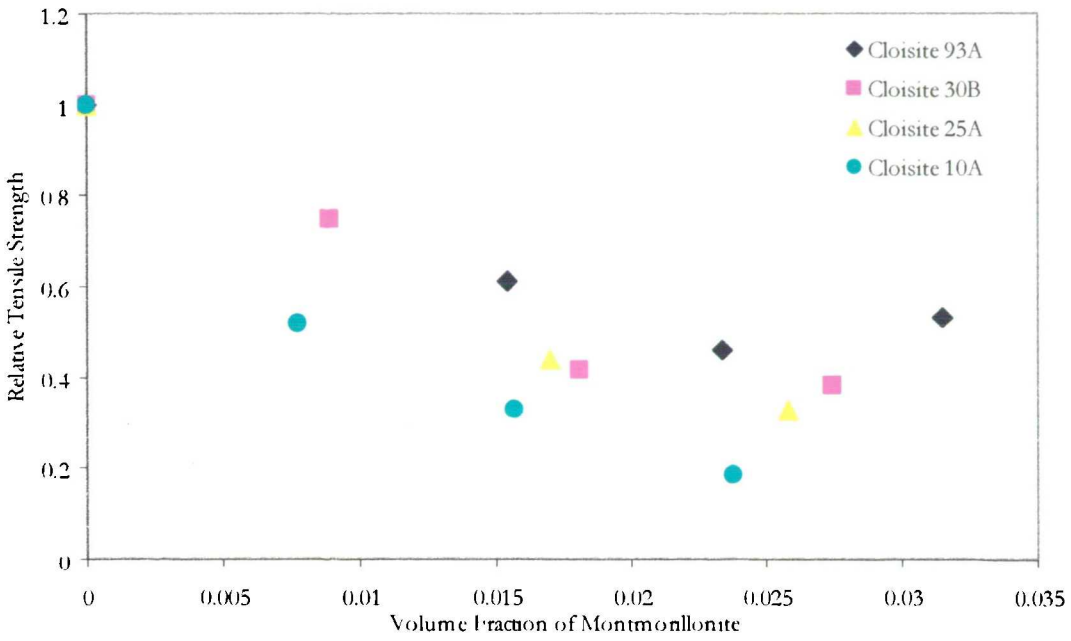


Figure 6.32: Variation of Relative Tensile Strength with Volume Fraction of Montmorillonite for PMMA-Organoclay Composites. (Data points have been normalised.)

6.3.4 Fracture Energy

The fracture energy of a composite is an important property since it determines the energy required to cause fracture in the presence of flaws. The theoretical model used here is based on the fracture mechanics and was developed by Faber and Evans[77]. The model they developed was a crack deflection model. For further details on the model see section 2.7.4. Figure 6.33 shows the Faber and Evans predictions for relative fracture energy for two different aspect ratio particles. It is clear from thus figure that the model predicts an increase in relative fracture energy on the addition of and increasing content of particles due to the crack deflection inducing mixed mode crack propagation.

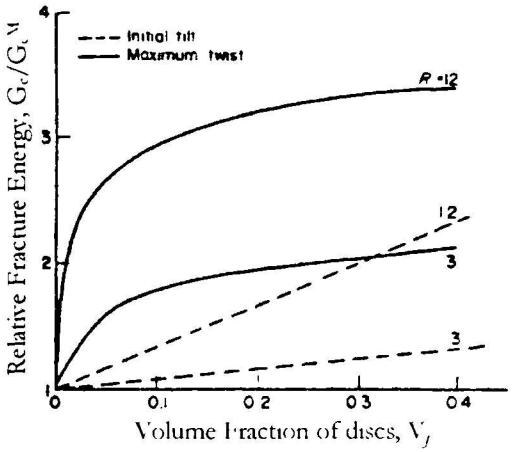


Figure 6.33: Relative Fracture Energy Predictions for Initial Tilt and for Maximum Twist based on Crack Deflection Model for Disc-shaped Particles of Two Aspect Ratios (R)[7].

Figure 6.34 presents the Faber and Evans predictions for relative fracture energy for two aspect ratios particles and the normalised experimental data for fracture energy of the composites formed.

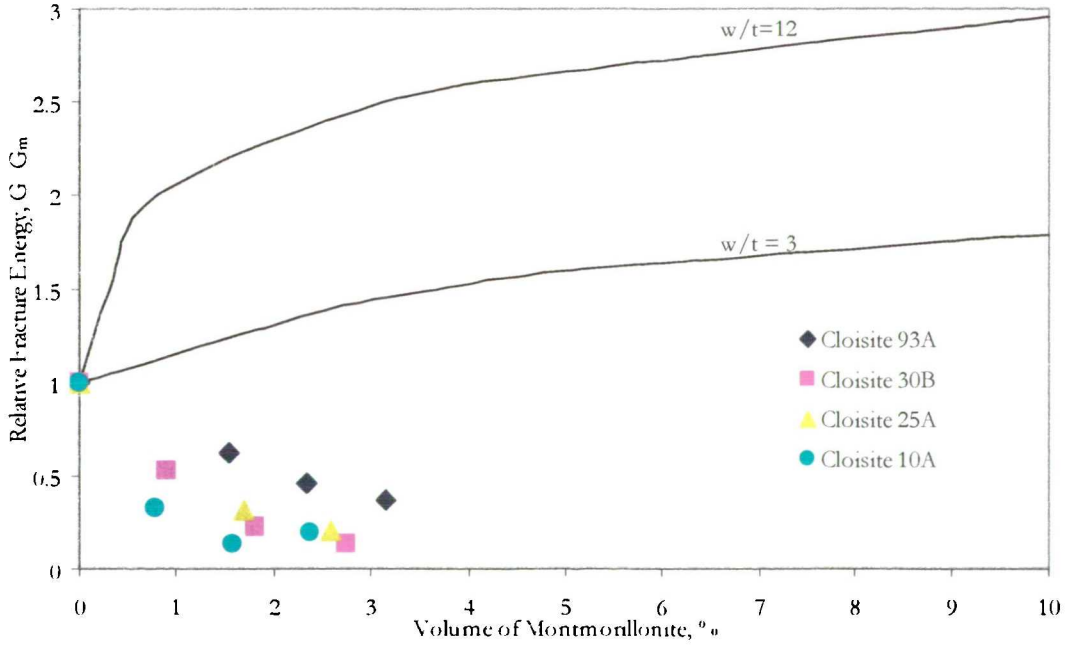


Figure 6.34: Experimental and Predicted Variation in Relative Fracture Energy with Volume of Montmorillonite. (Predicted data calculated using particle aspect ratios of 3 and 12.)

It is quite clear that the Faber and Evans model cannot be used to predict the relative fracture energy of the polymer-clay composites formed since the predictions show the fracture energy of the composite increasing whilst the experimental data decreases. The decrease seen in fracture energy has been shown in section 6.2.1 to be caused by the clay acting as sharp flaws negating any toughening effect that could the induce by increased surface roughness seen in the micrographs of the composites fracture surfaces.

6.4 Concluding Remarks

In summary, several conclusions can be drawn for the data presented in this chapter. From the tensile data presented it can be concluded that the addition of clay has increased the Young's modulus and decreased the tensile strength of the composites compared to the pristine polymer. It was also concluded that as the composites clay content increased, and the proportion of clay platelets at the maximum gallery spacing decreased, the rate of increase in Young's modulus decreased. The effect of increasing the clay content on the tensile strength was to cause it to decrease more rapidly.

The fracture toughness and fracture energy data presented here revealed that the addition of clay to the matrix caused a severe decrease in both these properties. This decrease also occurred in the fracture toughness and fracture energy of the core-shell toughened composites. However, when the fracture surfaces of the composites were examined they showed considerable roughness when compared to the fracture surfaces of the polymer, indicating that crack propagation proceeded along a tortuous path. However the extra energy required for this was not reflected in the values found for fracture energy. This led to the conclusion that the clay particles were not relieving the triaxial stresses, which would encourage the matrix to yield, but were present as sharp flaws in the matrix. From the fracture data for the toughened composites it was concluded that no synergist effects were occurring between the core-shell particles and the clay particles.

The tensile and fracture data were compared to data obtained from several theoretical models. For the Young's modulus good agreement existed between the experimental data and that calculated using either the van Es modified Halpin-Tsai or the Mori-Tanaka models. The fracture energy data obtained using the Faber and Evans model for crack deflection showed no agreement with the experimental fracture energy data.

The major findings of this study into the synthesis and structure-property relationships of thermoset acrylic-layered silicate nanocomposites are summarised in the next chapter, Chapter 7.

Chapter 7

Conclusions

In this penultimate chapter the main findings presented in this study will be summarised. This study has investigated the synthesis and structure-property relationships of thermoset PMMA-organoclay nanocomposites. The nanocomposites were fabricated using the in-situ intercalative polymerisation technique where the clay galleries are swollen with the monomers which are then subsequently polymerised. The formulation of the PMMA used was based on that of an acrylic adhesive and was lightly crosslinked. The organoclays used were commercially available and were all forms of surface modified montmorillonite. Nanocomposites were also fabricated using a core-shell toughened form of the PMMA used.

The microstructure of the composites formed was characterised using X-ray diffraction and transmission electron microscopy. The physical properties of the composites investigated were the glass transition temperature, storage modulus (a viscoelastic property), and the thermal stability. Dynamic mechanical thermal analysis was used to investigate both the glass transition temperature and the storage modulus whilst the thermal stability of the composites was investigated using thermogravimetric analysis. Tensile and fracture testing was used to assess the mechanical properties of Young's modulus, tensile strength, fracture toughness and fracture energy of the composites.

The microstructure results presented in Chapter 4 revealed that all of the composites formed possessed X-ray diffraction patterns that show their microstructure to be that of an intercalated nanocomposite, i.e. several strands of polymer chain were inserted between the clay platelets. This conclusion was confirmed by transmission electron micrographs of the composites. The X-ray diffraction results presented indicated for the polymer system used with these organoclays that each organoclay had a maximum spacing to which the clay platelet galleries would expand. It was found by increasing the clay loading that the proportion of clay platelets achieving the maximum spacing decreased. From the studies conducted varying the organoclays surfactant and varying the polymerisation initiator it was concluded, that given the right combination of surfactant and polymerisation initiator, then composites with microstructures other than that of an intercalated nanocomposite could be formed.

The dynamic mechanical thermal analysis results presented in Chapter 5 showed the effect of the formation of an intercalated nanocomposite microstructure on both the glass transition temperature, T_g, and the storage modulus was controlled by a delicate balance. The balance was between the T_g and storage modulus increasing effect of the confining and reinforcing effect of the polymer being near to, and between, the clay platelets and the T_g and storage modulus decreasing, due to the surfactant plasticising the matrix.

The thermogravimetric analysis results, revealed that several of the composites formed had excellent potential as char forming materials, with the composites formed using Cloisite 25A as the organoclay showing most promise. It was also found from the thermogravitmetric analysis that the onset temperature (the temperature at which the sample has lost 10% of its mass) of the composites was increased compared to that of the pristine polymer, i.e. the composites were more thermally stable than the pristine polymer. The main thermal degradation of the composites was found to occur at the same temperature as in the polymer, but this was only to be expected since the composites were mainly polymer.

The tensile tests data presented in Chapter 6 revealed that the clay addition to the polymer produced an increase in the composites Young's Modulus when compared to the pristine polymer. This was expected since the clay particles have a Young's modulus of 172 GPa and PMMA has a Young's modulus of 3.58 GPa. The tensile test data also revealed that the extent of the increase in Young's modulus decreases with increasing clay content. From this it can be concluded that, since the composites with high clay loadings had a smaller proportion of clay platelets at the maximum spacing than the low clay loaded composites, the extent of the increase in Young's modulus is controlled by the extent and uniformity of the clay platelets intercalation with the polymer. The effect of the inclusion of clay particles and the microstructure they adopted, on the tensile strength of the composites was to cause a decrease in the tensile strength of the composites when compared to the pristine polymer. The tensile test data suggests that the clay particles act as sharp flaws. This conclusion was later confirmed by the decrease seen in the fracture properties of the composites.

The fracture data presented in Chapter 6 showed that the presence of clay particles in the matrix caused a decrease in both the fracture toughness (of between 18% and 50%) and fracture energy (of between 37% and 68%). Examination of the fracture surfaces of the composites revealed significant roughness when compared to the fracture surfaces of the pristine polymer, indicating that crack propagation proceeded along a tortuous path. However the extra energy required for this was not reflected in the values found for fracture energy. This led to the conclusion that the clay particles were not relieving the triaxial stresses, which would encourage the matrix to yield, but were acting as sharp flaws in the matrix. The fracture data also revealed that there was no synergistic effect occurring between the clay and the core-shell particles to toughen the matrix. The data showed that the presence of clay in the toughened matrix severely reduced the toughening effectiveness of the core-shell particles. Again the fracture surfaces of the toughened composites did not mirror the data found in the fracture tests, as they were very textured.

The experimental data on Young's modulus, tensile strength and fracture energy were compared to the predicted data given by several theoretical models to establish if any of the models could be applied with confidence to composites with intercalated nanocomposite microstructures. From the data presented in Chapter 6 it was concluded that both the van Es modified Halpin-Tsai and the Mori-Tanaka models agreed very well with the experimental modulus data. Thus it was concluded that either of these models could be applied with confidence to composites with intercalated nanocomposite microstructures. It was also found that Faber and Evans model for predicting fracture energy did not show any agreement with the experimental data for fracture energy.

Although this study has fulfilled its objectives to produce PMMA-clay nanocomposites, and to characterise and investigate their structure-property relationship, in particular the fracture properties of the composites formed, there are still questions to be answered. In Chapter 8, future work, details what a few of these questions are and possible methods of answering them are discussed.

Chapter 8

Future Work

The work presented here has answered several questions but has also thrown up many more. In this final chapter a few of these questions will be posed and possible routes to answering them will be suggested. The work presented in this thesis has shown the structure-property relationships of PMMA-clay composites formed using commercially available organoclays and although many attempts were made by varying the processing conditions at forming other microstructures all the composites formed possessed intercalated nanocomposite microstructures.

Further variations to both the processing conditions and the polymer formulation could be made so as to possibly achieve other microstructures. In Chapter 2 it was stated that several researchers[27, 28] had found for composites formed using the melt intercalation method a critical factor in achieving composites with exfoliated nanocomposite microstructures was the amount of shear applied to force the clay platelet stacks apart. This could be also a critical factor in the formation of exfoliated nanocomposite microstructures using the in-situ intercalated polymerisation method when the system is thermodynamically unfavourable. It has been previously stated that this particular formulation of PMMA has an almost water-like viscosity. If the system had been favourable this low viscosity would have aided the monomers in entering the clay

galleries. However all the evidence presented in Chapter 4 shows this system to be not particularly favourable with the organoclays tried and thus this water-like viscosity could be detrimental to the chances of forming an exfoliated nanocomposite microstructure through the application of shearing forces. So as to raise the viscosity of the system and increase the chances of forming an exfoliated nanocomposite microstructure a proportion of the methyl methacrylate monomer could be replaced by a methyl methacrylate oligomer. Thus the viscosity of the system would be raised and the monomer-oligomer solution would be more effective at transferring the shearing force to the clay particles. Preliminary work conducted by the author has shown the use of oligomers to be promising.

From the data presented in Chapter 4 it can be seen that the particular system of polymer and organoclay do not produced a system that is thermodynamically favourable enough to produced composites with exfoliated nanocomposite microstructures. In an effort to produce a system that is more thermodynamically favourable changes could be made to the monomer solution or the surfactant on the clay. The main monomer used in this system is methyl methacrylate, which could be partially or completely changed for another monomer from the methacrylate family of monomers. This alteration would change the thermodynamics of the system as has been shown by a study conducted by Jon Hickey at Cambridge University[104]. Alternatively leaving the monomer solution unaltered the system thermodynamics could be altered by tailoring of the clay surfactant to the monomer system.

In Chapter 5 and 6 the "in bulk" properties of the composites formed have been investigated, but attempts were also made to investigate the "in joint" properties of the composites formed. However, when adhesive joints were fabricated it was found that the monomer solution evaporated before the adhesive joint could be completed and the gel point of the polymer reached. In order to alleviate this problem for future work on "in joint" properties a positive pressure environment could be imposed during the formation and polymerisation of the adhesive joints.

Several questions arose from the thermal stability work presented in Chapter 5. The data presented revealed that the PMMA-Cloisite 25A composites had excellent char-forming properties. However, the mechanisms behind this were hard to define and two possible mechanisms were proposed. The first proposed was that the rapid decomposition of the polymer/surfactant causes the now unsupported clay platelet edges to fold down, protecting the central proportion of polymer/surfactant. The second proposition made was that Cloisite 25A was an inherently "dry" clay and the other organoclays used were "wet". The moisture in these wet clays turned to steam, when the temperature was above 100°C, that blasted apart the clay platelets that were protecting the polymer. In the dry Cloisite 25A no moisture was present to turn to steam, thus the polymer in between the clay platelets was still protected. To verify which, if either, mechanism is correct more TGA experiments need to be performed. Along with this cone calorimetry experiments that will verify whether if other properties related to char formation also alter for these composites should also be performed.

Other questions thrown up first in Chapter 5 and subsequentially in Chapter 6 are what caused the phase separation seen in the PMMA toughened with KM355 core-shell particles. In addition, how the clay's presence in the system prevents the phase separation from occurring in the KM355 toughened PMMA- 6wt% Cloisite 25A composite should be considered.

The overriding questions that are posed for the work presented in Chapter 6 are concerned with the fracture properties of the composites formed, in particular those formed using Cloisite 93A as the organoclay. The composites formed with Cloisite 93A have an intercalated nanocomposite microstructure, as do all the other composites formed with the other organoclays. However, the Cloisite 93A composites do not have as large a decrease in fracture properties as the other clay composites. As well as this the composites formed with Cloisite 93A appear as if there is a threshold value of fracture toughness that once reached is independent of clay content. This may also be

true for the other organoclays used but further fracture testing is required using the same and other geometries.

Chapter 6 also demonstrated clearly that for the fracture properties of the toughened PMMA composites there is no synergistic effect between the clay and the core-shell particles and that the addition of clay to the system is extremely detrimental to the fracture properties. However, another avenue to attempt for toughened PMMA composites is the formation of toughened composites using not core shell particles but a liquid rubber. With the use of a liquid rubber instead of a preformed particle the clay particles could reside either in the PMMA phase or in the rubber phase thus hopeful producing synergy between the rubber phase and the clay particles.

An interesting extension to this work would be to investigate the effect of clay/polymer adhesion on the microstructures achieved, and what effect increasing the adhesion (perhaps using silane primers) between the clay and polymer would have on the mechanical properties, in particular the fracture toughness.

Another possible extension to this work would be to attempt to form acrylic nanocomposites with varying degrees of crosslinking and compare the microstructures that are possible, and their subsequent mechanical and physical properties.

References

1. http://www.zyvex.com/nanotech/feynman.html

2. P.M. Ajayan, S.C. Giannaris, and L.S. Schadler, Load transfer in carbon nanotube epoxy composites, *Applied Physics Letters*, **73**, 3842-3844 (1998).

3. C.O. Oriakhi, Polymer Nanocomposition approach to advanced materials, *Journal of Chemical Education*, **77**, 1138-1146 (2000).

4. J.M. Garces, D.J. Moll, J. Bicerano, R. Fibiger, and D.G. McLeod, Polymeric nanocomposites for automotive applications, *Advanced Materials*, **12**, 1835-1839 (2000).

5. A. Okada, M. Kawasumi, A. Usuki, Y. Kojima, T. Kurauchi, O. Kamigaito, and Y. Fukushima, Synthesis of nylon 6-clay hybrid, *J. Mater. Res.*, **8**, 1179-1184 (1993).

6. H.M. Jeong, J.W. Seo, and B.K. Kim, Morophology and properties of waterborne polyurethane/clay nanocomposites, *European Polymer Journal*, **39**, 85-91 (2003).

7. R.K. Bharadwaj, A.R. Mehrabi, C. Hamilton, C. Trujillo, M. Murga, R. Fan, A. Chavira, and A.K. Thompson, Structure-property relationships in cross-linked polyester-clay nanocomposites, *Polymer*, **43**, 3699-3705 (2002).

8. Z. Zhu, J. Yin, X. Wang, Z. Qi, and Y. Yong, Preparation and properties of hybrids of organo-soluble polyimide and montmorillonite with various chemical surface modification methods, *Polymer*, **40**, 4407-4414 (1999).

9. M. Kawasumi, N. Hasegawa, M. Kato, A. Usuki, and A. Okada, Preparation and Mechanical Properties of Polypropylene-Clay Hybrids, *Macromolecules*, **30**, 6333-6338 (1997).

10. E.P. Giannelis, and P.B. Messersmith, Synthesis and characterization of layered silicate-epoxy nanocomposites, *Chem. Mater.*, **6**, 1719-1725 (1994).

11. http://www.psrc.usm.edu/macrog/index.htm

12. R.J. Young and P.A. Lovell, Introduction to Polymers Second Edition, Chapman & Hall, London, 1991.

13. M.P. Stevens, An Introduction to Polymer Chemistry Third Edition, Oxford University Press, Oxford 1999.

14. J. Comyn, Adhesion Science, Royal Society of Chemistry, Information Services, Cambridge, 1997.

15. A. Putinis, Introduction to Mineral Sciences, Cambridge University Press, Cambridge, 1993.

16. R.E. Grim, Clay Mineralogy Second Edition, McGraw-Hill Book Company, London, 1968.

17. X. Kornmann, Synthesis and Characterisation of Thermoset-Layered Silicate Nanocomposites, PhD thesis, Lulea University of Technology, Luleå, 2001.

18. W.A. Deer, R.A. Howie, and J. Zussman, Introduction to the Rock Forming Minerals Second Edition, Longman Scientific & Technical, Harlow, England, 1992.

19. B. Velde, D. Righi, A. Meunier, A. Inoue, and S. Hiller, Origin and Mineralogy of Clays. Clays and the Environment Editor Bruce Velde, Springer-Verlag, Heidelberg, 1995.

20. X. Fu and S. Qutubuddin, Synthesis of polystyrene-clay nanocomposites, *Materials Letters*, **42**, 12-15 (2000).

21. E.P. Giannelis, Polymer layered silicate nanocomposites, *Advanced Materials*, **8**, 29-35 (1996).

22. X. Kornmann, L.A. Berglund, J. Sterte, and E.P. Giannelis, Nanocomposites based on montmorillonite and unsaturated polyester, *Polym. Eng. Sci.*, **38**, 1351-1358, (1998).

23. G.W. Beall, Tailoring of inorganic surface modified nanoparticles for polymer nanocomposites, Nanocomposites 2000, Brussels, (2000).

24. T.J. Pinnavaia, Z. Wang, and P.C. LeBaron, Polymer-layered silicate nanocomposites: an overview, *Applied Clay Science*, **15**, 11-29 (1999).

25. A. Okada, M. Kawasumi, A. Usuki, Y. Kojima, T. Kurauchi, and O. Kamigaito, Swelling behaviour of montmorillonite cation exchanged for ω-amino acids by ε-caprolactam, *J. Mater. Res.*, **8**, 1174-1178 (1993).

26. T.J. Pinnavaia, T. Lan, and H. Shi, Interfacial effects on the reinforcement properties of polymer-organoclay nanocomposites, *Chem. Mater.*, **8**, 1584-1587 (1996).

27. J.W. Cho and D.R. Paul, Nylon 6 nanocomposites by melt compounding, *Polymer*, **42**, 1083-1094 (2001).

28. J.-C. Huang, Z.-K Zhu, J. Yin, X.-F Qian, and Y.-Y Sun, Poly(etherimide)/montmorillonite nanocomposites prepared by melt intercalation: morphology, solvent resistance properties and thermal properties, *Polymer*, **42**, 873-877 (2001).

29. A. Okada, M. Kawasumi, A. Usuki, Y. Kojima, T. Kurauchi, and O. Kamigaito, Nylon 6-clay hybrid, *Mat. Res. Soc. Symp. Proc.*, **117**, 45-50 (1990).

30. Z. Qi, F. Wang., Z. Xue, and Q. Wu, Synthesis and characterization of PAn/clay nanocomposite with extended chain conformation of polyaniline, *Polymer*, **41**, 2029-2032 (2000).

31. K.T. Gam and H.J. Sue, Preparation and mechanical properties of epoxy-clay nanocomposites, *Division of Polymeric Materials: Science and Engineering*, San Francisco: American Chemical Society, 82, 288-289 (2000).

32. T.J. Pinnavaia and Z. Wang, Hybrid organic-inorganic nanocomposites: exfoliation of magadiite nanolayers in an elastomeric epoxy polymer, *Chem. Mater.*, **10**, 1820-1826 (1998).

33. T.J. Pinnavaia and T. Lan, Nanolayer ordering in an epoxy-exfoliated clay hybrid composite, *Mat. Res. Soc. Symp. Proc.*, **435**, 79-84 (1996).

34. T. Takeichi and T. Agag, Polybenzoxazine-montmorillonite hybrid nanocomposites: synthesis and characterization, *Polymer*, **41**, 7083-7090 (2000).

35. P. Dubois and M. Alexandre, Polymer layered silicate nanocomposites: preparation, properties and uses of a new class of materials, *Materials Science and Engineering*, **28**, 1-63 (2000).

36. C. Oriakhi, Nano sandwiches, *Chemistry in Britain*, **November**, 59-62 (1998).

37. R.A. Vaia, D. Curliss, and J.M. Brown, Thermoset-layered silicate nanocomposites. Quaternary ammonium montmorillonite with primary diamine cured epoxies, *Chem. Mater*, **12**, 3376-3384 (2000).

38. J.-J. Luo and I.M. Daniel, Characterization and modelling of mechanical behaviour of polymer/clay nanocomposites, *Composites Science and Technology*, **63**, 1607-1616 (2003).

39. M.F. Ashby and D.R.H. Jones, Engineering materials 1: an introduction to their properties and applications Second Edition, Butterworth-Heinemann, Oxford, 1996.

40. Y. Kojima, A. Usuki, M. Kawasumi, A. Okada, Y. Fukushima, T. Kurauchi, and O. Kamigaito, Mechanical properties of nylon 6-clay hybrid, *J. Mater. Res.*, **8**, 1185-1189 (1993).

41. Y.H. Zhang and K.C. Gong, Effect of quaternary ammonium-modified montmorillonites on mechanical properties of polypropylene, *Mat. Res. Soc. Symp. Proc.*, **520**, 191-195 (1998).

42. K.E. Strawhecker and E. Manias, Structure and properties of poly(vinyl alcohol)/Na^+ montmorillonite nanocomposites, *Chem. Mater.*, **12**, 2943-2949 (2000).

43. T. Takeichi, T. Koga, and T. Agag, Studies on thermal and mechanical properties of polyimide-clay nanocomposites, *Polymer*, **42**, 3399-3408 (2001).

44. G.S. Sur, H.L. Sun, S.G. Lyu, and J.E. Mark, Synthesis, structure, mechanical properties, and thermal stability of some polysulfone/organoclay nanocomposites, *Polymer*, **42**, 9783-9789 (2001).

45. T. Lan and T.J. Pinnavaia, Clay-reinforced epoxy nanocomposites, *Chem. Mater.*, **6**, 2216-2219 (1994).

46. A.C. Taylor, Mechanical properties of particulate-modified and nanocomposite thermoset polymers, Report, Imperial College London, 2003.

47. D. Shia, C.Y. Hui, S.D. Burnside and E.P. Giannelis, An interface model for the prediction of Young's modulus of layered silicate-elastomer nanocomposites, *Polymer Composites*, **19**, 608-617 (1998).

48. P. Reichert, H. Nitz, S. Klinke, R. Brandsch, R. Thomann, and R. Mülhaupt, Poly(propylene)/organoclay nanocomposite formation: Influence of compatibilizer functionality and organoclay modification, *Macromol. Mater. Eng.*, **275**, 8-17 (2000).

49. X. Kornmann, R. Thomann, R. Mulhaupt, J. Finter, and L. Berglund Synthesis of amine-cured, epoxy-layered silicate nanocomposites: The influence of the silicate surface modification on the properties, *Journal of Applied Polymer Science*, **86**, 2643-2652 (2002).

50. J. Massam and T.J. Pinnavaia, Clay nanolayer Reinforcement of a glassy epoxy polymer, *Mat. Res. Soc. Symp. Proc.*, **520**, 223-232 (1998).

51. S. Bandyopadhyay, E.P. Giannelis, and A.J. Hsieh, Thermal and thermo-mechanical properties of PMMA nanocomposites, *Polymeric Materials Science and Engineering*, **219:75**, 208-209 (2000).

52. D. Ratna, O. Beaker, R. Krishnamurthy, G.P. Simon, and R.J. Varley, Nanocomposites based on a combination of epoxy resin, hyperbranched epoxy and a layered silicate, *Polymer*, **44**, 7449-7457 (2003).

53. K. Yano, A. Usuki, A. Okada, T. Kurauchi, and O. Kamigaito, Synthesis and properties of polyimide-clay hybrid, *Journal of Polymer Science: Part A: Polymer Chemistry*, **31**, 2493-2498 (1993).

54. K. Yano, A. Usuki, and A. Okada, Synthesis and properties of polyimide-clay hybrid films, *J. Polym. Sci : Polym. Chem.*, **35**, 2289-2294 (1997).

55. C. Chen and D. Curliss, Organoclay-aerospace epoxy nanocomposites, *Proceedings of 46th International SAMPE Symposium*, 362-374 (2001).

56. T. Takeichi, R. Zeidam, and T. Agag, Polybenzoxazine/clay hybrid nanocomposites: influence of preparation method on the curing behaviour and properties of polybenzoxazines, *Polymer*, **43**, 45-53 (2002).

57. A.J. Kinloch and A.C. Taylor, Mechanical and fracture properties of epoxy/inorganic micro- and nano-composites, *Journal of Materials Science Letters*, **22**, 1439-1441 (2003).

58. C. Zilg, R. Thomann, J. Finter, and R. Mülhaupt, The influence of silicate modification and compatibilizers on mechanical properties and morphology of anhydride-cured epoxy nanocomposites, *Macromol. Mater. Eng.*, **280/281**, 41-46, (2000).

59. J.P. Harcup and A.F. Yee, Deformation and fracture of polymer silicate layer nanocomposites, *ANTEC'99 Conf. Proc.*, **3**, 3396-3398 (1999).

60. E. P. Giannelis, T. Takekoshi, and J. Lee, Fire retardant polyetherimide nanocomposites, *Mat. Res. Soc. Symp. Proc.*, **457**, 513-518 (1997).

61. A. Blumstein, Polymerisation of adsorbed monolayers: II. Thermal degradation of the inserted polymers, *J. Polym. Sci. A*, **3**, 2665 (1965).

62. J.W. Gilman, Flammability and thermal stability studies of polymer layered-silicate (clay) nanocomposites, *Applied Clay Science*, **15**, 31-49 (1999).

63. J. Zhu, P. Start, K.A. Mauritz, and C.A. Wilkie, Thermal stability and flame retardancy of poly(methyl methacrylate)-clay nanocomposites, *Polymer Degradation and Stability*, **77**, 253-258 (2002).

64. N. Salahuddin and M. Shehata, Polymethylmethacrylate-montmorillonite composites: preparation, characterization and properties, *Polymer*, **42**, 8379-8385 (2001).

65. G.S. Sur, H.L. Sun, S.G. Lyu, and J.E. Mark, Synthesis, structure, mechanical properties, and thermal stability of some polysulfone/organoclay nanocomposites, *Polymer*, **42**, 9783-9789 (2001).

66. C.A. Wilkie and J. ZHu, Thermal and fire studies on polystyrene-clay nanocomposites, *Polymer International*, **49**, 1158-1163 (2000).

67. R. Mulhaupt and F. Dietsche, Thermal properties and flammability of acrylic nanocomposites based upon organophilic layered silicates, *Polymer Bulletin*, **43**, 395-402 (1999).

68. J. Gilman, T. Kashiwagi, J.E.T. Brown, and S. Lomakin, Flammability studies of polymer layered silicate nanocomposites, *Proceedings of 43rd International SAMPE Symposium*, 1053-1066 (1998).

69. T.J. Pinnavaia, T. Lan, P.D. Kaviratna, and M.S. Wang, Clay-polymer nanocomposites: polyether and polyimide systems, *Mat. Res. Soc. Proc.*, **346**, 81-88 (1994).

70. L.E. Nielsen, Models for the permeability of filled polymer systems, *J. Macromol. Sci. (Chem.)*, **A1(5)**, 929-942 (1967).

71. T. Lan, P.D. Kaviratna, and T.J. Pinnavaia, On the nature of polyimide-clay hybrid composites, *Chem. Mater.*, **6**, 573-575 (1994).

72. T.D. Fornes, and D.R. Paul, Modelling properties of nylon 6/clay nanocomposites using composite theories, *Polymer*, **44**, 4993-5013 (2003).

73. M. van Es, A comparison of polymer-clay nanocomposites with conventional composites, Nanocomposites 2000, Brussels, Belgium (Emap Maclaren, 2000).

74. T. Mori and K. Tanaka, Average stress in matrix and average elastic energy of materials with misfitting inclusions, *Acta Metall.*, **21**, 571-574 (1973).

75. G.P. Tandon and G.J. Weng, The effect of aspect ratio of inclusions on the elastic properties of unidirectionally aligned composites, *Polymer Composites*, **5**, 327-333 (1984).

76. http://www.efunda.com/formulae/formula_index.cfm

77. K. T. Faber and A.G. Evans, Crack deflection processes-I. Theory, *Acta Metall.*, **31**, 565-576 (1983).

78. P.A. Lovell, Rubber-toughened plastics: Strategies for their preparation and evaluation, *Proceedings of 4th Annual UNESCO School & IUPAC Conference on Macromolecules & Materials Science*, Stellenbosch, South Africa (2001).

79. P.A. Lovell, J. McDonald, D.E.J. Saunders, M.N. Sherratt, and R.J. Young, Mechanical properties of rubber-toughened poly(methyl methacrylate), *Plast. Rubb. Comp. Process. Appl.*, **16**, 37-44 (1991).

80. J.M. Gloaguen, P. Heim, P. Gaillard and J.M. Lefebvre, Plasticity of rubber-toughened poly(methyl methacrylate): effect of rubber particle size, *Polymer*, **33**, 4741-4746 (1992).

81. C.B. Bucknall, J.U. Starke, R. Godehardt, and G.H. Michler, Mechanisms of cavitation over a range of temperatures in rubber-toughened PSAN modified with three-stage core-shell particles, Journal of Materials Science, 32, 1855-1860 (1997).

82. A.J. Kinloch and R.J. Young, Fracture behaviour of polymers, Chapman & Hall, London, Chapter 1 (1983).

83. A.J. Kinloch, Structural Adhesives, Applied Science, London (1986).

84. C.B. Bucknall, R. Rizzieri, and D.R. Moore, Detection of incipient rubber particle cavitation in toughened PMMA using dynamic mechanical tests, *Polymer*, **41**, 4149-4156 (2000).

85. C.J. Hooley, D.R. Moore, M. Whale and M.J. Williams, Fracture toughness of rubber modified PMMA, *Plast. Rubb. Process. Appl.*, **1**, 345-349 (1981).

86. Private communication ICI, 2003.

87. Private communication Rohm & Haas, 2003.

88. ISO13586:2000(E), Determination of fracture toughness (G_{1c} and K_{1c}) linear elastic fracture mechanics (LEFM) approach, 2000.

89. ASTM D638-01, Standard test method for tensile properties of plastics, 2001.

90. Private communication R. Sweeney, 2000.

91. http://www.nanoclay.com

92. G. Brown, The X-ray identification and crystal structures of clay minerals, Mineralogical Society, London, 1961.

93. B.D. Cullity, Elements of X-ray diffraction Second Edition, Page 292, Addison-Wesley Publishing Company, London, 1978.

94. A.J. Kinloch and A.C. Taylor, The mechanical properties and fracture behaviour of epoxy-inorganic micro- and nano-composites, *yet to be published.*

95. G.W. Brindley and G. Brown, Crystal structures of clay minerals and their X-ray identification Edited by G.W. Brindley and G. Brown, Mineralogical Society, London, 1980.

96. Private communication G. Seeley, 2001.

97. Private communication J. Hickey, 2002.

98. Private communication A.C. Taylor, 2001.

99. P. Bajaj, N.K. Jha, and R. Ananda Kumar, Effect of coupling agents on the mechanical properties of mica/epoxy and glass fibre/mica/epoxy composites, *Journal of Applied Polymer Science*, **44**, 1921-1930 (1992).

100. M. Ohta, Y. Nakamura, H. Hamada, and Z. Maekawa, Acoustic emission characteristics and fracture properties of epoxy moulding compound filled with spherical silica particles, Polymer & Polymer Composites, 2, 215-221 (1994).

101. A.J. Kinloch and A.C. Taylor, The toughening of cyanate-ester polymers: Part 1 - Physical modification using particles, fibres and woven-mats, *Journal of Materials Science*, **37**, 433-460 (2002).

102. E.H. Andrews, Fracture in polymer, Oliver & Boyd, London, 1968.

103. S. Ahmed and F.R. Jones, A review of particulate reinforcement theories for polymer composites, *J. Mater. Sci.*, **25**, 4933-494 (1990).

104. Private communication J. Hickey, 2002.